# Structural characterization of TRIM family proteins

Katarzyna A. Skorupka
Pabianice, Poland

M.S., Lodz University of Technology, 2013

A Dissertation Presented to the Graduate Faculty of the University of Virginia
in Candidacy for the Degree of Doctor of Philosophy

Interdisciplinary Program in Biophysics

University of Virginia
November 2018

# Abstract

TRIM proteins are E3 ubiquitin ligases that participate in many cellular processes and signaling pathways, such as immune system response. Several TRIM proteins were shown to form antiparallel coiled-coil dimers which position catalytic RING domains on the opposite sides of an elongated rod. As RING dimerization is necessary for its enzymatic activity, higher-order oligomerization is an attractive model for RING activation. In this dissertation, I present structural studies of two members of the TRIM superfamily.

TRIM5α is a restriction factor that leads to premature disassembly of the HIV-1 capsid at a post-entry but pre-integration step. The ubiquitination activity was linked to aborted reverse transcription of retroviral RNA. Despite multiple studies, understanding the mechanism of capsid recognition has remained incomplete. By cryo-electron tomographic reconstructions and subtomogram averaging I show how TRIM5α interacts with HIV-1 CA tubes that mimic the HIV-1 capsid. This work defines the spatial organization of the TRIM5α domains within a full-length protein, consistent with the models predicted from crystal structures of individual domains. Results further show that TRIM5α forms a continuous cage around the CA tubes. In contrast to models proposed before, the capsid-like tubes are not destabilized upon TRIM5α binding as no apparent discontinuities in the CA lattice were observed. I suggest that additional events are necessary to trigger capsid dissociation. I also show that the SPRY domains interact with the capsid lattice in a degenerate manner, probably binding different interfaces. These studies provide new insights into retroviral capsid recognition that is the first step in species-specific restriction by TRIM5α.

TRIM63 is a protein that is upregulated in response to atrophic stimuli and is responsible for muscle catabolism mediated by the proteasome system. I analyze the self-assembly properties

of TRIM63 by cross-linking probing and DEER-EPR. Results show that contrary to previously published work, TRIM63 dimerizes in an antiparallel orientation, consistent with other characterized members of the TRIM family. Similar to TRIM5α, TRIM63 may also require higher-order self-assembly architectures for its catalytic activity. Such a mechanism of E3 ligase activation may be conserved across the entire TRIM family.

# Dedication

To my family, Danuta, Tomasz, and Piotr Skorupka, and my lovely boyfriend, Pawel Janczyk, for their support and encouragement.

# Abbreviations

AIDS, acquired immune deficiency syndrome;

BIV, bovine immunodeficiency virus;

CA, capsid protein;

CA-CTD, CA C-terminal domain;

CA-NTD, CA N-terminal domain;

CC, coiled-coil;

CCD, charge-coupled device;

CET, cryo-electron tomography;

CHES, N-cyclohexyl-2-aminoethanesulfonic acid;

CRF, circulating recombinant form;

CTF, contrast transfer function;

CW EPR, continuous wavelength electron paramagnetic resonance;

DDD, direct detector device;

DEER, double electron-electron resonance;

DPR, differential phase residual;

DQE, detective quantum efficiency;

EDTA, ethylenediaminetetraacetic acid;

EIAV, equine infectious anemia virus;

EM, electron microscopy;

EPR, electron paramagnetic resonance;

FIV, feline immunodeficiency virus;

FSC, Fourier shell correlation;

FNC, Fourier neighbor correlation;

HECT, homologous to the E6AP carboxyl terminus;

HEPES, 4-(2-hydroxyethyl)-1-piperazineethanesulfonic acid;

IKK, IκB kinase complex;

IPTG, isopropyl β-D-1-thiogalactopyranoside

LB, lysogeny broth;

N-MLV, N-tropic murine leukemia virus;

NMR, nuclear magnetic resonance;

MES, 4-morpholineethanesulfonic acid;

MTSL, (1-oxyl-2,2,5,5-tetramethyl-3-pyrroline-3-methyl) methanethiosulfonate spin label;

MuRF, Muscle-specific RING finger protein;

O.D., optical density;

OSF, One-STrEP-FLAG;

PAMPs, Pathogen-Associated Molecular Patterns;

PCR, polymerase chain reaction;

PI3K, phosphatidylinositol 3-kinase;

PIC, pre-integration complex;

PRRs, Pattern Recognition Receptors;

RBR, RING-between-RING;

RING, Really Interesting New Gene;

SEC, size exclusion chromatography;

SEC-MALS, size exclusion chromatography with multi-angle light scattering;

SDS, sodium dodecyl sulfate;

SDS-PAGE, SDS polyacrylamide gel electrophoresis;

SIV, simian immunodeficiency virus;

SNR, signal-to-noise ratio;

SPA, single particle analysis;

SSNR, spectral signal-to-noise ratio;

TAK1, transforming growth factor-β-activated kinase 1;

TCEP, Tris (2-carboxyethyl) phosphine;

TEM, transmission electron microscopy;

TK, titin kinase domain;

TRIM, Tripartite Motif;

Ub, ubiquitin;

URF, unique recombinant form;

WT, wild-type;

β-ME, 2-mercaptoethanol.

# Table of Contents

# Chapter 1.

# Introduction

## 1.1. Overview of Human Immunodeficiency Virus Type 1

### 1.1.1. History and epidemiology

Human immunodeficiency virus (HIV), the causative agent of acquired immune deficiency syndrome (AIDS), is a lentivirus first isolated in 1983. It originated from a zoonotic transmission of simian immunodeficiency virus (SIV) from non-human primates around the 1920s [1]. There are two types of HIV: HIV-1, which is more virulent, easily transmittable, and is the leading cause of HIV infections worldwide; and HIV-2, which is less transmittable, and primarily confined to West Africa. Four separate transmission events for HIV-1 were recorded: three from chimpanzees and one from gorillas, giving rise to different HIV-1 groups: M (major), N (non-M, non-O) and O (outliers) from chimpanzees and P from gorillas. Group M has been divided into subtypes (A-D, F-H, J, K), sub-subtypes (A1-4, F1-2) and numerous circulating (CRF) and unique recombinant forms (URF). The genetic diversity is caused by the fast replication cycle of HIV and error-prone reverse transcriptase [2,3]. Globally, an estimated 36.7 million people were living with HIV in 2015, with the highest number in sub-Saharan Africa. Because of antiviral therapy, new infections decreased from 3.3 million in 2002 to 2.1 million in 2015, and AIDS-related deaths that peaked at 2.3 million in 2005 dropped to 1.1 million in 2015 [4,5]. HIV can be transmitted through the exchange

of body fluids that contain either an infectious virus or infected cells or a combination of both from infected individuals, predominantly blood, breast milk, semen and vaginal secretions [6]. Individuals cannot be infected through ordinary interactions like kissing, hugging, shaking hands, sharing personal objects, food or water [5]. According to the guidelines released by WHO in 2016, the key populations affected by HIV-1 epidemics include men who have sex with men, people who inject drugs, sex workers, transgender people and people in prisons and other closed settings.

### 1.1.2 Overview of the HIV-1 life cycle.

HIV-1 targets CD4-positive immune cells such as T-cells and macrophages. The envelope glycoprotein gp120 binds to the CD4 receptor and CCR5 or CXCR4 co-receptor exposed on the cell surface. This triggers a conformational change that results in fusion of the viral and cellular membranes, which is catalyzed by gp41. Upon fusion, the viral core, which consists of the capsid and its contents, is released into the cell cytoplasm. The single-stranded RNA genome is then reverse transcribed into double-stranded DNA. During this time, the capsid mediates trafficking to the nucleus and docks at the nuclear pore complex. The capsid disassembles in a process called uncoating, and the pre-integration complex (PIC) containing the viral DNA in complex with integrase is imported into the nucleus. Integrase introduces a break in host cell DNA and integrates the viral DNA into the host genome. This step establishes a life-long infection. The host RNA polymerase transcribes the viral DNA into viral mRNA, which is exported to the cytoplasm. Newly synthesized viral proteins are translocated to the cell surface and assemble with genomic RNA to form immature virions. The new virus buds off from the cell membrane and is released. The

viral protease then cleaves the precursor structural proteins in a process called maturation, resulting in a formation of the mature capsid that re-packages the genome and replicative enzymes in the virus core. The newly infectious virion can then go on to infect a new cell. A schematic representation of the HIV-1 life cycle is presented in Fig. 1.1.

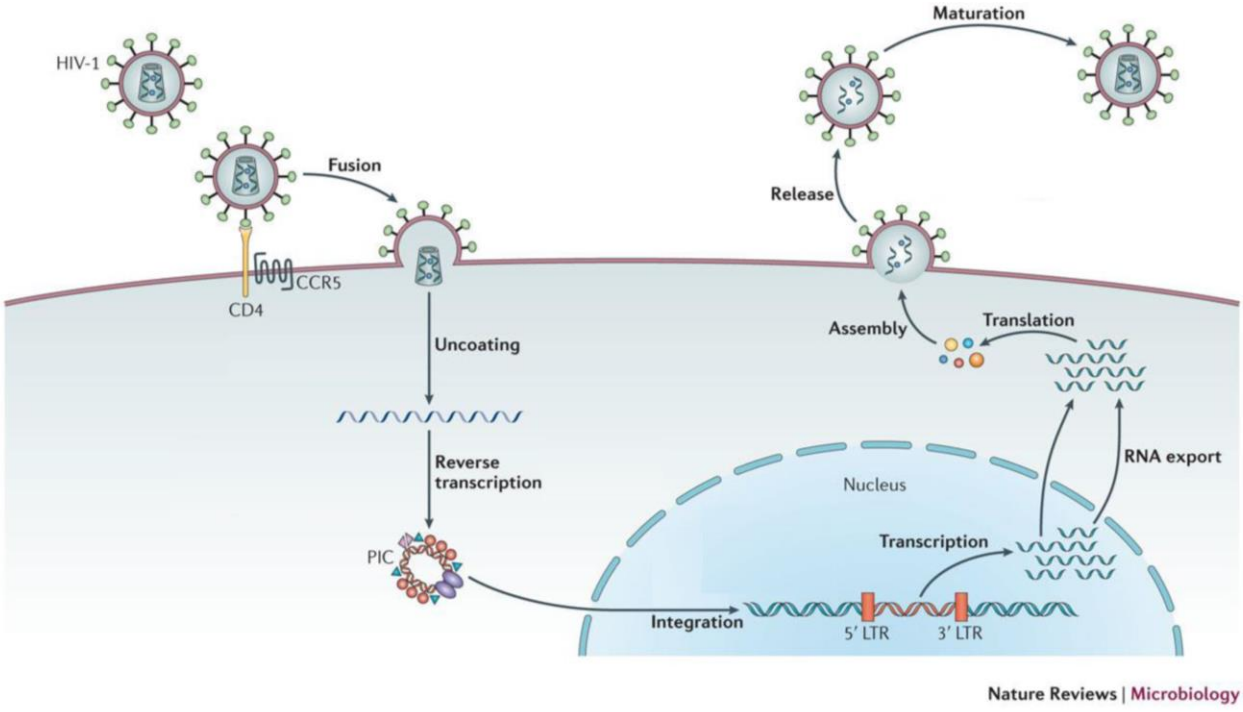


**Figure 1.1. Schematic overview of the HIV-1 life cycle**. Figure adapted with permission from Barré-Sinoussi, Ross and Delfraissy, 2013.

1.1.2. Molecular characteristics of the HIV-1 core

The HIV-1 core (Fig. 1.2.A) is built from the condensed genetic RNA bound to nucleocapsid (NC) protein and encapsulated within a conical capsid composed of ~1,500 CA protein monomers. The CA protein is produced during maturation of the viral particle and arises from the central region of the precursor Gag polyprotein. CA assembles into the mature capsid *de novo* after the immature lattice is dissociated (reviewed in Ganser-Pornillos, Yeager and Pornillos, 2012; Mattei *et al.*, 2016). HIV-1 capsids typically appear conical and are organized following the mathematical principles of a fullerene cone (Fig. 1.2.E) [9,10]. The closed cone is built from ~250 hexamers and 12 pentamers, with 7 at the broad end and 5 at the narrow end (Fig. 1.2.C, D). However, HIV-1 capsids display a wide range of polymorphism (Fig. 1.2.B), with cylindrical and spherical capsids also observed that arise from differing distributions of the hexamers and pentamers [11].

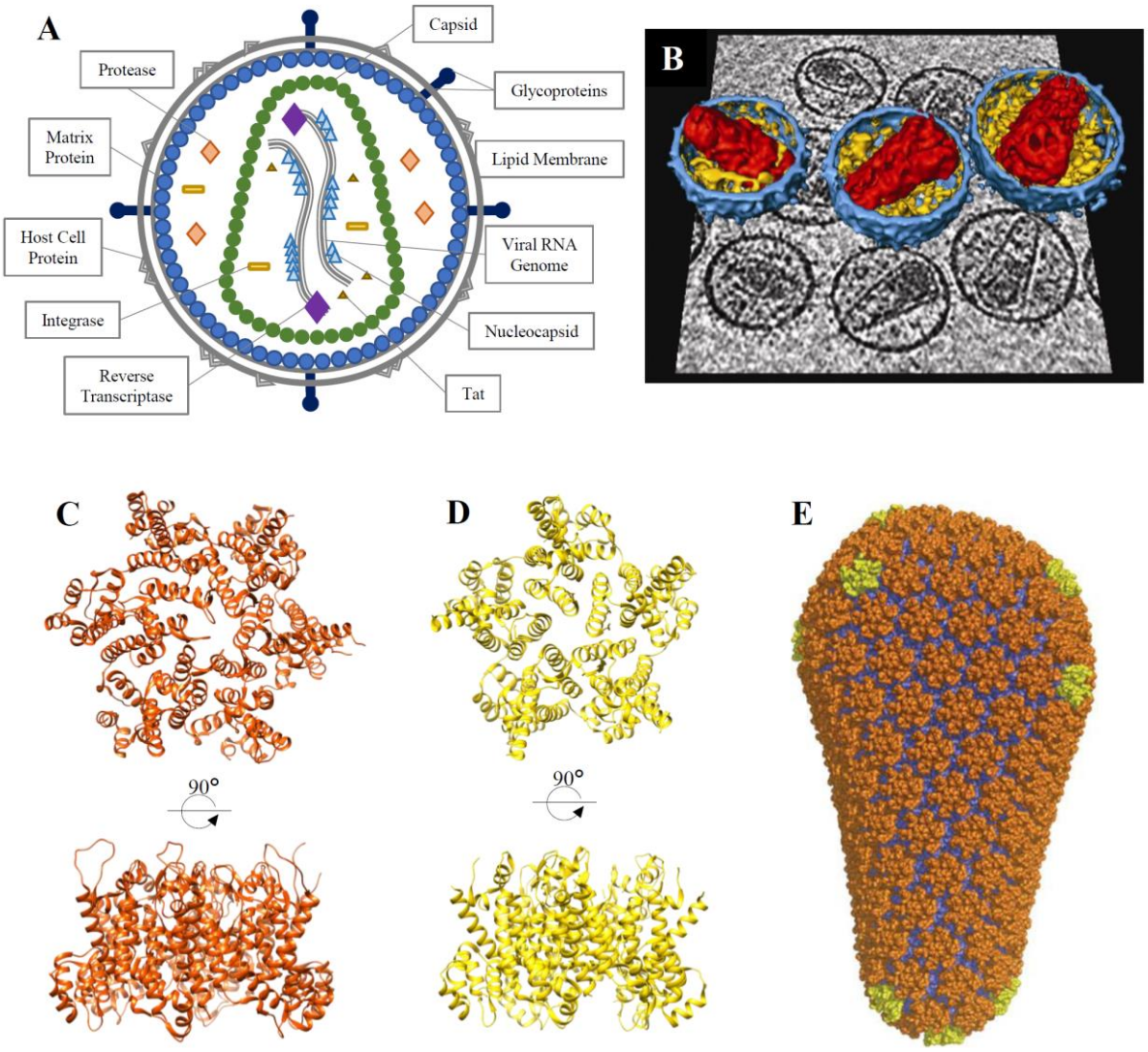


**Figure 1.2. Molecular characteristics of the HIV-1 core.** A – Schematic representation of mature HIV-1 virion showing the glycoproteins, the membrane-bound matrix proteins, retroviral genomic RNA bound to nucleocapsid protein protected within the capsid; non-structural proteins are present (Tat, protease, integrase). B – 3D rendering of cryo-electron tomography reconstruction of purified HIV-1 cores; viral membrane (blue), core (red) and intra-core density (yellow); figure adapted with permission from Briggs *et al.*, 2006. C, D – Top and side views of the hexameric (B) and pentameric (C) CA subunits that form the assembled HIV-1 capsid (PDB: 3H4E hexamer and 3P05 pentamer). E – The conical HIV-1 capsid assembled into fullerene cone contains around 250 CA hexamers (orange) and precisely 12 pentamers (yellow); figure adapted with permission from Pornillos, Ganser-Pornillos and Yeager, 2011.

The structure of the HIV-1 CA protein has been studied extensively through X-ray crystallography, cryo-EM and NMR techniques [8,12,21–27,13–20]. CA consists of two α-helical domains: an N-terminal assembly domain (CA-NTD spanning residues 1-145), and a C-terminal dimerization domain (CA-CTD spanning residues 150-231), which are connected by a flexible linker (146-149). The CA-NTD is composed of 7 α-helices that pack to form a domain that resembles an arrowhead. During maturation, the free N-terminal proline residue gets buried and the CA-NTD forms two β-strands stabilized by a salt bridge [28–30]. An extended loop connecting helix 4 and 5 binds cyclophilin A, a prolyl isomerase. The globular CA-CTD domain comprises a short $3_{10}$ helix followed by an extended strand and four α-helices (CA helices 8 - 11).

In assembled capsids, CA-NTDs form the outer surface while the interior part of the core is composed of CA-CTDs. An elaborate set of intermolecular interactions stabilizes the protein lattice. Contacts between adjacent CA molecules within a single hexamer are mediated by CA-NTD/CA-NTD interactions and are responsible for the formation of an inner 6-fold symmetric ring. Three N-terminal helices from each domain form an 18-helix bundle at the center of each hexamer. The interaction between CA-NTD of one domain and CA-CTD of the adjacent one reinforces the hexamer stability/structure [13,17] resulting in CA-CTD domains surrounding the central lobe of CA-NTD in a belt-like fashion [14]. The interaction between neighboring hexamers is mediated through dimerization of the CA-CTD domains that form the belts. The CA-CTD dimerization relies on hydrophobic interactions between adjacent CA molecules [11,20,28,31].

The HIV-1 CA protein can spontaneously assemble into wide range of particles *in vitro*, including 2D planar lattices and curved structures as cylinders, cones and small spheres [9–11,13,32–36]. These *in vitro* particles are made of the same hexamers and pentamers as found in authentic HIV-1 capsids and are used as model systems for self-assembly of the mature HIV-1 CA lattice.

## 1.2. Overview of the superfamily of TRIM proteins

Tripartite motif-containing proteins (TRIMs) make up a large family of ubiquitin E3 ligases conserved within the metazoan kingdom. Almost half of 80 known human TRIMs were shown to enhance the innate immune system response (reviewed in Hatakeyama, 2017), and a significant number of TRIM proteins were recently demonstrated to regulate autophagy [38–40]. TRIM proteins are characterized by the presence of the RBCC motif on their N-terminus that includes Really Interesting New Gene domain (RING), one or two B-box domains (B), and a coiled-coil domain (CC) [41–43].

The RING domains are small zinc-finger protein motifs that bind two zinc atoms by eight cysteine/histidine residues in a "cross-brace" topology [44]. The primary sequence organization of the RING domain is Cys-$X_2$-Cys-$X_{(9\text{-}39)}$-Cys-$X_{(1\text{-}3)}$-His-$X_{(2\text{-}3)}$-Cys-$X_2$-Cys-$X_{(4\text{-}48)}$-Cys-$X_2$-Cys (where X is any amino acid) [45,46]. Two types of RING domains can be distinguished – the C2 or H2 (cysteine or histidine) – but only C2 can be found in TRIM proteins. As an E3 ligase, a RING domain participates in the ubiquitin cascade (see section 1.3) [47–50].

The B-box zinc-finger domains are short protein motifs of around 40 amino acids. They are connected to the C-terminus of the RING finger by a conserved linker region of 32-39 a.a. The consensus sequence of the B-box is Cys-$X_2$-His-$X_7$-Cys-$X_7$-Cys-$X_2$-Cys-$X_5$-His-$X_2$-His, where X can be any amino acid. The B-box family is further sub-divided into two groups that differ from each other in amino acids that interact with the metal ligand: B-box 1 [Cys-$X_2$-Cys-$X_{(7–10)}$-Cys-$X_2$-Cys-$X_{(4–5)}$-Cys-$X_2$-Cys(His)-$X_{(3–6)}$-His-$X_{(2–8)}$-His] and B-box 2 [Cys-$X_{(2–4)}$-His(Cys)-$X_{(4–9)}$-Cys-$X_2$-Cys(His)-$X_4$-Cys(His)-$X_2$-His(Cys)] [46,51,52]. Some TRIM proteins contain only a B-box 2

domain, while others have B-box 1 followed by B-box 2 [42]. B-box domains were initially suspected to mediate E3 ligase activity, but this was shown to be incorrect [53]. They are commonly associated with protein-protein interactions, including self-assembly as well as higher-order oligomerization [54–58].

The B-box domains are followed by the CC domain of approximately 100 residues that has much less conserved sequence within the TRIM family. Crystal structures and biochemical analyses of the CC regions of TRIM5α, TRIM20, TRIM25, and TRIM69 show that these proteins homo-dimerize into elongated, antiparallel helices [59–62]. Homo- and hetero-oligomerization through the CC domain is used by TRIM proteins to target sub-cellular localization such as cytoskeletal filaments or cytoplasmic bodies [63]. Antiparallel dimerization arranges the hydrophobic residues in a distinctive 7-7-7-7-11-11-11-11-7-7-7-7 pattern of heptad and hendecad repeats, which appears to be a conserved feature of the TRIM family proteins [59]. Additionally, many CCs have a "trigger sequence" of 7-14 amino acids that is of critical importance as it initiates dimerization and may define a hydrogen bond network of buried polar residues [59,64].

TRIMs have been divided into eleven families based on their C-terminal domain [43,65] (Fig. 1.3). The most common C-terminal domains are B30.2 (also known as SPRY, RFP-like or PRYSPRY) [66], NHL-repeat [67] and PHD-BROMO [52]. Additionally, some TRIMs do not have a defined C-terminal domain, or this part does not bear a resemblance to any known protein domains [42]. TRIM C-terminal domains typically bind ubiquitination substrates or direct TRIM proteins to various sub-cellular compartments.

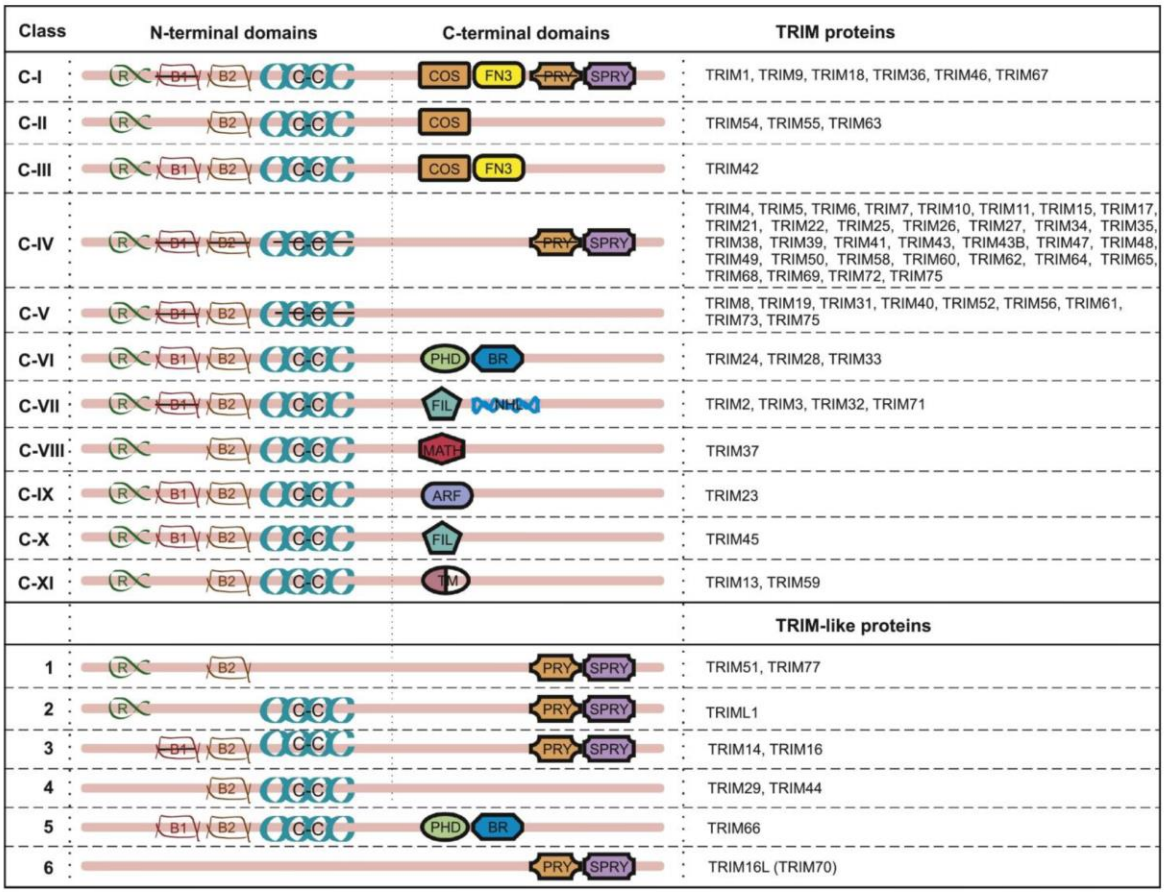


**Figure 1.3. Classification of TRIM proteins.** Sub-classification based on the C-terminal variable domain; the domain composition, subclass and TRIM proteins that belong to the specific class are shown. Reproduced with permission from Borlepawar, Frey and Rangrez, 2018.

### 1.2.1. The ubiquitin cascade

Ubiquitination is responsible for targeted degradation of misfolded proteins by the proteasome system and allows for protein-protein interactions required for signal transduction, DNA repair and gene transcription (reviewed in Goldberg, 2003; Geng, Wenzel and Tansey, 2012; Schwertman, Bekker-Jensen and Mailand, 2016). Ubiquitination is initiated by a ubiquitin-activating E1 enzyme, which activates the C-terminal tail of ubiquitin by forming a thioester bond in an ATP dependent manner (Fig. 1.4.A). The ubiquitin molecule is then transferred to an E2 ubiquitin-conjugating enzyme, and finally, an E3 ubiquitin ligase catalyzes its transfer to the substrate. The substrate ubiquitination site is typically a primary amine, most commonly a lysine residue, which forms a stable iso-peptide covalent bond with the C-terminus of ubiquitin. There are three major families of E3 enzymes: HECT (homologous to the E6AP carboxyl terminus), RING, and RBR (RING-between-RING) [71]. Both the HECT-type and RBR-type E3s form a thioester bond between ubiquitin and their catalytic cysteines prior to transfer to the substrate. RING-type E3s interact with the substrate and the E2-Ub complex and mediates the transfer of the ubiquitin molecule directly from the E2 [71–73]. Biochemical and biophysical analyses of RING-containing proteins show that upon dimerization, the enzymatic activity of RING domain is enhanced [74–77]. The human genome encodes two E1 enzymes, around forty E2 proteins, and more than six hundred E3 ligases. The specificity of substrate recognition is granted by the E3 ligase alone or with its bound E2 partner.

Substrates can be modified by one (monoubiquitination) or many (multi-monoubiquitination) ubiquitin molecules conjugated to substrates' lysine residues (Fig. 1.4.B). Moreover, the targeted protein can be modified by a chain of ubiquitin molecules (polyubiquitination), which are linked to each other through the 7 different lysine residues of

ubiquitin (Fig. 1.4.C). The type of ubiquitin modification dictates that fate of the protein, with Lys48-linked chains most commonly associated with proteasome-dependent proteolysis and Lys63-linked chains related to control of protein signaling and/or sub-cellular localization [44,78,79].

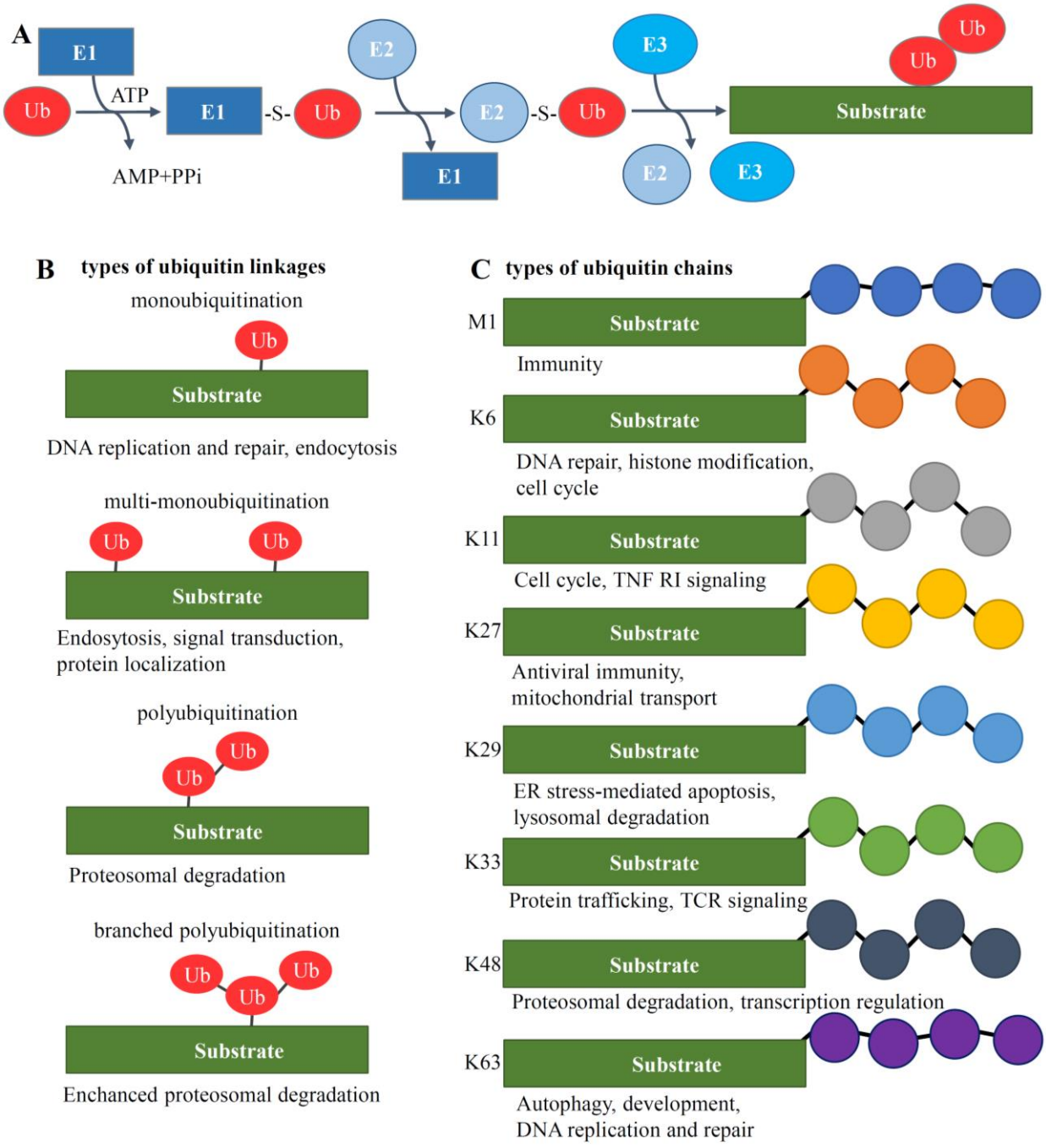

**Figure 1.4. An overview of the ubiquitin cascade.** A – Schematic representation of the ubiquitination system that leads to enzymatic modification of the substrate. B – Types of ubiquitin modifications and their subsequent roles. C – types of ubiquitin chains; homotypic ubiquitin chains are shown; however, mixed-linkage chains may also be produced depending on the E2-E3 complex [44].

## 1.3. TRIM5α, a restriction factor involved in the innate immune response to invading retroviruses

The innate immune system is the first-line defense mechanism against invading pathogens. Sensing of pathogens is achieved through various Pattern Recognition Receptors (PRRs) that recognize Pathogen-Associated Molecular Patterns (PAMPs) and induce an interferon response. Interferons are among the most critical cytokines that control viral infections. Unlike classical PRRs, TRIM5α directly disables the retrovirus, in a process termed restriction.

Cytoplasmic TRIM5α recognizes protein motifs on the incoming viral capsid and upon binding causes its premature disassembly and abolishes reverse transcription [54,80–88]. The exact mechanism of capsid restriction is not yet known; however, the restricted viral proteins appear to be removed in either a proteasome-dependent [89–95] or autophagosome-dependent manner [39,96].

TRIM5 restricts retroviral infections in a species-specific manner and serves as an essential barrier against zoonotic retroviral infections [87,97]. For example, HIV-1 enters cells of most primates. While it replicates efficiently in humans and chimpanzees, HIV-1 is restricted by TRIM5α in Old World monkeys. Although the human orthologue of TRIM5α is not very potent in limiting HIV-1 infection, it protects from infections by other retroviruses, such as N-tropic murine leukemia virus (N-MLV), equine infectious anemia virus (EIAV), feline immunodeficiency virus (FIV), and bovine immunodeficiency virus (BIV) [87,98–102]. The differing

abilities of TRIM5 orthologs to bind retroviral capsids correlate with their ability to restrict given retrovirus [88].

TRIM5α was shown to localize to cytoplasmic bodies [63,87,103]. These highly dynamic "TRIM bodies" are formed by TRIM5 multimerization, exchange protein between defined foci and the diffuse cytoplasmic fraction, and move within the cell in a microtubule-dependent manner [104]. On encountering a restriction-sensitive virus, new cytoplasmic bodies are formed around the virions as visualized by live-cell microscopy [105]. However, when TRIM5α is overexpressed in cells through transient transfection, it forms immense and dense aggregations, often from smaller ones, and retroviral infection is poorly inhibited [106]. In the case of cell lines stably expressing the protein, smaller, diffuse puncta are formed in the cytoplasm, and retroviral infection is inhibited potently [106]. Some groups reported that preexisting cytoplasmic bodies are not necessary for antiviral response of TRIM5α [107,108] but the mutants that failed to localize to the cytoplasmic bodies are also deficient in retroviral restriction ability [109].

The C-terminal SPRY domain of TRIM5α is essential for binding to retroviral capsids [87,110,111]. It adopts an immunoglobin-like fold that is commonly associated with protein-protein and protein-ligand interactions and does not have enzymatic activity [112,113]. Crystal structures of the rhesus TRIM5α SPRY domain shows a distorted β-sandwich fold of two seven-stranded antiparallel β-sheets and a helix at the N-terminus [114,115]. Four variable regions (V1-V4) that contain capsid-interacting residues are surface exposed elements [115–117]. The interaction between the HIV-1 capsid and SPRY domain resembles the interaction on IgM antibody with its antigens [114]. IgM is a polyreactive antibody capable of weak binding of multiple unrelated epitopes. The strength of the interaction is compensated by avidity [114,118]. Similarly, the HIV-1 restricting homologs of TRIM5α bind to the assembled capsid lattice but not to isolated monomers of CA and

very weakly to CA hexamers [80,83,88,110,114,115,119]. Protein constructs encompassing only intact SPRY domain bind to the capsid mimetics but are ineffective in blocking HIV-1 infection [111,120]. Multiple sites on the retroviral capsid, predominantly on the outer surface, including β1/ β2 hairpin, L4/5, L5/6 and helix 6 of CA protein, were shown to interact with TRIM5α [121–123]. Several models of SPRY binding to the HIV-1 capsid have been explored:

1) An individual SPRY domain interacting with a CA hexamer, possibly with more than one CA monomer [115] or two SPRY domains placed directly on top of a CA hexamer, with variable loops 2 and 3 positioned above the β-hairpins and V1 oriented towards its sides [124];

2) Two SPRY domains are predicted to form a dimer so their variable loops would extend in opposite directions and bridge two CA molecules [60,114,115];

3) The SPRY domains engage the CA proteins at the inter-hexamer interfaces present in the assembled capsid lattice; the most probable binding surface is an area shared between multiple capsid molecules, specifically in between CA hexamers [115,123]. Currently, no structural information is available to determine the CA/TRIM5 interaction unequivocally.

In cooperation with the L2 region, the CC domain mediates self-assembly of TRIM5α dimers. Crystal structures of rhesus TRIM5α, as well as CC from different TRIMs, show the proteins form an elongated antiparallel rod that serves as a scaffold for neighboring domains [59–62]. In such a configuration, the catalytical RING domains are separated by ~170 Å because they are placed on the opposite sides of the dimer. The majority of the L2 region is disordered in the crystal structure but it folds back on the CC dimer, and a terminal region forms a small helical segment that packs in the middle of the CC forming a four-helix bundle [59,60]. As such, it tethers two SPRY domains probably in a closed-pack configuration to CC-L2, limiting their flexibility and possible

orientations [60,125]. The intact L2 region is required for viral restriction, and destabilization of L2/CC packing disrupt TRIM5α self-association, higher-order oligomerization and capsid binding [109,125–127].

TRIM5α is auto-ubiquitinated by its RING domain and degraded in response to the restriction-sensitive virus [84,93,128]. In recent studies, the E2-conjugating enzyme Ube2W was shown to be essential to block viral reverse transcription [129]. Ube2W mono-ubiquitinates TRIM5α predominantly at Lys45 and Lys50 in the RING domain. Poly-ubiquitination by Ubc13/Mms2 follows this reaction, elongating the initial ubiquitin molecule with Lys63-linked chains. The capsid is not directly ubiquitinated, and so TRIM5α-anchored ubiquitin chains are thought to indirectly mark the capsid for degradation, thereby blocking reverse transcription in a proteasome-dependent manner [129]. Upon retroviral capsid recognition, TRIM5α also directly engages the E2 enzyme complex Ubc13/Mms2 to produce unanchored Lys63-linked polyubiquitin chains, which leads to activation of transforming growth factor-β-activated kinase 1 (TAK1). As a result, the downstream NF-κB nuclear translocation is activated, and antiviral gene expression is induced [82].

Higher-order oligomerization of TRIM5α is required for effective restriction of HIV-1 and is dependent on the B-box 2 domain [55,130,131]. Recombinant TRIM5α proteins spontaneously form an array of open-ring hexagons *in vitro*, both in the presence and absence of a capsid lattice [119,132]. Binding between TRIM5α and CA takes advantage of the TRIM5α hexagonal assembly that has a similar symmetry as the capsid lattice [58,119,127]. Recent crystallographic studies showed that the B-box 2/CC interface is inherently structurally flexible [58]. This may allow the SPRY domains to find most favorable positions on the capsid surface and strengthen local interactions creating a powerful avidity effect [59,85,119,132]. Mutations that block higher-order oligomerization results in reduced binding of TRIM5α to retroviral capsids and almost complete loss of the antiviral properties

[54,55,58,133]. Although the ability to form hexagonal assemblies around viral capsids is a conserved property, the TRIM5 lattice itself is not regular [119,132]. This lack of regularity was suggested to compensate for the irregularities within capsids, like the presence of pentamers. So far, the understanding of the molecular basis of capsid recognition is still incomplete.

## 1.4. TRIM63, a protein involved in muscle wasting

Muscle-specific RING finger 1 protein (MuRF1), also known as TRIM63, is a member of TRIM protein family found in striated muscle and iris [134–136]. TRIM63 is an E3 ubiquitin ligase responsible for muscle catabolism by the proteasome system. It is upregulated in response to atrophic stimuli such as immobilization, denervation, food deprivation, aging, and diseases, making it a well-recognized marker for muscle atrophy or muscle wasting [137–140]. In rodent models, the mRNA levels of TRIM63 raise rapidly within 48 h after the triggering of muscle wasting (such as denervation, hindlimb suspension), followed by sustained elevation for 7-10 days and gradual decrease to the base level by 14 days. Although no time studies have been performed in humans, spinal cord injuries were reported to result in a significant increase of TRIM63 mRNA within 48 h after the incident [141]. Current functional analysis on TRIM63 shows its role mainly in wasting and muscle gene expression; however, it is also essential to inhibit the development of and reverse pathological cardiac hypertrophy [138,142–144]. Yeast two-hybrid experiments using a skeletal muscle cDNA library identified two major classes of TRIM63 targets: proteins involved in ATP generation and myofibrillar proteins [145]. The interactions were found with parts of contractile sarcoskeleton such as myosin, troponin, titin and with a variety of cellular partners: titin filament,

isopeptidase T-3, GBEB-1 transcription regulator, CARP, SQSTM1, EEF1G. TRIM63 has been shown to localize at the M-lines and Z-lines of the sarcomere [140,146]. When TRIM63 or its central region was overexpressed in embryonic chick cardiac cells, the integrity of titin's M-line was disrupted, showing a role of TRIM63 in maintaining the stability of the thick filaments and tight regulation of its endogenous levels [140]. TRIM63 was also detected in the nuclei of cardiac myocytes. The RING domain was found to be solely responsible for that localization [147]. Data from TRIM63 KO mice show that the development of muscle atrophy after denervation was less extensive compared to WT mice. Disassembly of myofibrils and degradation of myosin heavy chains following ubiquitination, but not actin or other thin filament proteins, is a TRIM63 dependent event. Surprisingly, expression of endogenous TRIM63 does not induce muscle atrophy, suggesting that the substrates for TRIM63 are not expressed in resting muscle and/or it requires interaction with other signaling pathways [140,148–150].

It has been hypothesized that MuRF proteins (including MuRF 1, 2 and 3) can recognize and respond to stress [139,140,146,151]. Titin, a skeletal muscle protein involved in responding to mechanical load, was suggested to influence TRIM63 localization patterns under stress stimuli. One of the possible mediators may be MuRF2 (TRIM55) which oligomerizes with TRIM63. TRIM55 was shown to affect gene expression by responding to muscle-specific stimuli. Constant mechanical stress on myofilaments in cardiac muscle achieved by spontaneous rhythmic beating maintains the stability of the M-band protein complexes and leads to muscle hypertrophy. Mechanical arrest and denervation, one of many atrophic stimuli, leads to TRIM55 translocation to the nucleus and muscle wasting [145]. Muscle mass wasting has been shown to be induced by several cytokines, in particular, tumor necrosis factor α (TNFα), formerly called “cachectin.” It binds to its receptor inducing the activation of NF-κB family of transcription factors.

Phosphorylation of IκB by IKK (IκB kinase complex) leads to release of NF-κB from the inhibitory action of IκB, with degradation of the latter by the proteasome system. As a result, TRIM63 is expressed leading to muscle loss. Muscle atrophy is blocked by activation of insulin-like growth factor 1 (IGF1) and the downstream pathways. Activated phosphatidylinositol 3-kinase (PI3K) phosphorylates Akt (protein kinase B) that is translocated to the nucleus. There, FOXO3 (Forkhead family of transcription factors, subclass O) is phosphorylated and excluded from the nucleus. Renewed translocation to the nucleus upon dephosphorylation is necessary for upregulation of TRIM63 [140,142,152,153].

Targeting individual steps in the signaling pathways described above may lead to the development of anti-atrophy drugs. However, each alteration brings significant challenges and dangers. Inhibition of the PI3K/Akt pathway was shown to cause defects in cell survival [154], deregulation of FOXO3 affects in tumorigenesis [153,154], while suppressing the activity of NF-κB, which controls the transcription of DNA, influences regulation of the immune response to infections [155]. Inhibition of TRIM63 activity might be a suitable target for clinical intervention. TRIM63 was observed as a monomer, homodimer or heterodimer with TRIM55 and MuRF3 (TRIM54), proteins highly homologous to TRIM63 [144,151,156]. Both TRIM55 and TRIM54 act synergistically with TRIM63, for example during myosin degradation or modulation of cardiac hypertrophy [138,139,151]. Of particular interest for this study is the C-terminal part of TRIM63 that contains the both CC and COS-box domains. The CC region is hypothesized to take part in dimerization of TRIM63, and the COS-box is responsible for interaction with the muscle titin protein. The B-box domain on the N-terminus of CC induces higher-order association, approximated as hexameric or octameric formations [144] and the COS-box mediates targeting of TRIM63 to various parts of sarcoskeleton. When the COS-box is removed, TRIM63 is unable to

be appropriately targeted, and its ubiquitinating function is almost completely lost [157,158]. The structure of the A168-A170 domains of titin protein, built by Ig-Ig-Fn(III) motifs, forms an elongated sequence with short, rigid linkers. The titin kinase domain (TK) was found to be an inactive pseudokinase, without detectable levels of phosphorylation activity. A shallow groove mediates the specific interaction modulating the interaction [146]. It was suggested that TRIM63 and TK are parts of a shared stress-signaling pathway, as TK may have a mechanoactivation mechanism. The multi-domain interaction between TRIM63 CC/COS-box and titin domains A168-A170-TK has been proposed to be sensitive to the stretch-induced conformational changes of titin chain as pseudokinases are known to serve as scaffolds for the assembly of signaling complexes [156,159].

## 1.5. Basic overview of cryo-electron microscopy (EM) and subtomogram averaging

Biological samples are three-dimensional (3D) objects and resolving their structure is essential to understand their mechanism of action. Historically, light microscopes were the first tools used to visualize samples too small for a human eye. The source of illumination is photons, with a wavelength of ~390-700 nm. A resolution is understood as a minimum distance between two points of an image at which they can be distinguished from each other and is limited by the wavelength of the illumination source. The best resolution achieved by the light microscope is around 200 nm and does not provide much information on the subcellular structures. Although novel developments in light microscopy, such as super-resolution microscopy, can surpass that limitation, only the location of molecules, but not their shape nor atomic structure can be

visualized. One of the most successful techniques used in the 20th century to resolve atomic models of biological samples such as proteins and nucleic acids has been X-ray crystallography. However, when a sample is hard to crystallize, when it cannot be obtained in sufficient quantities or when there are multiple conformational states, structural determination by X-ray crystallography can be hard to achieve. Electron microscopy is an alternative method to crystallography and is used to address a wide range of biological questions such as the organization of compartments within tissues or cells, as well as to investigate the structure of individual particles. Microscopes use beams of electrons accelerated in vacuum as a source of illumination. In transmission electron microscopy (TEM), the beam passes through a sample of an electron-dense material and is subsequently magnified by an objective lens. The image can be viewed on a fluorescence screen, recorded on the photographic film or by a digital camera. As the sample is imaged under vacuum and subjected to electron damage, the specimen has to be protected. There are various methods to achieve this. In the case of large specimens, such as tissues, the sample is fixed to preserve the structure and embedded in plastic. Since the electrons must pass through the specimen to generate an image, thin slices are obtained by cutting the sample to 30-80 nm thick sections. This method is generally suitable to visualize relatively large systems; however, it introduces artifacts such as shrinkage of the tissue, protein precipitation and mechanical deformations caused by the knife. To view relatively small samples such as individual virions, proteins or protein complexes, a negative staining approach is generally used. The sample is adhered onto an EM grid and covered with a low-concentration solution of heavy metal salts, such as uranyl acetate or ammonium molybdate, and dried out. The stain scatters the electron beam, so a background appears to be dark. The sample deflects the electrons to a lesser extent and so appears lighter, giving rise to images with very high contrast. However, the effective resolution is about 2-1.5 nm under optimal conditions and

particles may be distorted by staining and drying. To preserve a specimen in a hydrated state and minimize the artifacts caused by staining, the sample can be flash-frozen in liquid ethane [160]. The high heat capacity and low melting temperature of ethane ensure that the water solidifies as vitreous ice and does not have a chance to crystallize. As the sample is in solution, the distortions caused by adhering to the grid and flattening against the supporting film are negligible. Optimizing specimen preparation and freezing conditions is essential to produce the high-resolution structure.

High-resolution signal recovery from an image-recording media was considered a limitation of cryo-EM. Traditionally, the micrographs are recorded on a photographic film or scintillator-based cameras such as CCD (charge-coupled device). The photographic film provides larger size and better detective quantum efficiency (DQE, a measure of film/camera performance as a function of spatial frequency [161]) at high frequencies than the cameras. However, the DQC of low frequencies responsible for contrast and particle visualization is poor. High defocus is needed to maximize the low-resolution contrast transfer function (CTF, a sine function with an envelope that reduces the amplitude at high resolution) but minimizes the envelope at high resolution [162]. Additionally, the film has to be developed and fixed chemically, followed by digitization by high-quality scanners. Photographic films do not provide immediate feedback and are not suited for high data throughput and rapid electronic readouts. This limitation was circumvented by CCD cameras as they convert primary electrons to photons using phosphor scintillator, which is coupled to the fiber optics and subsequently converted to a digital image. They are better at capturing low frequencies DQC as compared to analog film, which results in images with better contrast. Unfortunately, they are not very efficient in capturing high-frequency DQC that renders them not generally suitable for high-resolution reconstructions.

The 'resolution revolution' in single-particle cryo-EM was possible due to the application of the direct detector device (DDD) [163]. Those devices detect electrons without converting them to photons to generate an image. The DDDs have high DQEs compared to photographic film or scintillator-based cameras [164]. Additionally, instead of a single micrograph, a stack of images is generated, and the total electron dose is divided between subsequent images [165]. Creating the stack enables the correction of the motion caused by stage or beam, and improving the quality of an image significantly [166].

The resolution of a microscope (d) in 2D is described by Abbe criterion:

$$d = 0.61\frac{\lambda}{nsin\alpha} \quad (1.1)$$

where λ – the wavelength of the illumination source; n – the refractive index of the imaging medium; α – half of the cone angle of light from the specimen plane accepted by the objective.

The resolution of light microscopy is 250-420 nm as the visible light wavelength is 400-700 nm. The electron's wavelength depends on accelerating voltage (V) and in the classical approximation:

$$\lambda = \sqrt{h^2/2meV} \quad (1.2)$$

where h – Plank's constant; m – a mass of the electron; e – charge of the electron

Electrons generated under vacuum and accelerated at a high voltage (100-300 kV) have wavelengths between 3.7 pm (at 100 kV) and 2.0 pm (300 kV) giving rise to the theoretical resolution of 0.23 nm and 0.12 nm respectively. However, the observed resolution of electron microscopes is limited by many factors, including the quality of the electron microscope optics and recording device; low contrast and signal-to-noise ratio (SNR); radiation damage of the sample; artifacts and variability present in the datasets. To minimize the electron damage, the

micrographs are collected using a low dosage of electrons (typically 20-40 e/Å$^2$) that results in images with a low SNR and poor contrast. To increase SNR and reconstruct a 3D structure of a sample, various approaches can be employed.

One such example is a single particle analysis (SPA). Briefly, as the molecules are tumbling in the solution before freezing, each particle is oriented and positioned randomly. Structures are extracted from the micrographs, aligned and averaged together based on the two-dimensional (2D) similarities. This is an iterative process where the best averages from one run are used as references in the subsequent one. Within each image, noise presents as a random distribution of signal, but the signal coming from the particles presents as a structured pattern. By averaging multiple images of structurally similar particles, the information coming from the molecules is reinforced while the noise is smoothed out. The 3D reconstruction is obtained by combining projection views from different angles. The orientations of the particles defined by Euler angles are not known and have to be determined computationally. There are several algorithms to estimate relative Euler angles for each class. In the angular reconstitution method, the reference orientation coordinate system is established from three projections, and the orientation of particles is deduced from common lines among the images [167–169]. In the projection matching approach, an arbitrary 3D reference structure (a usually low-resolution model that may not bear much resemblance to the analyzed sample) is used to generate a series 2D reprojections that in turn serve as models for the collected 2D averages.

Another technique to reconstruct a 3D volume is cryo-electron tomography (cryo-ET) [170]. It allows the reconstruction of specimens like cells or tissues from a set of 2D projection images of the sample that was tilted along an axis. The aligned images are merged to generate a tomogram, the 3D reconstruction of the specimen (Fig. 1.5). Cryo-ET has been used to visualize cells and its

compartments [171–174], viral particles [25,175–177] and macromolecular co-assemblies [178–180]. In this method, only a single specimen is imaged at a time, so it provides a robust approach to obtain structures of individual samples as cells, organelles, and heterogeneous complexes. The biological sample is flash frozen in liquid ethane and thinned if necessary to less than 500 nm so the electron beam can pass through. The images are taken under multiple angles by an electron microscope. As the electron beam can easily inflict the damage upon the biological sample, a very low dosage of electrons is used which results in images with a low SNR and the effective resolution of reconstruction of about 4-6 nm.

As the sample cannot be imaged over a 180˚ tilt range, some views are missing. This is known as a 'missing-wedge problem' in Fourier space and results in a lower resolution of reconstruction parallel to the beam. To increase resolution and SNR, repeating macromolecular complexes within the tomograms can be computationally extracted, aligned to a reference, and averaged in a process called subtomogram averaging. The alignment is an iterative process. Extracted volumes are aligned to a reference, averaged together, and a newly generated structure is used as a new reference in the following steps until no change is observed. Since extracted volumes are oriented differently to the missing wedge, the missing information is gradually filled in in the process [181]. The final results include the 3D structures of the biological samples and their spatial distribution within the investigated volume. The resolution estimation is dependent on several factors - the number of copies of the averaging structure, the structural flexibility of the sample, and its thickness. Some dangers arise while evaluating subtomogram averaging. Reference bias occurs when the calculated average is heavily influenced by the initial starting model and display features that are only present in the model. Over-alignment results in a structure with high-resolution elements that arose from the alignment of noise against itself [181–184].

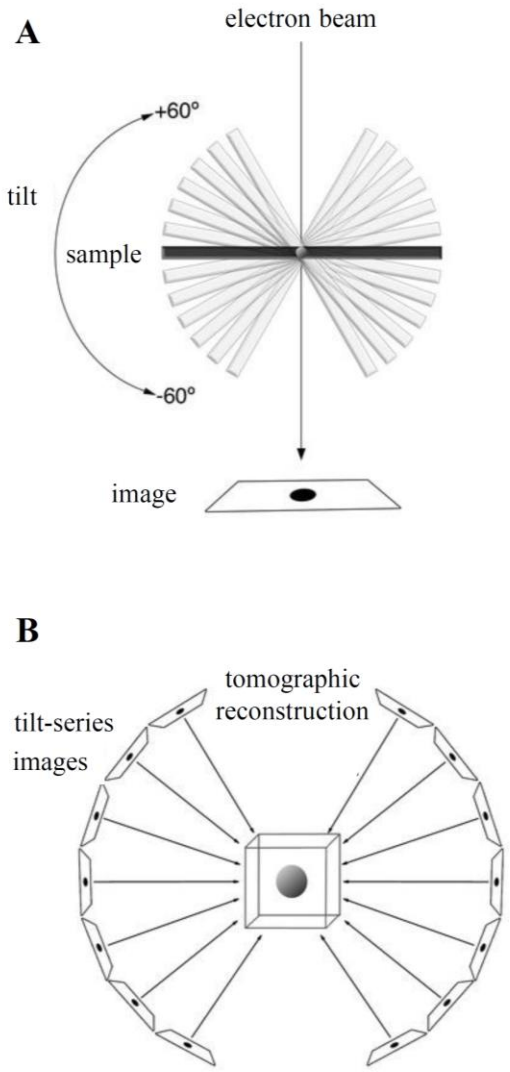


**Figure 1.5. Schematic representation of data collection and 3D reconstruction of a sample volume in CET.** A – a sample is imaged under different tilt angles (usually ± 60°) around the axis perpendicular to the electron beam. B – 3D volume is reconstructed from collected 2D images that are back-projected along the line-of-site [185]. Image by Eikosi - Own work, CC BY-SA 4.0, https://commons.wikimedia.org/w/index.php?curid=45403034

To obtain a correct reconstruction from the experimental data, validation tests should be applied from the very beginning [186]. Low contrast and model-based alignment may introduce artifacts that would result in generation of a wrong map. Most validation approaches were suggested with SPA in mind. The first step is visual assessment. The low-resolution map has to agree with collected images and generated classes. If the particles differ in size and shape from the calculated average, the resulting structure is most likely incorrect. The more advanced approach requires the map to agree with a set of particle views collected under different tilt angles, and shows the consistency of the map with structural characteristics of the particles and demonstrates that the angles in the reconstruction were assigned correctly [187]. Even more rigorous validation approach requires various independent low-resolution starting models to converge during refinement into a structure with the same structural features [188]. Finally, the structure can be validated in biochemical experiments, for example by adding antibodies or electron dense labels [189–191].

The Fourier shell correlation (FSC) is the most widely used measure of map resolution [192,193] and is briefly described in this section. Other methods include the differential phase residual (DPR) that measures the phase difference between two Fourier transforms; spectral signal-to-noise ratio (SSNR) that is based on multiple comparisons between all the images in the data set and the calculated average; Fourier neighbor correlation (FNC) that measures the relationship between the neighboring voxels in Fourier domain [194]. The FSC describes the correlation between the two halves of a dataset that were processed independently, resulting in two reconstructions, as a function of resolution. For low spatial frequencies, the FSC curve starts close to a value of one which indicates perfect correlation and falls down with the increasing spatial frequencies. The resolution of the map may be assigned when FSC declines below a certain threshold. The cutoff

of 0.143 is used when two maps are processed independently from the very beginning. If the maps are generated from the final step of the optimization, the 0.5 cutoff is advised to avoid overly optimistic resolution estimation [195].

## 1.6. Rationale of this study

TRIM5α was shown to form a hexagonal lattice *in vitro,* and capsid binding enhances ubiquitin activity [82,119,132,133]. Previous crystallographic studies show the structures of individual domains; however, the full-length structure has only been speculated. Additionally, the mechanism of HIV-1 capsid recognition by the restriction factor TRIM5α is still poorly understood. In this work, I describe structural characterization of higher-order TRIM5α assemblies and the lattice-lattice recognition model. I also aim to elucidate how the SPRY domain binds to the CA subunits and shed light on specificity towards different retroviruses. Through cryo-ET and subtomogram averaging, I determined the molecular organization of TRIM5α and visualized the interaction between HIV-1 capsid lattice and TRIM5α hexagonal lattice.

Previous crystallographic studies of TRIM63 suggest that the CC domain forms a parallel dimer [157], which would dictate a different arrangement of the two RING domains and as a consequence, a different mode of RING dimerization and activation. However, a structure-to-sequence alignment presented by Sanchez *et al.* (2014) showed that self-association of TRIM63 through its CC domain should exhibit similar architecture as other members characterized so far. In this work, I also investigate the structural properties of the CC region of TRIM63 and address whether its oligomerization mechanism is distinct from other members of TRIM superfamily.

# Chapter 2.

# Co-assembly of HIV-1 CA and TRIM5$\alpha_{AGM}$ for *in vitro* cryo-electron tomography studies

## 2.1 Introduction

Mammalian cells are equipped with many defenses against invading pathogens. The innate immune system response is initiated by Pathogen-Associated Molecular Patterns (PAMPs) that are recognized by intracellular sensors called Pattern Recognition Receptors (PRRs). Viral PAMPs are most commonly nucleic acids, both DNA and RNA [50,196,197]. Many proteins that belong to the tripartite motif (TRIM) family are shown to inhibit viral infection and initiate innate immune signaling cascades [82,198,199]. One such example is TRIM5, a restriction factor first identified in the Sodroski lab that acts at a post-entry step of the retroviral life cycle [87]. As a member of the TRIM superfamily, TRIM5α is characterized by the presence of a conserved RBCC motif on its N-terminus containing RING finger (R), zinc-finger B-box 2 domain (B) and a leucine-rich coiled-coil (CC) motif (Fig. 2.1.A). TRIM5α contains a SPRY domain at its C-terminus.

TRIM5α functions by intercepting and disabling incoming retroviral cores. It recognizes the capsid coat, and upon binding, initiates an immune system response, accelerates core disassembly and prevents proper reverse transcription of the viral genome [82,87,88,129,200]. TRIM5α is shown to assemble into a hexagonal lattice on the surface of retroviral capsids, and the

complementarity of the TRIM and capsid lattices is thought to facilitate an avidity-driven interaction [119,132]. Low-resolution structures of the TRIM5α lattice assembled on HIV-1 CA tubes and cross-linked HIV-1 cores show patches of 4-6 TRIM5α hexameric rings; however, unambiguous determination of domain organization in these complexes has not been achieved [132].

The purpose of this study was to understand at the molecular level how the TRIM5α protein from Old World monkeys recognize the HIV-1 capsid, by using cryo-electron tomography (CET) and subtomogram averaging for structural characterization. As we aimed to improve the efficiency of TRIM5α lattice formation, we developed and characterized a novel TRIM5α mutant that showed improved binding to HIV-1 CA tubes that were stabilized by cysteine crosslinking. Although the CA tubes are established capsid mimetics, cysteine stabilization appeared to limit the extent of TRIM5α binding [132]. To obtain high-quality structural data, we took advantage of the discovery that coordinated assembly of the two lattices can occur from soluble proteins *in vitro* [58,132]. To avoid perturbing the binding interaction, we used wildtype (WT) HIV-1 CA protein lacking cysteine-stabilizing mutations.

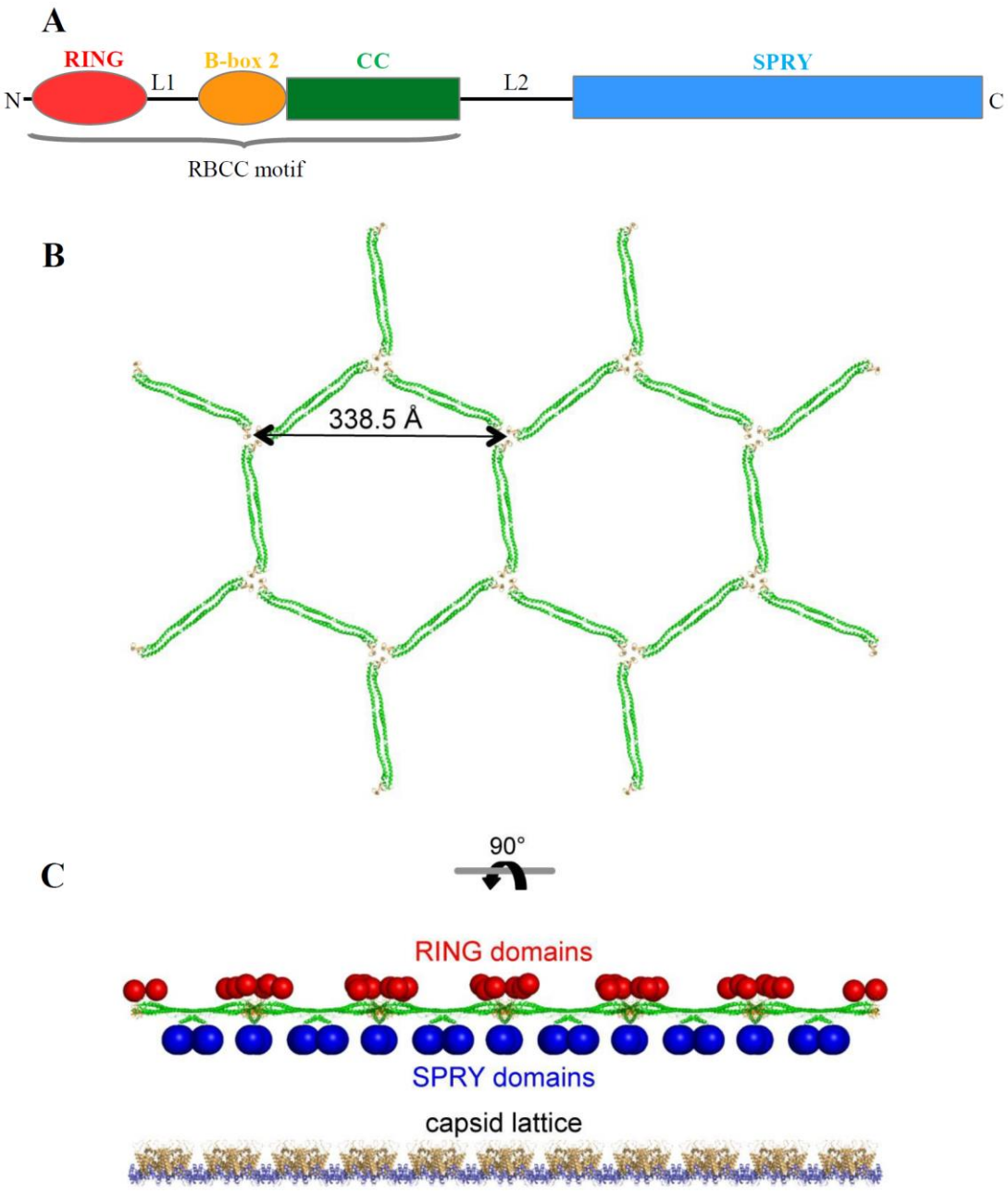


**Figure 2.1. Schematic overview of the TRIM5α structure and its co-assembly with HIV-1 CA.** A – Schematic representation of TRIM5α protein; RING (red), B-box 2 (orange) and CC (green) domains are followed by a SPRY domain (cyan); color-coding of the domains is retained within this work. B, C – Schematic representation of the hexagonal TRIM5α lattice (B) and its interaction with the capsid lattice (C). Figure adapted from [58].

## 2.2. Results

### 2.2.1. Characterization of an L81F mutant of TRIM5α

A schematic representation of TRIM5α domain organization is presented in Fig. 2.1.A. Based on structure-function predictions, we postulated that the L81F substitution in the RING domain would increase the stability of the TRIM5/CA co-assembly. We used TRIM5α from African green monkey (TRIM5$\alpha_{AGM}$) because it assembles very efficiently *in vitro* [132]. The following constructs were overexpressed in SF9 insect cells with N-terminal One-STrEP-FLAG (OSF) HRV14-3C protease-cleavable tag: WT, L81F, and R121E (which contains a mutation in the B-box 2 domain that prevents higher-order assembly). We purified the dimer fraction to homogeneity by using affinity chromatography, ion-exchange, and SEC (Fig. 2.2.A-C). In order to determine the effect of the L81F mutation on the capsid binding properties of TRIM5α, we used an established centrifugation assay [57,125]. Shown in Fig 3.2.D are the representative results of 3 independent experiments. Binding to the CA lattice is dependent on the SPRY domain, but higher-order oligomerization of TRIM5α proteins positively influences binding efficiency [110,119,201,202]. The majority of the WT protein (90%) co-pelleted with the stabilized HIV-1 CA tubes (Fig. 2.2.D, left) which is significantly higher than the previously reported value for TRIM5-21R [125] and further supports the choice of TRIM5$\alpha_{AGM}$ for our structural studies. As expected, the R121E mutation disrupted higher-order oligomerization and resulted in a weaker binding efficiency to CA tubes (Fig. 2.2.D, middle). The amount of R121E protein in the pelleted fraction was only about 45%, which is a drastic decrease compared to the WT protein. The L81F mutant also bound strongly and even had apparently greater binding to the CA tubes than WT (Fig. 2.2.D, right).

Additionally, we tested the ability of L81F to form hexagonal lattices *in vitro* under conditions that induced spontaneous assembly. Results of these experiments were visualized by negative stain electron microscopy. We screened various conditions for both tagged and untagged protein, and the best looking 2D crystals were recorded in a buffer containing 50 mM NaCl, 25 mM Tris-HCl pH 8.0. Both the WT and L81F proteins reproducibly formed a lattice of open, hexameric rings that looked similar to previously published images [119,132] (Fig 3.2.E, G). The lengths of the arms measured between the 3-fold vertices ranged from ~13 nm to ~26 nm, with the average of 19.1 nm and the median 19.1 nm (n=115; Fig. 2.2.G). As expected, the R121E mutation resulted in a complete loss of oligomerization properties (Fig. 2.2.F). These results show that the L81F mutant is not only capable of self-assembly but also exhibits stronger binding to a CA capsid. Unless noted otherwise, the protein with the intact tag was used throughout the study.

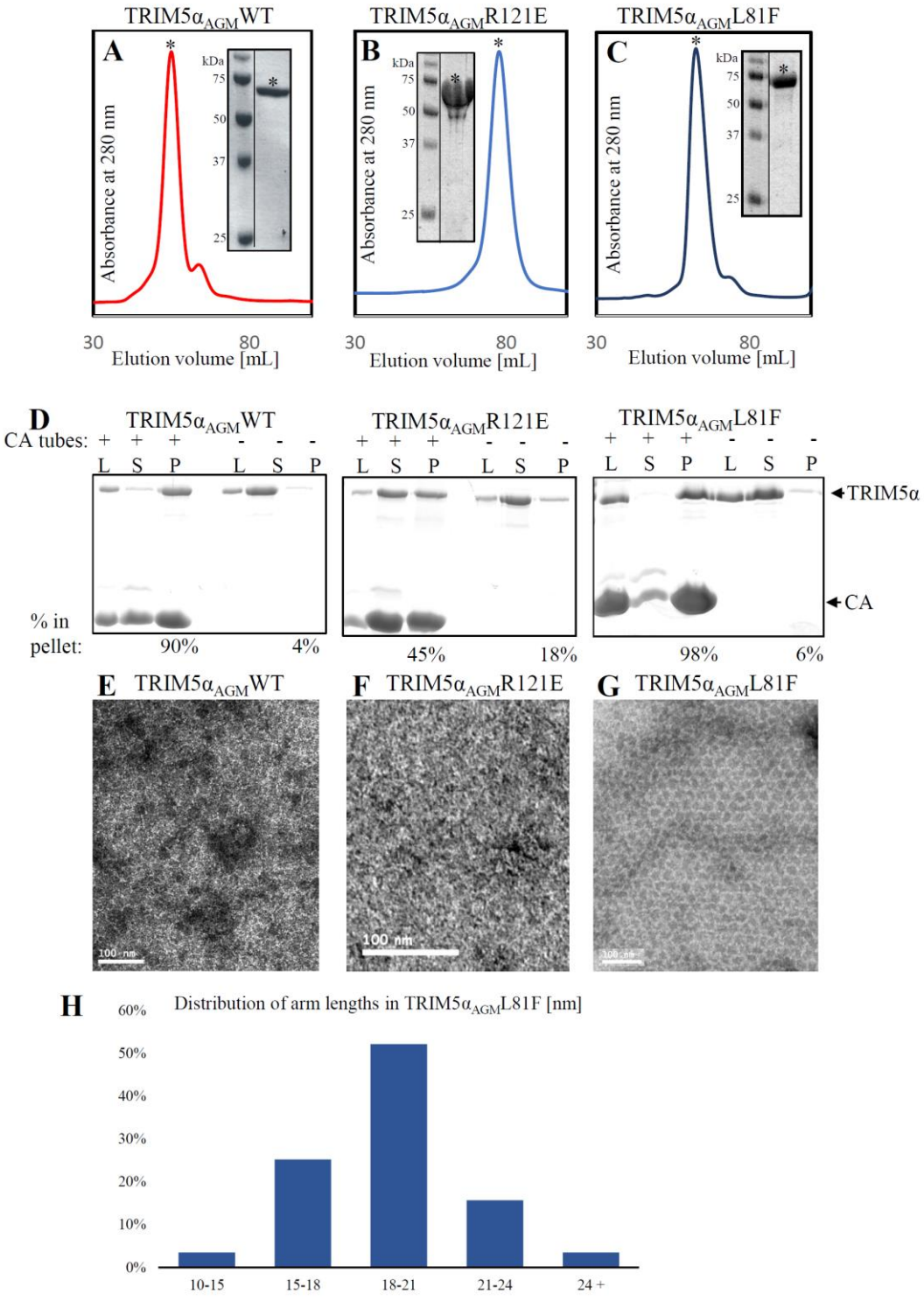


**Figure 2.2. Characterization of TRIM5α$_{AGM}$L81F protein used in this study.** A-C – Final SEC profiles of purified TRIM5α$_{AGM}$ WT (A), R121E (B), and L81F (C); the insets show SDS-PAGE with a Coomassie staining of the purified proteins. D – Capsid-binding experiment. TRIM5α$_{AGM}$

proteins (WT – left, R121E – middle; L81F - right) were incubated with or without assembled CA tubes (as indicated), fractionated by centrifugation, and resolved by SDS-PAGE with Coomassie staining. L –load; S – soluble fraction; P – pellet fraction. Band intensities were quantified using ImageJ software [203]. E-G – Representative negative stain micrographs of spontaneous assembled TRIM5$\alpha_{AGM}$ proteins at concentrations of ~3 mg/ml in 25 mM Tris-HCl pH 8.0, 50 mM NaCl. The WT protein self-assembled into a hexagonal lattice (positive control); R121E disrupted the higher-order oligomerization properties (negative control), and L81F resulted in similar phenotype of the hexagonal lattice as the WT; scale bar is 100 nm. H – Histogram showing the distribution of arm lengths measured between 3-fold vertices (n=115) of the lattice of L81F mutant.

### 2.2.2. Optimization of co-assembly protocol

We optimized the co-assembly protocol from Li *et al.* (2016) by incubating sub-saturating concentrations of WT HIV-1 CA protein and TRIM5$\alpha_{AGM}$L81F under different ionic strength conditions. The resulting tubes were imaged by negative stain EM, and representative micrographs are presented in Fig 3.3.A. In each case, the tubes assembled efficiently and in a reproducible manner but the degree of TRIM5α decorations varied in a salt-dependent manner. Tubes formed in a buffer containing 250 mM NaCl did not show any densities on top or on the sides of the tubes that could be convincingly interpreted as TRIM5α. Co-assembly in 150 mM NaCl resulted in a limited number of decorations (yellow arrows), noticed mostly as protrusions. In the case of tubes assembled under low salt conditions (20 mM and 50 mM NaCl), the decorations were quite visible. Protrusions on the sides of the tubes (yellow arrows) were regularly spaced along the length of the tube. Given the above results, we therefore used a buffer containing 20 mM NaCl for further experiments. Under these low salt conditions, spontaneous self-assembly of both the CA and TRIM5α proteins did not occur (data not shown), indicating that the tubes resulted from co-assembly of the two proteins present in the reaction mixture.

To confirm that the tube decorations corresponded to assembled TRIM5α, we calculated the spacings of the protrusions visible on the sides of the tubes assembled under low-ionic strength conditions (Fig. 2.3.B). These varied between 20 and 55 nm, with an average of 32.5 nm and a median of 31.7 nm (n=159). These are in excellent agreement with previously published data [119,132].

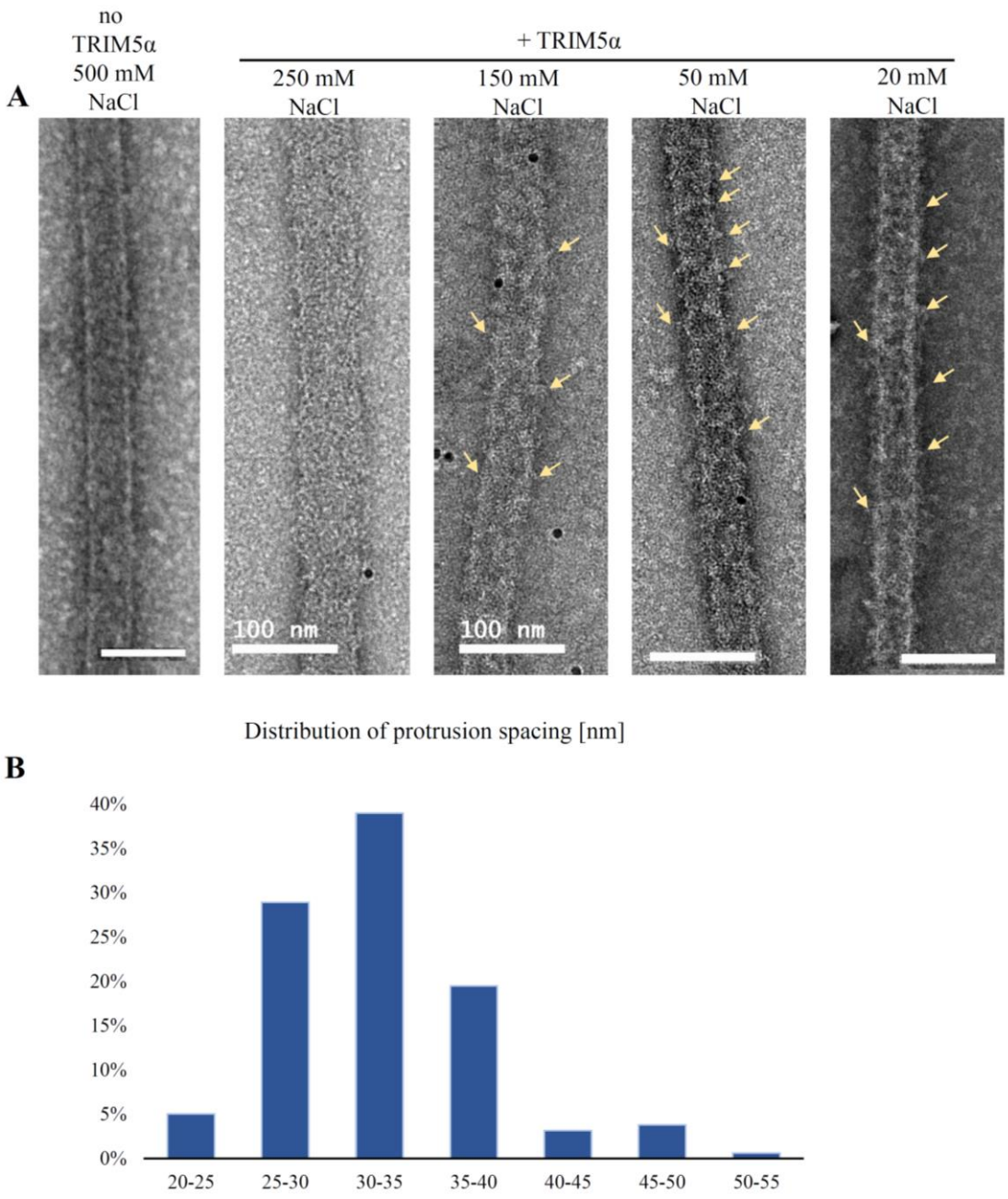


**Figure 2.3. Co-assembly of TRIM5α$_{AGM}$L81F and WT HIV-1 CA protein.** A – Representative negative stain micrographs of TRIM5α$_{AGM}$L81F incubated in 25 mM Tris-HCl pH 8.0 and various salt concentrations (as indicated). CA tubes formed under high salt conditions (first panel) appear not to be decorated with any protrusions. Visible protrusions are present when buffer containing 20 mM NaCl or 50 mM NaCl was used. In higher salt concentrations (150 mM and 250 mM), tube decorations disappear. Scale bar 100 nm. B – Histogram of the spacing between visible protrusions on the surfaces of the tubes (n=159). Scale bar is 100 nm.

2.2.3. Effect of HIV-1 CA mutations on co-assembly with TRIM5α

TRIM5α binding to HIV-1 capsids has been reported to be dependent on the N-terminal β-hairpin ($CA_{1-13}$) region and cyclophilin A binding loop ($CA_{80-98}$) [88,110,119]. We therefore expected that the TRIM5$\alpha_{AGM}$L81F would not co-assemble with mutants of the CA protein that lack either the β-strand ($CA_{\Delta 1-13}$, which lacks the first 13 residues) region or the cyclophilin A binding loop ($CA_{\Delta cypA4G}$, in which residues 80-98 were replaced by four glycine residues) (Fig. 2.5.A).

First, we tested the ability of the CA mutants to self-assemble in the absence of TRIM5α (Fig. 2.4.B). Under high-salt conditions (500 mM NaCl), tubes formed by the mutants resembled the ones formed by WT CA control. The tubular assemblies were of different lengths but similar diameters. As expected, none of the recorded tubes had any visible decorations on top or protrusions on the sides. In low-salt conditions (40 mM NaCl), no tubes were observed for either of the mutant CA proteins, which is also consistent with their expected behavior. Combining TRIM5α with WT CA but not the $CA_{\Delta 1-13}$ or $CA_{\Delta cypA4G}$ mutants under low-ionic strength conditions resulted in a significant number of tubes formed. Thus, the $CA_{\Delta 1-13}$ and $CA_{\Delta cypA4G}$ mutants did not produce any visible complexes in similar conditions when TRIM5αL81F was added, indicating that the mutations prevent binding.

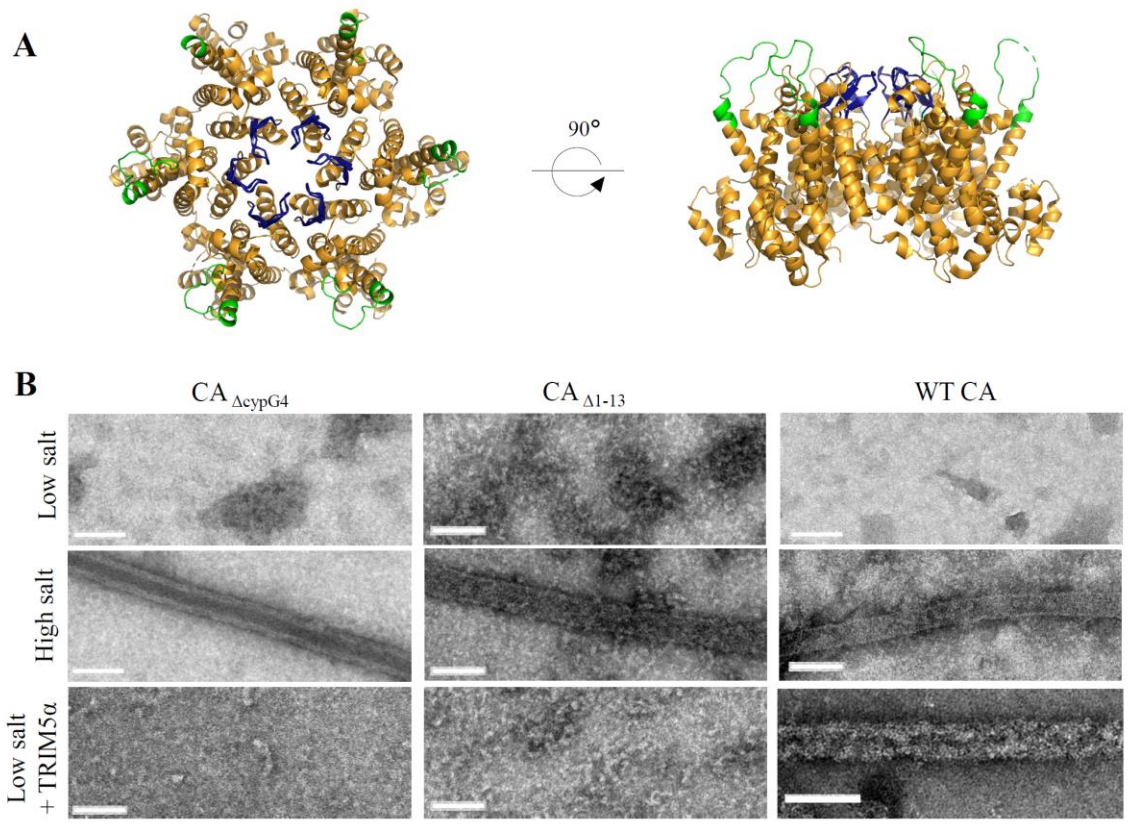


**Fig 2.4. Co-assembly of TRIM5α$_{AGM}$ and HIV-1 CA mutants.** A – Locations of the CA mutations on hexameric HIV-1 CA (PDB: 3H4B), with the β-hairpin capsid colored in navy and the cyclophilin A binding loop colored in green. B – Negative stain electron micrographs of *in vitro* assemblies. The purified CA proteins did not self-assemble under low-ionic strength conditions (top panels) but formed elongated, tubular assemblies under high-ionic-strength conditions (middle panels). In low salt buffer and the presence of TRIM5α$_{AGM}$ proteins (bottom panels), tubes were formed solely when WT CA was used. No tubes were seen when CA$_{Δ1-13}$ or CA$_{ΔcypG4}$ mutants were used. Scale bar is 100 nm.

## 2.3. Discussion

Successful restriction of an invading retrovirus requires higher order assembly of TRIM5α. The lattice assembly model of HIV-1 restriction postulates that multiple copies of TRIM5α molecules directly bind to the incoming retroviral capsid [58,119,132]. TRIM5α forms a hexagonal lattice *in vitro* of similar symmetry to the CA lattice that was suggested to amplify weak interactions between SPRY domains and the HIV-1 capsid in an avidity-driven manner [57–59,119,132]. Tubular assemblies of purified HIV-1 CA provide a model of a curved capsid lattice [10,32]. We optimized an efficient method of co-assembling the WT HIV-1 CA and TRIM5α by incubating the two proteins under low-ionic strength conditions. No mutations were introduced in the CA protein that would have stabilized the tubes through the formation of double-cysteine crosslinks [14,204], which precludes efficient binding. We also characterize a novel mutant, TRIM5αL81F, that shows similar assembly phenotype as WT protein. We find that the extent of TRIM5αL81F decorations is dependent on the salt concentration used during the co-assembly reaction – with increased ionic strength, the TRIM5αL81F decorations became less pronounced (Fig. 2.3.A). As low salt concentrations do not favor spontaneous self-assembly of CA proteins, tubular assemblies were only formed when TRIM5α was present. Sub-saturating concentrations of TRIM5α were used to avoid over-decoration of the CA tubes. We also confirmed that co-assembly of the tubes requires binding between TRIM5α and CA, by using two different CA mutations predicted to abrogate binding (Fig. 2.4.B).

In summary, these experiments established an optimized protocol to co-assemble TRIM5α and HIV-1 CA proteins. Optimal reconstitution of the complexes requires low salt concentrations that prevent spontaneous assembly of the two proteins separately. Negative stain EM indicates that

the CA tubes are covered with the TRIM5α lattice, and are well suited for further characterization by cryo-electron tomography.

## 2.4. Materials and methods

### 2.4.1. Construct design and site-directed mutagenesis

A synthetic DNA sequence corresponding to the TRIM5α$_{AGM}$ open reading frame was a generous gift from the Sundquist laboratory and sub-cloned into a pFastBac vector (Invitrogen). All mutants were generated by using a Quikchange Lightning kit using the manufacturer-provided protocol (Agilent Technologies, Inc). Primers were designed using the Agilent online tool https://www.genomics.agilent.com/primerDesignProgram.jsp. All plasmid constructs were confirmed by sequencing with pFastBac/pFastBac-terminator primers supplied by Genewiz Inc.

### 2.4.2. Bacmid production

The pFastBac vectors containing TRIM5α$_{AGM}$ sequences with N-terminal One-STrEP-FLAG (OSF) HRV14-3C protease-cleavable tag were transformed into *E. coli* DH10Bac competent cells and plated on LB-agar plates supplemented with kanamycin, gentamicin, tetracycline, Bluo-Gal and IPTG to final concentrations 50 µg/mL, 7 µg/mL, 10 µg/mL, 100 µg/mL, and 40 µg/ml respectively. The cells were incubated at 37 °C for two days. After that time, 2 white colonies were re-streaked on new plates and incubated at 37 °C. After 2 days, one isolated colony was used to start an overnight culture for a bacmid miniprep. Bacmid purification was done using the PureLink HiPure Plasmid DNA Purification Kit protocol (Invitrogen) and stored at 4 °C.

2.4.3. Virus generation

First generation baculovirus was obtained by transfecting suspension Sf9 cells grown in ESF-921 medium (Expression Systems) with the obtained bacmid. Briefly, freshly split SF9 at 1 x $10^6$ cells/ml were plated into a 24-well plate and mixed with a pre-incubated solution of purified bacmid and FuGENE (Promega) transfection reagent. Plates were covered with breathable seal and incubated with shaking at 27 °C, 130 rpm for 4 days. The cells were harvested by centrifugation and supernatant containing the virus was saved as a P0 generation. This virus was further propagated in Sf9 cells to obtain higher amounts for a large-scale protein expression step. The P2 generation was stored at 4 °C for up to 6 months.

2.4.4. Expression test

Suspension SF9 insect cells (40 ml at 2.5 x $10^6$ cells/ml) grown in ESF-921 medium (Expression Systems) were infected with recombinant baculoviruses, incubated with shaking at 27 °C, 130 rpm and harvested by centrifugation at 48 h later. Cells were resuspended in a lysis buffer (50 mM Tris-HCl pH 8.0, 1.5% Triton X-100, 50 mM NaCl, 1 mM TCEP, 1 mM PMSF) and lysed by sonication. The cell lysate was clarified by centrifugation at 20,000 g for 20 min (Beckman JA-25.50 rotor) at 4°C. The supernatant was loaded onto a Strep-Tactin Sepharose resin (IBA) pre-equilibrated with wash buffer (50 mM Tris-HCl pH 8.0, 50 mM NaCl, 1 mM TCEP) and incubated for 1 h with shaking at 4 °C. Beads were spun down for at 2,000 g for 5 min (Beckman JA-25.50 rotor) at 4°C and the supernatant removed. Beads were then washed with 50 column volumes (CV) of the wash buffer, spun down again for 5 min (Beckman JA-25.50 rotor) at 4°C, and the supernatant was removed. Beads were incubated with 2xSDS loading buffer with β-mercaptoethanol (βME) for 5 min at 100 °C. Samples were resolved by SDS-PAGE.

2.4.5. Expression and purification of HIV-1 CA protein

Four liters of *E. coli* BL21 (DE3) cells (Stratagene) transformed with the HIV-1 CA WT expression vector were grown to an $OD_{600}$ = 0.8 in LB medium at 37°C with shaking. Protein expression was induced with 1 mM isopropyl-β-D-thiogalactopyranoside (IPTG) followed by 4 h incubation at 25°C. Cells were harvested by centrifugation in a Beckman JLA-8.1000 rotor and stored at -80°C. HIV-1 CA WT protein was purified as previously described [204]. Briefly, cells were resuspended in 50 mM Tris-HCl pH 8.0, 50 mM NaCl, 100 mM βME, and 0.2% (w/v) deoxycholate, supplemented with cOmplete protease inhibitors cocktail tablets (Roche), and lysozyme and incubated on ice for 20 min with shaking. Cells were lysed using a sonicator. After centrifugation at 45,000 g for 45 min (Beckman JA-25.50 rotor) at 4°C, the protein was precipitated with ammonium sulfate to 25% saturation and incubated on ice for 10 minutes. The protein was pelleted by centrifugation at 9,000 g for 20 min, resuspended in 25 mM MOPS pH 6.8, 20 mM βME, and dialyzed overnight to the same buffer. The sample was applied to a series of ion-exchange columns: one 5-ml HiTrap Q HP + two 5-ml Hi-Load SP Sepharose HP (GE Healthcare) pre-equilibrated with the same buffer. After washing out the flow-through, the Q column was removed, and the protein was eluted with a linear gradient of NaCl (0–1 M) in the same buffer. Fractions containing CA proteins were pooled and dialyzed overnight against 25 mM Tris-HCl pH 8.0 and 10 mM βME. The CA protein was concentrated to about 30 mg/ml using a Vivaspin 20 concentrator (10,000 MWCO PES, Sartorius Stedim) and stored at -80°C. The $CA_{\Delta 1\text{-}13}$ and $CA_{\Delta cypA4G}$ mutant proteins were purified in the same way.

2.4.6. Expression and purification of TRIM5α$_{AGM}$

Suspension SF9 insect cells (0.4 l at 2.5 x $10^6$ cells/ml) grown in ESF-921 medium (Expression Systems) were infected with recombinant baculoviruses at an approximate MOI of 10 and harvested by centrifugation 48 h later. Cells were resuspended in a lysis buffer (75 mM CHES pH 10.0, 100 mM NDSB-256, 1.5% Triton X-100, 5 mM NaCl, 1 mM TCEP), supplemented with cOmplete protease inhibitors cocktail tablets (Roche) and lysed by mechanical breakage in a motorized dounce homogenizer. The cell lysate was clarified by centrifugation at 45,000 g for 45 min (Beckman JA-25.50 rotor) at 4°C. The supernatant was filtered (0.45 μm) and loaded onto a Strep-Tactin Sepharose resin (IBA) pre-equilibrated with wash buffer 25 mM CHES pH 10.0, 5 mM NaCl, 1 mM TCEP. The column was washed with 50 CV of the wash buffer. The protein was eluted in 15 CV wash buffer supplemented with 2.5 mM D-desthiobiotin (Sigma). The protein was applied to two 5 ml HiTrap Q HP (GE Healthcare) pre-equilibrated with the wash buffer. Protein was eluted with a linear gradient of NaCl (0–1 M) in the same buffer. Fractions containing TRIM5α proteins were pooled, dialyzed overnight against 25 mM CHES pH 10.0, 5 mM NaCl, 1 mM TCEP, loaded onto a HiLoad 16/600 Superdex 200 gel filtration column (GE Healthcare) pre-equilibrated with the same buffer, and eluted in 1 CV. Fractions corresponding to TRIM5α dimers were pooled and concentrated to ~5 mg/ml using a Vivaspin 20 concentrator (30,000 MWCO PES Sartorius Stedim). Freshly purified protein was used for self-assembly, and co-assembly experiments and the remaining portion was flash-frozen in liquid nitrogen and stored at -80°C.

2.4.7. Generation of disulfide-stabilized HIV-1 CA tubes

Purified HIV-1 CA containing the A14C and E45C mutations at 1 mg/ml was dialyzed at 4°C for 8 h in 50 mM Tris-HCl, pH 8.0, 1 M NaCl and 100 mM βME, followed by 8 h dialysis in 50 mM Tris-HCl, pH 8.0, 1 M NaCl. Finally, the sample was dialyzed for 8 h at 4°C against the CA buffer (20 mM Tris-HCl pH 8.0, 40 mM NaCl). Tubes were stored at 4°C until needed.

2.4.8. Capsid binding assays

Twenty μl of disulfide-stabilized HIV-1 CA tubes (A14C/E45C) (1 mg/ml) were incubated on ice with 5 μl of TRIM5$\alpha_{AGM}$ (1 mg/ml) for 1 h. Five μl of the reaction mixture were removed as a LOAD sample and mixed with equal volume of 2x SDS-PAGE sample buffer. The remaining sample was centrifuged at 16,000 g for 30 min at 4˚C. The supernatant (20 μl) was removed and mixed with an equal volume of 2x SDS-PAGE sample buffer ('SUPERNATANT' sample). The pellet was resuspended in 20 μl of TRIM5α buffer (25 mM CHES pH 10.0, 5 mM NaCl, 1 mM TCEP) and 20 μl of 2x SDS-PAGE sample buffer ('PELLET' sample). Samples were incubated for 10 min at 100˚C and analyzed by SDS-PAGE with subsequent Coomassie staining. Gels were scanned and quantified using ImageJ [203]. Binding efficiency was expressed as the fraction of TRIM5α protein in the pellet.

2.4.9. Self-assembly of HIV-1 CA

Purified HIV-1 CA protein was mixed with a self-assembly buffer containing 100 mM Tris-HCl, pH 8.0 and 1 M NaCl in 1:1 ratio. The reaction mixture was incubated for 15 min at RT. The resulting CA tubes were visualized by negative stain EM.

2.4.10. Self-assembly of TRIM5α

The purified TRIM5α proteins at ~5 mg/ml were mixed at a 1:1 ratio with buffer (25 mM Tris-HCl, pH 8.0 and varying concentrations of the concentration of NaCl (40, 100, 300 or 500 mM). The reaction mixture was incubated for 15 min at 37˚C and an additional 3 h at RT. The sample was analyzed by negative stain EM.

2.4.11. Co-assembly of TRIM5α and HIV-1 CA

Co-assembly was performed by mixing HIV-1 CA (~23.5 μM) with TRIM5$\alpha_{AGM}$ (~0.3 μM) in assembly buffer (20 mM Tris-HCl pH 8.0, 40 mM NaCl) and incubating the sample at 37°C for 15 min, followed by overnight incubation at room temperature (~16 h). The next day, the sample was analyzed by negative stain EM. 3.5 μl of the co-assembly reaction was incubated on carbon-coated EM grids (Electron Microscopy Sciences) for 3 min. Grids were washed with 0.1 M KCl, blotted and stained with 2% uranyl acetate for 45 secs, blotted, and air dried. Samples were analyzed on a Tecnai F20 microscope operating at 120 kV to check the quality of co-assembly.

# Chapter 3.

# The interaction between TRIM5α and HIV-1 capsid by cryo-electron tomography and subtomogram averaging

## 3.1. Introduction

The restriction factor TRIM5α averts retroviral infection by recognizing protein motifs on the incoming retroviral core and causing premature disassembly of the capsid, thereby disrupting reverse transcription [80,81,83,85,87,88,110,205–207]. Binding to the viral capsid also activates innate immune signaling pathways through the E3 ubiquitin ligase activity [82,129,133]. The exact mechanism of restriction is not yet known. However, the restricted viral proteins appear to be removed in proteasome-dependent [89,92–95,130,208] or autophagosome-dependent manner [39,96].

As a member of the TRIM superfamily of proteins, TRIM5α is characterized by the presence of a conserved RBCC motif on its N-terminus [42]. This canonical fold comprises RING (R), B-box 2 (B) and coiled-coil (CC) domains. The RING finger domain in its dimer form functions as an E3 ubiquitin ligase activity that facilitates the transfer of ubiquitin molecules from an E2 conjugating enzyme to a protein substrate [128,133]. The B-box 2 domain mediates higher-order assembly of the protein [54,55,57,58]. The CC domain, in cooperation with Linker 2 (L2) region mediates dimerization of TRIM5α [60,109,125]. The C-terminal SPRY domain is responsible for species-specific binding to retroviral cores [87,110,111,209,210]. TRIM5α was shown to assemble into a

hexagonal lattice of the same symmetry as the capsid lattice [119,132]. In the pattern recognition model, the SPRY domains are arranged to bind the surface of the capsid through a network of weak interactions mediated by hexagonal net formation.

The purpose of this study was to understand at the molecular level how TRIM5α recognizes the HIV-1 capsid. We have reconstituted TRIM5α/capsid complexes *in vitro* using purified components and analyzed these structures by cryo-electron tomography. Our tomographic reconstructions and subsequent subtomogram averaging indicate that the complexes consist of capsid-like tubes thoroughly coated by an outer layer of assembled TRIM5α proteins. We show the arrangement of individual domains in full-length TRIM5α which agrees with the prediction made from the X-ray crystal structures of individual domains. We reveal that the SPRY domain acts as a dimer when it binds to CA. However, we do not observe a preferred orientation and conclude that the SPRY domain dimer binds the capsid lattice in a degenerate manner.

## 3.2. Results

### 3.2.1. Optimization of freezing conditions and data collection

As described in Chapter 2 and published work, the CA and TRIM5α lattices influence each other's formation [119,132]. In an idealized binding model, a fully saturated capsid has a stoichiometry of the TRIM5α:CA of ~1:14 [132]. To ensure that all the formed tubes are covered with a single-layer lattice of TRIM5α we used a sub-saturating ratio of ~1:100. After optimizing the co-assembly (Chapter 2), we proceeded with optimization of freezing conditions and data collection.

First, we tested a variety of grids. The QUANTIFOIL (Electron Microscopy Sciences) is a type of holey carbon film supported on a copper grid. The thickness of the carbon film reaches 49

nm (± 8.5 nm) which results in reasonably deep holes [211]. We reasoned that such deep holes would result in thick ice that would encapsulate the co-assemblies. However, data collection requires the sample to be imaged under high tilt angles (reaching up to +/-70˚). This resulted in the hole walls obscuring the view and limiting the working area of the grids. Additionally, our reconstructions were negatively impacted by electron damage to the carbon layer that showed as bubbling of the foil and introduced a movement of the sample, rendering the collected micrographs unusable. We therefore changed the type of the grids to C-flat (Electron Microscopy Sciences) that are thinner (28 ± 3 nm) but more resistant to the electron damage[211]. However, as the thickness of the grids decreased, we experienced thinning of the ice layer within the holes. The protein complex co-assembles into relatively thick tubes (400-500 Å in diameter) that were only partially embedded within the ice layer. As a result, parts of the complex were stripped off by the vacuum in the microscope's column. To mediate the thickness of the ice, we added virus-like particles (VLPs) studied in the lab. Their sturdy spherical architecture counteracted the thinning of the ice in analogy to support provided by pillars. Finding appropriate grids and ways to increase ice thickness was crucial to proceed with the structural analysis.

3.2.2. Cryo-electron tomography of TRIM5α decorated HIV-1 tubes

After optimizing the co-assembly and grid preparations, we proceeded with structural studies of the TRIM5α-coated CA tubes. As indicated by negative stain analysis, the assembled complexes were not uniform. We observed variations in tube lengths and the decoration patterns at the top of the tubes differed significantly. We utilized cryo-electron tomography as this method is suitable for the imaging of individual samples with no uniform structure. First, we collected a far-from-focus dataset which had high contrast and enabled direct visual inspection of the co-

assemblies. The obtained tomograms were similar to those presented before [132]. We confirmed that each tube was formed by an inner, compact wall of CA (Fig. 3.1.A) decorated with an outer lattice of TRIM5α proteins most clearly observed on the sides and top (Fig. 3.1.B). The outer layer showed regions of repeating patterns: we distinguished hexagons, pentagons, and heptagons, as well as chains of connected V-shaped structures. Then, we collected close-to-focus datasets for the detailed structural studies. The overall quality of tomograms was good, but we observed significant tube-to-tube variations. To elucidate the arrangement within the TRIM5α-coated CA tubes, we proceeded with subtomogram averaging of individual tubes [182,183]. The subtomograms were subjected to reference-free, iterative alignment and averaging.

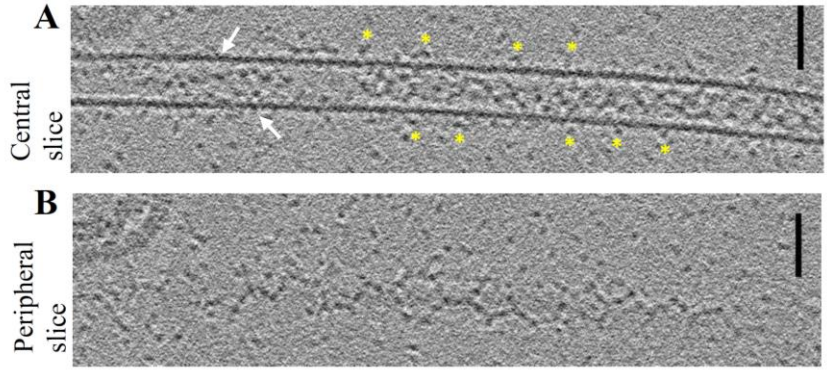


**Figure 3.1. Tomographic reconstruction of the TRIM5α-coated CA tubes.** A – A central slice through the tomogram showing walls of the tubular assembly (white arrows) and small regular protrusions on its sides (yellow asterisks). B – A peripheral slice through the tomogram showing the repeating patterns on the outskirts of the tube; one can distinguish hexagonal and pentagonal shapes and a chain of V-shapes. Scale bars 100 nm.

### 3.2.3. Subtomogram analysis of the inner lattice

Reconstruction of the inner wall – composed of the CA lattice – was conducted as described in the Materials and Methods section (Fig. 3.2). From the tomographic reconstruction, we defined segments that were uniformly distributed along the length of each tube. Subtomogram averaging revealed a helical arrangement of CA hexamers, similar to those published before [10,20]. The segments calculated for individual tubes differed from each other in diameter and helical family (data not shown). As the quality of the reconstruction and the number of details resolved in the segments varied, we proceeded with an analysis of the best seven reconstructions. For each tube, the positions of all the hexamers were determined and then re-averaged (Fig 3.4). This resulted in an average structure with a nominal resolution of ~16.3 Å (using a 0.5 cutoff and a spherical mask of a radius 102.2 Å) (Fig. 3.13).

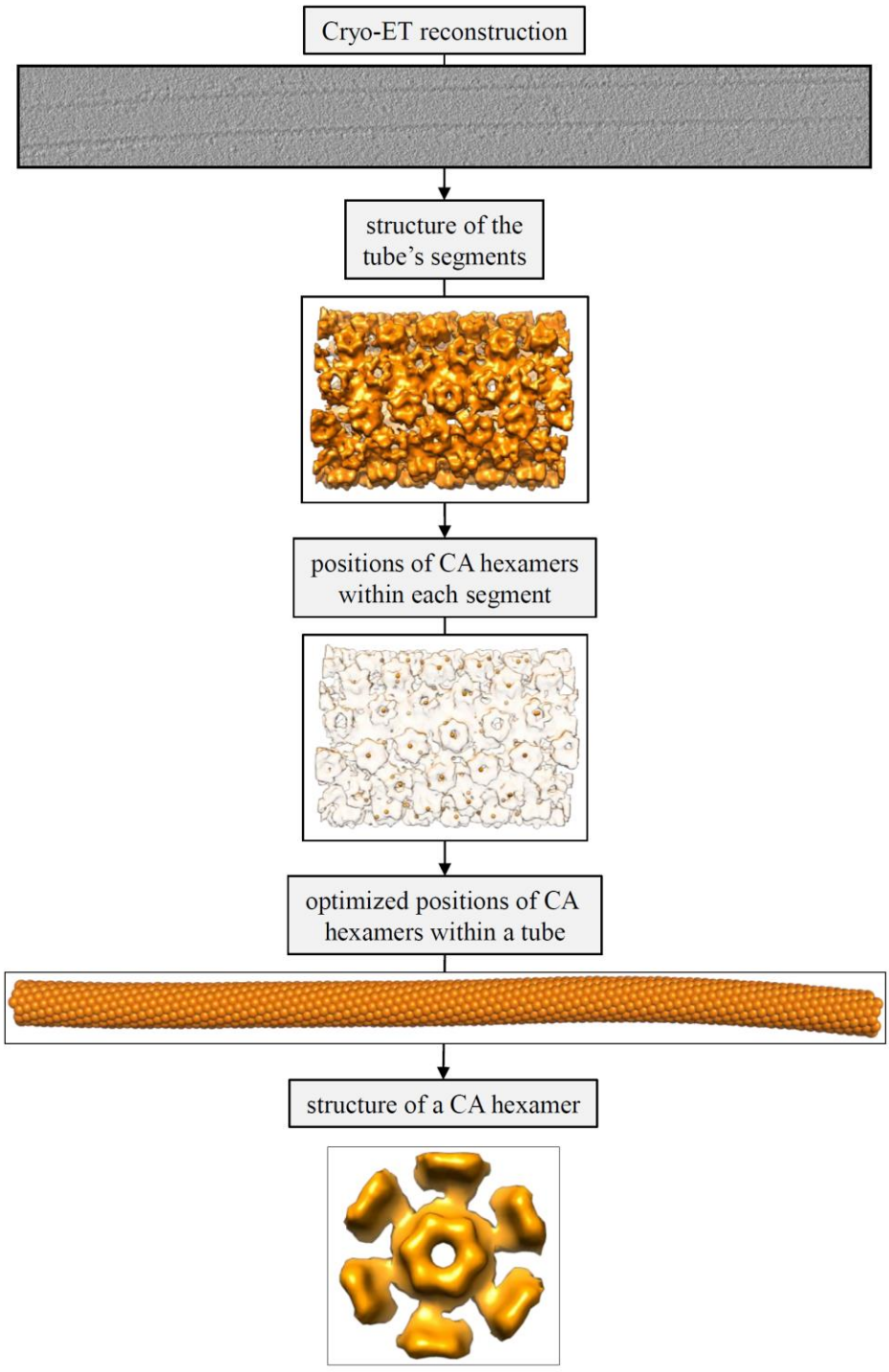


**Figure 3.2. Workflow of subtomogram averaging of the inner wall of TRIM5α-coated CA tubes.** From each tomographic reconstruction, we determined an average structure of a segment of the CA tube. We then optimized the positions of individual CA hexamers within each section and extrapolated to the whole tube. Final alignment successfully yielded the positions and orientations of individual CA hexamers.

We used a cross-correlation (cc) value to determine how well the individual hexamers were positioned within the tube, colored from red (low cc) to green (high cc) in Fig 3.6.A. The majority of the hexamers show high cc values (green). Weaker cc (yellow) corresponds to lower information content due to the missing wedge and may be observed on the sides of the tube. Low cc (red) was found only at the ends of the tube, where the reconstructed volumes curled towards the center of the tube; this is an artifact of the tube definition used by the averaging program. We did not observe any significant irregularities in the arrangement of the hexamers or misaligned particles that would signify breaks in the continuity of the CA lattice. Our observations therefore do not support the model that CA lattice destabilization occurs upon TRIM5α binding, as reported before [80]. We postulate that additional actions from the host cell are required to destabilize the HIV-1 cores besides TRIM5α binding.

We used USCF Chimera [212] to fit in structures of available CA hexamers into our averaged map. We used the following models: a crystal structure of cysteine-stabilized hexamer (PDB: 3H4E) [14]; the native full length CA hexamer (PDB: 4XFX) [19], and available structures obtained from cryo-EM studies of intact virions [8]. As expected, the PDB models fit the density well, to the limit of the map resolution (Fig. 3.3.A-C).

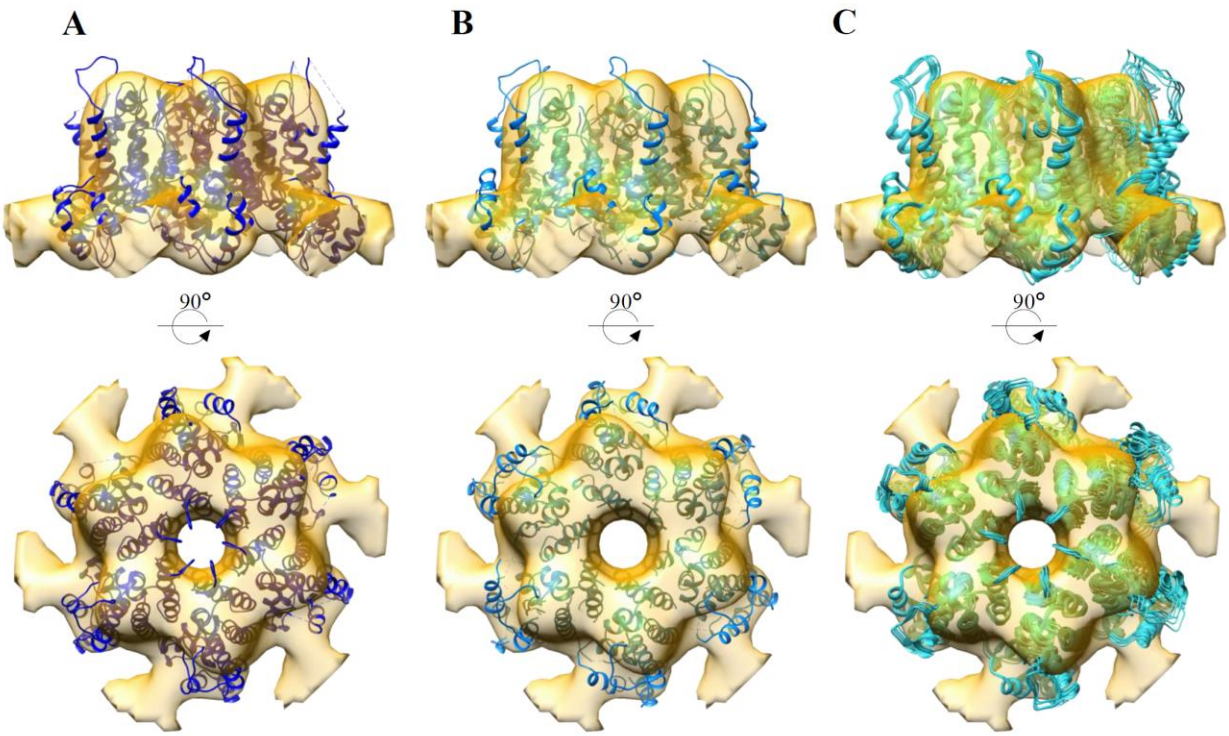


**Figure 3.3. Fitting of PDB models of CA hexamers into the subtomogram averaged reconstruction.** Structures of cross-linked (PDB: 3H4E) (A), native full-length (PDB:4XFX) (B), and cryo-em reconstructed (PDB: 5MCX, 5MD0, 5MD1, 5MDE, 5MDF, 5MDG) (C) CA hexamers were fit in the map obtained by subtomogram averaging of TRIM5α coated CA tubes using rigid-body fitting in USCF Chimera [212].

3.2.4. Subtomogram analysis of the outer lattice

TRIM5α was shown to form a hexameric lattice *in vitro* and hexameric densities when assembled on purified CA tubes and HIV-1 cores [119,132]. The connected antiparallel dimers were suggested to form the arms of the lattice, with B-box 2 trimers connecting the dimers at the vertices (three-fold) and two SPRY domains in the middle of the arms (two-folds). We generated two reference-free models from CTF-corrected tomographic reconstructions collected at a high defocus (~8 µm). We manually picked the positions at the vertices and in between them to generate a trimer model and a dimer model respectively (Fig. 3.4). Those models were subsequently used in an over-sampling approach to search for all trimer and dimer positions in the decorated tube. The positions and orientation of TRIM5α dimer and trimer units were determined independently, as described in the Materials and Methods section (Fig. 3.5).

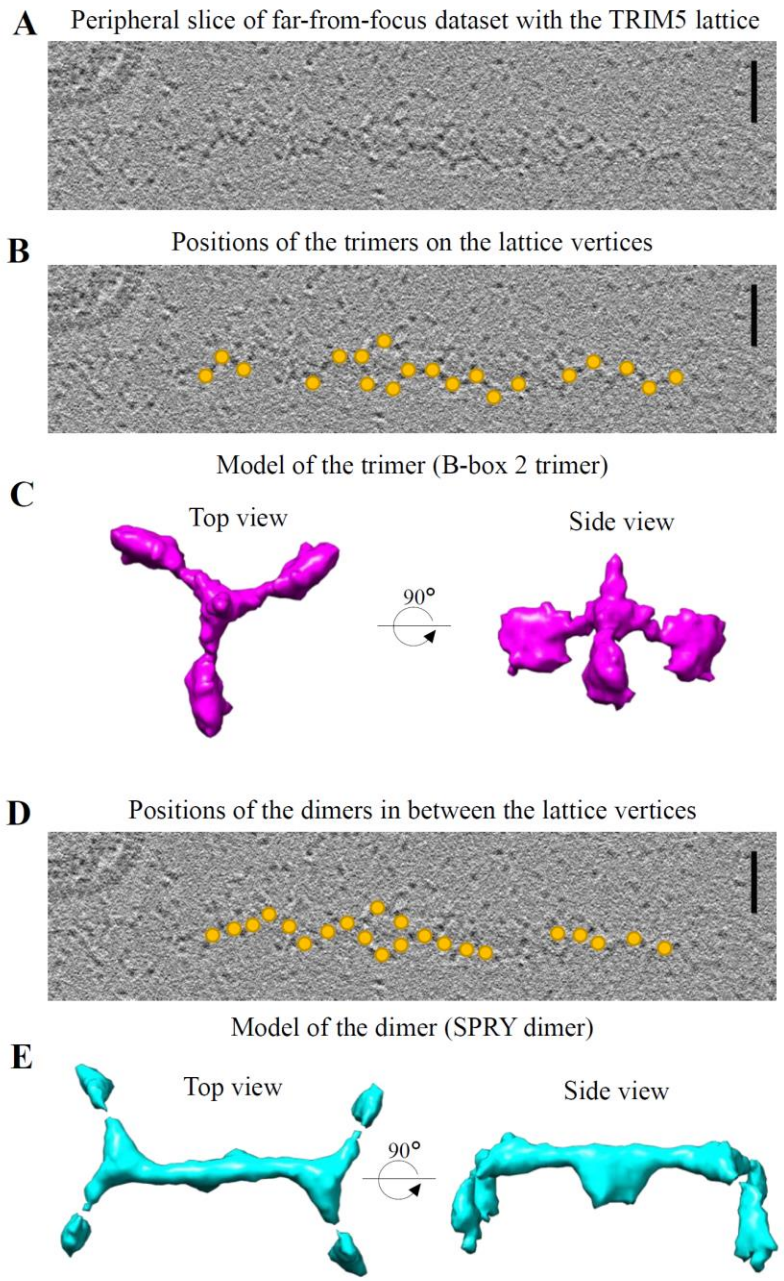


**Figure 3.4. Reference-free models of TRIM5 assembly units generated from the far-from-focus dataset.** A – Peripheral slice of the tomographic reconstruction showing a TRIM5α assembly; scale bar is 100 nm. B – Positions of the trimer units at the 3-fold vertices were manually selected as indicated by the yellow dots. C – Reference-free model of the trimer unit was generated by averaging the subtomogram volumes reported in B. D – Positions of the dimer units in between the 3-fold vertices were manually selected as indicated by the yellow dots. E – Reference-free model of the dimer unit was generated by averaging the subtomogram volumes indicated in D. The models of the trimer (magenta) and the dimer (cyan) units were used in the oversampling approach; color coding is retained in this chapter.

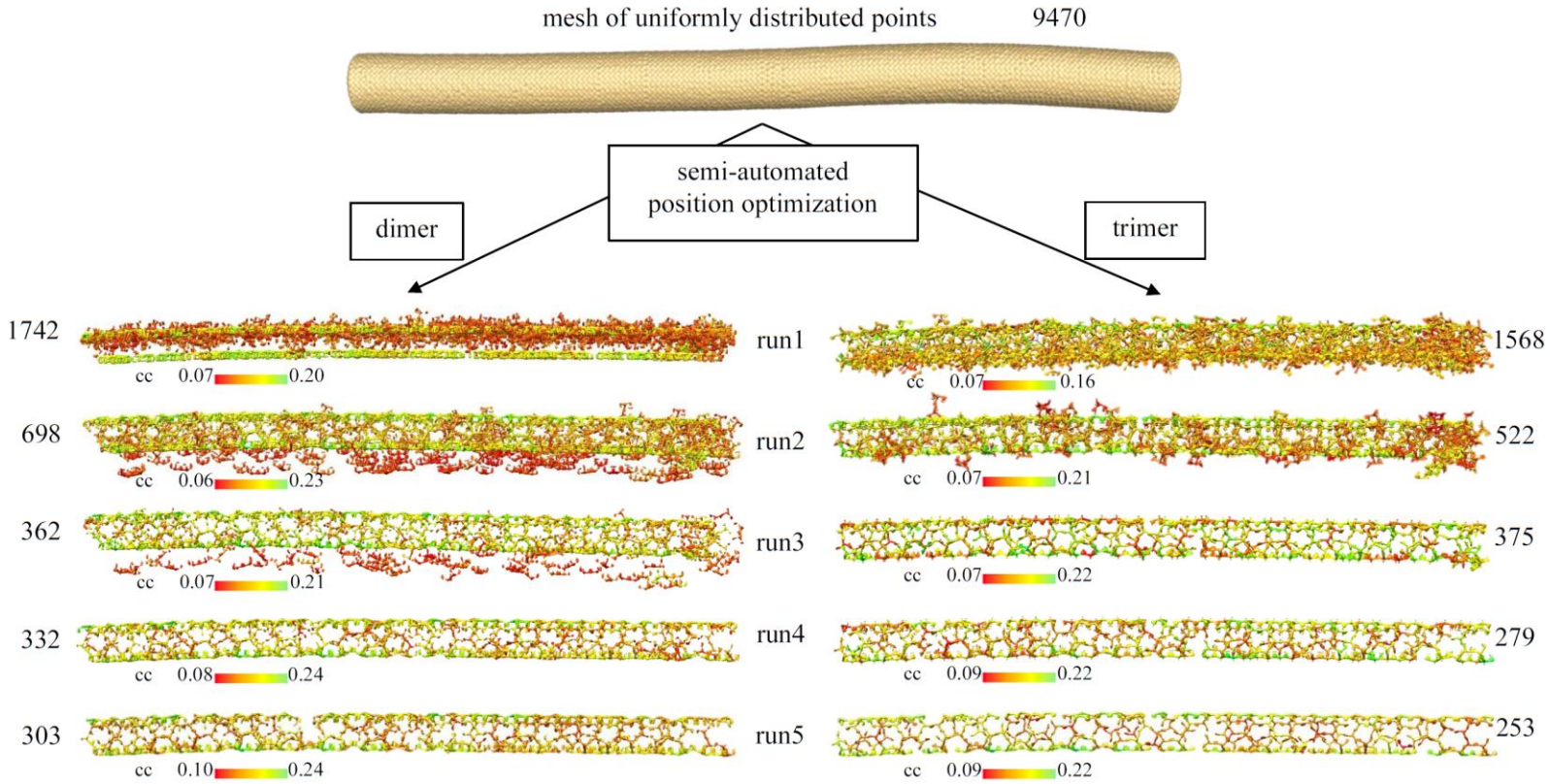


**Figure 3.5. Subtomogram averaging of the outer wall of TRIM5α-coated CA tubes by oversampling.** We determined a mesh of uniformly distributed points in a radius of ~250-290 Å from the CA tube's axis and extracted sub-volumes centered on these points. During subtomogram averaging either the trimer or dimer model generated from the far-from-focus dataset was used as search models. Overlapping particles were removed, keeping on with the highest cc values. Dimer and trimer reconstructions were performed independently as a cross-validation method. Individual particles are colored by their cc values.

The positions and orientations of dimer and trimer units within the lattice were determined independently of each other as a cross-validation method. The nominal resolution of TRIM5α dimers reached ~27 Å and was estimated by applying a spherical mask of radius 73 Å pixels and FSC cutoff of 0.5. The nominal resolution of TRIM5 trimer reached ~23.4 Å and was calculated by using a spherical mask of a radius 93.4 Å pixels and FSC cutoff of 0.5 (Fig. 3.13). The mapped positions of both dimer and trimer units were in excellent agreement, defining a single continuous lattice that thoroughly surrounded each tube (Fig. 3.6.B, C). Our reconstructions show that the majority of the lattice is formed by hexagons (Fig. 3.6.E, G) that would match the symmetry of the capsid. Pentagons and heptagons (Fig. 3.6.F), always adjacent to each other, are also present. These pentagons and heptagons would usually introduce sharp curvature into the hexagonal lattice and change the lattice directionality. However, in the case of the tubes, having the pentagons and heptagons always adjacent to each other preserves the curvature. Incorporating pentagons/heptagons may enable the net to adapt to various capsid shapes and dimensions. Furthermore, they may afford the SPRY domains some degree of flexibility to optimize local points of interactions.

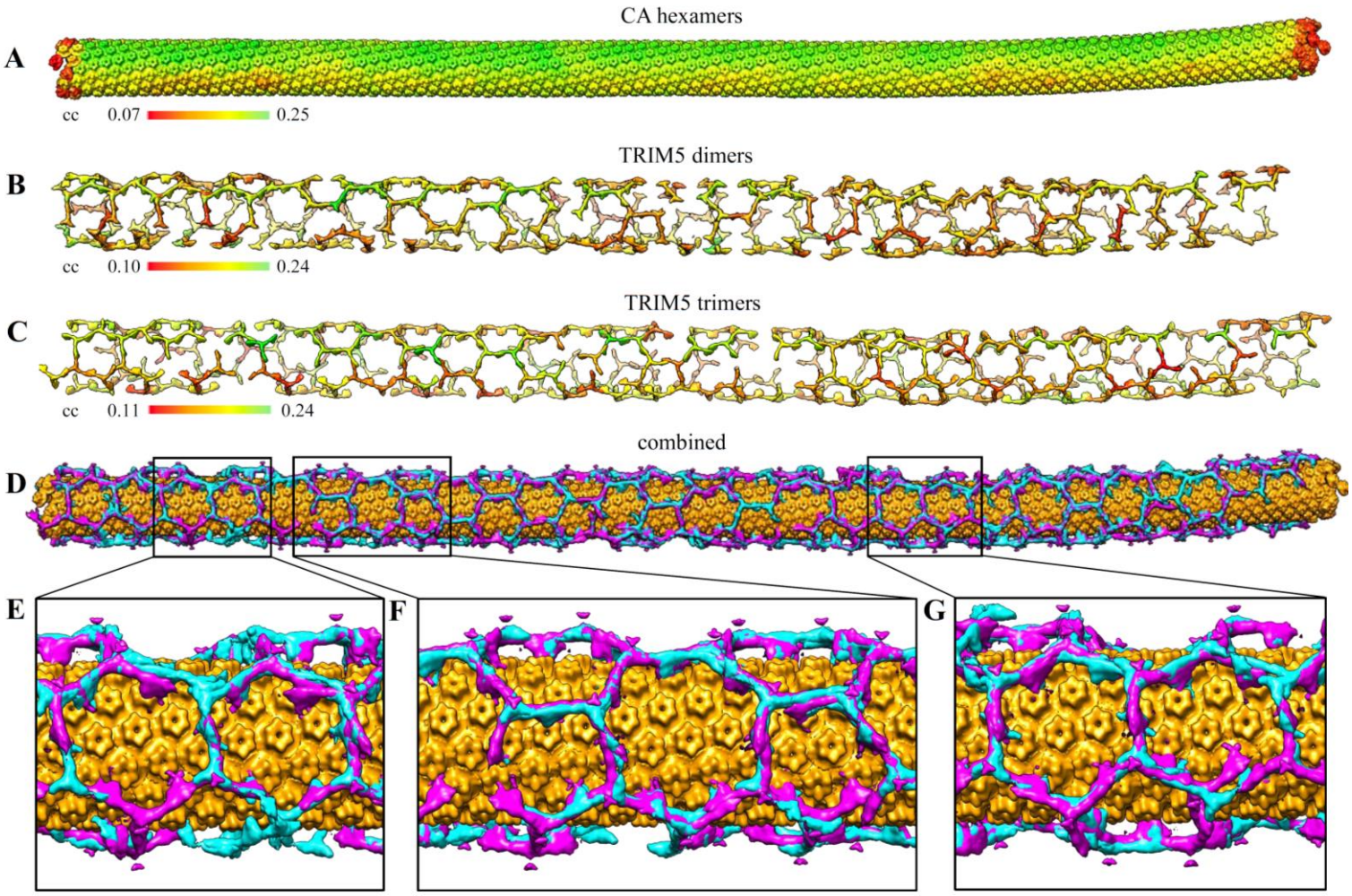


**Figure 3.6. Reconstruction of the TRIM5α-covered CA tube by the subtomogram averaging.** A – Reconstruction of the CA tube; individual hexamers are colored by the corresponding cross-correlation values from lowest (red) to highest (green). B, C – Reconstruction of the TRIM5α lattice using TRIM5α dimer (B) or trimer (C) units as a search model; individual units are colored by

the corresponding cross-correlation values from lowest (red) to highest (green). D – Reconstruction of TRIM5α-covered CA tube obtained from combined reconstructions of CA hexamers (orange), TRIM5α dimer (cyan) and TRIM5α trimer (magenta). The dimer and trimer reconstructions agree with each other and describe the same TRIM5 lattice that encapsulated the CA tube. E, F, G – Close-up views on the TRIM5α lattice show that it is built mostly from hexagons (E, G); however, the pentagons and the heptagons are also present (F).

We generated pseudo-atomic models by rigid body fitting of the available crystal structures of individual domains of TRIM5α into our EM maps (Fig. 3.7). The crystal structures of the B-box/CC dimer (PDB:4TN3) [60] and B-box/CC trimer (PDB: 5IEA) [58] fit into the trimer reconstruction unambiguously. Additional density was observed above the 3-fold vertices at a low contour level. We determined that this density corresponds to the RING domain as it was absent from reconstructions made with TRIM5α lacking this domain (Fig. 3.8). In an attempt to improve the resolution of the RING density, we re-calculated the fragment of the map corresponding to the RING by applying a tight mask above the 3-fold and performing additional optimization. Although the resulting density was stronger, the quality did not improve sufficiently to unambiguously fit in the crystal structure of the RING dimer (data not shown) [133]. This was likely because the RING is a small, 5 kDa domain, and the image quality, as well as SNR of the tomographic reconstructions, were not sufficient to allow unambiguous alignment of the sub-volumes.

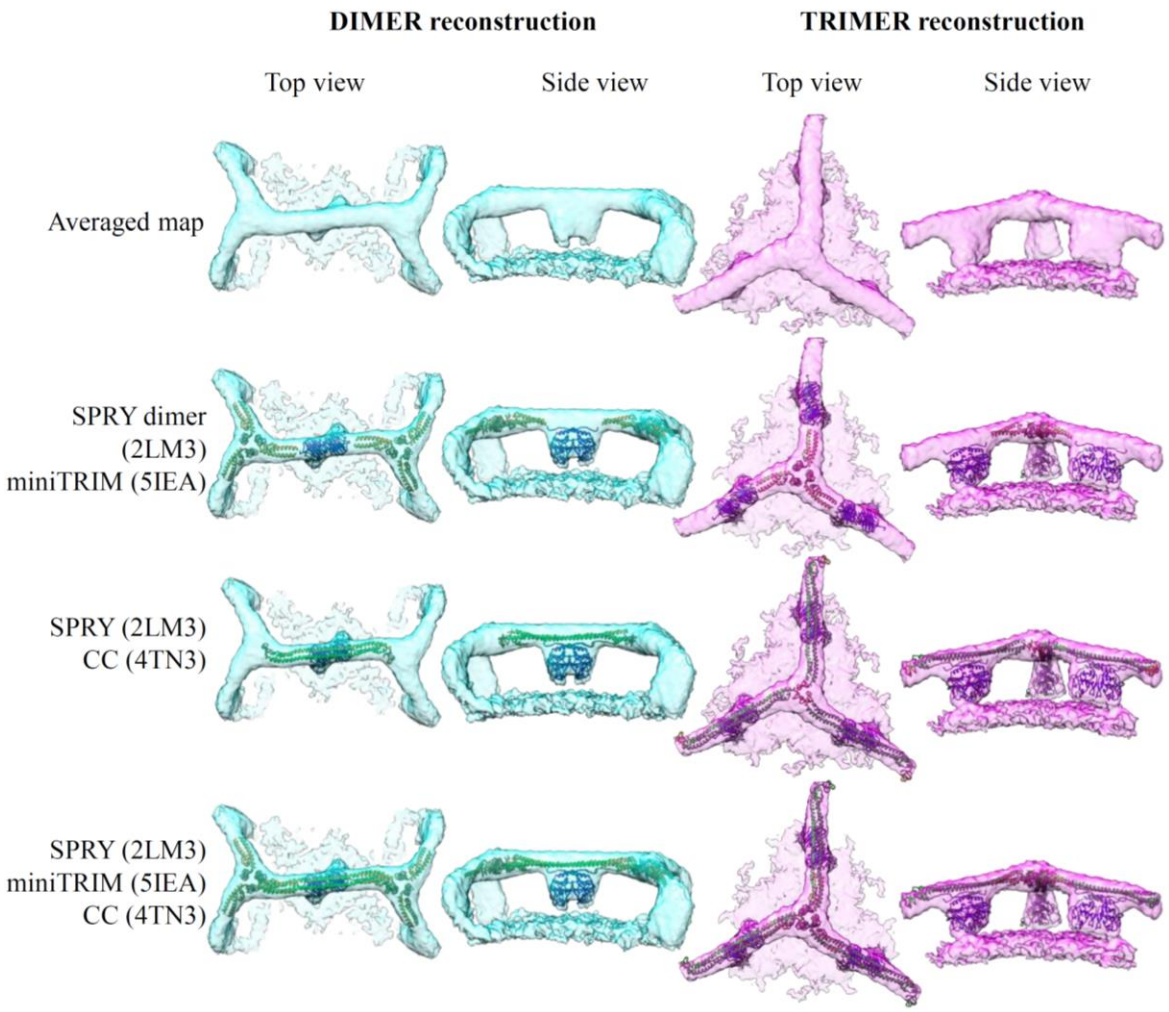


**Figure 3.7. Pseudo-atomic models of trimer and dimer units.** Available crystal structures of TRIM5α domains (as indicated on the left side of the figure) were rigid-body fitted into the calculated maps. Positions of the domains can be assigned unambiguously.

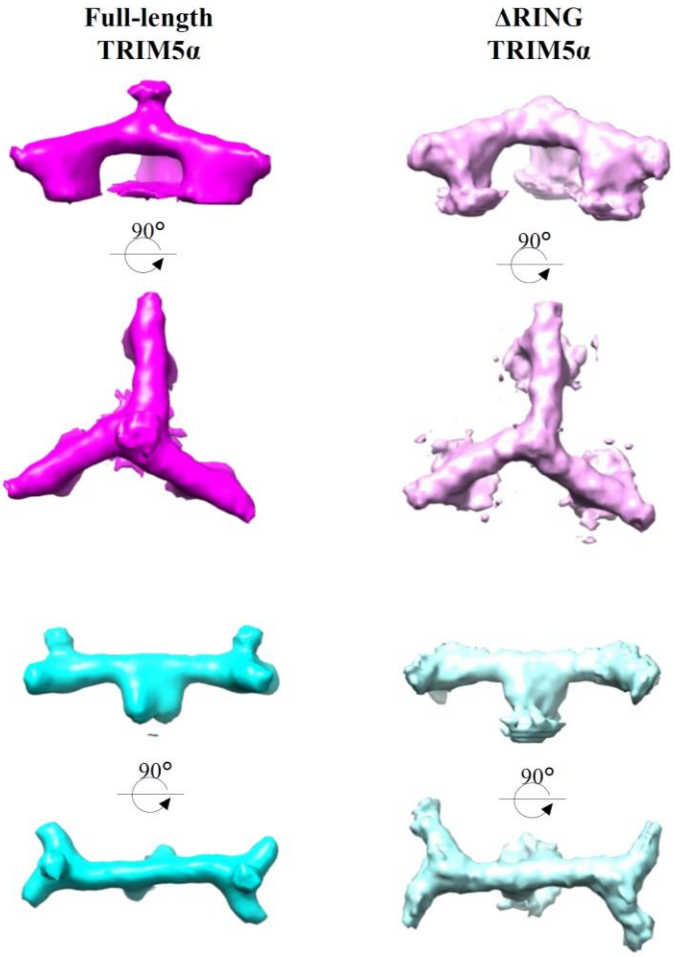


**Figure 3.8. The RING domain is positioned on top of the B-box 2 trimers at the lattice vertices.** The additional density is visible in both a trimer (magenta) and a dimer (cyan) reconstructions of full-length TRIM5α but is missing from the reconstruction of ΔRING construct.

### 3.2.5. Subtomogram analysis of the SPRY domain and a lattice-lattice interaction

The SPRY domain is responsible for species-specific binding of the TRIM5α proteins to retroviral capsids. Our reconstructions show that the SPRY dimer is placed in the middle of each CC, and as it is oriented towards the capsid, it serves as the only point of interaction between the two lattices. This observation supports the proposal that two SPRY domains engage the retroviral capsid at the same time as a single interaction unit [58–60,125]. To gain a better understanding of the molecular basis of the lattice-lattice interaction, we focused on the SPRY domain alone and its recognition of the underlying capsid. First, we applied a tight mask around the SPRY to minimize the influence of the capsid lattice on the reconstructions and performed additional optimizations that included azimuthal refinement. The new map has clearly defined lobes oriented away from each other, and the surface is no longer smooth, indicating that the higher-resolution features become more pronounced. The nominal resolution of the SPRY domain was estimated ~18.7 Å after application of a spherical mask of a radius 73 Å and FSC cutoff of 0.5 (Fig. 3.13).

We fitted the available structure of the SPRY domain (PDB: 2LM3) into the newly defined density (Fig. 3.9). Both monomers fit unambiguously into their corresponding bi-lobes as rigid bodies; however, the V1 loop is not encapsulated within the density. The V1 loop can adopt multiple conformations [83], and may serve as an anchor to position TRIM5α dimers on the capsid surface. In these reconstructions, the density corresponding to the capsid lattice had no distinct features, indicating that the relative positions of the two lattices are not aligned by preferential binding. Thus, binding of SPRYs to the CA subunits occurs in a degenerate manner.

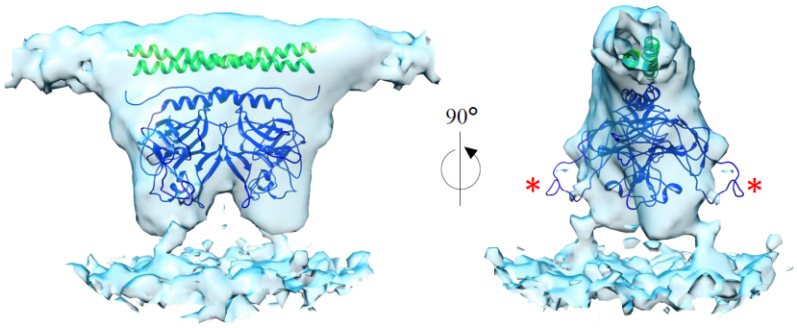


**Figure 3.9. Pseudoatomic model of the SPRY domain.** Crystal structures of two SPRY domains (PDB: 2LM3) were fitted independently in the calculated density. The red stars indicate the flexible V1 loops stretching outside the density

Visual analysis of the positions of the SPRY domains on the CA lattice revealed that the SPRY dimers can be positioned on top of a single hexamer, between two hexamers, or at the interface between three hexamers (Fig. 3.10.A, B). To confirm that the SPRY densities were indeed at degenerate positions, we plotted their centers of mass relative to the CA hexamer. The SPRY domain centers appeared randomly distributed (Fig. 3.10.C). We then divided the SPRY sub-volumes into three zones, as determined by their positions relative to the hexamer (Fig. 3.10.D). Zone 1 includes the particles that were in close proximity to a single hexamer, which was defined as an area of radius 35 Å from the center of the CA hexamer; this corresponds to about one-third of all SPRY positions. Zone 2 includes all SPRY domains that did not co-localize with a single hexamer and were located in an area defined as less than 87.6 Å but more than 35 Å from the center of CA hexamer. Subsequently, we distinguished the third zone within this subset that includes the SPRY domains that are positioned above the two-fold axis between two neighboring hexamers.

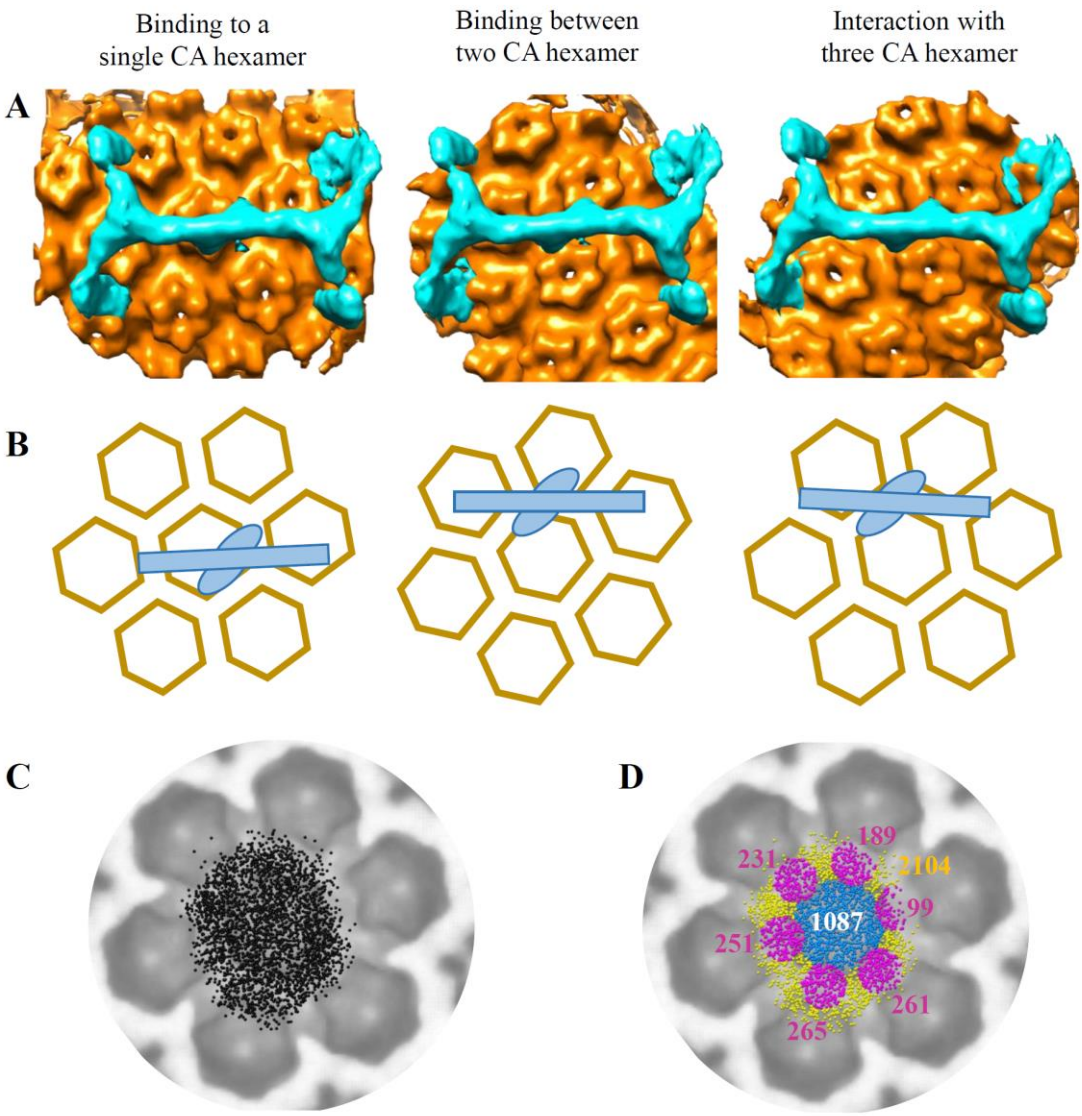


**Figure 3.10. Models of the SPRY domain binding.** A – From the reconstructed TRIM5α-coated CA tubes, we determined that the SPRY domain can be positioned on top of a single hexamer (left), between two hexamers (middle) or in between three hexamers. B – Schematic representation of SPRY dimer binding to the CA lattice, as seen in A. C – Positions of the centers of the SPRY dimers with respect to the closest single hexamer were plotted on a single plane. D – The centers of the SPRY domains were divided into three zones. Zone 1 (blue) includes the SPRY centers that co-localized with a single CA hexamer. Zone 2 (yellow) contains all SPRY domains that do not fall into zone 1 category. Zone 3 is a subset of the SPRY domain centers from the zone 2 that are positioned between two neighboring hexamers. The number of particles in each group is shown.

After defining the zones, we re-calculated the new averages of the CA hexamers corresponding to the zones described above, applying tight masks. The resulting maps were subtracted from each other, with the expectation that the difference density would indicate the predominant position of the SPRY dimer for each zone (Fig 3.11). As expected from the visual inspection, strong difference density was observed right above the central hexamer for zone 1; more diffuse density was seen around the central hexamer for zone 2; and localized density between two hexamers was found for zone 3. These confirm that the SPRY positions were obtained with reasonable accuracy.

In a complementary analysis, we re-averaged the TRIM5α dimer units and obtained difference density maps (Fig. 3.12). The zone 1 subset showed a strong density below the SPRY domain, whereas the zone 2 and 3 subsets again had more diffuse difference densities at the periphery of the SPRY density. Altogether, these confirm that the SPRY domains can indeed occupy degenerate positions relative to the CA hexamer.

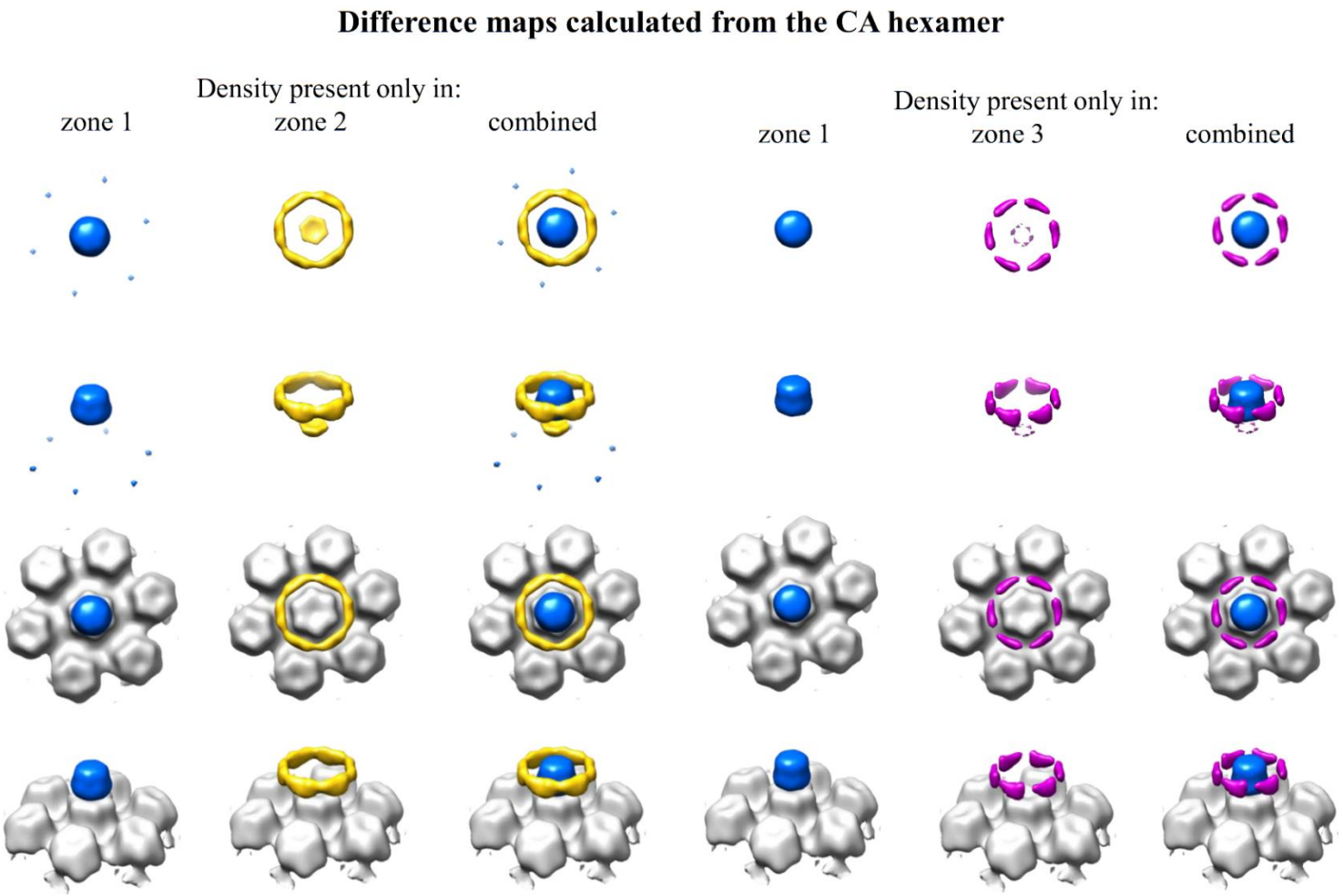


**Figure 3.11. Cryo-EM difference density maps from the respective zones calculated from the positions of CA hexamers.** The map of the CA hexamers is used as a reference; the difference maps of the respective zones are color-coded as in Figure 3.9.D. The positive components are labeled accordingly.

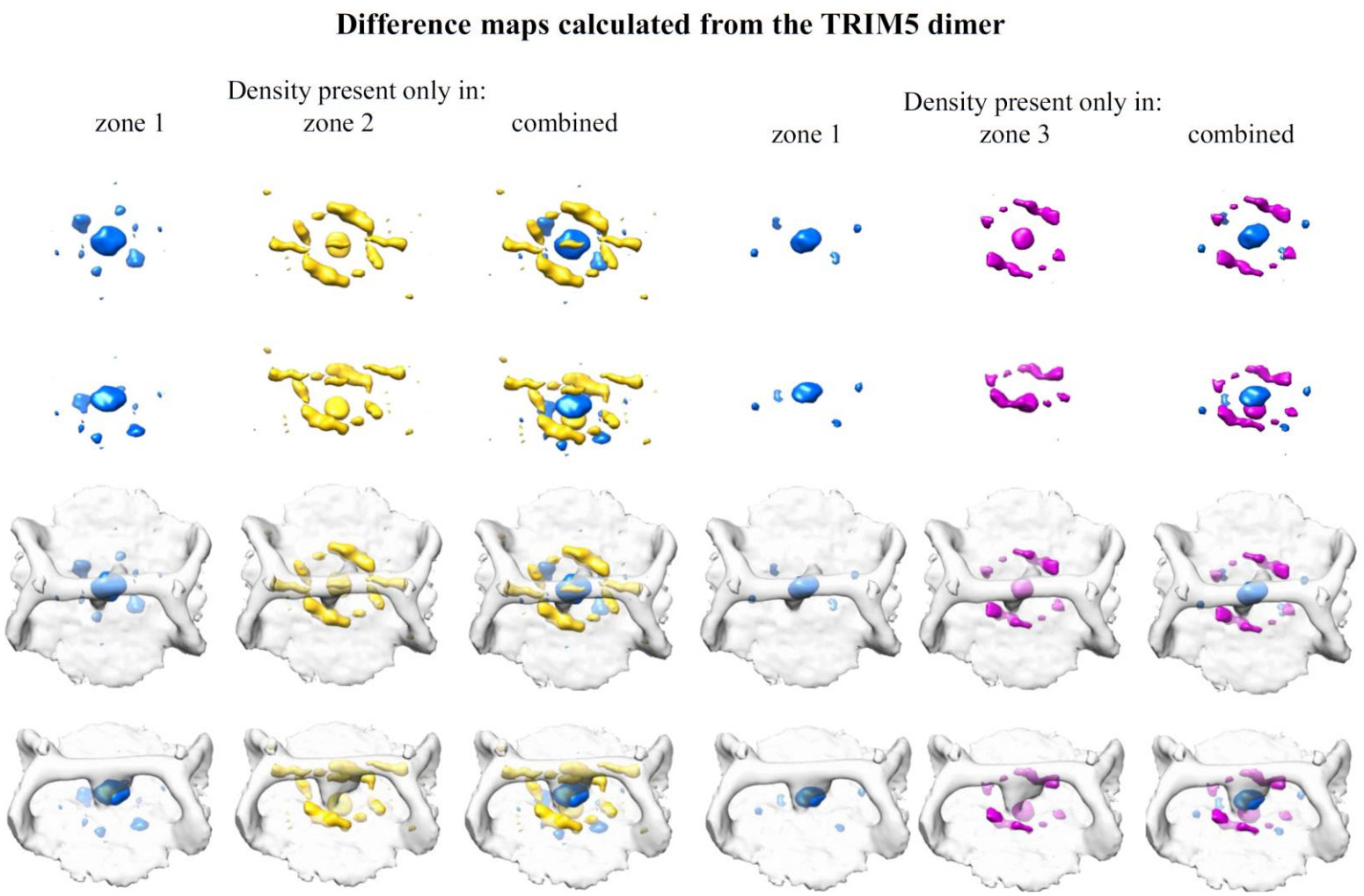


**Figure 3.12. Cryo-EM difference density maps from the respective zones calculated from the positions of TRIM5α dimer units.** The map of the TRIM5α dimer unit is used as a reference; the difference maps of the respective zones are color-coded as in Figure 3.9.D. The positive components are labeled accordingly.

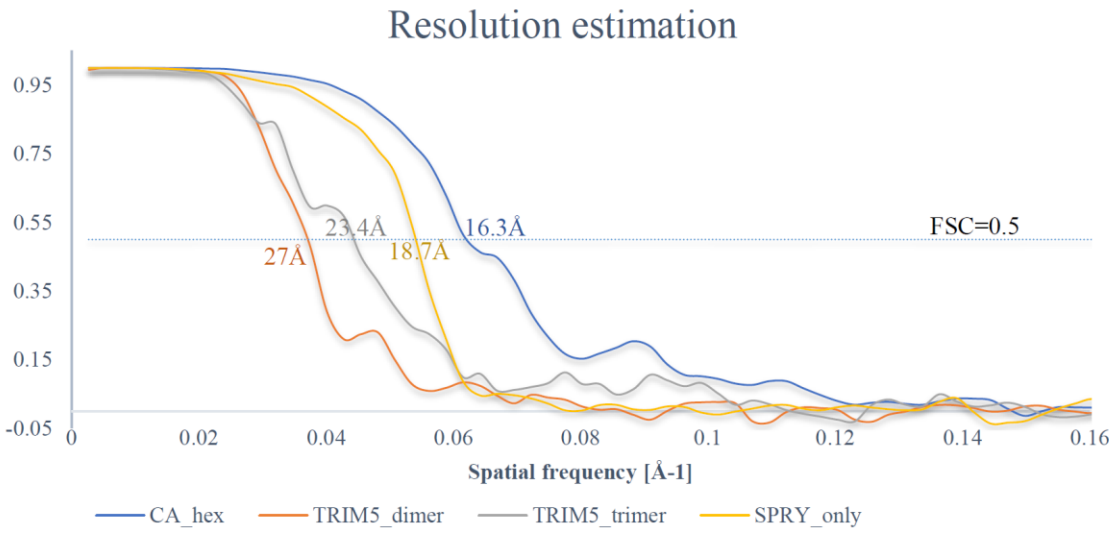


**Figure 3.13. Resolution estimation of subtomogram averaged maps.** Fourier shell correlation (FSC) curves, showing the overall nominal resolution of CA hexamer, TRIM5α dimer and trimer units, and the SPRY domain only at 27 Å (orange), 23.4 Å (grey), 18.7 Å (yellow), and 16.3 Å (blue) respectively.

## 3.3. Discussion

The C-terminal SPRY domain of TRIM5α is responsible for capsid binding and determines the species-specificity of the restriction [87,107,110,111,122,209]. Weak binding affinity towards retroviral capsids is compensated by higher-order oligomerization of the TRIM5α proteins that creates powerful avidity effects. Here, we used cryo-electron tomography and subtomogram averaging to solve structures of TRIM5α-coated CA tubes. We found that all CA tubes regardless of length, diameter, or helical family, were equally caged by the TRIM5α lattice (Fig. 3.6.B, C). Previous cryo-ET reconstructions suggested that the CA tubes and stabilized HIV-1 capsids may have been only partially covered with the TRIM5 lattice[132], yet we detected densities corresponding to the TRIM5α protein along the whole length and at all sides of each of the 7 tubes examined in detail. The resolved TRIM5α lattice appears as a hexagonal net, and fitting crystal structures of individual domains and generated a pseudoatomic model of TRIM5α (Fig. 3.7). Our reconstructions show that the RING domains are situated above the B-box 2 trimers and oriented away from the capsid lattice, towards the host cell cytoplasm (Fig. 3.8). The SPRY dimers are the only domains in direct contact with the capsid lattice. The reconstructions of both TRIM5α units include an additional density that corresponds to the CA lattice; however, no distinct features of the lattice were visible. We determined that the capsid lattice is intact upon TRIM5α binding, suggesting that the single binding does not cause capsid disassembly (Fig. 3.6.A). It is possible that the cage created in such a manner serves as a scaffold for other cellular components. Dimerization of the RING domain is required for the enzymatic activity and formation of the hexagonal lattice brings three RING domains together. Subsequent recruitment of other components of ubiquitin cascade leads to premature capsid disassembly and inhibition of reverse transcription [129,133,208]. However, even

when RING activity is impaired, and the viral life cycle progresses through the reverse transcription, viral replication is still restricted [111,120,129].

The specificity of the restriction is mediated by the SPRY domain, specifically by the variable loop regions (V1-V4). We show that the SPRY domain dimer acts as a single binding unit that recognizes multiple epitopes on the capsid surface (Fig. 3.9). The SPRY domain binds predominantly at the interface between the hexamers; however, we are not yet able to determine its precise position due to the degenerate mode of binding (Fig. 3.10).

In summary, our studies show that TRIM5α forms a predominantly hexagonal cage around capsid mimetics, with pentagonal and heptagonal insertions that would allow the TRIM lattice to follow the trajectory of the CA tube. The TRIM5α lattice is very flexible as it encapsulates tubes of various diameters and belonging to different helical families and provides a glimpse of how capsids of various shapes and sizes are recognized. Higher order assembly serves as a mechanistic link between capsid binding and enzymatic activity of the RING domain. It brings catalytically active domains close to each other as E3 ligase activity requires RING dimerization [133]. Modulation of retroviral restriction and TRIM5α turnover in the cells were shown to be dependent higher order assembly of the restriction factor [57,130] as large assemblies were degraded more rapidly than the non-assembled proteins. Capsid lattice promotes higher order oligomerization of TRIM5α and may serve as a regulatory mechanism for the immune system [119]. Without the retroviral lattice, the TRIM5 assembly is not promoted, and lack of RING domain dimerization does not recruit the members of the ubiquitin cascade.

## 3.4. Materials and methods

### 3.4.1. Expression and purification of TRIM5α$_{AGM}$ and HIV-1 CA

Protein expression and purification were performed as described in 2.4.6 and 2.4.7.

### 3.4.2. Co-assembly of TRIM5α and HIV-1 CA

Co-assembly experiment was performed by mixing HIV-1 CA with TRIM5α$_{AGM}$ (~1:100 ratio) in an assembly buffer (20 mM Tris-HCl pH 8.0, 40 mM NaCl) and incubating the sample at 37°C for 15 min, followed by an overnight incubation at room temperature (~16 h). The next day, the sample was analyzed by negative stain EM. 3.5 µL of the co-assembly reaction was incubated on carbon-coated EM grids (Electron Microscopy Sciences) for 3 min. Grids were washed with 0.1 M KCl, blotted and stained with 2% uranyl acetate for 45 secs, blotted, and air dried. Samples were analyzed on a Tecnai F20 microscope operating at 120 kV to check the quality of co-assembly. The remaining sample was used for the cryo-tomography experiment.

### 3.4.3. Expression and purification and of the Gag-like protein of HIV-1

4L of *E. coli* BL21 (DE3) cells (Stratagene) transformed with the Gag construct expression vector was grown to an $OD_{600}$ = 0.8 in LB medium at 37°C with shaking. Protein expression was induced with 1 mM isopropyl-β-D-thiogalactopyranoside (IPTG) followed by 4 h incubation at 25°C. Cells were harvested by centrifugation in a Beckman JLA-8.1000 rotor and stored at -80°C. The cell pellet was resuspended in 50 mM Tris-HCl pH 8.3, 1 M LiCl, 1 mM EDTA, 100 mM βME, and 0.2% (w/v) deoxycholate, supplemented with cOmplete protease inhibitors cocktail tablets

(Roche), and lysozyme and incubated on ice for 20 min with shaking. Cells were lysed using a sonicator. After centrifugation at 45,000 g for 45 min (Beckman JA-25.50 rotor) at 4°C, the protein was precipitated with ammonium sulfate to 25% saturation and incubated on ice for 10 minutes. The protein was pelleted by centrifugation at 9,000 g for 20 min, resuspended in 25 mM Tris-HCl pH 8.5, 500 mM NaCl, one mM EDTA and 20 mM βME. Filtered sample was applied to an ion-exchange column (5 ml HiTrap Q HP, GE Healthcare) pre-equilibrated with the same buffer and eluted with the same buffer. Fractions containing the protein were pooled, and the protein was precipitated with ammonium sulfate to 25% saturation and incubated on ice for 10 minutes. After centrifugation for 20 min at 9,000 g, protein pellet was resuspended 20 ml 25 mM MOPS pH 6.5, 200 mM NaCl, 1mM EDTA and 20mM βME. Filtered sample was applied to an ion-exchange column (5 ml Hi-Load SP Sepharose High Performance, GE Healthcare) pre-equilibrated with 25 mM MOPS, pH 6.5, 150 mM NaCl, 1mM EDTA, and 20mM βME. Protein was eluted with a linear gradient of NaCl (0.1 – 1 M) in the same buffer. Fractions containing CA proteins were pooled, and the protein was precipitated with ammonium sulfate to 25% saturation, incubated on ice for 10 minutes. After centrifugation for 20 min at 9,000 g, protein pellet was resuspended in 25 mM MOPS pH 6.5, 200 mM NaCl, 1 mM EDTA and 20mM βME to a final concentration of 10 mg/ml and stored at -80°C until needed.

3.4.4. Assembly of virus-like particles of HIV-1

0.5 mg of purified Gag protein was incubated for 2 h at 37 °C in a buffer containing 100 mM Tris-HCl pH 7.5, and 375 mM tartrate. The sample was centrifuged at 17,000 g for 10 min at room temperature, and the protein pellet was resuspended in a buffer containing 100 mM Tris-HCl pH 7.5 and 500 mM NaCl. This step was repeated three times. After the final centrifugation step, the

assembled protein was resuspended in 100 µl of 100 mM Tris-HCl pH 7.5 and 500 mM NaCl and stored at room temperature.

3.4.5. Sample preparation and data acquisition for cryo-electron tomography

An aliquot (20 µl) of the co-assembled TRIM5α/CA sample was mixed with 20 µl of 10-nm BSA Gold Tracer (Electron Microscopy Sciences, Hatfield, PA) mixed 1:1 with assembled VLPs. 3.5 µl of the TRIM5α-coated CA tubes was applied on glow-discharged holey carbon grids (C-flat; Protochips, Raleigh, NC) and plunge-frozen in liquid ethane. Cryo-electron tomograms were acquired using FEI Titan Krios electron microscope operated at 300 kV at liquid nitrogen temperature equipped with a Falcon 2 camera. Digital micrographs were recorded under low-dose conditions. Tilt series were collected using semi-automatic data collection software Tomography 3.0 (FEI) with an angular range of −60° to +60°, the angular increment of 1°, and a nominal magnification of 29,000×, with a pixel size of 2.92 Å. Two data sets were collected on the FEI Titan Krios. First, one of defocus of 8 µm was used to generate initial reference-free maps that were used as in a close-to focus (2.5-4 µm) datasets as search models.

3.3.6. Data processing

The tilt series were aligned using gold fiducials as position markers using IMOD [213] software packages. Weighted back-projection was used to reconstructed tomograms, and contrast transfer function (CTF) correction was applied in IMOD. To determine the positions and orientations of the subtomogram averaged volumes, binned tomograms of pixel size 5.84 Å were used. Final structural calculations and FCS estimations were conducted on un-binned tomograms of a pixel size 2.92 Å.

3.4.7. Subtomogram averaging

Subtomogram averaging was carried out using the Dynamo package [214].

Determination of the CA lattice by subtomogram averaging

For each tube from a binned dataset with pixel size 5.84 Å, the subtomograms were extracted in $100^3$ voxels uniformly distributed on the surface of the tubes, spaced by 17 pixels. Initial Euler angles were assigned based on the positions of the subtomogram volumes relative to the tube axis. 16 rounds of optimizations were performed, applying no symmetry. The resulting cubic segments for each tube showed 6-fold symmetric hexamers arranged into distinct helical lattices of different directionalities. We determined the positions of individual hexamers and extracted them in voxels of $64^3$ pixels. The starting Euler angles were defined as normal towards the newly calculated axis running through the center of each tube using in-house scripts (Appendix 1). The positions were refined within the next iterations until there was no more improvement. The final subtomogram averaging was performed on original unbinned data, with the positions and angles defined in binned tomograms. After reaching convergence, the datasets from each tube were combined into the final reconstruction which contained ~10,000 subtomograms, and 2-fold symmetry was applied. Resolution of a central hexamer was estimated by Fourier shell correlation of the two averages after masking with a spherical mask with a 2-pixel Gaussian cut-off.

Determination of the TRIM5α lattice by subtomogram averaging

All initial calculations and position optimizations were performed on binned datasets, with a pixel size of 5.84 Å. We generated two reference models by calculating the averages from far-from-focus datasets. Positions of the initial subtomograms were manually selected on the vertices of the lattice (3-fold trimer) or in the middle of the lattice arms (2-fold dimer) and were averaged together to generate initial models. For each of the tubes from close-to-focus datasets, we created a mesh

of uniformly distributed points within a 250-290 Å radius from the tube axis. The over-sampled datasets differed for each tube, from ~5,000 to ~11,000 subtomograms. We extracted volumes of $64^3$ pixels, and initial Euler angles were defined as perpendicular towards the axis. We determined positions of trimers and dimers for each lattice, independently of each other. The inner layer of CA lattice was masked out. Within next three runs, subtomograms that aligned to the same position as another one were removed based on their cross-correlation value and misaligned particles that were not on the surface of the tube were excluded as assessed by visual inspection. Within the next rounds, we refined positions of subtomogram volumes until they reached convergence. The final averages were calculated on original data, with the positions and angles defined in binned tomograms. After achieving convergence, the datasets from each tube were combined into the final reconstruction which contained ~3,200 subtomograms for a trimer and ~2,200 for a dimer. Resolutions of the maps without the underlying lattice were estimated by Fourier shell correlation of the two averages after masking with a cylindrical mask with a 2-pixel Gaussian cut-off.

SPRY domain dimer subtomogram averaging

Once the positions and orientations of TRIM5α dimer units were generated in binned tomograms, we applied a tight mask surrounding the SPRY domain only and proceeded with additional azimuthal and horizontal search in un-binned tomograms. The soft mask with a Gaussian cutoff of 2 pixels was generated using cryoSPARK [215] which encapsulated the SPRY dimer and a part of the CC region placed on top of it.

### 3.4.8. Fitting of the crystal structures

Structures were rigid body fitted into calculated density maps using Chimera [212]. For the analysis of TRIM5 lattice, the crystal structures of B-box 2 trimer from a chimeric "miniTRIM" (PDB: 5IEA), rhesus CC dimer (3TN3), and solution NMR structure od SPRY (2LM3) were used. The crystal structures of CA hexamers used: cysteine-stabilized (PDB: 3H4E) and native (PDB: 4XFX). The structures of the mature HIV-1 CA hexameric lattices of different curvatures (PDB: 5MCX, 5MD0, 5MD1, 5MDE, 5MDF, 5MDG) were used to generate respective CA hexamers that were subsequently fitted into the density map.

### 3.4.9. Defining the zones

The following calculations were done for binned tomograms with a pixel size of 5.84 Å. Using in-house scripts (Appendix 1), we calculated the distances between the centers of mass of TRIM5α dimer (determined in UCSF Chimera) and the centers of mass of all the CA hexamers to assess, which CA hexamer is the closest one to the TRIM5α dimer unit. We saved the centers of all SPRY dimers in a new coordinate system, using a single hexamer as a reference point. An arbitrarily defined z-plane was chosen, and all points were positioned on the same plane. The center of a reference hexamer and the neighboring hexamers were also saved on the same plane. We determined the zones by calculating the circular areas of radius smaller or equal to 6 pixels (~35 Å), the area between radiuses of 6 pixels and 15 (35-87.6 Å) and in an area between the neighboring hexamers in a radius of 3 pixels (~17.5 Å) as measured from the point in the middle between the centers of the adjacent hexamers. Because each subtomogram averaged volume has a unique numeral identificatory (tag), only the particles with the correct tags were re-averaged.

# Chapter 4.
# Biophysical characterization of the TRIM63 coiled-coil region

## 4.1. Introduction

Muscle-specific RING finger 1 protein (MuRF1), also known as TRIM63, is a member of the TRIM protein family found in striated muscle and iris [134–136]. It shares a conserved N-terminal RBCC fold containing RING finger (R), zinc-finger B-box 2 domain (B) and a leucine-rich coiled-coil (CC) motif. The variable C-terminal domain comprises a COS-box (C-terminal subgroup one signature box) motif followed by the acidic tail (AT) [148,156,157] (Fig. 2.1.A). TRIM63 is an E3 ubiquitin ligase that directs for muscle catabolism by the proteasome system. Although TRIM63 is expressed in muscle cells even when atrophic stimuli are not present, it is upregulated in response to stimuli such as immobilization, denervation, food deprivation, aging, and diseases, making it a well-recognized marker for muscle atrophy [137–140].

Of particular interest for this study is the C-terminal part of TRIM63 that contains the both CC and COS-box domains. The CC region is hypothesized to take part in dimerization of TRIM63, and the COS-box is responsible for targeting TRIM63 to sarcomeric structures [157]. The B-box domain on the N-terminus of CC induces higher-order association, approximated to hexameric or octameric formations [144] and the COS-box mediates the targeting of TRIM63 to various parts of sarcoskeleton. When the RING domain is removed, TRIM63 is unable to be appropriately targeted, and its ubiquitinating function is lost [157,158]. Titin is a protein that responds to mechanical stress

and was suggested to influence TRIM63 localization patterns. The titin kinase domain (TK) was found to be an inactive pseudokinase, without detectable levels of phosphorylation activity [159]. The structure of the A168-A170 domains of titin protein, built by Ig-Ig-Fn(III) motifs, forms an elongated sequence with short, rigid linkers. A shallow groove mediates the specific interaction between titin and TRIM63 on the surface and the unique loop insertion of A169 with critical residues 102-KTLE-105 modulates the interaction [146]. It was suggested that TRIM63 and TK are parts of a shared stress-signaling pathway, as TK may have a mechanoactivation mechanism. The multi-domain interaction between TRIM63 CC/COS-box and titin domains A168-A170-TK has been proposed to be sensitive to the stretch-induced conformational changes of the titin chain as pseudokinases are known to serve as scaffolds for the assembly of signaling complexes [156,159]. Even though the regions of contact have been mapped, the molecular basis of this interaction is not fully known.

A crystal structure of the predicted TRIM63 CC region (residues 214-271) was published by Franke *et al.* (2014) (Fig. 2.1.B). The crystallized construct does not form dimers in solution even though the helical part of protein has been previously reported to do so [146,159]. Based on this crystal structure, a model of dimerization was proposed (Fig. 2.1.C) with two RING domains on the same side of the CC. This model is inconsistent with findings that the CC regions of TRIM25 and TRIM5α are obligatory dimers in solution and form antiparallel dimers with a common heptad/hendecad pattern [59] (Fig. 2.1.E). Additional work presented on the CC regions of TRIM69, TRIM5α, and TRIM20 confirm that these TRIM proteins also form antiparallel dimers [60,62,216].

The relative orientations of the CC domains dictate the spatial organization of the other domains, and determining this is essential for understanding TRIM63 function. In the parallel model, the two RING domains would be constitutively adjacent to each other [157], whereas in the

antiparallel model, the RING domains would be separated by around 170 Å and effectively monomeric [59]. Here, we use biochemical crosslinking and EPR experiments to analyze the oligomerization properties and CC packing orientation of TRIM63. We show that a fragment of TRIM63 spanning the CC and COS-box regions forms dimers in solution. Additionally, the subunits are packed in an antiparallel orientation, suggesting that this architecture is conserved among TRIM family members.

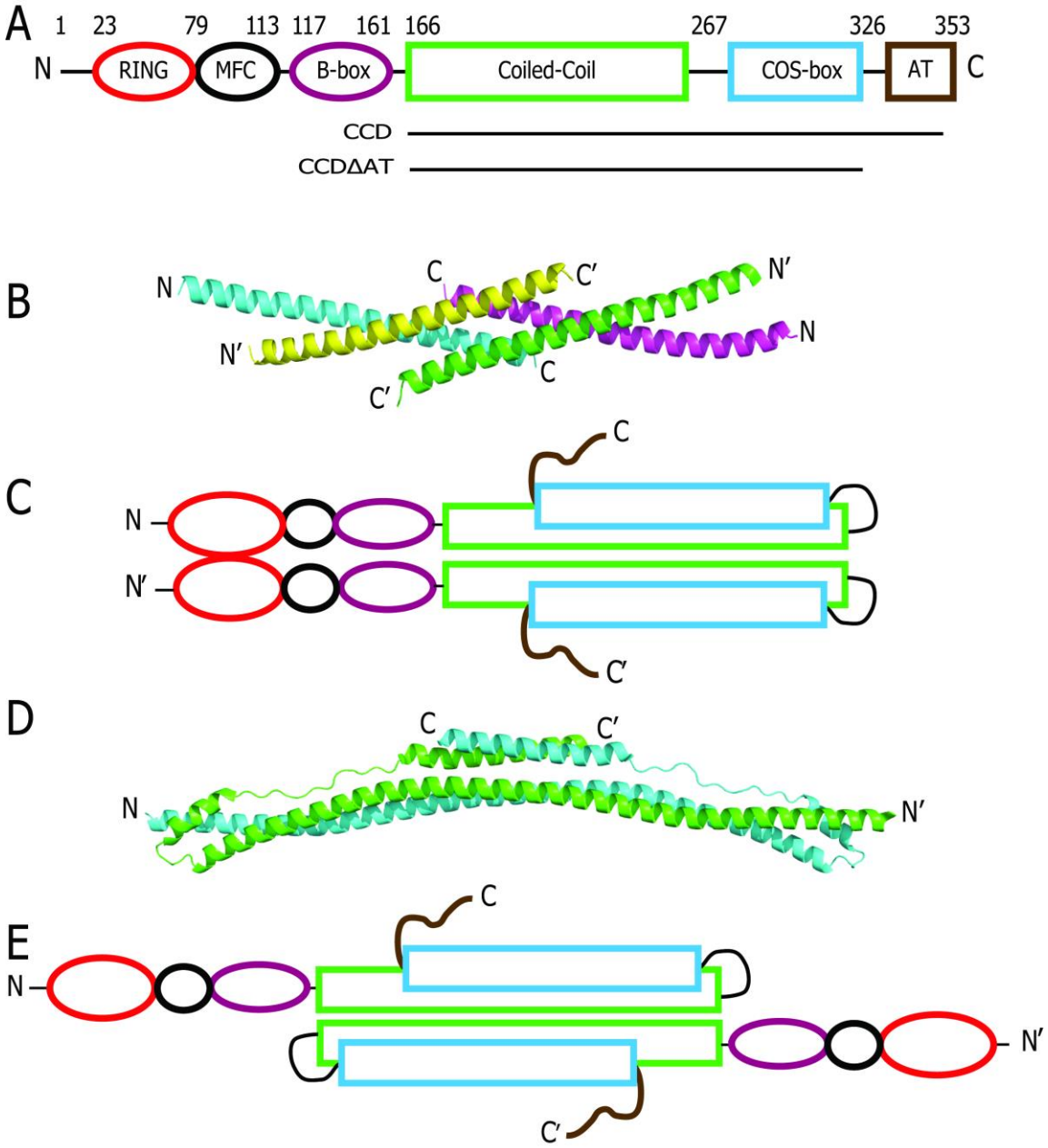


**Figure 4.1. Schematic representation of TRIM63 domain organization and suggested models of self-association. A** – Schematic diagram of TRIM63 sequence and its domain organization. Constructs used in this study are indicated below; MFC - MuRF family conserved motif, AT - acidic tail, CCD - dimerization domain containing the CC and COS-box, CCDΔAT - CCD lacking the acidic tail. Because the CCD construct was prone to aggregation, we focused on the CCDΔAT construct. **B** – Crystal structure of $TRIM63_{214-271}$ tetrameric palindrome, published by Franke *et al.* (2014). **C** – Parallel dimerization model, based on a crystal structure in B. **D** – Crystal structure of $TRIM25_{189-379}$ antiparallel dimer, published by Sanchez *et al.* (2014). **E** – Antiparallel dimerization model, based on a crystal structure in E.

## 4.2. Results

### 4.2.1. TRIM63$_{155\text{-}328}$ forms an antiparallel dimer of similar architecture to TRIM25 and TRIM5α.

Using JPRED [217] and COILS [218] prediction programs, we have determined that the TRIM63 CCDΔAT region containing the CC and COS-box is mostly helical and scores highly for the presence of CC motifs (data not shown). This construct is similar to minimal dimerization domains of TRIM5α, TRIM20, TRIM25, and TRIM69 [59–62]. On the other hand, the reported crystal structure of TRIM63 are shorter fragments spanning residues 214 and 271 and divides the predicted helical region (166-267) into two parts [157]. In our initial experiments, we found that the TRIM63 CCD construct (residues 155-353) elutes as an oligomer on a gel filtration chromatography (data not shown). After optimization, we identified CCDΔAT, a better-behaved construct spanning residues 155-328 that includes the entire predicted CC region as well as a COS-box but lacking the acidic tail (Fig. 4.1.A). This construct also eludes rapidly on gel filtration (Fig. 4.2.A), consistent with an elongated shape and/or oligomeric state. Two major peaks were observed, which were fractionated and re-examined separately using size exclusion chromatography coupled with multi-angle light scattering (SEC-MALS). The high molecular weight peak re-eluted as two peaks with apparent molecular masses of 133.2 and 82.6 kDa, consistent with a heptamer and a tetramer, respectively (Fig. 4.2.B). The second peak re-eluted as a primarily single peak at the same position, with an apparent molecular mass of 39.1 kDa, consistent with a dimer (Fig. 4.2.C). The re-elution profile also had a minor peak corresponding to a tetramer (apparent mass = 78.7 kDa), which we presume corresponds to residual contamination from the initial separation (Fig. 4.2.C). The calculated molecular masses of the CCDΔAT dimer

and tetramer are 39.2 and 78.4 Da, respectively. These results indicate that similar to TRIM25 and other TRIM proteins, the TRIM63 CCD is also an obligate dimer.

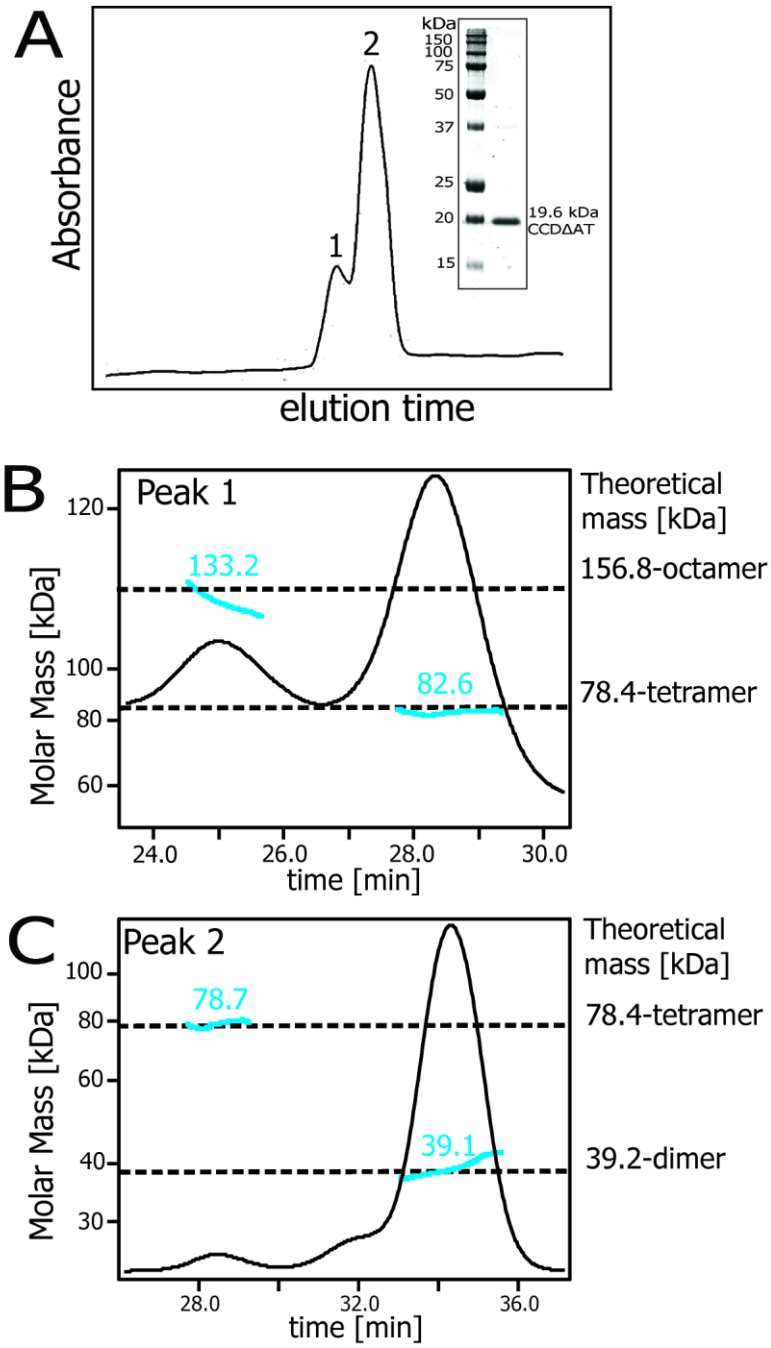


**Figure 4.2. Biophysical characterization of TRIM63$_{155\text{-}328}$.** A – Size exclusion chromatography profile of the CCDΔAT construct, indicating two peaks labeled 1 and 2. B – SEC-MALS analysis of peak 1 from A, which re-eluted as apparent tetramers and heptamers (perhaps octamers). Curves show the population-averaged molecular mass per volume unit (cyan), normalized UV absorbance profile (black, continuous line) and theoretical molecular masses (dashed lines). C – SEC-MALS analysis of peak 2, which was almost predominantly dimeric, with a minor tetramer fraction.

To determine the molecular basis for TRIM63 dimerization, we attempted crystallization of the construct. As we were unsuccessful in producing any crystals, we utilized alternative approaches to determine the packing orientation of the helices. Based on a structure-to-sequence alignment [59], we introduced three different pairs of cysteine mutations (F163C/L276C, V184C/L253C, and S202C/Q235C) which would cross-link the two subunits if the dimer were antiparallel (Fig. 4.3A). To avoid non-specific, background cross-linking, we mutated native cysteines to serines (C173S and C293S). For comparison, we designed two additional pairs of cysteines (L228C/Q235C and S282C/A289C) based on the crystal structure of TRIM63 (PDB code: 4M3L) (Fig. 4.3B). Intermolecular disulfide bond formation was then used to evaluate whether the TRIM63 dimer was antiparallel similar to TRIM25 [59] or parallel as indicated in the crystal structure of TRIM63 [157]. As shown in Fig. 2.3.C, under non-reducing conditions the double-cysteine mutants designed based on TRIM25 formed intermolecular disulfide crosslinks very efficiently and migrated almost exclusively as crosslinked dimers on a denaturing SDS-PAGE gel (lanes 4-6). In contrast, the two mutants designed from the TRIM63 crystal structure migrated as monomers under the same conditions (lanes 7-8). We therefore conclude that TRIM63 is an antiparallel dimer similar to TRIM25.

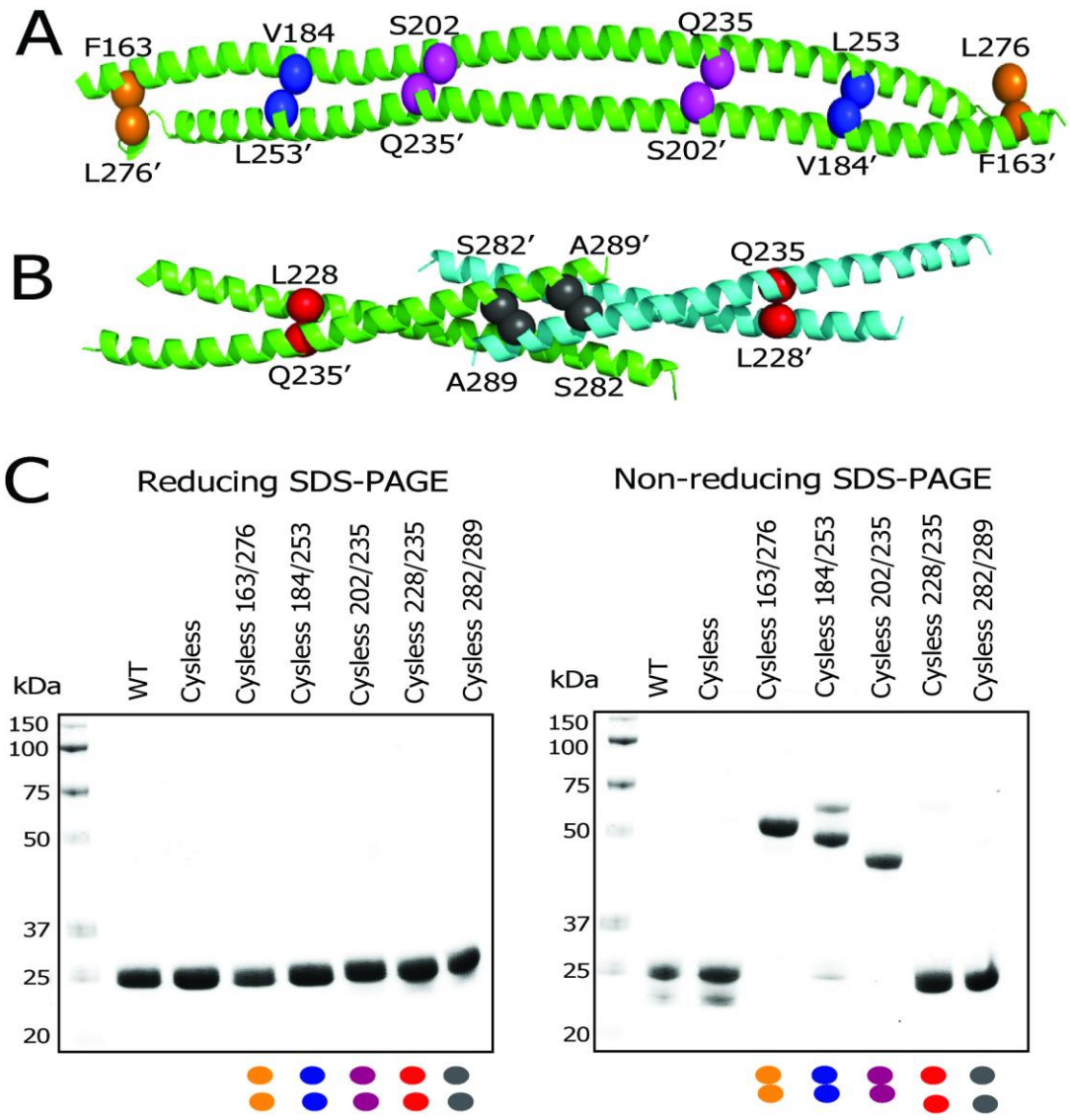


**Figure 4.3. Disulfide crosslinking of the TRIM63$_{155-328}$ dimer.** A – Homology model of the TRIM63 CC region based on the crystal structure of the TRIM25$_{189–379}$. Positions of residue pairs chosen for cysteine mutagenesis are shown as colored spheres. B - Crystal structure of TRIM69$_{214-271}$ showing positions of residue pairs selected for cysteine mutagenesis as spheres. C – SDS-PAGE profiles of purified double-cysteine mutants of TRIM63 CCDΔAT. Proteins were dialyzed into a non-reducing buffer and then resolved under reducing (left) and non-reducing (right) conditions. Colored dots indicate the cysteine pairs and match the color scheme in A.

4.2.2. EPR analysis of the TRIM63 dimer

To confirm that the TRIM63 CCDΔAT construct forms an antiparallel dimer, we used site-directed spin labeling and electron paramagnetic resonance spectroscopy analysis. The positions of the spin labels are shown in Fig. 4.4A. The normalized continuous wave (CW) EPR X-band spectra of the single-labeled constructs show distinct line shapes, indicating that proteins were labeled correctly (Fig 4.4B).

Since the protein dimerizes, two spin labels are obtained for each oligomeric unit. We then used double electron-electron resonance (DEER) spectroscopy to measure distances between the pair of labels. The background subtracted DEER signals (V(T)/V(0)) are plotted in Fig. 4.4.C and the corresponding interspin distance distributions are presented in Fig. 2.4.D. The DEER distances with proper signal-to-noise ratios can be estimated with precision (distance between 20-50 Å), but longer ones (50-60 Å) have higher uncertainty. Distances larger than 70 Å were not fitted (Table 2.1). Calculated distances between E200R1, D214R1, and E222R1 pairs were in close agreement with predicted distances from the TRIM25 homology model. Fitting of the data for E192R1, E243R1 and Q247R1 could not be performed because the labels were too far apart. This is also in good agreement with prediction because each of these pairs is> 70 Å apart in the homology model. We conclude that TRIM63 adopts not only a similar dimeric structure as TRIM25 but is also elongated.

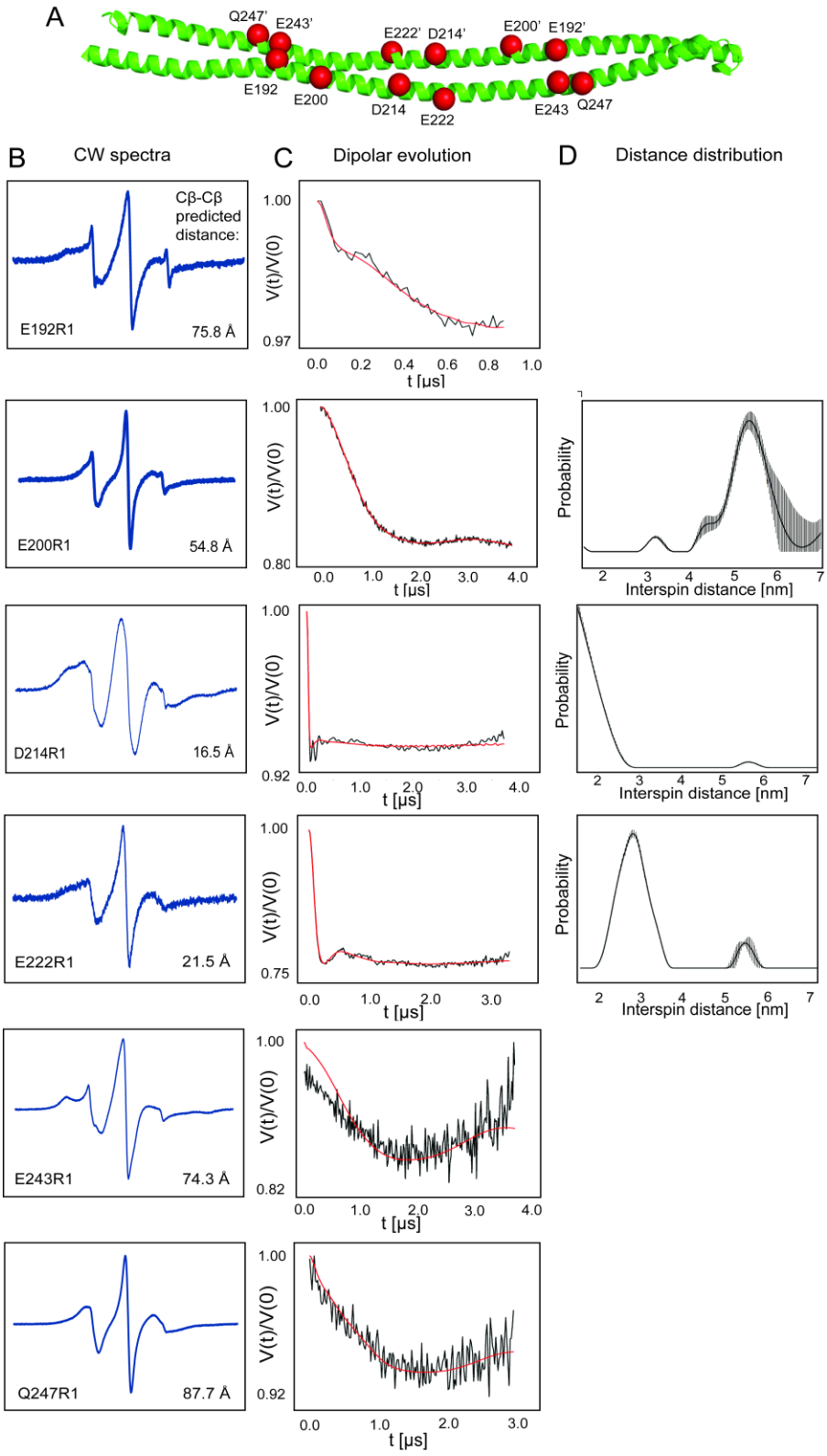


**Figure 4.4. TRIM63 dimerizes in an antiparallel mode shown by DEER EPR.** A – Homology model for the TRIM63 CC based on TRIM25 [59], showing positions of spin labels. Since the protein

is a dimer, a single cysteine substitution places two labels whose distance from each other can be measured by DEER. B – Normalized X-band EPR spectra of MTSL-labeled CCDΔAT. Predicted Cβ - Cβ distances from the homology model are indicated. C - Background corrected DEER data (black) and best-fit curves (red); data for the 192R1, 243R1 and 247R1 mutants were not fitted as the spin label distances were longer than 55 Å. D – Distance probability distribution curves calculated from the DEER data; the error bars show fits with RMSD within 15% of the best solution [219].

**Table 4.1. Distances between spin pairs in TRIM69 derived from DEER.**

| Mutant | Predicted Cβ-Cβ distance in [Å] | Experimental interspin distance in [Å] |
|---|---|---|
| E192R1 | 78.8 | N/A |
| E200R1 | 54.8 | ~55 |
| D214R1 | 16.5 | <20 |
| E222R1 | 21.5 | ~30 |
| E243R1 | 74.3 | N/A |
| Q247R1 | 87.7 | N/A |

4.2.3. The COS-box domain adopts a loose α-helical structure.

It has been shown that the COS-box is an essential motif in sarcomere targeting and it is likely that its high mobility may facilitate binding of TRIM63 to titin [157]. This portion of TRIM63 corresponds in position to the terminal helix of the TRIM25 CCD [59] (Fig. 4.5A). Continuous wavelength electron paramagnetic resonance (CW EPR) is a potent tool for analyzing the secondary structure of a protein as the relative motion of the spin label is mirrored in the shape of the spectrum [220]. This provided us an opportunity also to examine the COS-box and determine its

secondary structure. Secondary structural prediction indicated that residues 312-327 of the COS-box might be helical (Fig. 4.5B). To test this, the spectra of CCDΔAT with individual labels at residues 312-327 were recorded and compared. In these spectra, a sharp spectral line shape would indicate that the label has a relatively fast motion, whereas a broader central peak would mean more restricted movement (Fig. 4.5C). The inverse central line width ($\Delta Hpp^{-1}$) and its amplitude have been used as a semi-quantitative measure of spin label mobility, where increased values of $\Delta Hpp^{-1}$ suggest increased mobility [220–222]. Both plots for CCDΔAT as a function of spin label location shows semi-helical periodicity between positions 312-324, suggesting that this part of the protein may indeed adopt α-helical secondary structure (Fig. 4.5D-E). Consistent with this interpretation, predicted solvent-exposed hydrophilic residues of this α-helix have lower $\Delta Hpp^{-1}$ values than the hydrophobic residues which are predicted to be buried (Fig. 4.5.C).

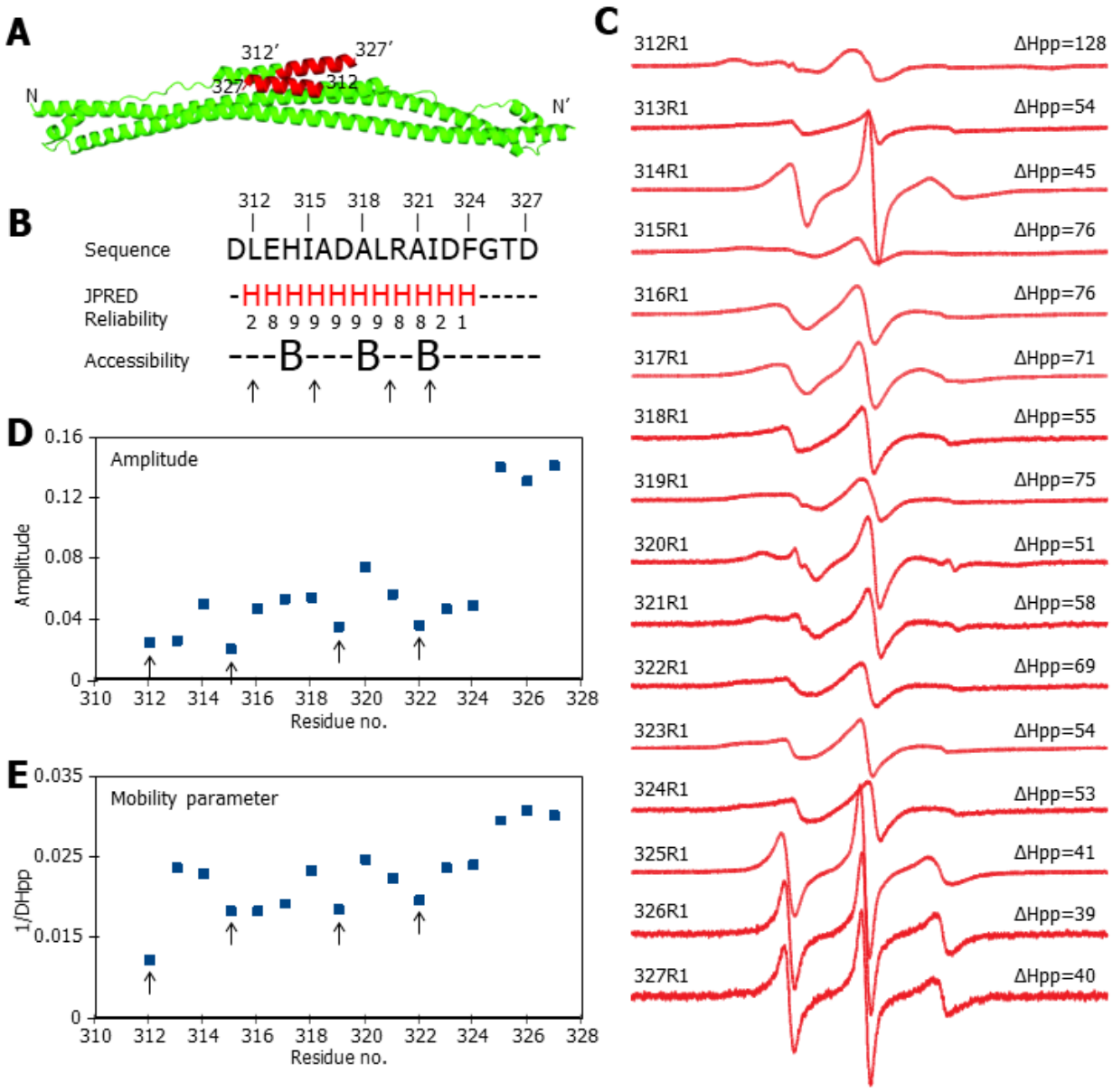


**Figure 4.5. EPR analysis of the COS-box.** A – Homology model shows the COS-box region to be positioned on top of the CC region, forming a four-helix bundle in the middle of the symmetric dimer. B – Sequence and JPRED secondary structure prediction of the COS-box region; predicted buried residues are labeled; arrows point to residues that are likely buried based on EPR results. C – Normalized X-band CW EPR spectra of TRIM63 CCDΔAT spin-labeled at the positions shown in A. D – Normalized amplitudes of CW EPR spectra as a function of residue position; labels with more mobility show high intensities. E – Plot of the mobility parameter ($\Delta Hpp^{-1}$) as a function of residue position.

4.2.4. The COS-box region is situated in the middle of the CC domain

In order to determine the position of the COS-box region in relation to CC, we performed a triangulation experiment. Labels were attached to E192 in the CC and R320 in the COS-box, and distance distributions were determined by DEER (Fig. 4.6.A). In control DEER experiments with R320R1 labels alone, the distance distribution was in close agreement with the prediction made using the homology model (observed distances = 26.7 Å and 28.7 Å; predicted distance = 15.2 Å). (Fig. 4.6.B-C, upper panels). Although we had a single predicted distance, we speculate that local mobility of the spin label may explain the observed binary distance distribution. Measurements on E192R1 alone was not performed, as the expected distance here is 74.9 Å and could not have been accurately measured.

We then collected DEER data on protein labeled at both positions, for a total of 4 labels. Because the E192R1 pair is too far apart, we expected the distance distribution to only indicate the R320R1-R320R1 pair and the E192R1-R320R1 pairs; of the latter, there are 4 possible combinations (Fig. 4.6.A). Recorded distances of ~28 Å, 36.6 Å, 41.7 Å, and 48.8 Å were obtained (Fig. 4.6.B-C, lower panels). The smallest value reflects the distance between the R320R1 labels as found in the control experiment (Fig. 4.6.B-C, upper panels). The remaining distances correspond well with the predicted distances between residues E192 and R320, although at this point we cannot assign these to the 4 possible combinations. These results indicate that the two COS-box helices in the TRIM63 dimer are situated in the middle of the elongated CC domain and may be in a stable configuration, similar to the C-terminal helices of TRIM25 [59].

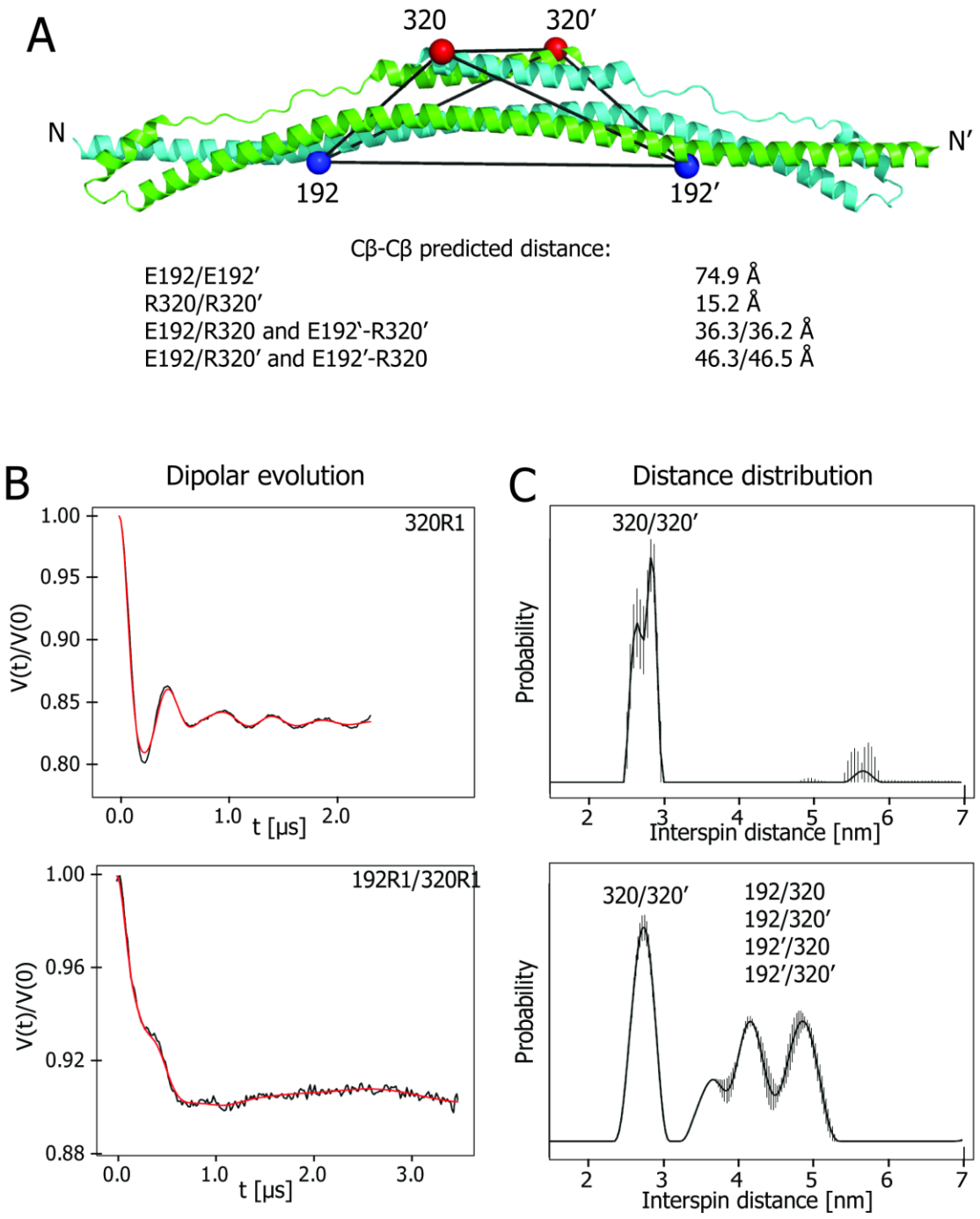


**Figure 4.6. The COS-box position determined relative to the CC by an EPR triangulation experiment.** A – Schematic representation of the experimental setup; DEER measurements were performed on protein labeled on one (E192), or both (E192/R320) indicated positions; distances between Cβ-Cβ atoms in the homology model are listed. B – Background corrected DEER data (black) with best-fit curves (red). C – Distance probability distributions.

## 4.3. Discussion

Muscle atrophy occurs when protein degradation is faster than protein synthesis. Many diseases and conditions such as cachexia, bedrest, extended inactivity or starvation cause muscle loss. One of the proteins that regulate degradation of muscle proteins is TRIM63, which is part of a family of muscle-specific TRIM proteins, which includes TRIM54 and TRIM55 (and also known as MuRFs) [223]. TRIM63 is upregulated in response to atrophic stimuli and causes muscle catabolism in a proteasome-dependent manner. To develop effective countermeasures, a molecular organization of TRIM63 and its role in pathways leading to muscle atrophy should be understood in detail.

The coiled-coil regions of TRIM proteins are obligatory dimers, responsible for the relative spatial organization of the flanking domains. Crystal structures of several TRIM proteins indicate that these dimers have an antiparallel arrangement [59–62]. In contrast, a crystal structure of TRIM63 suggested a parallel architecture [157]. By using crosslinking and DEER EPR, we found that the TRIM63 CC in indeed antiparallel. A TRIM63 CCD construct behaves as an obligatory dimer, similar to equivalent segments of TRIM25 and TRIM5α. Both cross-linking and DEER EPR experiments further indicate that the dimer has the expected elongated architecture. Our data, therefore, support the idea that all TRIM family members have the same oligomeric structure. It appears that in crystallizing TRIM63, Franke *et al.* truncated the CC too far, and as a result, the symmetry of the dimer was disturbed.

We further provide evidence that the TRIM63 COS-box forms a loose α-helix that packs against the center of the CC region, similar to the C-terminal helix of the TRIM25 CCD [59]. The COS-box does not appear to be mobile, which may suggest that the interaction with its binding

partners is well-defined. The COS-box domain is necessary and sufficient for targeting TRIM63 to sarcoskeleton, but the CC region is responsible for its interaction with titin [157]. The synergistic activities of these two domains suggest that destabilizing the COS-box could block the proper cellular targeting of the TRIM63 and may be a viable target for therapeutics against muscle atrophy. Finally, the RING domain that carries the enzymatic activity most likely requires dimerization for functionality as shown for other members of the TRIM family. Since the TRIM63 dimer is similar to other TRIMs, we suggest that its RING domain activity is also regulated by higher order oligomerization.

## 4.4. Methods

### 4.4.1. Construct design

A synthetic DNA sequence corresponding to TRIM63$_{155-356}$ was purchased from Genewiz Inc. and sub-cloned into a pCA528 vector with His$_6$-tagged yeast Smt3p (SUMO) leader sequence. To increase solubility and stability of the protein, the acidic tail (residues 328-356) was removed using a PCR-based linearization and re-ligation protocol. To decrease non-specific crosslinking interactions, native cysteines C173 and C293 were mutated to serines. All mutants were generated by PCR mutagenesis using the Quikchange Lightning kit and the protocol provided by the manufacturer (Agilent Technologies, Inc). All plasmid constructs were confirmed by sequencing with T7/T7-terminator primers provided by Genewiz Inc.

### 4.4.2. Protein expression and purification

The expression vector was transformed into *E. coli* BL21(DE3) competent cells and grown in LB medium supplemented with kanamycin to a final concentration of 25 μg/ml. Cells were incubated at 37 °C with shaking until the $OD_{600}$ reached 0.8-1.2, upon which expression was induced by the addition of isopropyl β-D-1-thiogalactopyranoside (IPTG) to a final concentration of 0.2 mM. The cells were harvested by centrifugation after 3.5 h. Next, the cells from 1 liter of culture were resuspended in 30 ml of lysis buffer (50 mM Tris–HCl pH 8.0, 500 mM NaCl, 5% glycerol, 5 mM βME) with the addition of 2 mM PMSF, 10 mM imidazole and lysed using a microfluidizer (Microfluidics model M110P). The soluble fraction (supernatant) was loaded onto a Ni–NTA metal-affinity resin (Qiagen) and incubated for 1 h with shaking at 4 °C. The resin was washed with 500 ml of lysis buffer containing 30 mM imidazole. The protein was eluted with 50

mM Tris–HCl pH 8.0, 100 mM NaCl, 1 M imidazole, 5 mM βME. Appropriate fractions were dialyzed against 30 mM Tris, pH 8.0, 100 mM NaCl, 5 mM βME with the addition of Ulp1 SUMO-specific protease to remove the His-SUMO-tag. Additional purification included Ni-NTA metal affinity chromatography to remove the tag and the protease, and ion exchange chromatography (5 ml HiTrap Q XL column, GE Healthcare) to remove other impurities. Fractions containing TRIM63 protein were concentrated to ~5 ml using a centrifugation unit with a 10 kDa cutoff (Sartorius stedim, Lab Technology Products) and purified to homogeneity on HiLoad 16/600 Superdex 75 column (GE Healthcare) equilibrated with 20 mM Tris–HCl pH 8.0, 100 mM NaCl, 5 mM βME). Correct peak fractions were pooled and concentrated to 50-150 µM, flash-frozen in liquid nitrogen and stored at -80 °C.

4.4.3. Cross-linking Analysis

Purified double cysteine mutants were diluted to equal concentrations and dialyzed overnight at 4 °C in 20 mM Tris–HCl pH 8.0, 100 mM NaCl. No reducing agent was added to ensure the formation of stable disulfide crosslinks. Samples were mixed with equal volumes of 4× SDS-PAGE sample buffer containing either 1 M βME (for reducing conditions) or 0 M βME (for non-reducing conditions). Samples were incubated for 10 min at 100 °C in a dry bath and analyzed immediately by SDS-PAGE with Coomassie blue staining.

4.4.4. Size exclusion chromatography and multi-angle laser light scattering (SEC-MALS)

Measurements were performed on Dionex UltiMate3000 HPLC system with UV detector (ThermoFisher, Waltham, MA) connected to a miniDAWN TREOS static light scattering detector

(Wyatt Technology, Santa Barbara, CA) and Optilab T-rEX differential refractometer (Wyatt Technology). A sample volume of 40 µl at 0.9 mM concentration was applied to a Superdex 200 HR 10/300 GL column (GE Healthcare) and developed in 20 mM Tris-HCl pH 8.0, 100 mM NaCl at a flow rate of 0.4 ml/min. Data were recorded and processed using ASTRA software (Wyatt Technology).

4.4.5. Spin labeling of purified mutants

Following the purification of cysteine mutants, βME present in size exclusion buffer was removed using desalting column (HiPrep 26/10, GE Healthcare) equilibrated with degassed 20 mM HEPES pH 8.0 and 100 mM NaCl. At least 20-fold molar excess of 1-oxyl- 2,2,5,5-tetramethyl-3-pyrroline-3-methyl methanethiosulfonate (MTSL, Toronto Research Chemicals) was added and incubated for 1 h at room temperature followed by overnight incubation at 4 °C. The free label was removed using a desalting column. Proteins were concentrated to 50-150 µM and stored on ice until needed.

4.4.6. CW EPR spectroscopy

CW EPR measurements were performed at room temperature (approximately 295 K) using an EMX X-band EPR Spectrometer (Bruker, Billerica, MA). Labeled samples (typically 6 µl) were loaded into glass capillaries with 0.6 mm inner diameter and 0.84 mm outer diameter. (VitroCom, Mountain Lakes, NJ). Spectra were used to determine the secondary structure of COS-box domain and to ensure labeling of the protein for DEER EPR experiments. Measurements were carried out at 2 mW incident microwave power using 1 G modulation amplitude and frequency of 100 Hz. Up

to 30 scans were performed to increase the signal-to-noise ratio. The spectra were processed using the LabVIEW program (Christian Altenbach, University of California, Los Angeles, CA). All spectra were normalized to the same area.

4.4.7. DEER EPR spectroscopy

For DEER measurements, labeled protein samples (100-150 μM) were supplemented with 10% (v/v) deuterated glycerol, loaded into quartz capillaries (2.0 mm i.d. and 2.4 mm o.d.) and flash frozen in liquid nitrogen. The pulse experiments were carried out at Bruker Elexsys E580 spectrometer at X-band using an ER4118X-MS3 split-ring resonator or at Q-band using an EN5107D2 dielectric resonator (Bruker Biospin, Billerica, MA). Data in pulse mode were acquired using a four-pulse DEER sequence (19) with 16-ns p/2 and 32-ns p observe pulses separated by a 32-ns p pump pulse. The dipolar evolution times were typically 2–4 ms. The pump frequency was set to the center maximum of the nitroxide spectrum, and the observed frequency was set to the low-field maximum, typically 15–25 MHz higher in frequency. Model-free distance distributions were obtained from the raw dipolar evolution data using Tikhonov regularization incorporated into the DeerAnalysis 2015 software implemented in Matlab program, written and provided by Gunnar Jeschke ETH Zurich, Zurich, Switzerland. This program contains an error analysis routine that was used to assess the error produced by background subtraction upon the distance distributions. At each distance in the distribution, ranges were plotted that represent fits that are within 15% RMSD of the best fit. The experimental distance distributions obtained by DEER were compared with the predictions based upon a crystal structure.

# Chapter 5.

# Summary and Conclusions

## 5.1. Overall summary

TRIM family proteins, represented by more than 80 members in humans, participate in various cellular processes such as innate immune response, intracellular signaling, autophagy. They are characterized by a conserved RBCC motif comprised RING finger, one or two B-box domains and a CC region. Based on the C-terminal domain, the family has been divided into 11 sub-families [43,65,224]. Many TRIMs have been shown to multimerize through the CC region into homo- and heterodimers [63]. Most members of TRIM family have a catalytically active RING domain that serves as an E3 ligase and participates in the ubiquitin cascade [51,63]. Ubiquitination is a post-translational modification that has been shown to play a crucial role in numerous intracellular processes, including immune responses [44].

In this dissertation, I presented structural studies of two TRIM family members, TRIM5α and TRIM63.

5.1.1. TRIM5α and HIV-1 restriction.

TRIM5α inhibits (or restricts) HIV-1 replication by intercepting the incoming core of the retrovirus. It binds to the capsid that surrounds and protects the core and causes premature capsid disassembly, thereby disrupting reverse transcription. While it appears established that assembly of TRIM5α on the surface of the HIV-1 capsid results in the formation of a TRIM5 hexagonal lattice, the molecular details of these TRIM5α/capsid complexes have not been known. As described in Chapters 2 and 3, we co-assembled TRIM5α and HIV-1 CA proteins and analyzed the structures of the resulting tubular assemblies using cryo-electron tomography and subtomogram averaging. This allowed us to determine the positions and orientations of TRIM5α proteins arranged to form the lattice. We show that the tubes are entirely covered by the TRIM5α lattice, indicating that the restriction factor completely cages the HIV-1 capsid during restriction. We obtained independent reconstructions of the TRIM5α dimer and trimer units to nominal resolutions of 27 Å and 23.4 Å, respectively. The two lattices generated by these different search models overlapped extensively and collectively described the complete TRIM5α lattice. In both reconstructions, densities corresponding to the capsid lattice were devoid of any visible features, suggesting multiple points of interaction between the TRIM5 and CA lattices.

Our reconstructions also confirm the arrangement of TRIM5α domains that was deduced from crystal structures of individual domains and sub-complexes, as well as low-resolution cryo-EM maps [58–60,119,125,132]. The TRIM5α lattice is a net of open hexagon rings, with the antiparallel dimers of the CC domains forming the arms of each hexagon and the B-box 2 trimers forming the lattice vertices. The RING domains are also sufficiently resolved in our maps to allow unambiguous assignment of their positions on top of the B-box trimers, where they are oriented towards the cell cytoplasm to facilitate subsequent recruitment of components of the ubiquitin

cascade. We also confirmed that the SPRY domain binds the CA subunits as a dimer and serves as the only point of interaction between the TRIM and CA lattices. In our reconstructions, the SPRY domain dimer has a clearly bi-lobed structure. The bulk of the domain folds appear close-packed whereas the flexible loops splay away from each other to contact the capsid surface. Although our reconstructions do not have sufficient resolution to visualize these contacts, we found that a subset of the SPRY dimers (about 1/3) binds to a single CA hexamer, with the remaining binding at the interface between two hexamers. These results indicate that SPRY/CA contacts are degenerate.

Some groups reported massive destruction of HIV-1 CA assemblies under high concentrations of the protein construct spanning CC-SPRY region [80]. Other groups reported minor destabilization of the capsid upon TRIM5 binding [85]. Our reconstructions reveal that the underlying CA lattice in the tubes is retained, indicating that TRIM5α binding does not induce significant structural changes or discontinuities in the capsid. This result indicates that the accelerated capsid dissociation observed during restriction is not merely caused by TRIM5α binding but requires other factors, such as proteasome or autophagosome recruitment. Future studies should address this question.

### 5.1.2 Structure of the TRIM63 dimer.

The second part of this study was dedicated to structural analysis of TRIM63. TRIM63 is upregulated in response to atrophic stimuli and was previously shown to mark muscle proteins for degradation by the proteasome system [138,140,148,225]. It has been suggested that the CC domain of TRIM63 forms a parallel dimer, unlike all other characterized TRIM proteins so far [157]. As described in Chapter 4, however, we show using cross-linking and EPR that TRIM63 indeed has

the same antiparallel dimer architecture as TRIM5α and other well-characterized TRIMs. The details of CC dimerization are very important for regulating the E3 ligase enzymatic activity of TRIMs, which is dependent on dimerization of the RING domains [74,76,77,133,226]. A parallel arrangement of the CC region would bring two RING domains close to each other and result in constitutive activation, while the antiparallel CC would orient two RING domains to the distant ends of the dimer. In the latter case, additional oligomerization would be required for enzymatic activity. Non-constitutive activation of the TRIM63 RING domain can be intuitively understood as a mechanism that prevents unregulated ubiquitination and runaway degradation of muscle proteins. Further studies are now needed to learn what factors promote or prevent RING activation, and how these factors contribute to muscle atrophy associated with TRIM63.

## 5.2 General implications for TRIM protein function

The studies presented here implicate higher-order oligomerization and assembly as critical features of TRIM5α and TRIM63 function. We suggest that antiparallel dimerization is a conserved feature of TRIMs. Additionally, further higher-order oligomerization of TRIM proteins is an attractive concept for RING activation. An increasing number of TRIM proteins are now being characterized, all with apparently the same CC dimerization and RING activation requirements. It will be interesting to see the various specific manifestations of how these properties regulate the many cellular processes TRIM proteins are implicated in.

# References


1. Becerra, J. C., Bildstein, L. S. & Gach, J. S. Recent Insights into the HIV/AIDS Pandemic. *Microb. Cell* **3,** 450–474 (2016).

2. Gao, F. *et al.* Origin of HIV-1 in the chimpanzee Pan troglodytes troglodytes. *Nature* **397,** 436–441 (1999).

3. Sharp, P. M. & Hahn, B. H. Origins of HIV and the AIDS pandemic. *Cold Spring Harb. Perspect. Med.* **1,** 1–22 (2011).

4. Pustil, R. Global AIDS. *Aids* **17 Suppl 4,** S3-11 (2016).

5. World Health Organization. HIV Prevention, Diagnosis, Treatment and Care for Key Populations (2016 Update). *World Heal. Organ.* 155 (2016). doi:ISBN 978 92 4 150743 1

6. Hewson, T., Lone, N., Moore, M. & Howie, S. Interactions of HIV-1 with antigen-presenting cells. *Immunology and Cell Biology* **77,** 289–303 (1999).

7. Ganser-Pornillos, B. K., Yeager, M. & Pornillos, O. Assembly and architecture of HIV. *Adv. Exp. Med. Biol.* **726,** 441–465 (2012).

8. Mattei, S., Glass, B., Hagen, W. J. H., Kräusslich, H.-G. & Briggs, J. A. G. The structure and flexibility of conical HIV-1 capsids determined within intact virions. *Science (80-. ).* **354,** 1434–1437 (2016).

9. Ganser, B. K., Li, S., Klishko, V. Y., Finch, J. T. & Sundquist, W. I. Assembly and Analysis of Conical Models for the HIV-1 Core. *Science (80-. ).* **283,** 80–83 (1999).

10. Li, S., Hill, C. P., Sundquist, W. I. & Finch, J. T. Image reconstructions of helical assemblies of the HIV-1 CA protein. *Nature* **407,** 409–413 (2000).

11. Ganser-Pornillos, B. K., von Schwedler, U. K., Stray, K. M., Aiken, C. & Sundquist, W. I. Assembly properties of the human immunodeficiency virus type 1 CA protein. *J. Virol.* **78,** 2545–52 (2004).

12. Deshmukh, L. *et al.* Structure and Dynamics of Full Length HIV-1 Capsid Protein in Solution. *J Am Chem Soc* **135,** 16133–16147 (2013).

13. Ganser-Pornillos, B. K., Cheng, A. & Yeager, M. Structure of Full-Length HIV-1 CA: A Model for the Mature Capsid Lattice. *Cell* **131,** 70–79 (2007).

14. Pornillos, O. *et al.* X-ray Structures of the Hexameric Building Block of the HIV Capsid. *Cell* **137,** 1282–1292 (2009).

15. Pornillos, O., Ganser-Pornillos, B. K. & Yeager, M. Atomic-level modelling of the HIV capsid. *Nature* **469,** 424–427 (2011).

16. Cornilescu, C. C., Bouamr, F., Carter, C. & Tjandra, N. Backbone $^{15}$ N relaxation analysis of the N-terminal domain of the HTLV-I capsid protein and comparison with the capsid protein of HIV-1. *Protein Sci.* **12,** 973–981 (2003).

17. Mortuza, G. B. *et al.* High-resolution structure of a retroviral capsid hexameric amino-terminal domain. *Nature* **431,** 481–485 (2004).

18. Tang, C., Ndassa, Y. & Summers, M. F. Structure of the N-terminal 283-residue fragment of the immature HIV-1 Gag polyprotein. *Nat. Struct. Biol.* **9,** 537–543 (2002).

19. Gres, A. T. *et al.* X-ray crystal structures of native HIV-1 capsid protein reveal conformational variability. *Science (80-. ).* **349,** 99–103 (2015).

20. Byeon, I.-J. L. *et al.* Structural Convergence between CryoEM and NMR Reveals Novel Intersubunit Interactions Critical for HIV-1 Capsid Function. *Cell* **139,** 780–790 (2009).

21. Gamble, T. R. *et al.* Structure of the carboxyl-terminal dimerization domain of the HIV-1 capsid protein. *Science (80-. ).* **278,** 849–853 (1997).

22. Worthylake, D. K., Wang, H., Yoo, S., Wesley, I. & Christopher, P. research papers Structures of the HIV-1 capsid protein dimerization Ê resolution domain at 2 . 6 A research papers. *Acta Crystallogr. Sect. D* 85–92 (1999).

23. Bharat, T. A. M. *et al.* Structure of the immature retroviral capsid at 8 Å resolution by cryo-electron microscopy. *Nature* **487,** 385–9 (2012).

24. Bharat, T. A. M. *et al.* Cryo-electron microscopy of tubular arrays of HIV-1 Gag resolves structures essential for immature virus assembly. *Proc. Natl. Acad. Sci.* **111,** 8233–8238 (2014).

25. Schur, F. K. M. *et al.* Structure of the immature HIV-1 capsid in intact virus particles at 8.8 Å resolution. *Nature* **517,** 505–508 (2015).

26. Wright, E. R. *et al.* Electron cryotomography of immature HIV-1 virions reveals the structure of the CA and SP1 Gag shells. *EMBO J.* **26,** 2218–26 (2007).

27. Zhao, G. *et al.* Mature HIV-1 capsid structure by cryo-electron microscopy and all-atom molecular dynamics. *Nature* **497,** 643–646 (2013).

28. Gamble, T. R. *et al.* Crystal structure of human cyclophilin A bound to the amino-terminal domain of HIV-1 capsid. *Cell* **87,** 1285–1294 (1996).

29. Gitti, R. K. *et al.* Structure of the Amino-Terminal Core Domain of the HIV-1 Capsid Protein. **273,** (1996).

30. Von Schwedler, U. K. *et al.* Proteolytic refolding of the HIV-1 capsid protein amino-terminus facilitates viral core assembly. *EMBO J.* **17,** 1555–1568 (1998).

31. von Schwedler, U. K., Stray, K. M., Garrus, J. E. & Sundquist, W. I. Functional surfaces of the human immunodeficiency virus type 1 capsid protein. *J. Virol.* **77,** 5439–50 (2003).

32. Campbell, S. & Vogt, V. M. Self-assembly in vitro of purified CA-NC proteins from Rous sarcoma virus and human immunodeficiency virus type 1. *J. Virol.* **69,** 6487–6497 (1995).

33. Gross, I., Hohenberg, H. & Krausslich, H. G. In vitro assembly properties of purified bacterially expressed capsid proteins of human immunodeficiency virus. *Eur J Biochem* **249,** 592–600 (1997).

34. Gross, I., Hohenberg, H., Huckhagel, C. & Kräusslich, H. G. N-Terminal extension of human immunodeficiency virus capsid protein converts the in vitro assembly phenotype from tubular to spherical particles. *J. Virol.* **72,** 4798–4810 (1998).

35. Gross, I. A conformational switch controlling HIV-1 morphogenesis. *EMBO J.* **19,** 103–113 (2000).

36. Ehrlich, L. S., Agresta, B. E. & Carter, C. A. Assembly of Recombinant Human Immunodeficiency Virus Type 1 Capsid Protein In Vitro. *J. Virol.* **66,** 4874–4883 (1992).

37. Hatakeyama, S. TRIM Family Proteins: Roles in Autophagy, Immunity, and Carcinogenesis. *Trends Biochem. Sci.* **42,** 297–311 (2017).

38. Sparrer, K. M. J. & Gack, M. U. TRIM proteins: New players in virus-induced autophagy. *PLoS Pathog.* **14,** 1–6 (2018).

39. Mandell, M. A. *et al.* TRIM Proteins Regulate Autophagy and Can Target Autophagic Substrates by Direct Recognition. *Dev. Cell* **30,** 394–409 (2014).

40. Kimura, T. *et al.* TRIM-mediated precision autophagy targets cytoplasmic regulators of innate immunity. *J. Cell Biol.* **210,** 973–989 (2015).

41. Freemont, P. S. Ubiquitination : RING for destruction? *Curr. Biol.* **10,** 84–87 (2000).

42. Meroni, G. & Diez-Roux, G. TRIM/RBCC, a novel class of 'single protein RING finger' E3 ubiquitin ligases. *BioEssays* **27,** 1147–1157 (2005).

43. Short, K. M. & Cox, T. C. Subclassification of the RBCC/TRIM superfamily reveals a novel motif necessary for microtubule binding. *J. Biol. Chem.* **281,** 8970–8980 (2006).

44. Ebner, P., Versteeg, G. A. & Ikeda, F. Ubiquitin enzymes in the regulation of immune responses. *Crit. Rev. Biochem. Mol. Biol.* **52,** 425–460 (2017).

45. Reddy, B. A., Etkin, L. D. & Freemont, P. S. A novel zinc finger coiled-coil domain in a family of nuclear proteins. *Trends Biochem. Sci.* **17,** 344–345 (1992).

46. Borden, K. L. B. & Freemont, P. S. The RING finger domain: a recent example of a sequence-structure family. *Curr. Opin. Struct. Biol.* **6,** 395–401 (1996).

47. Chaplin, D. D. 1 . Overview of the human immune response. 430–435 (2006). doi:10.1016/j.jaci.2005.09.034

48. Hoffmann, J., Akira, S. & Hoffmann, J. Innate immunity Editorial Overview. *Curr. Opin.*

*Immunol.* **25,** 1–3 (2013).

49. Alberts, B. *et al. Molecular biology of the cell*. (Garland Science, 2002).

50. Takeuchi, O. & Akira, S. Pattern Recognition Receptors and Inflammation. *Cell* **140,** 805–820 (2010).

51. Freemont, P. S. The RING Finger: A novel Protein Sequence Motif Related to the Zinc Finger. *Ann. New York Acad. Scences* **684,** 174–192 (1993).

52. Torok, M. & Etkin, L. D. Two B or not two B? Overview of the rapidly expanding B-box family of proteins. *Differentiation* **67,** 63–71 (2001).

53. Bell, J. L. *et al.* TRIM16 acts as an E3 ubiquitin ligase and can heterodimerize with other TRIM family members. *PLoS One* **7,** 1–9 (2012).

54. Diaz-Griffero, F. *et al.* A B-Box 2 Surface Patch Important for TRIM5α Self-Association, Capsid Binding Avidity, and Retrovirus Restriction. *J. Virol.* **83,** 10737–10751 (2009).

55. Li, X. & Sodroski, J. The TRIM5alpha B-box 2 domain promotes cooperative binding to the retroviral capsid by mediating higher-order self-association. *J. Virol.* **82,** 11495–502 (2008).

56. Keown, J. R., Yang, J. X., Douglas, J. & Goldstone, D. C. Characterisation of assembly and ubiquitylation by the RBCC motif of Trim5α. *Sci. Rep.* **6,** 1–11 (2016).

57. Wagner, J. M. *et al.* A general model for retroviral capsid pattern recognition by TRIM5 proteins. *J. Virol.* **92,** JVI.01563-17 (2018).

58. Wagner, J. M. *et al.* Mechanism of B-box 2 domain-mediated higher-order assembly of the retroviral restriction factor TRIM5α. *Elife* **5,** (2016).

59. Sanchez, J. G. *et al.* The tripartite motif coiled-coil is an elongated antiparallel hairpin dimer. *Proc. Natl. Acad. Sci.* **111,** 2494–2499 (2014).

60. Goldstone, D. C. *et al.* Structural studies of postentry restriction factors reveal antiparallel dimers that enable avid binding to the HIV-1 capsid lattice. *Proc. Natl. Acad. Sci.* **111,** 9609–9614 (2014).

61. Weinert, C., Morger, D., Djekic, A., Grütter, M. G. & Mittl, P. R. E. Crystal structure of TRIM20 C-terminal coiled-coil/B30.2 fragment: implications for the recognition of higher order oligomers. *Sci. Rep.* **5,** 10819 (2015).

62. Li, Y. *et al.* Structural insights into the TRIM family of ubiquitin E3 ligases. *Cell Res.* **24,** 762–765 (2014).

63. Reymond, A. *et al.* The tripartite motif family identifies cell compartments. *EMBO J.* **20,** 2140–2151 (2001).

64. Steinmetz, M. O. *et al.* Molecular basis of coiled-coil formation. *Proc. Natl. Acad. Sci.*

**104,** 7062–7067 (2007).

65. Ozato, K., Shin, D. M., Chang, T. H. & Morse, H. C. TRIM Famiy Proteins and Their Emerging Roles in Innate Immunity. *Nat. Rev. Immunol.* **8,** 849–860 (2012).

66. Henry, J., Mather, I. H., McDermott, M. F. & Pontarotti, P. B30.2-like domain proteins: update and new insights into a rapidly expanding family of proteins. *Mol Biol Evol* **15,** 1696–1705 (1998).

67. Slack, F. J. & Ruvkun, G. A novel repeat domain that is often associated with RING finger and B-box motifs. *Trends Biochem. Sci.* **23,** 474–475 (1998).

68. Schwertman, P., Bekker-Jensen, S. & Mailand, N. Regulation of DNA double-strand break repair by ubiquitin and ubiquitin-like modifiers. *Nat. Rev. Mol. Cell Biol.* **17,** 379–394 (2016).

69. Geng, F., Wenzel, S. & Tansey, W. P. Ubiquiting and proteasome in transcription. *Annu. Rev. Biochem.* **81,** 177–201 (2012).

70. Goldberg, A. L. Protein degradation and protection against misfolded or damaged proteins. *Nature* **426,** 895–899 (2003).

71. Morreale, F. E. & Walden, H. SnapShot : Types of Ubiquitin Ligases SnapShot : Types of Ubiquitin Ligases. *Cell* **165,** 248–248.e1 (2016).

72. Ye, Y. & Rape, M. Building ubiquitin chains: E2 enzymes at work. *Nat. Rev. Mol. Cell Biol.* **10,** 755–764 (2009).

73. Weissman, A. M. THEMES AND VARIATIONS ON UBIQUITYLATION. *Nat. Rev. Mol. Cell Biol.* **2,** 169–178 (2001).

74. Sanchez, J. G. *et al.* Mechanism of TRIM25 Catalytic Activation in the Antiviral RIG-I Pathway. *Cell Rep.* **16,** 1315–1325 (2016).

75. Koliopoulos, M. G., Esposito, D., Christodoulou, E., Taylor, I. A. & Rittinger, K. Functional role of TRIM E 3 ligase oligomerization and regulation of catalytic activity. *EMBO J.* **35,** 1–15 (2016).

76. Plechanovov, A., Jaffray, E. G., Tatham, M. H., Naismith, J. H. & Hay, R. T. Structure of a RING E3 ligase and ubiquitin-loaded E2 primed for catalysis. *Nature* **489,** 115–120 (2012).

77. Brzovic, P. S., Rajagopal, P., Hoyt, D. W., King, M.-C. & Klevit, R. E. Structure of a BRCA1– BARD1 heterodimeric RING–RING complex. *Nat. Struct. Biol.* **8,** 833–837 (2001).

78. Metzger, M. B., Pruneda, J. N., Klevit, R. E. & Weissman, A. M. RING-type E3 ligases: Master manipulators of E2 ubiquitin-conjugating enzymes and ubiquitination. *Biochim. Biophys. Acta - Mol. Cell Res.* **1843,** 47–60 (2014).

79. Park, C. W. & Ryu, K. Y. Cellular ubiquitin pool dynamics and homeostasis. *BMB Rep.* **47,** 475–482 (2014).

80. Zhao, G. *et al.* Rhesus TRIM5α disrupts the HIV-1 capsid at the inter-hexamer interfaces. *PLoS Pathog.* **7,** (2011).

81. Black, L. R. & Aiken, C. TRIM5 Disrupts the Structure of Assembled HIV-1 Capsid Complexes In Vitro. *J. Virol.* **84,** 6564–6569 (2010).

82. Pertel, T. *et al.* TRIM5 is an innate immune sensor for the retrovirus capsid lattice. *Nature* **472,** 361–365 (2011).

83. Biris, N., Tomashevski, A., Bhattacharya, A., Diaz-Griffero, F. & Ivanov, D. N. Rhesus Monkey TRIM5a SPRY Domain Recognizes Multiple Epitopes That Span Several Capsid Monomers on the Surface of the HIV-1 Mature Viral Core. *J. Mol. Biol.* **425,** 5032–5044 (2013).

84. Diaz-Griffero, F. *et al.* Rapid turnover and polyubiquitylation of the retroviral restriction factor TRIM5. *Virology* **349,** 300–315 (2006).

85. Langelier, C. R. *et al.* Biochemical Characterization of a Recombinant TRIM5 Protein That Restricts Human Immunodeficiency Virus Type 1 Replication. *J. Virol.* **82,** 11682–11694 (2008).

86. Sayah, D. M., Sokolskaja, E., Berthoux, L. & Luban, J. Cyclophilin A retrotransposition into TRIM5 explains owl monkey resistance to HIV-1. *Nature* **430,** 569–573 (2004).

87. Stremlau, M. *et al.* The cytoplasmic body component TRIM5alpha restricts HIV-1 infection in Old World monkeys. *Nature* **427,** 848–853 (2004).

88. Stremlau, M. *et al.* Specific recognition and accelerated uncoating of retroviral capsids by the TRIM5alpha restriction factor. *Proc. Natl. Acad. Sci. U. S. A.* **103,** 5514–9 (2006).

89. Anderson, J. L. *et al.* Proteasome Inhibition Reveals that a Functional Preintegration Complex Intermediate Can Be Generated during Restriction by Diverse TRIM5 Proteins. *J. Virol.* **80,** 9754–9760 (2006).

90. Campbell, E. M., Perez, O., Anderson, J. L. & Hope, T. J. Visualization of a proteasome-independent intermediate during restriction of HIV-1 by rhesus TRIM5α. *J. Cell Biol.* **180,** 549–561 (2008).

91. Diaz-Griffero, F. *et al.* Comparative requirements for the restriction of retrovirus infection by TRIM5?? and TRIMCyp. *Virology* **369,** 400–410 (2007).

92. Lukic, Z. *et al.* TRIM5α associates with proteasomal subunits in cells while in complex with HIV-1 virions. *Retrovirology* **8,** 93 (2011).

93. Rold, C. J. & Aiken, C. Proteasomal degradation of TRIM5?? during retrovirus restriction. *PLoS Pathog.* **4,** (2008).

94. Wu, X., Anderson, J. L., Campbell, E. M., Joseph, A. M. & Hope, T. J. Proteasome inhibitors uncouple rhesus TRIM5alpha restriction of HIV-1 reverse transcription and infection. *Proc. Natl. Acad. Sci. U. S. A.* **103,** 7465–70 (2006).

95. Kutluay, S. B., Perez-Caballero, D. & Bieniasz, P. D. Fates of Retroviral Core Components during Unrestricted and TRIM5-Restricted Infection. *PLoS Pathog.* **9,** (2013).

96. Mandell, M. A., Kimura, T., Jain, A., Johansen, T. & Deretic, V. TRIM proteins regulate autophagy: TRIM5 is a selective autophagy receptor mediating HIV-1 restriction. *Autophagy* **10,** 2387–2388 (2014).

97. Wu, F. *et al.* TRIM5 alpha Drives SIVsmm Evolution in Rhesus Macaques. *PLoS Pathog.* **9,** (2013).

98. Yap, M. W., Nisole, S., Lynch, C. & Stoye, J. P. Trim5alpha protein restricts both HIV-1 and murine leukemia virus. *Proc. Natl. Acad. Sci. U. S. A.* **101,** 10786–91 (2004).

99. Hatziioannou, T., Cowan, S., Goff, S. P., Bieniasz, P. D. & Towers, G. J. Restriction of multiple divergent retroviruses by Lv1 and Ref1. *EMBO J.* **22,** 385–394 (2003).

100. Perron, M. J. *et al.* TRIM5alpha mediates the postentry block to N-tropic murine leukemia viruses in human cells. *Proc. Natl. Acad. Sci. U. S. A.* **101,** 11827–32 (2004).

101. Song, B. *et al.* Retrovirus Restriction by TRIM5 α Variants from Old World and New World Primates. *J. Virol.* **79,** 3930–3937 (2005).

102. Li, X. *et al.* Unique features of TRIM5α among closely related human TRIM family members. *Virology* **360,** 419–433 (2007).

103. Xu, L. *et al.* BTBD1 and BTBD2 colocalize to cytoplasmic bodies with the RBCC/tripartite motif protein, TRIM5δ. *Exp. Cell Res.* **288,** 84–93 (2003).

104. Campbell, E. M., Perez, O., Melar, M. & Hope, T. J. Labeling HIV-1 virions with two fluorescent proteins allows identification of virions that have productively entered the target cell. *Virology* **360,** 286–293 (2007).

105. Campbell, E. M. *et al.* TRIM5 Cytoplasmic Bodies Are Highly Dynamic Structures. *Mol. Biol. Cell* **18,** 2102–2111 (2007).

106. Lukic, Z. & Campbell, E. M. The Cell Biology of TRIM5α. *Curr. Opin. Virol.* **9,** 73–80 (2012).

107. Song, B. *et al.* TRIM5α association with cytoplasmic bodies is not required for antiretroviral activity. *Virology* **343,** 201–211 (2005).

108. Perez-Caballero, D., Hatziioannou, T., Zhang, F., Cowan, S. & Bieniasz, P. D. Restriction of human immunodeficiency virus type 1 by TRIM-CypA occurs with rapid kinetics and independently of cytoplasmic bodies, ubiquitin, and proteasome activity. *J. Virol.* **79,** 15567–72 (2005).

109. Sastri, J. *et al.* Identification of residues within the L2 region of rhesus TRIM5a that are required for retroviral restriction and cytoplasmic body localization. *Virology* **405,** 259–266 (2010).

110. Sebastian, S. & Luban, J. TRIM5alpha selectively binds a restriction-sensitive retroviral capsid. *Retrovirology* **2,** 40 (2005).

111. Perez-Caballero, D., Hatziioannou, T., Yang, A., Cowan, S. & Bieniasz, P. D. Human tripartite motif 5alpha domains responsible for retrovirus restriction activity and specificity. *J. Virol.* **79,** 8969–78 (2005).

112. Barclay, A. N. Ig-like domains : Evolution from simple interaction molecules to sophisticated antigen recognition. *Proc. …* **96,** 14672–14674 (1999).

113. Alzari, P. M. Domains, Immunoglobulin-Type. *Encycl. Immunol.* 775–778 (1998). doi:10.1006/RWEI.1999.0204

114. Biris, N. *et al.* Structure of the rhesus monkey TRIM5 PRYSPRY domain, the HIV capsid recognition module. *Proc. Natl. Acad. Sci.* **109,** 13278–13283 (2012).

115. Yang, H. *et al.* Structural insight into HIV-1 capsid recognition by rhesus TRIM5. *Proc. Natl. Acad. Sci.* **109,** 18372–18377 (2012).

116. Perron, M. J., Stremlau, M. & Sodroski, J. Two surface-exposed elements of the B30.2/SPRY domain as potency determinants of N-tropic murine leukemia virus restriction by human TRIM5alpha. *J. Virol.* **80,** 5631–5636 (2006).

117. Ohkura, S., Yap, M. W., Sheldon, T. & Stoye, J. P. All three variable regions of the TRIM5alpha B30.2 domain can contribute to the specificity of retrovirus restriction. *J. Virol.* **80,** 8554–8565 (2006).

118. Notkins, A. L. Polyreactivity of antibody molecules. *Trends Immunol.* **25,** 174–179 (2004).

119. Ganser-Pornillos, B. K. *et al.* Hexagonal assembly of a restricting TRIM5alpha protein. *Proc Natl Acad Sci U S A* **108,** 534–539 (2011).

120. Javanbakht, H., Diaz-Griffero, F., Stremlau, M., Si, Z. & Sodroski, J. The contribution of RING and B-box 2 domains to retroviral restriction mediated by monkey TRIM5α. *J. Biol. Chem.* **280,** 26933–26940 (2005).

121. Ohkura, S. *et al.* Novel escape mutants suggest an extensive TRIM5α binding site spanning the entire outer surface of the murine leukemia virus capsid protein. *PLoS Pathog.* **7,** e1002011 (2011).

122. Song, H. *et al.* A single amino acid of the human immunodeficiency virus type 2 capsid affects its replication in the presence of cynomolgus monkey and human TRIM5alphas. *J. Virol.* **81,** 7280–7285 (2007).

123. Morger, D. *et al.* The three-fold axis of the HIV-1 capsid lattice is the species-specific

binding interface for TRIM5α. *J. Virol.* **92,** 1–16 (2018).

124. McCarthy, K. R., Kirmaier, A., Autissier, P. & Johnson, W. E. Evolutionary and Functional Analysis of Old World Primate TRIM5 Reveals the Ancient Emergence of Primate Lentiviruses and Convergent Evolution Targeting a Conserved Capsid Interface. *PLoS Pathog.* **11,** 1–26 (2015).

125. Roganowicz, M. D. *et al.* TRIM5α SPRY/coiled-coil interactions optimize avid retroviral capsid recognition. *PLoS Pathog.* **13,** 1–21 (2017).

126. Sastri, J. *et al.* Restriction of HIV-1 by rhesus TRIM5α is governed by alpha helices in the Linker2 region. *J. Virol.* **88,** 8911–23 (2014).

127. Li, X., Yeung, D. F., Fiegen, A. M. & Sodroski, J. Determinants of the higher order association of the restriction factor TRIM5α and other tripartite motif (TRIM) proteins. *J. Biol. Chem.* **286,** 27959–27970 (2011).

128. Lienlaf, M. *et al.* Contribution of E3-Ubiquitin Ligase Activity to HIV-1 Restriction by TRIM5 rh: Structure of the RING Domain of TRIM5. *J. Virol.* **85,** 8725–8737 (2011).

129. Fletcher, A. J. *et al.* TRIM5α requires Ube2W to anchor Lys63-linked ubiquitin chains and restrict reverse transcription. *EMBO J.* **34,** 1–18 (2015).

130. Diaz-Griffero, F. *et al.* Modulation of retroviral restriction and proteasome inhibitor-resistant turnover by changes in the TRIM5alpha B-box 2 domain. *J. Virol.* **81,** 10362–78 (2007).

131. Wagner, J. M. *et al.* Crystal structure of an HIV assembly and maturation switch. *Elife* **5,** 1–18 (2016).

132. Li, Y.-L. *et al.* Primate TRIM5 proteins form hexagonal nets on HIV-1 capsids. *Elife* **5,** 1–33 (2016).

133. Yudina, Z. *et al.* RING Dimerization Links Higher-Order Assembly of TRIM5α to Synthesis of K63-Linked Polyubiquitin. *Cell Rep.* **12,** 788–797 (2015).

134. Yuan, L. *et al.* Muscle-specific E3 ubiquitin ligases are involved in muscle atrophy of cancer cachexia: An in vitro and in vivo study. *Oncol. Rep.* **33,** 2261–2268 (2015).

135. Höllriegel, R. *et al.* Anabolic effects of exercise training in patients with advanced chronic heart failure (NYHA IIIb): Impact on ubiquitin-protein ligases expression and skeletal muscle size. *Int. J. Cardiol.* **167,** 975–980 (2013).

136. Eddins, M. J. *et al.* Targeting the Ubiquitin E3 Ligase MuRF1 to Inhibit Muscle Atrophy. *Cell Biochem. Biophys.* **60,** 113–118 (2011).

137. Salanova, M. *et al.* Disuse deterioration of human skeletal muscle challenged by resistive exercise superimposed with vibration: Evidence from structural and proteomic analysis. *FASEB J.* **28,** 4748–4763 (2014).

138. Willis, M. S. *et al.* Muscle ring finger 1 mediates cardiac atrophy in vivo. *Am. J. Physiol. Heart Circ. Physiol.* **296,** H997–H1006 (2009).

139. Willis, M. S. *et al.* Muscle ring finger 1, but not muscle ring finger 2, regulates cardiac hypertrophy in vivo. *Circ. Res.* **100,** 456–9 (2007).

140. Bodine, S. C. & Baehr, L. M. Skeletal muscle atrophy and the E3 ubiquitin ligases MuRF1 and MAFbx/atrogin-1. *AJP Endocrinol. Metab.* **307,** E469–E484 (2014).

141. Raue, U., Slivka, D., Jemiolo, B., Hollon, C. & Trappe, S. Proteolytic gene expression differs at rest and after resistance exercise between young and old women. *J Gerontol A Biol Sci Med Sci* **62,** 1407–12 OD–2008/01/02 (2007).

142. Glass, D. J. Molecular mechanisms modulating muscle mass. *Trends Mol. Med.* **9,** 344–350 (2003).

143. Cohen, S. *et al.* During muscle atrophy, thick, but not thin, filament components are degraded by MuRF1-dependent ubiquitylation. *J. Cell Biol.* **185,** 1083–1095 (2009).

144. Mrosek, M. *et al.* Structural analysis of B-box 2 from MuRF1: Identification of a novel self-association pattern in a RING-like fold. *Biochemistry* **47,** 10722–10730 (2008).

145. Witt, S. H., Granzier, H., Witt, C. C. & Labeit, S. MURF-1 and MURF-2 target a specific subset of myofibrillar proteins redundantly: Towards understanding MURF-dependent muscle ubiquitination. *J. Mol. Biol.* **350,** 713–722 (2005).

146. Mrosek, M. *et al.* Molecular determinants for the recruitment of the ubiquitin-ligase MuRF-1 onto M-line titin. *FASEB J.* **21,** 1383–1392 (2007).

147. McElhinny, A. S., Kakinuma, K., Sorimachi, H., Labeit, S. & Gregorio, C. C. Muscle-specific RING finger-1 interacts with titin to regulate sarcomeric M-line and thick filament structure and may have nuclear functions via its interaction with glucocorticoid modulatory element binding protein-1. *J. Cell Biol.* **157,** 125–136 (2002).

148. Bodine, S. C. *et al.* Identification of Ubiquitin Ligases Required for Skeletal Muscle Atrophy. *Science (80-. ).* **294,** 1704–1708 (2001).

149. Moresi, V. *et al.* Myogenin and class II HDACs control neurogenic muscle atrophy by inducing E3 ubiquitin ligases. *Cell* **143,** 35–45 (2010).

150. Hirner, S. *et al.* MuRF1-dependent Regulation of Systemic Carbohydrate Metabolism as Revealed from Transgenic Mouse Studies. *J. Mol. Biol.* **379,** 666–677 (2008).

151. Willis, M. S. *et al.* Muscle ring finger 1 and muscle ring finger 2 are necessary but functionally redundant during developmental cardiac growth and regulate E2F1-mediated gene expression in vivo. *Cell Biochem. Funct.* **32,** 39–50 (2014).

152. Glass, D. J. Skeletal muscle hypertrophy and atrophy signaling pathways. *Int. J. Biochem. Cell Biol.* **37,** 1974–1984 (2005).

153. Sandri, M. *et al.* Foxo Transcription Factors Induce the Atrophy- Related Ubiquitin Ligase Atrogin-1 and Cause Skeletal Muscle Atrophy. *Cell* **117,** 399–412 (2004).

154. Myatt, S. S. & Lam, E. W.-F. The emerging roles of forkhead box (FOX) proteins in cancer. *Nat. Rev. Cancer* **7,** 847–859 (2007).

155. Liu, T., Zhang, L., Joo, D. & Sun, S.-C. NF-κB signaling in inflammation. *Signal Transduct. Target. Ther.* **2,** 17023 (2017).

156. Centner, T. *et al.* Identification of muscle specific ring finger proteins as potential regulators of the titin kinase domain. *J. Mol. Biol.* **306,** 717–726 (2001).

157. Franke, B. *et al.* Molecular basis for the fold organization and sarcomeric targeting of the muscle atrogin MuRF1. *Open Biol.* **4,** 130172–130172 (2014).

158. Chen, S. N. *et al.* Human molecular genetic and functional studies identify TRIM63, encoding muscle RING finger protein 1, as a novel gene for human hypertrophic cardiomyopathy. *Circ. Res.* **111,** 907–919 (2012).

159. Bogomolovas, J. *et al.* Titin kinase is an inactive pseudokinase scaffold that supports MuRF1 recruitment to the sarcomeric M-line. *Open Biol.* **4,** 140041–140041 (2014).

160. Dubochet, J. *et al.* Cryo-electron microscopy of vitrified specimens. *Q. Rev. Biophys.* **21,** 129–228 (1988).

161. Wu, S., Armache, J.-P. & Cheng, Y. Single-particle cryo-EM data acquisition by using direct electron detection camera. *Reprod. Syst. Sex. Disord.* **65,** 35–41 (2016).

162. Cheng, Y. Single-particle cryo-EM at crystallographic resolution Yifan. *Cell* **161,** 450–457 (2015).

163. Kühlbrandt, W. The Resolution Revolution. *Science (80-. ).* **343,** 1443–1444 (2014).

164. McMullan, G., Faruqi, A. R., Clare, D. & Henderson, R. Comparison of optimal performance at 300keV of three direct electron detectors for use in low dose electron microscopy. *Ultramicroscopy* **147,** 156–63 (2014).

165. Brilot, A. F. *et al.* Beam-Induced Motion of Vitrified Specimen on Holey Carbon Film. *J Struct Biol* **177,** 630–637 (2012).

166. Li, X. *et al.* Electron counting and beam-induced motion correction enable near-atomic-resolution single-particle cryo-EM. *Nat. Methods* **10,** 584–590 (2013).

167. Singer, A., Coifman, R. R., Sigworth, F. J., Chester, D. W. & Shkolnisky, Y. Detecting Consistent Common Lines in Cryo-EM by Voting. *J. Struct. Biol.* **169,** 312–322 (2010).

168. Van Heel, M. Angular reconstitution: A posteriori assignment of projection directions for 3D reconstruction. *Ultramicroscopy* **21,** 111–123 (1987).

169. Greenberg, I. & Shkolnisky, Y. Common lines modeling for reference free Ab-initio

reconstruction in cryo-EM. *J. Struct. Biol.* **200,** 106–117 (2017).

170. Baumeister, W., Grimm, R. & Walz, J. Electron tomography of molecules and cells. *Trends Cell Biol.* **9,** 81–85 (1999).

171. Gan, L. & Jensen, G. J. Electron tomography of cells. *Q. Rev. Biophys.* **45,** 27–56 (2012).

172. Ladinsky, M. S., Mastronarde, D. N., McIntosh, J. R., Howell, K. E. & Staehlin, L. A. Golgi structure in three dimensions: functional insights from the {NRK} cell. *J. Cell Biol.* **144,** 1135–1149 (1999).

173. Henderson, G. P., Gan, L. & Jensen, G. J. 3-D ultrastructure of O. tauri: Electron cryotomography of an entire Eukaryotic cell. *PLoS One* **2,** (2007).

174. Redemann, S. *et al.* C. elegans chromosomes connect to centrosomes by anchoring into the spindle network. *Nat. Commun.* **8,** 1–13 (2017).

175. Cyrklaff, M. *et al.* Cryo-electron tomography of vaccinia virus. *Proc Natl Acad Sci U S A* **102,** 2772–7 (2005).

176. Briggs, J. A. G. *et al.* The mechanism of HIV-1 core assembly: Insights from three-dimensional reconstructions of authentic virions. *Structure* **14,** 15–20 (2006).

177. Cardone, G. *et al.* Visualization of the herpes simplex virus portal in situ by cryo-electron tomography. *Virology* **361,** 426–434 (2007).

178. Zanetti, G. *et al.* The structure of the COPII transport-vesicle coat assembled on membranes. *Elife* **2013,** 1–15 (2013).

179. Kosinski, J. *et al.* Molecular architecture of the inner ring scffold of the human nuclear pore complex. *Science (80-. ).* **352,** 363–366 (2016).

180. Dodonova, S. O. *et al.* 9Å structure of the COPI coat reveals that the Arf1 GTPase occupies two contrasting molecular environments. *Elife* **6,** 1–29 (2017).

181. Schmid, M. F. & Booth, C. R. Methods for aligning and for averaging 3D volumes with missing data. *J. Struct. Biol.* **161,** 243–248 (2008).

182. Wan, W. & Briggs, J. A. G. Cryo-Electron Tomography and Subtomogram Averaging. *Methods Enzymol.* **579,** 329–367 (2016).

183. Briggs, J. A. G. Structural biology in situ — the potential of subtomogram averaging. *Curr. Opin. Struct. Biol.* **23,** 261–267 (2013).

184. Schmid, M. F. *Single-particle electron cryotomography (cryoET)*. *Advances in Protein Chemistry and Structural Biology* **82,** (Elsevier Inc., 2011).

185. Steven, A. C. & Aebi, U. The next ice age: Cryo-electron tomography of intact cells. *Trends Cell Biol.* **13,** 107–110 (2003).

186. Henderson, R. *et al.* Outcome of the first electron microscopy validation task force

meeting. *Structure* **20,** 205–214 (2012).

187. Wasilewski, S. & Rosenthal, P. B. Web server for tilt-pair validation of single particle maps from electron cryomicroscopy. *J. Struct. Biol.* **186,** 122–131 (2014).

188. Rosenthal, P. B. & Rubinstein, J. L. Validating maps from single particle electron cryomicroscopy. *Curr. Opin. Struct. Biol.* **34,** 135–144 (2015).

189. Al-Bassam, J., Ozer, R. S., Safer, D., Halpain, S. & Milligan, R. A. MAP2 and tau bind longitudinally along the outer ridges of microtubule protofilaments. *J. Cell Biol.* **157,** 1187–1196 (2002).

190. Kim, J. M. *et al.* Subnanometre-resolution electron cryomicroscopy structure of a heterodimeric ABC exporter. *Nature* **517,** 396–400 (2015).

191. Vinothkumar, K. R., McMullan, G. & Henderson, R. Molecular mechanism of antibody-mediated activation of β-galactosidase. *Structure* **22,** 621–627 (2014).

192. van Heel, M. & Harauz, G. Resolution criteria for three dimensional reconstruction. *Optik* **73,** 119–122 (1986).

193. Saxton, W. O. & Baumeister, W. The correlation averaging of a regularly arranged bacterial cell envelope protein. *J. Microsc.* **127,** 127–138 (1982).

194. Liao, H. Y. & Frank, J. Definition and estimation of resolution in single-particle reconstructions. *Structure* **18,** 768–775 (2010).

195. Grigorieff, N. & Harrison, S. C. Near-atomic resolution reconstructions of icosahedral viruses from electron cryo-microscopy. *Curr. Opin. Struct. Biol.* **21,** 265–273 (2011).

196. Martín-Vicente, M., Medrano, L. M., Resino, S., García-Sastre, A. & Martínez, I. TRIM25 in the regulation of the antiviral innate immunity. *Front. Immunol.* **8,** 1–9 (2017).

197. Oudshoorn, D., Versteeg, G. A. & Kikkert, M. Regulation of the innate immune system by ubiquitin and ubiquitin-like modifiers. *Cytokine Growth Factor Rev.* **23,** 273–282 (2012).

198. Uchil, P. D. *et al.* TRIM Protein-Mediated Regulation of Inflammatory and Innate Immune Signaling and Its Association with Antiretroviral Activity. *J. Virol.* **87,** 257–272 (2013).

199. Versteeg, G. A. *et al.* The E3-ligase TRIM family of proteins regulates signaling pathways triggered by innate immune pattern-recognition receptors. *Immunity* **38,** 384–398 (2013).

200. Nakayama, E. E. & Shioda, T. Role of human TRIM5α in intrinsic immunity. *Front. Microbiol.* **3,** 1–13 (2012).

201. Woo, J. S. *et al.* Structural and functional insights into the B30.2/SPRY domain. *EMBO J.* **25,** 1353–1363 (2006).

202. Yap, M. W., Nisole, S. & Stoye, J. P. A single Amino Acid Change in the SPRY Domain

of Human TRIM5 Leads to HIV-1 Restriction. *2Current Biol.* **15,** 73–78 (2005).

203. Schneider, C. A., Rasband, W. S. & Eliceiri, K. W. NIH Image to ImageJ: 25 years of image analysis. *Nat. Methods* **9,** 671–675 (2012).

204. Pornillos, O., Ganser-Pornillos, B. K., Banumathi, S., Hua, Y. & Yeager, M. Disulfide Bond Stabilization of the Hexameric Capsomer of Human Immunodeficiency Virus. *J. Mol. Biol.* **401,** 985–995 (2010).

205. Diaz-Griffero, F. *et al.* Requirements for capsid-binding and an effector function in TRIMCyp-mediated restriction of HIV-1. *Virology* **351,** 404–419 (2006).

206. Kovalskyy, D. B. & Ivanov, D. N. Recognition of the HIV capsid by the TRIM5α restriction factor is mediated by a subset of pre-existing conformations of the TRIM5α SPRY domain. *Biochemistry* **53,** 1466–1476 (2014).

207. Campbell, E. M. *et al.* TRIM5α-Mediated Ubiquitin Chain Conjugation Is Required for Inhibition of HIV-1 Reverse Transcription and Capsid Destabilization. *J. Virol.* **90,** 1849–1857 (2016).

208. Campbell, E. M. & Hope, T. J. Live cell imaging of the HIV-1 life cycle. *Trends in microbilogy* **16,** 580–587 (2008).

209. Stremlau, M., Perron, M. J., Welikala, S. & Sodroski, J. Species-Specific Variation in the B30.2 ( SPRY) Domain of TRIM5alpha Determines the Potency of Human Immunodeficiency Virus Restriction. *J. Virol.* **79,** 3139–3145 (2005).

210. Song, B. *et al.* The B30.2(SPRY) Domain of the Retroviral Restriction Factor TRIM5 Exhibits Lineage-Specific Length and Sequence Variation in Primates. *J. Virol.* **79,** 6111–6121 (2005).

211. Cho, H.-J. *et al.* Measurement of ice thickness on vitreous ice embedded cryo-EM grids: investigation of optimizing condition for visualizing macromolecules. *J. Anal. Sci. Technol.* **4,** 5 (2013).

212. Pettersen, E. F. *et al.* UCSF Chimera - A visualization system for exploratory research and analysis. *J. Comput. Chem.* **25,** 1605–1612 (2004).

213. Kremer, J. R., Mastronarde, D. N. & McIntosh, J. R. Computer visualization of three-dimensional image data using IMOD. *J. Struct. Biol.* **116,** 71–6 (1996).

214. Castaño-Díez, D., Kudryashev, M., Arheit, M. & Stahlberg, H. Dynamo: A flexible, user-friendly development tool for subtomogram averaging of cryo-EM data in high-performance computing environments. *J. Struct. Biol.* **178,** 139–151 (2012).

215. Punjani, A., Rubinstein, J. L., Fleet, D. J. & Brubaker, M. A. CryoSPARC: Algorithms for rapid unsupervised cryo-EM structure determination. *Nat. Methods* **14,** 290–296 (2017).

216. Weinert, B. T., Moustafa, T., Iesmantavicius, V., Zechner, R. & Choudhary, C. Analysis of acetylation stoichiometry suggests that SIRT3 repairs nonenzymatic acetylation lesions.

*EMBO J.* **34,** 2620–2632 (2015).

217. Drozdetskiy, A., Cole, C., Procter, J. & Barton, G. J. JPred4: A protein secondary structure prediction server. *Nucleic Acids Res.* **43,** W389–W394 (2015).

218. Lupas, A., Van Dyke, M. & Stock, J. Predicting coiled coils from protein sequences. *Science (80-. ).* **252,** 1162–1164 (1991).

219. Jeschke, G. *et al.* DeerAnalysis2006—a comprehensive software package for analyzing pulsed ELDOR data. *Appl. Magn. Reson.* **30,** 473–498 (2006).

220. Mchaourab, H. S., Lietzow, M. A., Hideg, K. & Hubbell, W. L. Motion of spin-labeled side chains in T4 lysozyme. Correlation with protein structure and dynamics. *Biochemistry* **35,** 7692–7704 (1996).

221. Francis, D. J., Hubbell, W. L. & Klug, C. S. Probing Protein Secondary Structure Using EPR: Investigating a Dynamic Region of Visual Arrestin. *Appl. Magn. Reson.* **43,** 405–419 (2012).

222. Hubbell, W. L., Cafiso, D. S. & Altenbach, C. Identifying conformational changes with site-directed spin labeling. *Nat. Struct. Biol.* **7,** 735–739 (2000).

223. Bodine, S. C. *et al.* Akt/mTOR pathway is a crucial regulator of skeletal muscle hypertrophy and can prevent muscle atrophy in vivo. *Nat. Cell Biol.* **3,** 1014–1019 (2001).

224. McNab, F. W., Rajsbaum, R., Stoye, J. P. & O'Garra, A. Tripartite-motif proteins and innate immune regulation. *Curr. Opin. Immunol.* **23,** 46–56 (2011).

225. Clarke, B. A. *et al.* The E3 Ligase MuRF1 Degrades Myosin Heavy Chain Protein in Dexamethasone-Treated Skeletal Muscle. *Cell Metab.* **6,** 376–385 (2007).

226. Dawidziak, D. M., Sanchez, J. G., Wagner, J. M., Ganser-Pornillos, B. K. & Pornillos, O. Structure and catalytic activation of the TRIM23 RING E3 ubiquitin ligase. *Protein Sci.* **85,** 1957–1961 (2017).

227. Agulleiro, J. I. & Fernandez, J. J. Fast tomographic reconstruction on multicore computers. *Bioinformatics* **27,** 582–583 (2011).

# Appendix 1.

# In-house scripts used in this study

In this section, I list the in-house scripts written to help in data analysis. Lines starting with "#" provide comments for the scripts and explain the role of the function used

A1.1. Rotate tomographic reconstruction

In tomo3d [227], we rotated our tomograms so the coordinate systems were the same between IMOD, the program package that aligns micrographs [213] and dynamo [214], a program for subtomogram averaging.

*#checks the header of the aligned stack for the minimum value, removes the dot from the end and converts it to a positive number*

```
min_val=`header -minimum input.ali`
min_val1=${min_val%%"."*}
min_val2=$((100-min_val1))
```

*#creates a new stack from input file, scales all sections by multiplying by first value (1) then adding the second (min_val2); The "bin" command bins images by a given value*

```
newstack -input input.ali -output output_b0.ali -multadd 1,$min_val2
newstack -input input.ali -output output_b2.ali -bin 2 -multadd 1,$min_val2
```

*#creates a tomographic reconstruction of a desired thickness from an input file generated in a previous step using a list of tilt angles; "RotateBy90" outputs slices parallel to the plane of the specimen without inverting handedness*

```
tilt -input output_b2.ali -output final_output_b2.mrc -TILTFILE tilt_angles.tlt -RotateBy90 -THICKNESS 1000
```

The output is a tomographic reconstruction that is subsequently used in dynamo

A1.2 test_transform.pl

The optimized positions of CA hexamers in a tube segment were saved in a dynamo transformation matrix. We generated a PDB file with the coordinates of the centers of all CA hexamers from a tube segment

*#USE: ./test_transform.pl [x] [y] [z] [dynamo transformation matrix of a tube segment] [output file in PDB format]*

```
#x, y, z are the coordinates of the center of a hexameric CA reconstruction determined by UCSF Chimera command: measure center #0 mark true
$x = $ARGV[0]; chomp $x;
$y = $ARGV[1]; chomp $y;
$z = $ARGV[2]; chomp $z;
$matrix = $ARGV[3]; chomp $matrix;
$outfile = $ARGV[4]; chomp $outfile;
open (MATRIX, "$matrix"); @matrix = <MATRIX>; close (MATRIX);
open (OUT, ">$outfile");

#opens a dynamo transformation matrix; if the line starts with "Model", the program reads the three subsequent lines that describe the positions of the CA hexamers and transforms them into coordinate system compatible with structure-viewing programs like UCSF Chimera
$atomcounter = 1;
foreach $counter (0..$#matrix) {
    @line0 = split(" ",$matrix[$counter]);
    @line1 = split(" ",$matrix[$counter+1]);
    @line2 = split(" ",$matrix[$counter+2]);
    @line3 = split(" ",$matrix[$counter+3]);
    if ($line0[0] eq "Model") {
        @resnum = split "/\./, $line[1]";
        $newx = $line1[0]*$x + $line1[1]*$y + $line1[2]*$z + $line1[3];
        $newy = $line2[0]*$x + $line2[1]*$y + $line2[2]*$z + $line2[3];
        $newz = $line3[0]*$x + $line3[1]*$y + $line3[2]*$z + $line3[3];
#prints the newly calculated coordinates in a PDB format
        if ($atomcounter < 10000) {
        printf OUT "HETATM%5s CD  CD  C%4s  %8.3f%8.3f%8.3f  1.00 20.00 Cd\n",$atomcounter,$resnum[0],$newx,$newy,$newz;
        } else {
            printf OUT "HETATM%5s CD  CD  C%5s  %8.3f%8.3f%8.3f  1.00 20.00 Cd\n",$atomcounter,$resnum[0],$newx,$newy,$newz;
        }
        $atomcounter++;
    }
}
close (OUT);
```

The output is a PDB file with positions of CA hexamer centers from a single tube segment

A1.3. test_transform_pdb.pl

The dymano transformation matrix stores information about the position of the segments of the CA tube. Each segment has a number of CA hexamers. This program creates a PDB file with all segments described by the positions of CA hexamers within

```
#USE: ./test_transform_pdb.pl [CA hexamer centers in a PDB format] [dynamo transformation matrix of a tube] [output file]

$center_coordinates = $ARGV[0]; chomp $center_coordinate;
$matrix = $ARGV[1]; chomp $matrix;
$outfile = $ARGV[2]; chomp $outfile;
open (COORDS, "$center_coordinates"); @coords = <COORDS>; close (COORDS);
open (MATRIX, "$matrix"); @matrix = <MATRIX>; close (MATRIX);
open (OUT, ">$outfile");
$atomcounter = 1;

#it reads the coordinates of the CA hexamers from the PDB file
foreach $coordline (@coords) {
$header = substr($coordline,0,6);
if (($header eq "HETATM") or ($header eq "ATOM")) {
        $x = substr($coordline,30,8);
        $y = substr($coordline,38,8);
        $z = substr($coordline,46,8);

#reads the coordinates of segments of CA tubes from the transformation matrix and convers them to PDB format; then each segment is described by the coordinates of all CA hexamers from the segment and all the points are saved in a PDB format
        foreach $counter (0..$#matrix) {
        @line0 = split(" ",$matrix[$counter]);
        @line1 = split(" ",$matrix[$counter+1]);
        @line2 = split(" ",$matrix[$counter+2]);
        @line3 = split(" ",$matrix[$counter+3]);
        if ($line0[0] eq "Model") {
                @resnum = split "/\./, $line[1]";
                $newx = $line1[0]*$x + $line1[1]*$y + $line1[2]*$z + $line1[3];
                $newy = $line2[0]*$x + $line2[1]*$y + $line2[2]*$z + $line2[3];
                $newz = $line3[0]*$x + $line3[1]*$y + $line3[2]*$z + $line3[3];
```

```
                    if ($atomcounter < 10000) {
#prints the newly calculated coordinates in a PDB format
                    printf OUT "HETATM%5s CD  CD  C%4s  %8.3f%8.3f%8.3f  1.00  20.00
Cd\n",$atomcounter,$resnum[0],$newx,$newy,$newz;
                    } else {
                  printf OUT "HETATM%5s CD  CD  C%5s  %8.3f%8.3f%8.3f  1.00  20.00
Cd\n",$atomcounter,$resnum[0],$newx,$newy,$newz;
                    }
          $atomcounter++;
                    }
                    }
          }
}
close (OUT);
```

The output is a PDB file with positions of CA hexamer centers translated over every every segment of a tube

A1.4. merge_clusters.pl

This program creates a PDB file with the positions of CA hexamers along the tube that are calculated from the overlapping regions of high-abundance CA points

```
#USE: ./merge_clusters.pl [PDB file with all the positions of CA hexamers] [radius of a zone that the particles will be merged into a single one]

$pdb = $ARGV[0]; chomp ($pdb);
@pdb_head = split(/\./, $pdb);
$outfile = "$pdb_head[0]"."_clustered.pdb";
$limit = $ARGV[1]; chomp $limit;
open (PDB, "$pdb"); @pdb = <PDB>; close (PDB);

# STEP 1: Make temporary holder file
open (OUT, ">$outfile");
#reads in x, y, z coordinated from the PDB file
foreach $line (@pdb) {
        $header = substr($line,0,6);
        if (($header eq "HETATM") or ($header eq "ATOM")) {
```

```
                ($atom,$x,$y,$z) = (substr($line,6,5),substr($line,30,8),substr($line,38,8),substr($line,46,8));
                printf OUT "$atom $x $y $z\n";
        }
}
close (OUT);

# STEP 2: Assign residue numbers
$counter = 0;
@assigned = ();
open (PDB, "$outfile"); @pdb = <PDB>; close (PDB);
open (OUT, ">$outfile");
foreach $line (@pdb) {
        @fld = split(" ",$line);
        ($x1,$y1,$z1) = ($fld[1],$fld[2],$fld[3]);
        if (grep(/^$fld[0]$/, @assigned)) {
        }
        else {
                $counter++;
                print "Assigning residue $counter ... ";
                print OUT "$fld[0] $fld[1] $fld[2] $fld[3] $counter\n";
                get_partner_list($x1,$y1,$z1);
                print "done!\n";
        }
}
close (OUT);
print "Total no. of residues = $counter\n";

# STEP 3: Average coordinates for each residue
open (PDB, "$outfile"); @pdb = <PDB>; close (PDB);
print "Writing final PDB file: $outfile\n";
open (OUT, ">$outfile");
foreach $res (1..$counter) {
        $partnercount = 0;
        @x_list = @y_list = @z_list = ();
        foreach $line (@pdb) {
                @fld = split(" ",$line);
```

```
                if ($fld[4] eq $res) {
                        $partnercount++;
                        push (@x_list,$fld[1]);
                        push (@y_list,$fld[2]);
                        push (@z_list,$fld[3]);
                }
                elsif ($fld[4] > $res) { last }
        }
        $avex = average(@x_list);
        $avey = average(@y_list);
        $avez = average(@z_list);
#prints the coordinates calculated as an average from the points in a zone of desired radius
        printf OUT "HETATM%5s CD   CD  C%5s   %8.3f%8.3f%8.3f  1.00 20.00
Cd\n",$res,$res,$avex,$avey,$avez;
        printf "HETATM%5s CD   CD  C%5s   %8.3f%8.3f%8.3f  1.00 20.00
Cd\n",$res,$res,$avex,$avey,$avez;
}
close (OUT);

#sub-command that calculates the average position of a point from the zone
sub get_partner_list {
        foreach $testline (@pdb) {
                @testfld = split (" ",$testline);
                #calculates the average
                ($x2,$y2,$z2) = ($testfld[1],$testfld[2],$testfld[3]);
        $d = sqrt(($x1-$x2)*($x1-$x2)+($y1-$y2)*($y1-$y2)+($z1-$z2)*($z1-$z2));
                if (($d > 0) and ($d < $limit)) {
                        print OUT "$testfld[0] $testfld[1] $testfld[2] $testfld[3] $counter\n";
                        push (@assigned, $testfld[0]);
                }       }       }

sub average {
        #saves the array passed to this function
        my @array = @_;
        #creates a variable to hold the sum of the array's values
        my $sum;
        #adds each element of the array to the sum
```

```
    foreach (@array) { $sum += $_ }
    #divides sum by the number of elements in the array to find the mean
    return ($sum/@array); }
```

The output is a PDB file with approximately optimized positions of all CA hexamer centers in a tube segment

A1.5. create_new_backbone.pl

This program creates a PDB file with the positions of CA hexamers along the tube that are calculated from the overlapping regions of high-abundance CA points

```
# USE: ./create_new_backbone.pl [input PDB file with the positions of the CA hexamers] [number of segments]

# STEP 1: Calculate principal axis and orient along the principal axis
$pdb = $ARGV[0]; chomp $pdb;
print "PDB $pdb\n";
@pdb_head = split (/\./,$pdb);
$newback = "$pdb_head[0]"."_backbone.pdb";
$no_of_segments = $ARGV[1]; chomp $no_of_segments;
print "n $no_of_segments\n";
open (PDB, "$pdb"); @pdb = <PDB>; close (PDB);
# counts number of atoms
count_atoms(@pdb);
# extracts xyz and places them in three arrays, one each for x, y, and z
put_coordinates_in_arrays(@pdb);
# calculates slope and angle
($slope,$angle) = linear_regression($#x_list+1,$sumx,$sumy);
print "angle $angle radians\n";
rotate($pdb,$angle);

# STEP 2: Split into n segments
$pdb = "$rotate_outfile";
open (PDB, "$pdb"); @pdb = <PDB>; close (PDB);
# counts number of atoms
count_atoms(@pdb);
# extracts xyz and places them in three arrays, one each for x, y, and z
```

```
($minx,$maxx) = put_coordinates_in_arrays(@pdb);
split_into_segments($no_of_segments);

# STEP 3: Calculate center coordinates of each segment
print "Segment centers of mass (transformed/back-transformed)\n";
open (OUT, ">$newback");
$counter;
foreach $line (@segfiles) {
        $counter++;
        @fld = split (" ", $line);
        $pdb = $fld[0];
        @pdb_head = split (/\./,$pdb);
        print "$counter ";
        open (PDB, "$pdb"); @pdb = <PDB>; close (PDB);
        count_atoms(@pdb);
         # extracts xyz and places them in three arrays, one each for x, y, and z
        make_backbone_coordinates(@pdb);
}
close (OUT);

sub count_atoms {
        $count = 0;
        foreach $line (@_) {
                $header = substr($line,0,6);
                if (($header eq "HETATM") or ($header eq "ATOM")) { $count++ }
        }
}

sub put_coordinates_in_arrays {
        @x_list = @y_list = @z_list = ();
        foreach $line (@_) {
                $header = substr($line,0,6);
                if (($header eq "HETATM") or ($header eq "ATOM")) {
                        $x = substr($line,30,8);
                        $y = substr($line,38,8);
                        $z = substr($line,46,8);
```

```
                        push(@x_list,$x);
                        push(@y_list,$y);
                        push(@z_list,$z);
                }
        }
        open (OUTOUT, ">tempout.txt");
         foreach $try (@z_list) { print OUTOUT $try; print OUTOUT "\n"; }
        close (OUTOUT);
        ($avex, $sumx) = average(@x_list);
        ($avey, $sumy) = average(@y_list);
        ($avez, $sumz) = average(@z_list);
        return (min(@x_list), max(@x_list));
}

sub average {
        # save the array passed to this function
        my @array = @_;
        # create a variable to hold the sum of the array's values
        my $sum;
        # add each element of the array to the sum
        foreach (@array) { $sum += $_ }
        # divide sum by the number of elements in the array to find the mean
        return ($sum/@array, $sum);
}

sub linear_regression {
        my $slope;
        my $angle;
        $numinputs = $_[0];
        $sumx = $_[1];
        $sumy = $_[2];
        ($sumxy, $sumxsq) = sumxysq();
        $slope = ( $numinputs * $sumxy - $sumx * $sumy )/ ( $numinputs * $sumxsq - $sumx ** 2 );
        $angle = atan($slope);
        return ($slope, $angle);
}
```

```
sub sumxysq {
	my $sumxy;
	my $sumxsq;
	foreach $i (0..$#x_list) {
		$sumxy += $x_list[$i] * $y_list[$i];
		$sumxsq += $x_list[$i] ** 2;
	}
	return ($sumxy, $sumxsq);
}
sub rotate {
	$file = "$_[0]";
	$angle = -$_[1];
	@matrix1 = ([ cos($angle), -sin($angle), 0 ], [ sin($angle), cos($angle), 0 ], [ 0, 0, 1 ] );
	open (FILE, "$file"); @file = <FILE>; close (FILE);
	$rotate_outfile = "temp/rotated.pdb";
	$rotated = $rotate_outfile;
	open (OUT, ">$rotate_outfile");
	$atomcounter = 1;
	foreach $line (@file) {
		$header = substr($line,0,6);
		if (($header eq "HETATM") or ($header eq "ATOM")) {
		$resnum = substr($line,22,5);
		@coords = (substr($line,30,8),substr($line,38,8),substr($line,46,8));
		$newx = $matrix1[0][0]*$coords[0] + $matrix1[0][1]*$coords[1] + $matrix1[0][2]*$coords[2];
		$newy = $matrix1[1][0]*$coords[0] + $matrix1[1][1]*$coords[1] + $matrix1[1][2]*$coords[2];
		$newz = $matrix1[2][0]*$coords[0] + $matrix1[2][1]*$coords[1] + $matrix1[2][2]*$coords[2];
		@newcoords = ($newx, $newy, $newz);
		printf OUT "HETATM%5s CD  CD  C%5s  %8.3f%8.3f%8.3f  1.00 20.00
Cd\n",$atomcounter,$resnum,$newx,$newy,$newz;
		$atomcounter++;
		}
	}
	close (OUT);
	print "Transformation matrix\n";
	printf "%9.6f %9.6f %9.6f\n",$matrix1[0][0],$matrix1[1][0],$matrix1[2][0];
	printf "%9.6f %9.6f %9.6f\n",$matrix1[0][1],$matrix1[1][1],$matrix1[2][1];
```

```
	printf "%9.6f %9.6f %9.6f\n",$matrix1[0][2],$matrix1[1][2],$matrix1[2][2];
	@matrix1back = ([ cos(-$angle), -sin(-$angle), 0 ], [ sin(-$angle), cos(-$angle), 0 ], [ 0, 0, 1 ] );
	print "Back-transformation matrix\n";
	printf "%9.6f %9.6f %9.6f\n",$matrix1back[0][0],$matrix1back[1][0],$matrix1back[2][0];
	printf "%9.6f %9.6f %9.6f\n",$matrix1back[0][1],$matrix1back[1][1],$matrix1back[2][1];
	printf "%9.6f %9.6f %9.6f\n",$matrix1back[0][2],$matrix1back[1][2],$matrix1back[2][2];
	$matback = "$rotate_outfile".".matrixback";
}

sub flatten {
	$file = "$_[0]";
	$axis = "$_[1]";
	$n = $_[2];
	$outfile = "$pdb_head[0]"."_flattened_onx.pdb";
	open (FILE, "$file"); @file = <FILE>; close (FILE);
	open (OUT, ">$outfile");
	foreach $line (@file) {
		$header = substr($line,0,6);
		if (($header eq "HETATM") or ($header eq "ATOM")) {
			if ($axis eq "x") { printf OUT "%30s%8.3f%40s\n",substr($line,0,30),$n,substr($line,38,40) }
			if ($axis eq "y") { printf OUT "%38s%8.3f%32s\n",substr($line,0,38),$n,substr($line,46,32) }
		if ($axis eq "z") { printf OUT "%46s%8.3f%24s\n",substr($line,0,46),$n,substr($line,54,24) }
	}
   }
   close (OUT);
   print " output file: $outfile\n";
}

sub split_into_segments {
	print "Segment x ranges\n";
	@segfiles;
	$no_of_segments = $_[0];
	$seg_length = ($maxx-$minx)/$no_of_segments;
	foreach $seg (1..$no_of_segments) {
		printf "$seg %8.3f %8.3f\n",$minx+($seg-1)*$seg_length,$minx+$seg*$seg_length;
```

```
		my $count;
		foreach $x (@x_list) {
			if (($x >= $minx+($seg-1)*$seg_length) and ($x <= $minx+$seg*$seg_length)) {
				push (@newx_list, $x);
				$count++;
			}
		}
	}
	foreach $seg (1..$no_of_segments) {
		$segfile = "temp/"."$pdb_head[0]"."_seg"."$seg".".pdb";
		open (OUT, ">$segfile");
		foreach $line (@pdb) {
			$x = substr($line,30,8);
			if (($x >= $minx+($seg-1)*$seg_length) and ($x <= $minx+$seg*$seg_length)) {
				print OUT $line;
			}
		}
		close (OUT);
		push (@segfiles, $segfile);
	}
	$seglist = "temp/"."$pdb_head[0]"."_seglist.txt";
	open (OUT, ">$seglist");
	foreach $segfile (@segfiles) { print OUT "$segfile\n" }
	close (OUT);
}

#creates coordinates of the backbone in a PDB format
sub make_backbone_coordinates {
	@x_list = @y_list = @z_list = ();
	foreach $line (@_) {
		$header = substr($line,0,6);
		if (($header eq "HETATM") or ($header eq "ATOM")) {
			$x = substr($line,30,8);
			$y = substr($line,38,8);
			$z = substr($line,46,8);
			push(@x_list,$x);
```

```
                push(@y_list,$y);
                push(@z_list,$z);
            }
        }
        ($avex, $sumx) = average(@x_list);
        ($avey, $sumy) = average(@y_list);
        ($avez, $sumz) = average(@z_list);
        @coords = ($avex,$avey,$avez);
        $newx = $matrix1back[0][0]*$coords[0] + $matrix1back[0][1]*$coords[1] + $matrix1back[0][2]*$coords[2];
        $newy = $matrix1back[1][0]*$coords[0] + $matrix1back[1][1]*$coords[1] + $matrix1back[1][2]*$coords[2];
        $newz = $matrix1back[2][0]*$coords[0] + $matrix1back[2][1]*$coords[1] + $matrix1back[2][2]*$coords[2];
        printf "%8.3f %8.3f %8.3f %8.3f %8.3f %8.3f\n",$avex,$avey,$avez,$newx,$newy,$newz;
        printf OUT "HETATM%5s CD CD C%4s %8.3f%8.3f%8.3f 1.00 0.00 Cd\n",$counter,$counter,$newx,$newy,$newz;
}
```

The output is a PDB file with positions of the backbone running through the center of a CA tube

A1.6. print_tags_from_table.pl

This program creates a PDB file with the positions of CA hexamers along the tube that are calculated from the overlapping regions of high-abundance CA points

```
#USE: ./print_tags_from_table.pl [table with tags] [PDB file with desired TAGS] [ca/trim]

# TABLE with tags
$tbl_all = $ARGV[0];
chomp $tbl_all;
# PDB file containing tags for CA and matching TRIM
$tbl_tags = $ARGV[1];
chomp $tbl_tags;
#determines if the tags in the PDB files are trim or CA
$what = $ARGV[2]; chomp $what;
open (TBL, "$tbl_all"); @tbl_all = <TBL>; close (TBL);
open (TBL2, "$tbl_tags"); @tbl_tags = <TBL2>; close (TBL2);
```

```
$out = "$tbl_tags"."."."$what"."tbl";
open (OUT, ">$out");

#reads each line of the PDB file, searches for the desired tags and prints those lines in a new file
foreach my $line_tags (@tbl_tags) {
        if ($what eq "ca") { $tag = substr($line_tags,6,5) }
        elsif ($what eq "trim") { $tag = substr($line_tags,22,4) }
        print "Looking for $tag ... ";
  foreach $line_all (@tbl_all) {
                        @fld2 = split (" ", $line_all);
                        $testtag = $fld2[0];
                        if ($tag == $testtag) {
        print OUT $line_all;
        print "found it!\n";
        last;
       }
  }
}
close (OUT);
```

The output is a table file than includes only the entries specified by the PDB file

A1.7. place_all_SPRYs_on_plane.pl

This program creates a PDB file with the positions of SPRY centers and writes them on a single plane

*USE: ./ place_all_SPRYs_on_plane.pl*

```
#reads all PDB files in the folder that describe dimer-closest CA pairs
my $x;
my $y;
my $z;
my $dirname = '.';
open (my $outfile, '>', 'out.txt');
opendir(DIR, $dirname) or die "Could not open $dirname\n";
my @files = grep ( -f ,<*.pdb>);
```

```
#creates first half of a final PDB file with a CA tag and a corresponding dimer tag
  foreach my $file (@files) {
 ( my $vol, my $volnumber, my $dim, my $dimnumber, my $ca, my $canumber) = split (/(\d+)/, $file);
  $volnumber = sprintf("%04d", $volnumber);
  $dimnumber = sprintf("%04d", $dimnumber);
  $canumber = sprintf("%05d", $canumber);
  printf $outfile "ATOM  $canumber  CA  ALA A%4.0f    \n",$dimnumber;
 }
close ($outfile);
closedir(DIR);


#reads x,y,z coordinates from the PDBs and created the second half of a final PDB file
open (my $outfile2, '>', 'out2.txt');
opendir(DIR, $dirname) or die "Could not open $dirname\n";
my @docs = grep(/\.pdb$/,readdir(DIR));
foreach my $line (@docs){
open (RES, $line ) or die "Can't open @docs: $!";
            while ( <RES> ) {
       if ( $_ =~ /HETATM/ ) {
                        my $x = substr($line,30,8);
                        my $y = substr($line,38,8);
                        #arbitrary plane
                        my $z = 40;
       printf $outfile2 "$x$y  %5.3f  1.00 20.00           C  \n",$z;
       }
            }
}
close ($outfile2);
closedir(DIR);

#merge created files
open(IN1, "<", "out.txt");
open(IN2, "<", "out2.txt");
my @file1_lines;
```

```
my @file2_lines;
while (<IN1>) {
   push (@file1_lines, $_);
}
close IN1;
while (<IN2>) {
   push (@file2_lines, $_);
}
close IN2;
my $file1_items = @file1_lines;
my $file2_items = @file2_lines;
open(OUT, ">", "final.txt");
my $i = 0;
while (($i < $file1_items) || ($i < $file2_items)) {
   if (defined($file1_lines[$i])) {
      print OUT $file1_lines[$i];
   }
   if (defined($file2_lines[$i])) {
      print OUT $file2_lines[$i];
   }
   $i++
}
close OUT;

#combines two lines from final.txt into a single line to create a properly formated PDB file
open my $fh, "<", "final.txt";
open(OUT, ">", "final1.pdb");
while (<$fh>) {
  if ($. %2){ chomp } else { s/^// }
  print OUT;
}
close OUT;
```

The output is a single PDB file that has positions of all SPRY domain dimer centers saved in respect to a single CA hexamer

A1.8. calculate_radius_zone1.pl

This program creates a PDB file with the positions of SPRY domain dimer centers that belong to a zone of defined parameters. The input is a file with all SPRY centers save on a single plane.

```
#USE: ./calculate_radius.pl [the PDB file with SPRY centers] [radius of the zone]


my $tbl = $ARGV[0]; chomp $tbl;
my $cutoff = $ARGV[1];
open (TBL, "$tbl"); my @tbl = <TBL>; close (TBL);

#calculations for zone 1, coordinates of the zone center were determined in UCSF Chimera
my $x0 = 32.00;
my $y0 = 32.00;
my $z0 = 40.00;
open my $in,  "<", $tbl    or die ;
open(my $out, ">", "less_then_$cutoff.pdb");
my $counter = 0;
foreach my $line (<$in>) {
        my @fld = split (" ", $line);
        my $x = substr($line,30,8);
        my $y = substr($line,38,8);
        my $z = substr($line,46,5);
print "$x, $y, $z\n";
                my $r = sqrt(($x0-$x)*($x0-$x)+($y0-$y)*($y0-$y));
                        print "$r\n";
                        if ($r <= $cutoff){
                        print $out "$line";
                        print $out "TER\n";
                        $counter++;
                        }
                }
print $out "There are $counter SPRY dimers in $cutoff distance";
close (OUT);

#calculations for zone 2, coordinates of the zone center were determined in UCSF Chimera
my $tbl = $ARGV[0]; chomp $tbl;
```

```
my $cutoff = $ARGV[1];
my $cutoff2 = $ARGV[2];
open (TBL, "$tbl"); my @tbl = <TBL>; close (TBL);
my $x0 = 32.00;
my $y0 = 32.00;
my $z0 = 40.00;
open my $in,  "<", $tbl    or die ;
open(my $out, ">", "zone2_less_then_$cutoff.pdb");
my $counter = 0;
foreach my $line (<$in>) {
        my @fld = split (" ", $line);
        my $x = substr($line,30,8);
        my $y = substr($line,38,8);
        my $z = substr($line,46,5);
print "$x, $y, $z\n";
                my $r = sqrt(($x0-$x)*($x0-$x)+($y0-$y)*($y0-$y));
                        print "$r\n";
                        if ($r <= $cutoff and $r >= $cutoff2){
                        print $out "$line";
                        print $out "TER\n";
                        $counter++;
                        }
        }
print $out "There are $counter SPRY dimers in $cutoff distance";
close (OUT);

#calculations for zone 3, coordinates of the centers were determined in UCSF Chimera
my $x1 = 24.50;
my $y1 = 30.25;
my $x2 = 26.25;
my $y2 = 38.00;
my $x3 = 34.00;
my $y3 = 40.25;
my $x4 = 39.75;
my $y4 = 34.25;
my $x5 = 37.50;
```

```
my $y5 = 26.00;
my $x6 = 30.00;
my $y6 = 24.00;
open my $in,  "<", $tbl    or die ;
open(my $out, ">", "zone3_less_then_$cutoff.pdb");
my $counter = 0;
foreach my $line (<$in>) {
        my @fld = split (" ", $line);
        my $x = substr($line,30,8);
        my $y = substr($line,38,8);
        my $z = substr($line,46,5);
print "$x, $y, $z\n";
#calculates the distances of the SPRY centers from the center of the zones
                my $r1 = sqrt(($x1-$x)*($x1-$x)+($y1-$y)*($y1-$y));
                        my $r2 = sqrt(($x2-$x)*($x2-$x)+($y2-$y)*($y2-$y));
                        my $r3 = sqrt(($x3-$x)*($x3-$x)+($y3-$y)*($y3-$y));
                        my $r4 = sqrt(($x4-$x)*($x4-$x)+($y4-$y)*($y4-$y));
                        my $r5 = sqrt(($x5-$x)*($x5-$x)+($y5-$y)*($y5-$y));
                        my $r6 = sqrt(($x6-$x)*($x6-$x)+($y6-$y)*($y6-$y));
                        print "$r1, $r2, $r3, $r4, $r5, $r6 \n";
                        if ($r1 <= $cutoff) {
                        print $out "$line";
                        print $out "TER\n";
                        $counter++;
                        }
                        elsif ($r2 <= $cutoff) {
                        print $out "$line";
                        print $out "TER\n";
                        $counter++;
                        }
                        elsif ($r3 <= $cutoff) {
                        print $out "$line";
                        print $out "TER\n";
                        $counter++;
                        }
                        elsif ($r4 <= $cutoff) {
```

```
                print $out "$line";
                print $out "TER\n";
                $counter++;
                }
                elsif ($r5 <= $cutoff) {
                print $out "$line";
                print $out "TER\n";
                $counter++;
                }
                elsif ($r6 <= $cutoff){
                print $out "$line";
                print $out "TER\n";
                $counter++;
                }
}
print $out "There are $counter SPRY dimers in $cutoff distance";
close (OUT);
```

The output is a PDB file that has positions of all SPRY centers that belong to the same zone based on a desired radius

A1.9. get_cc_from_table.pl

This program reads the cross-correlation values from the final table created by the dynamo, sorts them, and assigns colors from RBG system

```
#USE: ./get_cc_from_tbl.pl [table file from a dynamo] [chimera command script]

$tbl = $ARGV[0]; chomp $tbl;
$cutoff = $ARGV[1]; chomp $cutoff;
open (TBL, "$tbl"); @tbl = <TBL>; close (TBL);
foreach $tblline (@tbl) {
        @fld = split (" ", $tblline);
        # array of particle tags
        push @particles, $fld[0];
        # array of cc values
```

```
	push @correlations, $fld[9];
}
$number = @particles;
$min = min @correlations;
$max = max @correlations;
print "Total number of particles = $number\n";
print "Minimum correlation = $min\n";
print "Maximum correlation = $max\n";

foreach $count (1..$number) {
	print "$particles[$count-1] ";
	$adjusted = 0.5*(($correlations[$count-1]-$min)/($max - $min));
	$h = $adjusted*240; $s = 1; $l = 0.5;
	print "$correlations[$count-1] $adjusted $h ";
	convert_to_rgb();
	push @rs, $r; push @gs, $g; push @bs, $b;
}

open (OUT, ">color.cmd");
foreach $count (1..$number) {
	$count = $count - 1;
	$adjusted = 0.5*(($correlations[$count]-$min)/($max - $min));
	print OUT "color $rs[$count],$gs[$count],$bs[$count] #$count\n";
	if ($correlations[$count] < $cutoff) { print OUT "close #$count\n" }
}
exclude();
close (OUT);
sub exclude {
	foreach $this (@exclude) {
		print OUT "close #";
		print OUT "$this\n";
	}
}

#converts the cross-correlation values into color from RGB palet from red to green (low-high)
sub convert_to_rgb {
```

```
$temporary1 = $l*(1+$s);
$temporary2 = 2*$l - $temporary1;
$h = $h/360;
$temporary_r = $h + 0.333;
if ($temporary_r > 1) { $temporary_r = $temporary_r - 1 }
elsif ($temporary_r < 0) { $temporary_r = $temporary_r + 1 }
$temporary_g = $h;
$temporary_b = $h - 0.333;
if ($temporary_b > 1) { $temporary_b = $temporary_b - 1 }
elsif ($temporary_b < 0) { $temporary_b = $temporary_b + 1 }
$test = $temporary_r; get_color(); $r = $colorvalue; print "$r ";
$test = $temporary_g; get_color(); $g = $colorvalue; print "$g ";
$test = $temporary_b; get_color(); $b = $colorvalue; print "$b ";
print "\n";
}

sub get_color {
$gotit = "no";
$test1 = 6*$test;
if (($test1 <= 1)&&($gotit = "no")) { $gotit = "yes"; $colorvalue = $temporary2 + ($temporary1 +
$temporary2)*6*$test; return }
$test2 = 2*$test;
if (($test2 <= 1)&&($gotit = "no")) { $gotit = "yes"; $colorvalue = $temporary1; return }
$test3 = 3*$test;
if (($test3 <= 2)&&($gotit = "no")) { $gotit = "yes"; $colorvalue = $temporary2 + ($temporary1 -
$temporary2)*(0.666 - $test)*6; return }
if ($gotit eq "no") { $gotit = "yes"; $colorvalue = $temporary2 }
}
```

The output is a USCF Chimera command file that colors the particles from red to green based on their cross-correlation values from lowest to highest

# Appendix 2.

# Mechanism of B-box 2 domain-mediated higher-order assembly of the retroviral restriction factor TRIM5α

Jonathan M. Wagner, Marcin D. Roganowicz, Katarzyna Skorupka, Steven L. Alam, Devin Christensen, Ginna Doss, Yueping Wan, Gabriel A. Frank, Barbie K Ganser-Pornillos, Wesley I. Sundquist, Owen Pornillos

*eLife*, 5(JUNE2016). doi: 10.7554/eLife.16309

eLIFE elifesciences.org

RESEARCH ARTICLE

# Mechanism of B-box 2 domain-mediated higher-order assembly of the retroviral restriction factor TRIM5α

**Jonathan M Wagner[1], Marcin D Roganowicz[1], Katarzyna Skorupka[1], Steven L Alam[2], Devin Christensen[2], Ginna Doss[1], Yueping Wan[1], Gabriel A Frank[3,4], Barbie K Ganser-Pornillos[1], Wesley I Sundquist[2], Owen Pornillos[1]***

[1]Department of Molecular Physiology and Biological Physics, University of Virginia, Charlottesville, United States; [2]Department of Biochemistry, University of Utah, Salt Lake City, United States; [3]The National Institute for Biotechnology in the Negev, Ben-Gurion University of the Negev, Beer-Sheeva, Israel; [4]Department of Life Sciences, Ben-Gurion University of the Negev, Beer-Sheeva, Israel

**Abstract** Restriction factors and pattern recognition receptors are important components of intrinsic cellular defenses against viral infection. Mammalian TRIM5α proteins are restriction factors and receptors that target the capsid cores of retroviruses and activate ubiquitin-dependent antiviral responses upon capsid recognition. Here, we report crystallographic and functional studies of the TRIM5α B-box 2 domain, which mediates higher-order assembly of TRIM5 proteins. The B-box can form both dimers and trimers, and the trimers can link multiple TRIM5α proteins into a hexagonal net that matches the lattice arrangement of capsid subunits and enables avid capsid binding. Two modes of conformational flexibility allow TRIM5α to accommodate the variable curvature of retroviral capsids. B-box mediated interactions also modulate TRIM5α's E3 ubiquitin ligase activity, by stereochemically restricting how the N-terminal RING domain can dimerize. Overall, these studies define important molecular details of cellular recognition of retroviruses, and how recognition links to downstream processes to disable the virus.
DOI: 10.7554/eLife.16309.001

***For correspondence:** owp3a@eservices.virginia.edu

**Competing interest:** See page 23

**Funding:** See page 23

**Received:** 23 March 2016
**Accepted:** 20 May 2016
**Published:** 02 June 2016

**Reviewing editor:** Stephen P Goff, Howard Hughes Medical Institute, Columbia University, United States



## Introduction

TRIM5α is a restriction factor that intercepts the incoming capsids of diverse retroviruses, including HIV-1, and inhibits viral replication. The mechanism of restriction is not yet fully understood, but is primarily associated with premature termination of reverse transcription and accelerated dissociation of the viral core (***Sayah et al., 2004***; ***Stremlau et al., 2004***; ***2006***). TRIM5α is also proposed to be a pattern recognition receptor for retroviral capsids, in that it initiates a signaling cascade to induce type I interferon upon capsid binding (***Pertel et al., 2011***). Ubiquitin (Ub) is implicated in both the antiviral (restriction) and signaling activities of TRIM5α. In particular, TRIM5α's E3 ligase activity creates K63-linked polyUb chains. Although the functional target or targets of ubiquitination have not been established definitively, TRIM5α self-ligation correlates with the block in reverse transcription (***Campbell et al., 2015***; ***Fletcher et al., 2015***; ***Roa et al., 2012***), whereas unanchored chains have been proposed to mediate interferon signaling (***Pertel et al., 2011***).

Like all TRIM proteins, TRIM5α consists of an N-terminal tripartite or RBCC motif (RING, B-box 2, and coiled-coil domains), followed by a C-terminal domain (***Figure 1A***) (***Meroni and Diez-Roux, 2005***). The B-box 2 and coiled-coil domains make an integrated antiparallel dimer fold (***Goldstone et al., 2014***; ***Sanchez et al., 2014***; ***Weinert et al., 2015***), which acts as a scaffold that

**eLife digest** After infecting a cell, a virus reprograms the cell to produce new copies of the virus, which then spread to other cells. However, cells have evolved ways to fight back against this infection. For example, many mammalian cells contain proteins called restriction factors that prevent the virus from multiplying. The TRIM5 proteins form one common set of restriction factors that act against a class of viruses called retroviruses.

HIV-1 and related retroviruses have a protein shell known as a capsid that surrounds the genetic material of the virus. The capsid contains several hundred repeating units, each of which consists of a hexagonal ring of six capsid proteins. Although this basic pattern is maintained across different retroviruses, the overall shape of the capsids can vary considerably. For instance, HIV-1 capsids are shaped like a cone, but other retroviruses can form cylinders or spheres.

Soon after a retrovirus enters a mammalian cell, TRIM5 proteins bind to the capsid. This causes the capsid to be destroyed, which prevents replication of the virus. Previous research has shown that many TRIM5 proteins must link up with each other via a region of their structure called the 'B-box 2' domain in order to efficiently recognize capsids. How this assembly process occurs, and why it enables the TRIM5 proteins to recognize different capsids was not fully understood. Now, Wagner et al. (and independently Li, Chandrasekaran et al.) have investigated these questions.

Wagner et al. engineered short versions of a type of TRIM5 protein called TRIM5α and used a technique called X-ray crystallography to determine the structure of its B-box domain. This revealed that the B-box present in one molecule of TRIM5α can associate with the B-boxes on two other TRIM5α molecules. By working in groups of three (or trimers), the B-box domains connect several TRIM5α proteins to form a hexagonal net. The TRIM5α net matches the arrangement of the capsid proteins in the shell of the virus, which enables TRIM5α to bind strongly to HIV-1 capsids.

Wagner et al. also found that B-box trimers are flexible, which allows the TRIM5α net to adapt to the shape of the HIV-1 capsid and wrap around regions where it curves. In addition, computer modelling suggested that the B-box trimer may also enable TRIM5α to carry out the next steps in the process of disabling the virus. Further work is now needed to understand in more detail how the trimers have this effect.

DOI: 10.7554/eLife.16309.002

organizes the upstream and downstream domains (***Figure 1B***). In TRIM5α, the C-terminal domain is a β-sandwich fold called SPRY (or PRYSPRY/B30.2), which mediates direct binding to retroviral capsids (***Biris et al., 2012***; ***2013***; ***Diaz-Griffero et al., 2006b***; ***Kovalskyy and Ivanov, 2014***; ***Sawyer et al., 2005***; ***Sayah et al., 2004***; ***Sebastian and Luban, 2005***; ***Stremlau et al., 2006***; ***Yang et al., 2012***). The L2 linker that connects the SPRY domain to the coiled-coil packs against the coiled-coil scaffold, and so in the TRIM5α dimer, two SPRY domains are oriented to bind the capsid simultaneously (***Figure 1B***) (***Goldstone et al., 2014***; ***Li et al., 2014***; ***Sanchez et al., 2014***; ***Weinert et al., 2015***). Capsid recognition by TRIM5α is an avidity-driven interaction; that is, productive binding only occurs in context of assembled capsid and assembled TRIM5α (***Sebastian and Luban, 2005***; ***Stremlau et al., 2006***). Higher-order assembly of TRIM5α requires the B-box 2 domain, which is thought to mediate three-fold symmetric interactions that connect coiled-coil mediated TRIM5α dimers into a hexagonal net (***Diaz-Griffero et al., 2009***; ***Ganser-Pornillos et al., 2011***; ***Javanbakht et al., 2005***; ***Li and Sodroski, 2008***; ***Li et al., 2016***). This hexagonal scaffold is proposed to position the SPRY domains to match the orientations – both translational and rotational – of their corresponding binding epitopes on retroviral capsids, and thereby generate powerful avidity effects that amplify very weak (millimolar level (***Biris et al., 2013***)) intrinsic affinities between the SPRY and capsid subunits.

Higher-order TRIM5α assembly is also reported to promote the E3 ligase activity of the upstream RING domain (***Pertel et al., 2011***; ***Yudina et al., 2015***), which is connected to the B-box 2 domain by the L1 linker (***Figure 1A and B***). A segment of the L1 linker forms a 4-helix bundle that mediates dimerization of the RING domain, which is required for productive interactions with Ub-conjugated E2 enzymes and formation of the catalytically active Ub ligation complex (***Yudina et al., 2015***). Although the B-box 2 domain does not appear to have a direct role in catalysis, B-box/B-box

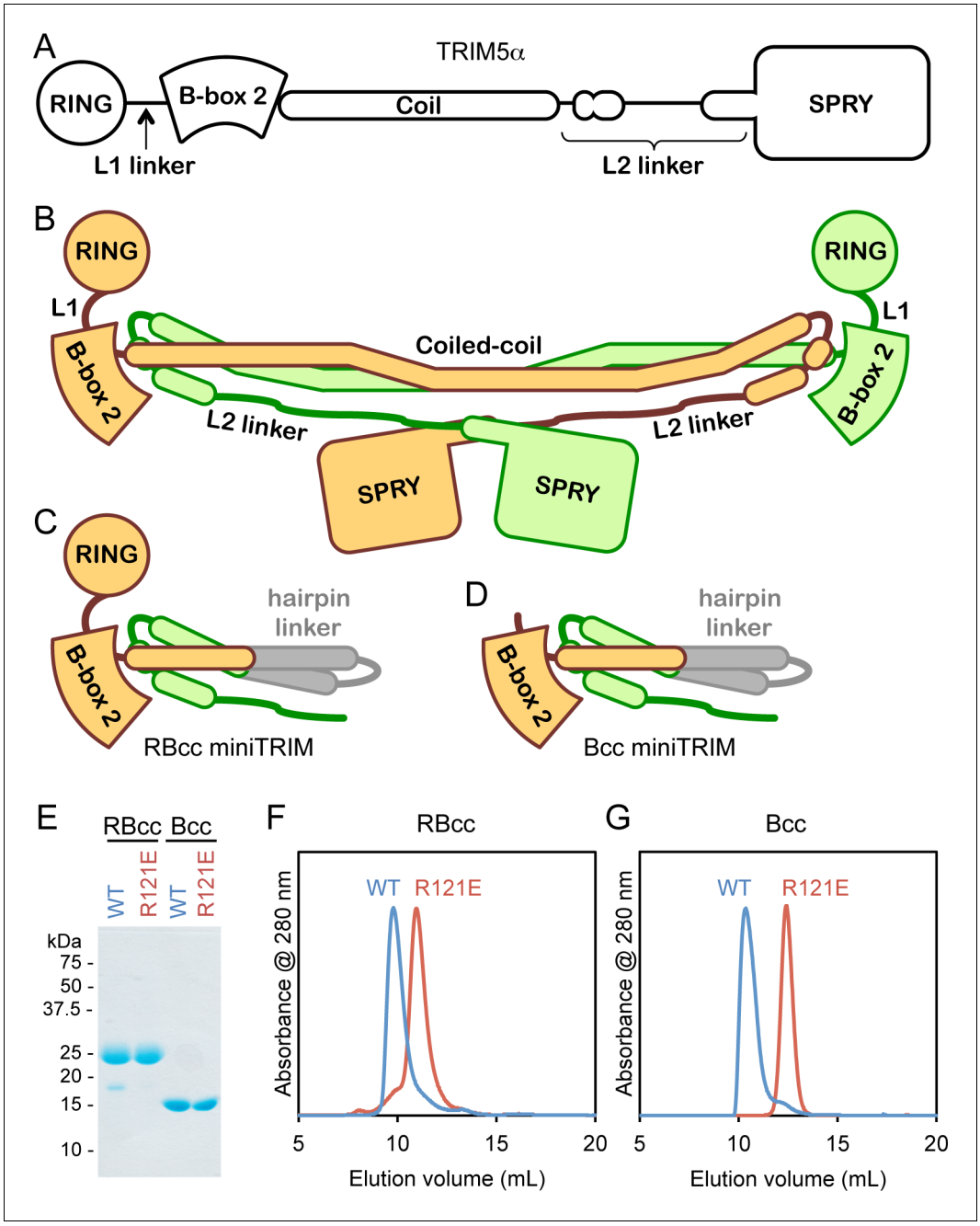


**Figure 1.** Design and oligomeric behavior of miniTRIM proteins. (**A**) Schematic of the TRIM5α primary sequence. (**B**) Schematic of the antiparallel full-length dimer. (**C–D**) Schematic of the (**C**) RBcc miniTRIM and (**D**) Bcc miniTRIM. (**E**) SDS-PAGE profiles of purified miniTRIMs. (**F–G**) Size exclusion elution profiles of (**F**) RBcc and (**G**) Bcc miniTRIMs. Wildtype (WT) constructs eluted early (blue traces), whereas R121E mutants eluted late (red traces).
DOI: 10.7554/eLife.16309.003
The following figure supplement is available for figure 1:

**Figure supplement 1.** Primary sequence of the miniTRIMs.
DOI: 10.7554/eLife.16309.004

interactions are expected to cluster their associated RING domains and promote RING dimerization. In context of the TRIM hexagonal lattice, the apparent juxtaposition of three-way head-to-head interactions between the B-boxes and two-way interactions between the catalytic RING domains is suggested to facilitate TRIM5α self-ubiquitination (***Yudina et al., 2015***).

The structural basis by which the B-box 2 domain promotes higher-order assembly of TRIM5α dimers has been challenging to decipher, largely because the bivalent nature of the TRIM5α dimer and the flexible architectures of both the TRIM dimer and hexagonal lattice have impeded crystallographic characterization. Analysis of the isolated B-box 2 domain has been likewise problematic, because separating the B-box from the coiled-coil exposes a 'backside' hydrophobic surface that makes it prone to aggregation. We therefore engineered artificial constructs – which we call miniTRIMs – that retain the integrated B-box/coiled-coil fold of the full-length dimer but are more amenable to biochemical and structural analyses. These novel reagents allowed us to define the molecular details of how the B-box 2 domain facilitates higher-order assembly of TRIM5α, and how pattern recognition of retroviral capsids is coupled to ubiquitin-dependent downstream processes.

# Results

## Design and initial characterization of miniTRIMs

Our miniTRIM constructs were designed to be monovalent with respect to the RING and B-box 2 domains (to uncouple interactions mediated by these domains from the coiled-coil dimer), and yet preserve the native, quaternary B-box/coiled-coil interface (to prevent exposure of the backside hydrophobic B-box surface and non-specific aggregation). The 'RBcc' miniTRIM contained residues 1–159 from rhesus TRIM5α (which includes the RING, B-box 2, and the first 26 residues of the coiled-coil) (***Figure 1C*** and ***Figure 1—figure supplement 1***, colored in orange), followed by an antiparallel coiled-coil hairpin derived from a bacterial seryl-tRNA synthetase (residues 49–78 of PDB 1SRY, gray), and then residues 225–265 of the TRIM5α coiled-coil (green). To further uncouple the B-box from potential dimeric interactions of the upstream RING domain, we also designed a second construct denoted 'Bcc' that lacks the RING (residues 1–88) (***Figure 1D***). Both the RBcc and Bcc miniTRIMs proved well behaved in solution, and could be purified to homogeneity (***Figure 1E***).

Higher-order assembly of full-length TRIM5α protein dimers requires interactions mediated by a surface patch on the B-box 2 domain that includes Arg121 (rhesus TRIM5α numbering). Biochemical and cell-based assays show that R121A and R121E mutants are deficient in capsid binding and restriction activities, and this correlates with defects in higher-order assembly (***Diaz-Griffero et al., 2009***; ***Ganser-Pornillos et al., 2011***; ***Li and Sodroski, 2008***). The same patch also mediates self-association of the isolated B-box 2 domain in solution (***Diaz-Griffero et al., 2009***). We therefore expected the miniTRIMs to exhibit Arg121-dependent oligomeric behavior, and we tested this by using size exclusion chromatography. Consistent with expectation, both the RBcc miniTRIM (***Figure 1F***) and Bcc miniTRIM (***Figure 1G***) eluted early from a Superdex 75 size exclusion column as asymmetric peaks with sharp leading edges and pronounced tails (blue traces). In contrast, miniTRIMs harboring the R121E mutation eluted late as more symmetrical peaks (***Figure 1F and G***, red traces), with elution volumes consistent with monomeric species. These results indicate that the protein-protein interactions required for higher-order assembly of full-length TRIM5α are also essential for miniTRIM oligomerization.

## Bcc miniTRIM recapitulates the B-box/coiled-coil head of TRIM5α

Despite the polydisperse nature of the miniTRIMs, we obtained numerous crystal hits. We obtained high quality synchrotron diffraction data from three crystal forms of Bcc miniTRIM. A $P2_12_12_1$ crystal contained two trimers in the asymmetric unit (3.26 Å resolution, $R/R_{free}$ = 0.26/0.30), a C2 form contained one dimer (2.1 Å, $R/R_{free}$ = 0.18/0.22), and a P1 form contained two dimers (2.3 Å, $R/R_{free}$ = 0.22/0.26) (***Table 1*** and ***Supplementary file 1A***). Altogether, these yielded 12 crystallographically independent views of Bcc miniTRIM. All 12 structures were very similar to each other (***Figure 2—figure supplement 1***), and a complete structure is shown in ***Figure 2A***. In general, electron densities for the B-box 2 domains and proximal regions of the coiled-coil domains were well defined (***Figure 2B***), whereas densities for the hairpin linker were of poorer quality or, in some cases, missing (***Figure 2C***). (Densities in ***Figure 2B and C*** are illustrated with a trimer subunit.) Thus, our structures are of high quality at the functionally relevant regions, even though the artificial linker displayed significant disorder in some cases and may not be optimally designed. Our 12 Bcc miniTRIM structures superimpose very well with the crystal structure of the TRIM5α B-box 2/coiled-coil dimer (PDB 4TN3) (***Goldstone et al., 2014***) (***Figure 2D–F*** and ***Supplementary file 1B***). This indicates that our

**Table 1.** Crystallographic statistics.

| | Dimer | Dimer | Trimer |
|---|---|---|---|
| *Diffraction Data* | | | |
| Beamline | APS 22ID | APS 22ID | APS 22ID |
| Wavelength (Å) | 1.0 | 1.0 | 1.0 |
| Processing program | HKL2000 | HKL2000 | HKL2000 |
| Space group | C2 | P1 | P212121 |
| Cell dimensions | *a* = 72.7 Å | *a* = 45.8 Å | *a* = 71.2 Å |
| | *b* = 41.5 Å | *b* = 52.3 Å | *b* = 71.5 Å |
| | *c* = 111.3 Å | *c* = 69.7 Å | *c* = 213.8 Å |
| | α = 90°, β = 110°, γ = 90° | α = 94.8°, β = 105.5°, γ = 103° | α = 90°, β = 90°, γ = 90° |
| Resolution range, Å | 50-1.90 (1.97-1.90) | 50-2.30 (2.38-2.30) | 50-3.25 (3.37-3.25) |
| $R_{sym}/R_{meas}$ /$R_{pim}$ | 0.18(0.43) /0.12(0.90) /0.06(0.50) | 0.07(0.16) /0.10(0.23) /0.07(0.16) | 0.08(1.0) /0.05(1.0) /0.08(1.0) |
| Mean I/σ<I> | 14.0 (1.2) | 9.4 (4.0) | 26.8 (1.6) |
| Completeness,% | 98.6 (90.4) | 93.9 (80.0) | 100 (100) |
| Average redundancy | 3.5 (2.7) | 1.9 (1.7) | 13.6 (9.4) |
| Wilson B-factor, $Å^2$ | 40.5 | 36.0 | 35.1 |
| *Refinement Statistics* | | | |
| Refinement program | PHENIX | PHENIX | PHENIX |
| Resolution range | 32.5-1.91 (1.98-1.91) | 35.05-2.29 (2.38-2.29) | 36.70-3.26 (3.37-3.26) |
| No. of unique reflections | 25,300 (2,301) | 25,156 (2,171) | 14,789 (181) |
| Reflections in free set | 1254 (117) | 1301 (113) | 1431 (30) |
| $R_{work}$ | 0.18 (0.30) | 0.22 (0.26) | 0.26 (0.30) |
| $R_{free}$ | 0.22 (0.31) | 0.26 (0.31) | 0.30 (0.39) |
| NCS copies | 2 | 4 | 6 |
| No. of nonhydrogen atoms | | | |
| protein and zinc | 2,240 | 4,349 | 5,052 |
| solvent | 112 | 52 | 0 |
| Average B-factor ($Å^2$) | | | |
| protein and zinc | 63 | 58.9 | 72.77 |
| solvent | 53 | 53.1 | |
| Coordinate deviations | | | |
| bond lengths, Å | 0.019 | 0.004 | 0.005 |
| bond angles,° | 1.644 | 0.724 | 0.375 |
| *Validation and Deposition* | | | |
| Ramachandran plot | | | |
| favored,% | 99 | 99 | 97.4 |
| outliers,% | 0 | 0 | 0 |

*Table 1 continued on next page*

*Table 1 continued*

| | Dimer | Dimer | Trimer |
|---|---|---|---|
| MolProbity clashscore | 3.73 | 2.00 | 2.31 |
| PDB ID | 5EIU | 5F7T | 5IEA |

Values in parenthesis are for the highest resolution shell.

DOI: 10.7554/eLife.16309.005

miniTRIM constructs are excellent structural surrogates for the B-box/coiled-coil core of the full RBCC motif.

## Structures of the Bcc miniTRIM trimer and dimer

The Bcc miniTRIM trimer is organized as a triskelion: three B-box 2 domains make a central three-fold symmetric vertex from which the coiled-coil domains emanate as spokes (***Figure 3A***). As expected, the trimerization interactions are principally mediated by the B-box domain, burying 578 Å$^2$ of the available surface area from each subunit. This result indicates that the three-fold vertexes of the TRIM5α hexagonal lattice are made by B-box trimers. The B-box packs against the N-terminal end of the coiled-coil helix through a hydrophobic interface (***Figure 3A***, asterisks), suggesting that trimer formation requires the presence of the coiled-coil. This observation is consistent with the idea that higher-order assembly into a hexagonal lattice is a function of the integrated tripartite motif of TRIM5α, and does not simply arise from combining otherwise independent self-association motifs.

Interestingly, the majority of Bcc miniTRIM crystals we obtained (including three other forms that we did not refine) were composed of dimers (***Figure 3G*** and ***Supplementary file 1A***). The dimer is quasi-equivalent to the trimer: the same sets of residues make the same interactions but with valence of two instead of three. The dimer buries a smaller surface area per subunit (450 Å$^2$) compared to the trimer.

Both the trimer and dimer are stabilized by three layers of interactions, with a hydrophobic layer sandwiched between two hydrophilic layers (***Figure 3B,H***). The top layers (closest to the N-termini of the B-boxes) make a ring of salt bridges mediated by Glu102 and Lys103 from each subunit (***Figure 3D,J***). The middle, hydrophobic layers center on Trp117 (***Figure 3E,K***). In both oligomers, these indole sidechains make a hydrophobic core surrounded by a collar of close packed leucine sidechains (Leu105, Leu106, Leu118, and Leu132). The third, bottom layers also consist of a ring of salt bridges, this time with Glu120 and Arg121 (***Figure 3F,L***). At the periphery of this layer, the sidechain hydroxyl of Thr30 donates a hydrogen bond to Glu120. Interactions between the layers consist of a hydrogen bond between Glu102 (top) and the indole amide of Trp117 (middle), and close packing between the Trp117 sidechain (middle) and the Arg121 sidechain guanidinium group (bottom) (***Figure 3C,I***). The Trp117 indoles in the trimer form a channel that would be expected to have a highly negatively charged hole at the center (***Figure 3E***), which is likely to be partially stabilized by the positively charged Arg121 sidechains.

Comparison of the trimer and dimer bonding interactions revealed that the two oligomers are distinguished primarily by intermolecular packing between the Trp117, Leu118, and Leu132 sidechains in the hydrophobic layer. In particular, Leu118 and Leu132, which are located at the outer edges of the binding surface, are in van der Waals contact in the trimer, but more separated in the dimer (***Figure 3—figure supplement 1***). Another distinction is that the first two turns of the coiled-coil helix are overwound and bent in the dimer form (***Figure 3—figure supplement 2***), which might indicate some structural communication between the interacting B-boxes and the coiled-coil domain.

The apparent propensity of the B-box 2 domain to dimerize in our crystals prompted us to more closely analyze the oligomerization behavior of the miniTRIMs in solution. In order to avoid possible contributions from proximity-induced RING/RING interactions, we focused on the Bcc miniTRIM construct. We first analyzed Bcc miniTRIM by using sedimentation equilibrium analytical ultracentrifugation (AUC) at three different loading concentrations and three rotor speeds, and the combined data set was fit globally. In control experiments, both the W117E and R121E Bcc miniTRIM mutants were monomeric, in agreement with the structures (not shown), whereas the wildtype (WT) Bcc distributions indicated self-association (***Figure 3—figure supplement 3***). Global fitting of the WT

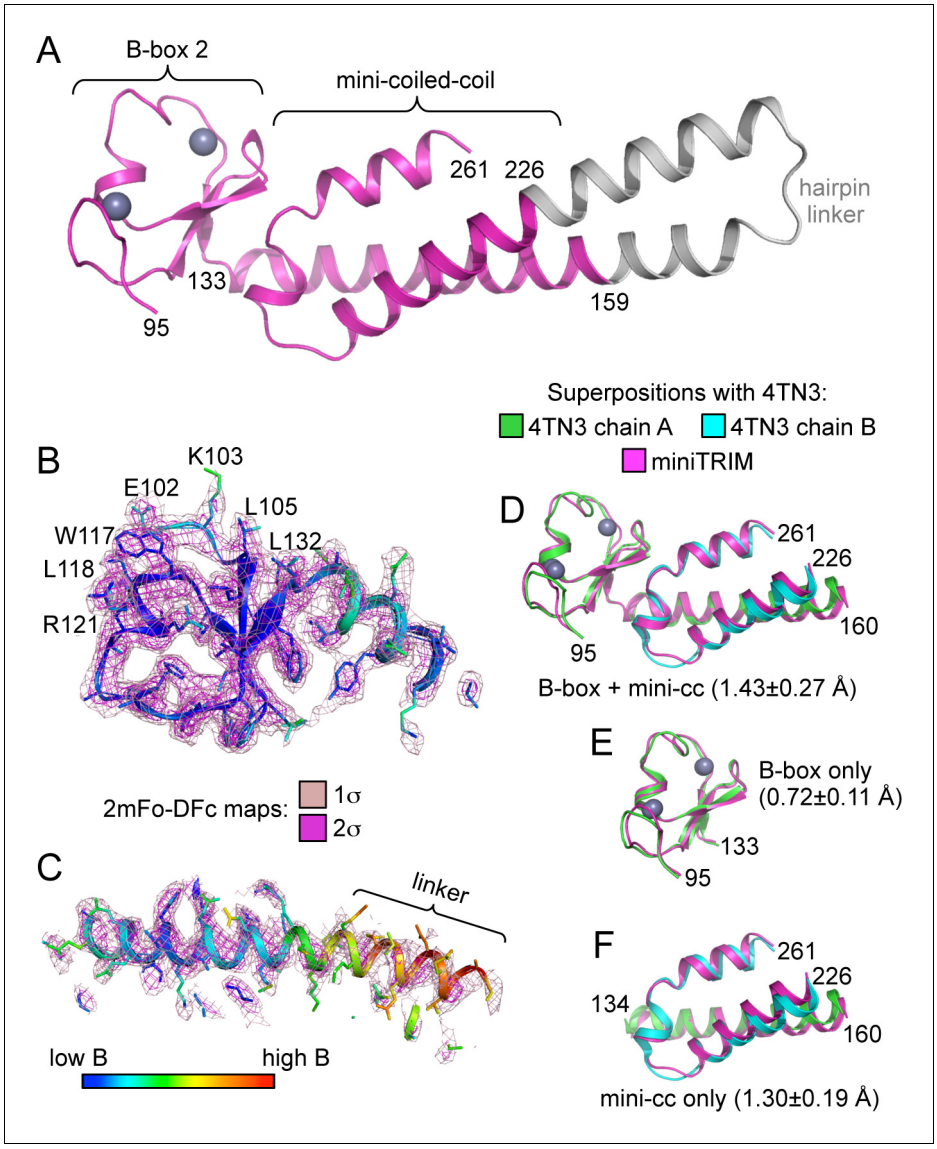


**Figure 2.** Structure of the Bcc miniTRIM. (**A**) Complete structure of the Bcc miniTRIM, from a dimer subunit. Residues derived from TRIM5α are colored in magenta, and the artificial hairpin linker is in gray. Charcoal gray spheres indicate zinc atoms. Residue numbers are indicated. (**B–C**) Electron density maps at two contour levels for (**B**) the B-box 2 domain and (**C**) the coiled-coil region of a trimeric Bcc subunit. The model is colored according to B-factor, which indicates that the B-box and proximal coiled-coil regions are well defined. B-box 2 sidechains within oligomerization interfaces are labeled to illustrate that these residues are well defined by the density. (**D–F**) Superposition of Bcc miniTRIM (magenta) with the corresponding B-box 2 and coiled-coil regions in the crystal structure of the rhesus TRIM5α B-box/coiled-coil fragment (PDB 4TN3) (***Goldstone et al., 2014***): (**D**) B-box and coiled-coil regions, (**E**) B-box alone, (**F**) coiled-coil alone. Residue ranges used in the superposition are indicated, as are the average mean square deviations ± s.d. from pair-wise superpositions of each of the 12 monomer structures. Deviations from each individual superposition are in ***Supplementary file 1B***.

DOI: 10.7554/eLife.16309.006

The following figure supplement is available for figure 2:

**Figure supplement 1.** Ribbon representations of the 12 crystallographically independent Bcc miniTRIM structures solved in this study.

DOI: 10.7554/eLife.16309.007

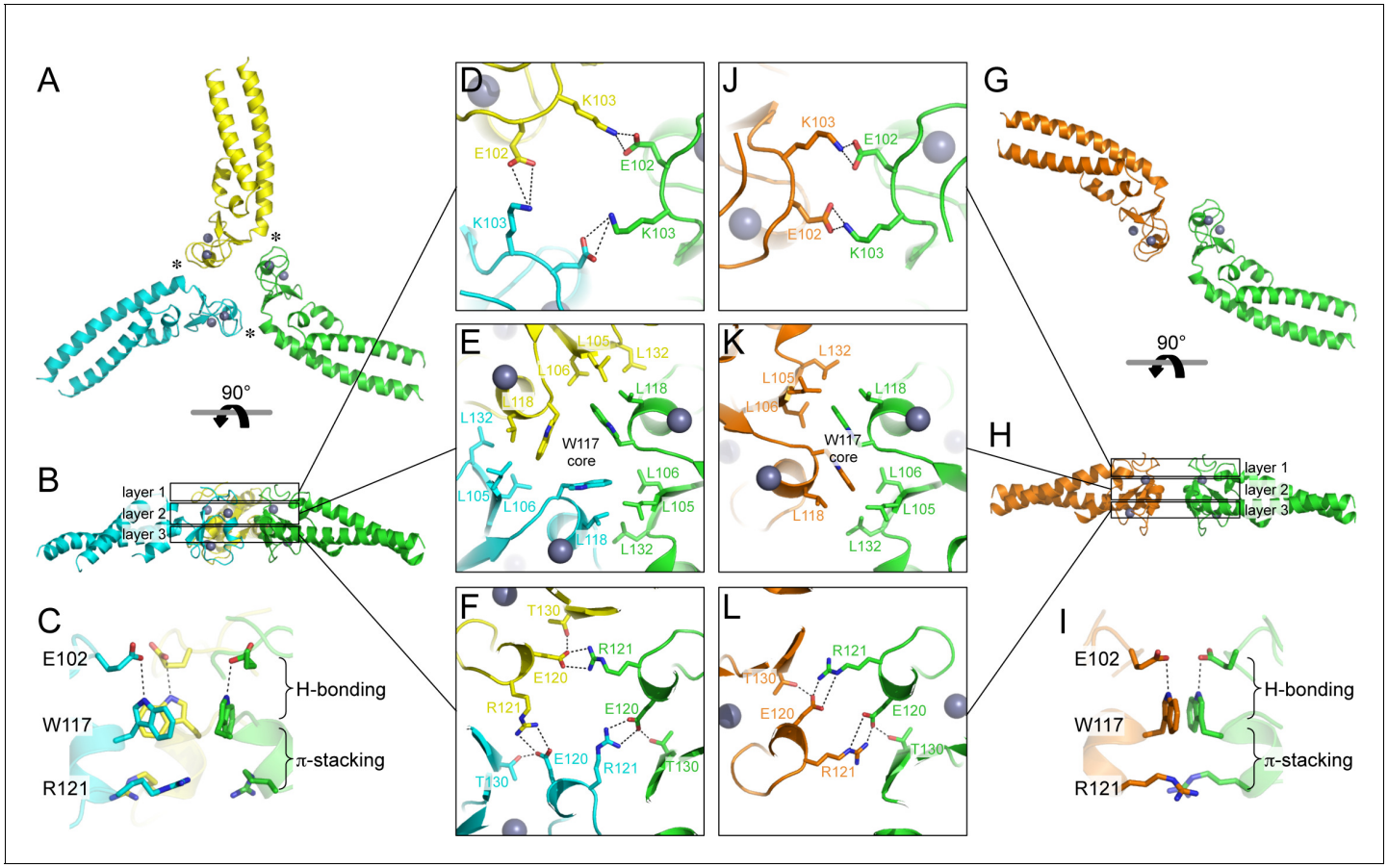


**Figure 3.** Oligomeric structures of Bcc miniTRIM. (**A**) Trimer crystal structure and (**G**) dimer crystal structure, viewed from the 'top' (closest to the N-termini). (**B,H**) Side views. Three layers of interactions are boxed and expanded in the central panels. Asterisks in A indicate a site of close packing between the B-box and the N-terminal end of the coiled-coil helix. (**C,I**) Interactions between layers. (**D–F,J–L**) Expanded views of three layers of interactions, in the same orientations as A and G. Relevant sidechains are shown as sticks and labeled. Hydrogen bonds and salt bridges are indicated by black dashed lines. Zinc atoms are shown as gray spheres.

DOI: 10.7554/eLife.16309.008

The following figure supplements are available for figure 3:

**Figure supplement 1.** Comparison of the B-box trimer (**A**) and dimer (**B**).

DOI: 10.7554/eLife.16309.009

**Figure supplement 2.** Superposition of representative subunits from the trimer (cyan) and dimer (green) indicate local bending of the coiled-coil helix spanning residues 133–139.

DOI: 10.7554/eLife.16309.010

**Figure supplement 3.** Sedimentation equilibrium analytical ultracentrifugation profiles of Bcc miniTRIM.

DOI: 10.7554/eLife.16309.011

**Figure supplement 4.** SEC-MALS analysis of Bcc miniTRIM.

DOI: 10.7554/eLife.16309.012

**Figure supplement 5.** Slight clam shell-like opening of the B-box dimer interface.

DOI: 10.7554/eLife.16309.013

equilibrium distributions to a monomer-dimer-trimer model only returned stable values for the monomer-dimer dissociation constant (1 μM). Indeed, the AUC data gave a satisfactory fit to a monomer-dimer equilibrium model, indicating that trimers (or higher-order oligomers than dimers) were disfavored in solution. To determine whether higher-order oligomers would form at higher protein concentrations, we also analyzed the Bcc miniTRIM at 0.9 mM by using analytical size exclusion chromatography with multi-angle light scattering (SEC-MALS). The mass trace (blue curve in ***Figure 3—figure supplement 4***) had a sharp peak at the leading edge of the protein absorbance peak (black curve), a curved plateau in the central region above the expected mass for a dimer, and

tapered towards the expected monomer mass at the tail. This again indicated dynamic equilibrium between monomer and dimer states, and that higher-order species were also present in the main peak, but at a much smaller fraction than dimers. Thus, the Bcc miniTRIM was predominantly dimeric in solution.

The solution behavior of Bcc miniTRIM is in sharp contrast to that of full-length protein. Published AUC analysis of freshly purified full-length TRIM5 did not show evidence of B-box mediated self-association, even at a loading concentration that is six-fold higher than our measured miniTRIM dimerization affinity (***Langelier et al., 2008***). Uncoupling of the B-box from the full coiled-coil and RING domains therefore appears to have amplified its propensity for oligomerization. Another difference is that, upon incubation, full-length TRIM5α has a clear propensity to assemble into hexagonal arrays – and by inference, three-way B-box/B-box interactions – even at low μM concentrations (***Ganser-Pornillos et al., 2011***; ***Li et al., 2016***; and this study). Since the miniTRIMs lack an intact coiled-coil, extended incubation did not result in lattice formation but only produced higher molecular weight aggregates (not shown). Our interpretation of all of these observations is that artificial uncoupling of the B-box 2 domain from the full coiled-coil and RING domains has stabilized the B-box dimer form. In context of the full-length protein, assembly cooperativity drives the B-box into the trimer form, and so the B-box dimer might represent an intermediate state that can incorporate an additional B-box domain to form the trimer. Consistent with this interpretation, our structures indicate that the Bcc miniTRIM dimers can open slightly like a clam shell, which we imagine can lead to a wider opening and provide access to a third subunit (***Figure 3—figure supplement 5***). We note that this interpretation does not preclude a functional role for a B-box dimer. For example, it is possible that B-box dimerization might be a mechanism to promote RING dimerization and E3 ligase activation. Nevertheless, it seems clear that the B-box trimer is what facilitates hexagonal lattice assembly, at least in vitro.

## Structure-based TRIM5α B-box 2 mutants are impaired in restriction and capsid binding

To test the functional relevance of the B-box mediated interactions in our structures, we generated structure-based mutations in full-length rhesus TRIM5α and tested the mutant proteins for their ability to inhibit transduction of GFP-labeled HIV-1 in HeLa cells (***Figure 4***, ***Table 2***). Charge reversal mutations in the top layer of interactions (E102K, K103E, E102K/K103E) diminished restriction activity (***Figure 4A***), confirming that this ring of salt bridges has an appreciable contribution to higher-order TRIM5α assembly. Individual charge reversals in the bottom layer (E120R, R121E) severely abrogated restriction activity (***Figure 4B***), in agreement with previous work (***Diaz-Griffero et al., 2009***; ***Li and Sodroski, 2008***). However, the E120R/R121E double mutation did not have a compensatory effect. This is in contrast with previous studies (***Diaz-Griffero et al., 2009***; ***Li and Sodroski, 2008***) but is consistent with the structures since Arg121 is involved in both a salt bridge and a hydrophobic packing interaction with Trp117. The repositioned guanidinium group in E120R seems unlikely to generate the optimal geometry for these interactions.

In the middle, hydrophobic layer, the W117E mutation was previously shown to abolish restriction activity (***Diaz-Griffero et al., 2009***), which we have confirmed here (***Figure 4C***). Interestingly, however, the W117A mutant still harbored some restriction activity, most likely because the hydrophobic layer remains stabilized by an outer ring of leucines. As with Trp117, alanine substitution mutants for Leu118 (***Figure 4D***) and Leu132 (***Figure 4E***) had measurable restriction activity, whereas aspartate substitutions were more significantly disruptive. Of the remaining two leucines, L105A had full activity and L106A did not restrict HIV-1 (***Figure 4F***). These results are again consistent with the structures since Leu105 is only partially buried, whereas Leu106 is completely buried within both the dimer and trimer interfaces. Interestingly, we found that steady state expression levels of the TRIM5α B-box 2 domain mutants varied considerably, as noted previously (***Diaz-Griffero et al., 2007***), and that furthermore there was an inverse correlation between the steady state expression levels of the mutant proteins and restriction activity (***Figure 4G***). The best expressing mutants (e.g., W117E and R121E) did not restrict HIV, whereas the lowest expressing mutant (L105A) had WT-like restriction activity. The expression levels also inversely correlated with in vitro assembly efficiency – W117E and R121E did not assemble, whereas L105A assembled efficiently (***Ganser-Pornillos et al., 2011***; also see below). We therefore speculate that the ability to assemble reduces steady state protein levels because TRIM5α proteins that assemble are turned over more rapidly in cells. An

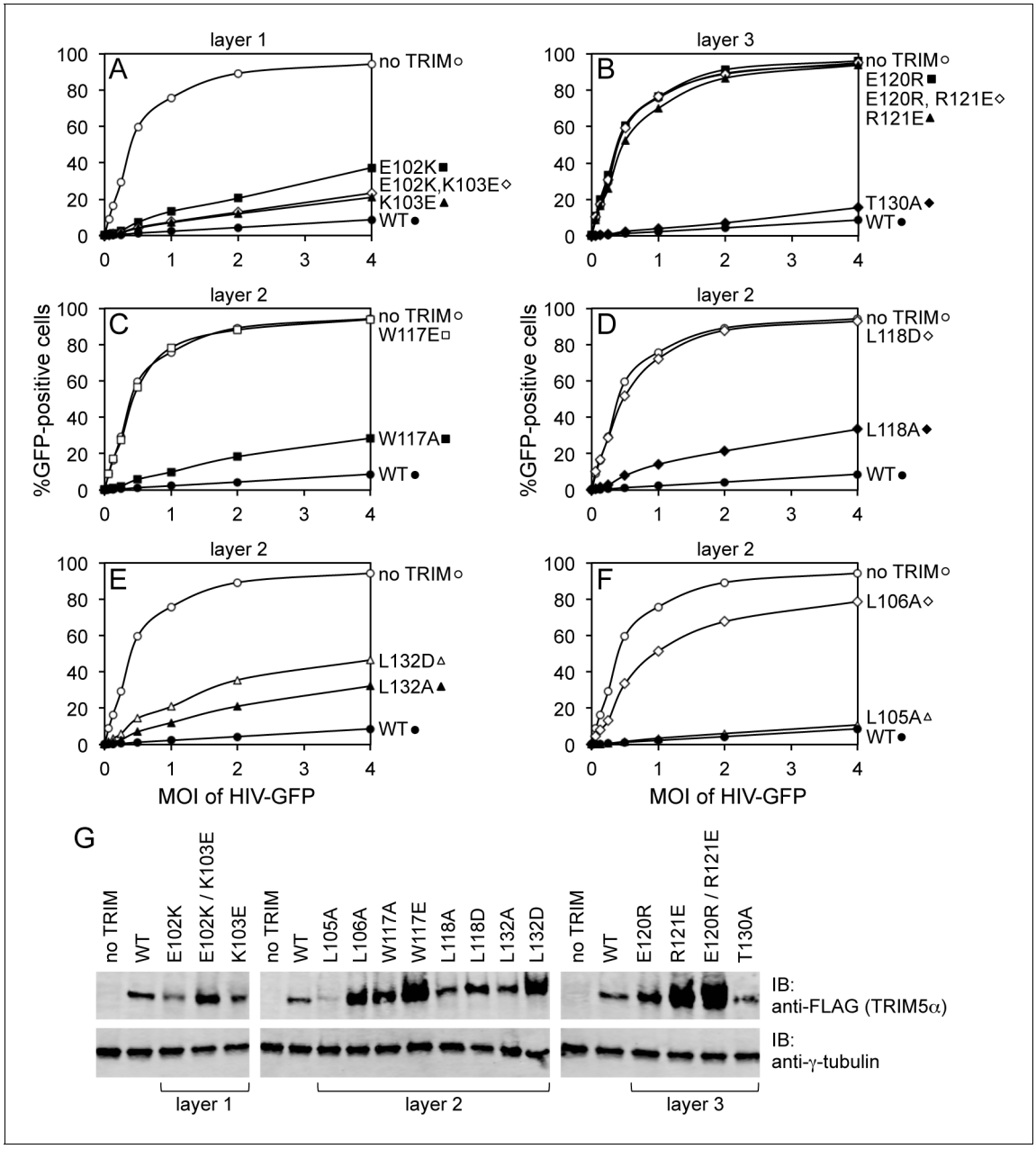


**Figure 4.** Restriction activities of rhesus TRIM5α containing structure-based B-box 2 domain mutations. For clarity, the data are presented in multiple panels. (**A–F**) GFP-labeled HIV-1 efficiently transduced HeLa cells that did not express exogenous TRIM5α (no TRIM, open spheres). Transduction was significantly inhibited in cells that expressed WT TRIM5α (WT, filled spheres). The same results were obtained in two independent experiments. (**G**) Immunoblots (IB) of whole cell lysates with anti-FLAG antibody to determine expression levels of rhesus TRIM5α mutants (upper). Anti-tubulin blots indicate that equivalent samples were loaded into each lane (lower).

DOI: 10.7554/eLife.16309.014

extension of this argument is that the ability of TRIM5α to assemble correlates with its ability to restrict HIV-1.

We also tested the effect of the hydrophobic B-box 2 domain mutations on capsid binding activity in vitro. For these experiments, we used TRIM5-21R, a chimeric construct described in previous studies as a functional and structural surrogate for TRIM5α due to its more favorable biochemical properties (***Diaz-Griffero et al., 2006a***; ***Ganser-Pornillos et al., 2011***; ***Kar et al., 2008***; ***Langelier et al., 2008***). We incubated crosslinked HIV-1 CA tubes (biochemical surrogates for the HIV-1 capsid) with WT and mutant TRIM5-21R proteins, and then measured binding in a co-pelleting

**Table 2.** Summary of structure-based mutagenesis.

| Mutation | Structure context | Restriction activity | Capsid binding | Spontaneous assembly | Co-assembly | Templated assembly |
|---|---|---|---|---|---|---|
| None (WT) | | ++ | ++ | hexagonal[1] | ++ | ++ |
| E102A | top layer | + | n.d. | n.d. | n.d. | n.d. |
| K103A | top layer | + | n.d. | n.d. | n.d. | n.d. |
| E102A,K103A | top layer | + | n.d. | n.d. | n.d. | n.d. |
| L105A | middle layer | ++ | ++ | macramé[1] | ++ | – |
| L106A | middle layer | – | + | –[1,2] | – | n.d. |
| W117A | middle layer | + | + | –[1,2], striated[3] | + | – |
| W117E | middle layer | – | + | –[1,2] | – | n.d. |
| L118A | middle layer | + | ++ | –[1], hexagonal[2] | n.d. | n.d. |
| L118D | middle layer | – | – | –[1,2] | – | n.d. |
| L132A | middle layer | + | + | –[1], hexagonal[2] | n.d. | n.d. |
| L132D | middle layer | +/– | + | –[1,2] | – | n.d. |
| E120R | bottom layer | – | n.d. | n.d. | n.d. | n.d. |
| R121E | bottom layer | – | +* | n.d. | n.d. | n.d. |
| E120R,R121E | bottom layer | – | n.d. | n.d. | n.d. | n.d. |
| T130A | bottom layer | ++ | n.d. | n.d. | n.d. | n.d. |

[1]At 1 mg/mL in standard low salt buffer
[2]At >5 mg/mL in standard low salt buffer
[3]At >5 mg/mL in high salt buffer
*from previous study (***Ganser-Pornillos et al., 2011**)
n.d. – not determined
DOI: 10.7554/eLife.16309.015

assay (***Fribourgh et al., 2014***; ***Ganser-Pornillos et al., 2011***; ***Stremlau et al., 2006***). In control experiments, about 50% of WT TRIM5-21R was consistently found in the pellet (***Figure 5A***). Mutants were analyzed in parallel with a WT control, and results in ***Figure 5B*** are representative of mutant binding efficiencies relative to WT from at least two experiments with independent protein preparations. Essentially all of the B-box mutants tested had detectable capsid binding activity, which was expected because all of these constructs contained an intact SPRY domain and because the R121E mutation that abolished restriction still supported capsid binding in a similar assay (***Ganser-Pornillos et al., 2011***). Nevertheless, our results showed that weaker or no capsid binding correlated with weaker or no restriction activity (***Table 2***), confirming that B-box 2 domain mediated interactions promote efficient capsid recognition.

## Assembly properties of TRIM5α B-box 2 domain mutants

We then directly determined the effects of the B-box mutations on TRIM5α assembly activity in vitro (***Figures 6–8***, and ***Table 2***). For this analysis, we focused on the hydrophobic (layer 2) mutations. Previously, purified TRIM5-21R was shown to assemble spontaneously into hexagonal arrays when incubated in low salt buffer at about 1 mg/mL (***Ganser-Pornillos et al., 2011***). These micron-sized arrays can be readily visualized by negative stain electron microscopy (***Figure 6A***). In contrast, the R121E mutant did not assemble spontaneously even at concentrations up to 30 mg/mL (***Ganser-Pornillos et al., 2011***). We therefore tested our TRIM5-21R mutants for spontaneous assembly at both low (1 mg/mL) and high (>5 mg/mL) protein concentrations. We found that mutations that gave the most significant reductions in restriction activity (L106A, W117E, L118D, and L132D) also prevented assembly at all protein concentrations tested (up to 18 mg/mL) (***Table 2*** and data not shown). Two of the mutations that supported intermediate restriction activity (L118A and L132A) also supported hexagonal lattice assembly, but only at high protein concentrations and to a more limited extent compared to WT (***Figure 6B,C***). A third intermediate mutation, W117A, altered the

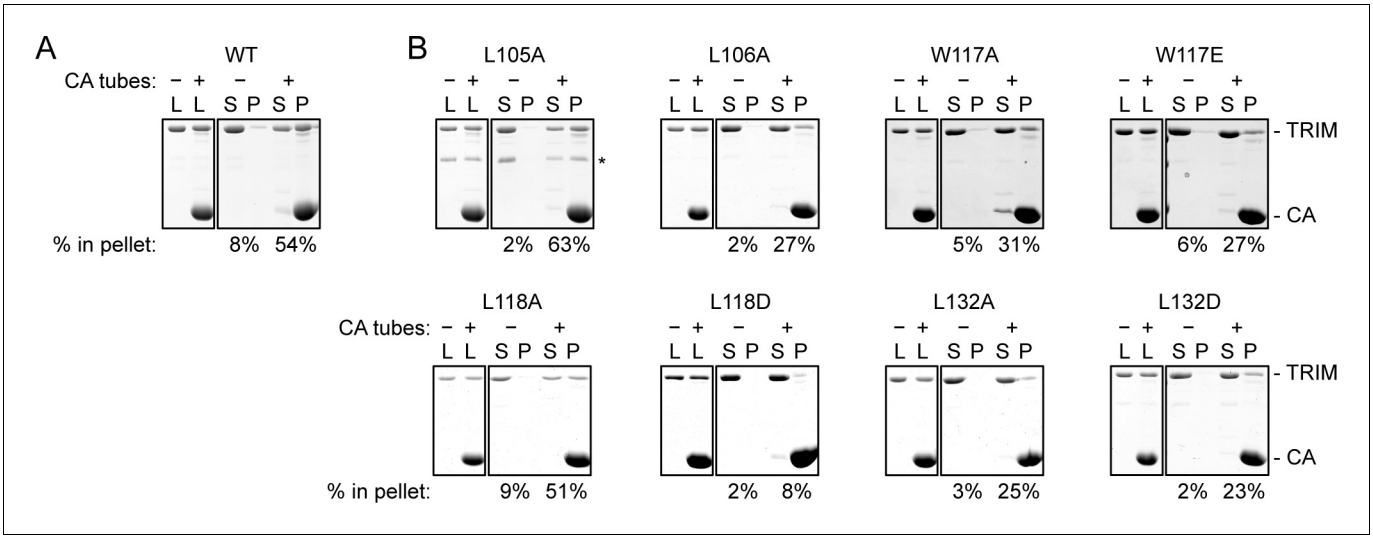


**Figure 5.** CA tube pull-down assay. (**A**) WT control. (**B**) Indicated mutants. Purified TRIM5-21R proteins were incubated with disulfide-stabilized CA tubes and pelleted in a microcentrifuge. Bound (pellet) and unbound (supernatant) proteins were visualized by SDS-PAGE with Coomassie staining and quantified. Percentage values indicate the fraction of protein in the pellet. Results are representative of at least two experiments per mutant, each done with an independent protein preparation. L, load; S, supernatant; P, pellet. CA and TRIM bands are indicated. The asterisk indicates an apparent proteolytic fragment of TRIM5-21R.

DOI: 10.7554/eLife.16309.016

assembly phenotype of TRIM5-21R. This mutant failed to assemble in standard low salt buffer at both 1 and 5 mg/mL, but at high protein concentrations and higher salt (>250 mM NaCl), it assembled into striated arrays (***Figure 6D***). Interestingly, the L105A mutation (full restriction activity) also altered the spontaneous assembly behavior of TRIM5-21R. Under the same conditions as WT (low salt buffer and 1 mg/mL protein), L105A formed macramé-like networks that appeared distinct from either the hexagonal or striated arrays (***Figure 6E***).

Two-dimensional crystals of HIV-1 CA-NC, which mimic the hexagonal HIV capsid lattice at its planar limit, can promote assembly of TRIM5-21R and native TRIM5α proteins into flat hexagonal arrays (***Ganser-Pornillos et al., 2011***; ***Li et al., 2016***). We therefore tested whether the CA-NC arrays can 'rescue' the altered spontaneous assembly phenotype of L105A and W117A. However, results were inconclusive; although the TRIM proteins appeared to associate with the CA-NC arrays, diffraction patterns that would indicate overlaying lattices were not observed (***Table 2*** and data not shown). We therefore used an alternative assay wherein soluble TRIM5α and HIV-1 CA are mixed and incubated under basic conditions and moderate salt concentrations, which results in formation of CA tubes that are almost uniformly decorated with TRIM (***Li et al., 2016***). The overlaying TRIM lattice on these tubes is related to the flat hexagonal arrays, except that it now follows the basal curvature of the CA tubes. Both WT TRIM5-21R (***Figure 7A***) and the L105A mutant (***Figure 7B***) showed similar behavior in this assay; that is, virtually all the tubes were uniformly decorated, and the decorations looked similar to each other and to those made by WT TRIM5α (***Li et al., 2016***). In contrast to the flat arrays, hexagon shapes were more difficult to discern in projection images of the curved arrays, and so we also analyzed negatively stained samples by electron tomography. As observed with vitrified samples (***Li et al., 2016***), densities surrounding the CA tubes were readily discernible in the tomograms of our negatively-stained samples (***Figure 8***). As expected, the peripheral TRIM5α layers exhibited a high degree of disorder, but for both WT (***Figure 8A***) and L105A (***Figure 8B***), we could clearly observe regions of local order with hexagonal rings having the expected dimensions for a TRIM hexamer. Interestingly, a proportion of the L105A decorations appeared more ladder-like (***Figure 8C***), but again the distances between the repeating units were similar to the TRIM hexagon dimensions. We therefore conclude that, although there is no clear structural explanation for the spontaneous assembly behavior of the L105A mutant, it can nevertheless form hexagonal arrays when it binds CA tubes in vitro. The inability of this mutant to form flat lattices (the endpoints of

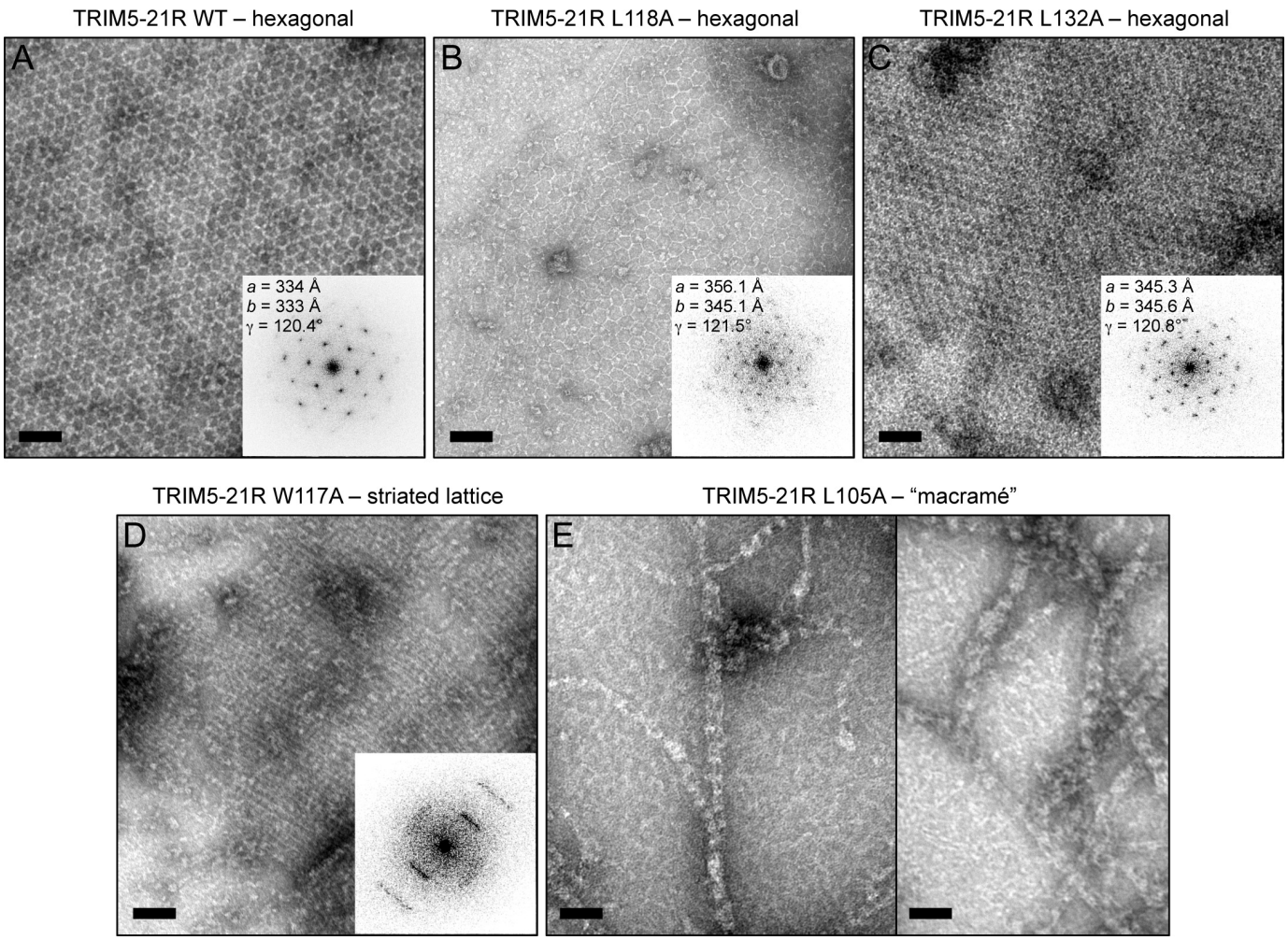


**Figure 6.** Spontaneous assembly of TRIM5-21R. (**A**) WT TRIM5-21R spontaneously assembled into hexagonal arrays at a concentration of 1 mg/mL in 25 mM Tris, pH 8, 25 mM NaCl, 1 mM TCEP (standard conditions) (***Ganser-Pornillos et al., 2011***). Main panel shows a representative negatively stained image of the arrays; inset shows a Fourier transform of the image. The unit cell spacing (symmetry unimposed) calculated from the diffraction pattern is indicated. (**B**) L118A and (**C**) L132A, which gave intermediate restriction phenotypes in context of rhesus TRIM5α, also assembled into hexagonal nets, but at higher protein concentrations (2 and 9 mg/mL, respectively). (**D**) W117A aggregated under standard conditions but at >5 mg/mL and 250 mM NaCl assembled into a striated array. (**E**) L105A, which was fully restriction competent, assembled spontaneously under standard conditions into networks that were neither hexagonal not striated. Results are representative of two or three experiments per construct, each done with an independent protein preparation. Scale bars = 100 nm.

DOI: 10.7554/eLife.16309.017

both the spontaneous assembly and template driven methods) suggests that B-box/B-box interactions might have some link to lattice curvature.

We also used the co-assembly assay to characterize the W117A mutant that assembled into striated arrays (***Figure 6D***). This mutant also decorated the CA tubes, but the decorations were more limited in extent compared to either WT or L105A, and regions of undecorated CA were more readily apparent in the projection images (***Figure 7C***). Similarly, the tomograms revealed considerable disorder in the overlaying TRIM lattice, and hexagon-shaped decorations were not easily discerned (not shown).

In summary, our analysis of structure-based B-box 2 domain mutations support a general correlation between TRIM5α restriction activity in cells, capsid binding efficiency in vitro, and hexagonal lattice assembly in vitro. Our results therefore fit the model wherein both capsid recognition and

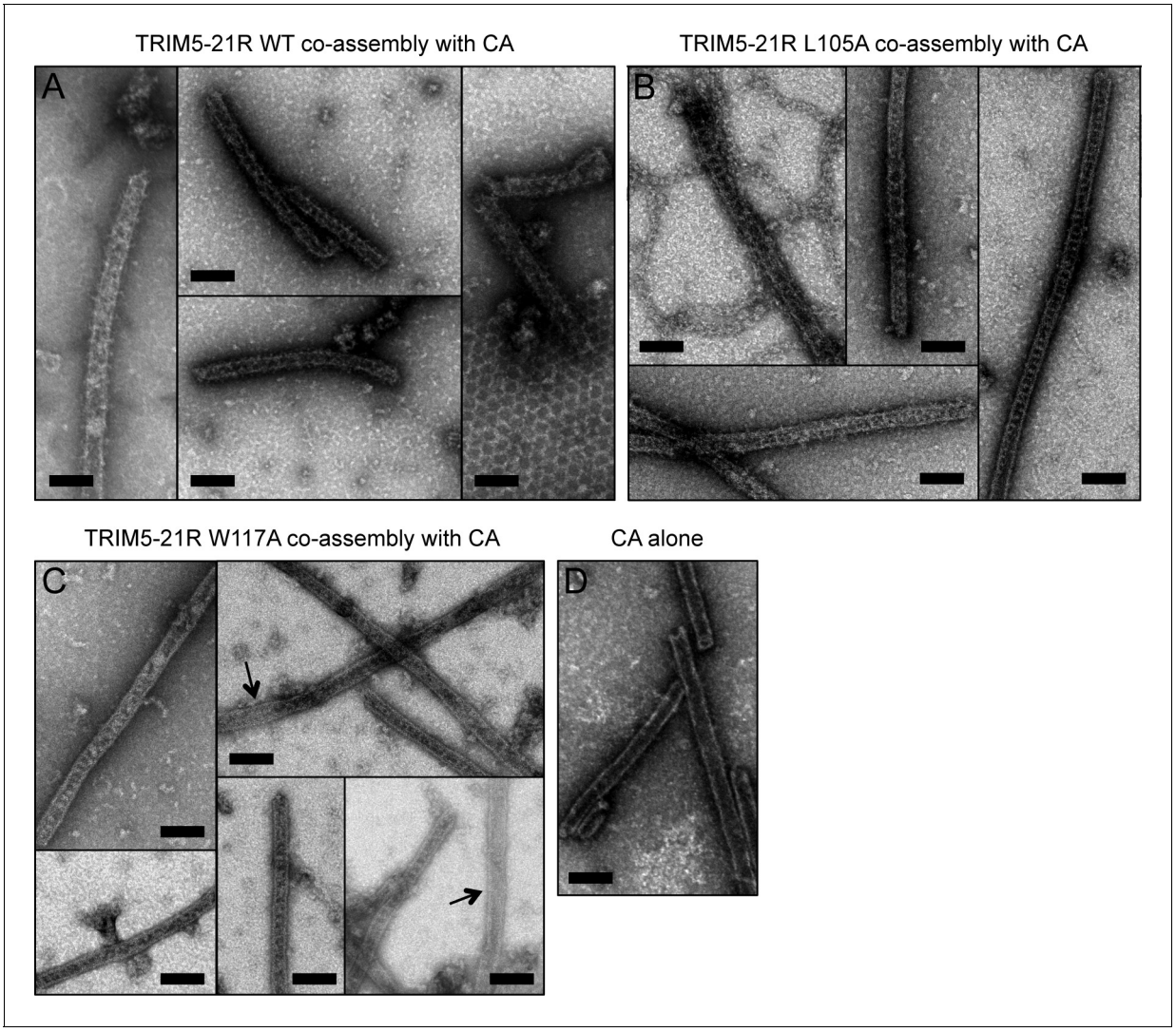


**Figure 7.** Co-assembly of TRIM5-21R with HIV-1 CA. (**A**) Incubation of WT TRIM5-21R with soluble HIV-1 CA protein induced assembly of TRIM-coated capsid tubes. A similar phenotype was observed when co-assembly is performed with African green monkey TRIM5α (***Li et al., 2016***). (**B**) TRIM5-21R with the L105A mutation made similar decorated tubes as WT in this assay. (**C**) W117A also made similar decorations, but to a more limited extent. Partially decorated and undecorated tubes were more prevalent (arrows). Results are representative of two or three experiments per construct, each done with an independent protein preparation. (**D**) Undecorated CA tubes shown for comparison. Scale bars = 100 nm.
DOI: 10.7554/eLife.16309.018

antiviral restriction are facilitated by B-box mediated assembly of TRIM5α into a hexagonal lattice that wraps around the viral capsid.

## Molecular modeling of the TRIM5 hexagonal lattice

The low-resolution structure of the TRIM5α hexagonal lattice consists of large lobes of density at the two-fold and three-fold symmetric positions connected by thin linkers of density (***Ganser-Pornillos et al., 2011***; ***Li et al., 2016***). The thin linkers are made by the antiparallel coiled-coil dimer scaffold and the two-fold lobes are made by the SPRY domain (***Ganser-Pornillos et al., 2011***; ***Goldstone et al., 2014***; ***Li et al., 2016***; ***Sanchez et al., 2014***; ***Weinert et al., 2015***; ***Li et al., 2016***). Our structural and biochemical analyses indicate that the three-fold vertexes are made by B-box 2 domain trimers. By combining our miniTRIM trimer crystal structure with that of the B-box/coiled-coil dimer (PDB 4TN3) (***Goldstone et al., 2014***), we built a molecular model of a flat TRIM5α hexagonal lattice (***Figure 9A***). The unit cell spacing of this model is 338.5 Å, which is an almost exact match to the observed value for rhesus TRIM5α (340 Å) (***Li et al., 2016***). All of the SPRY domains

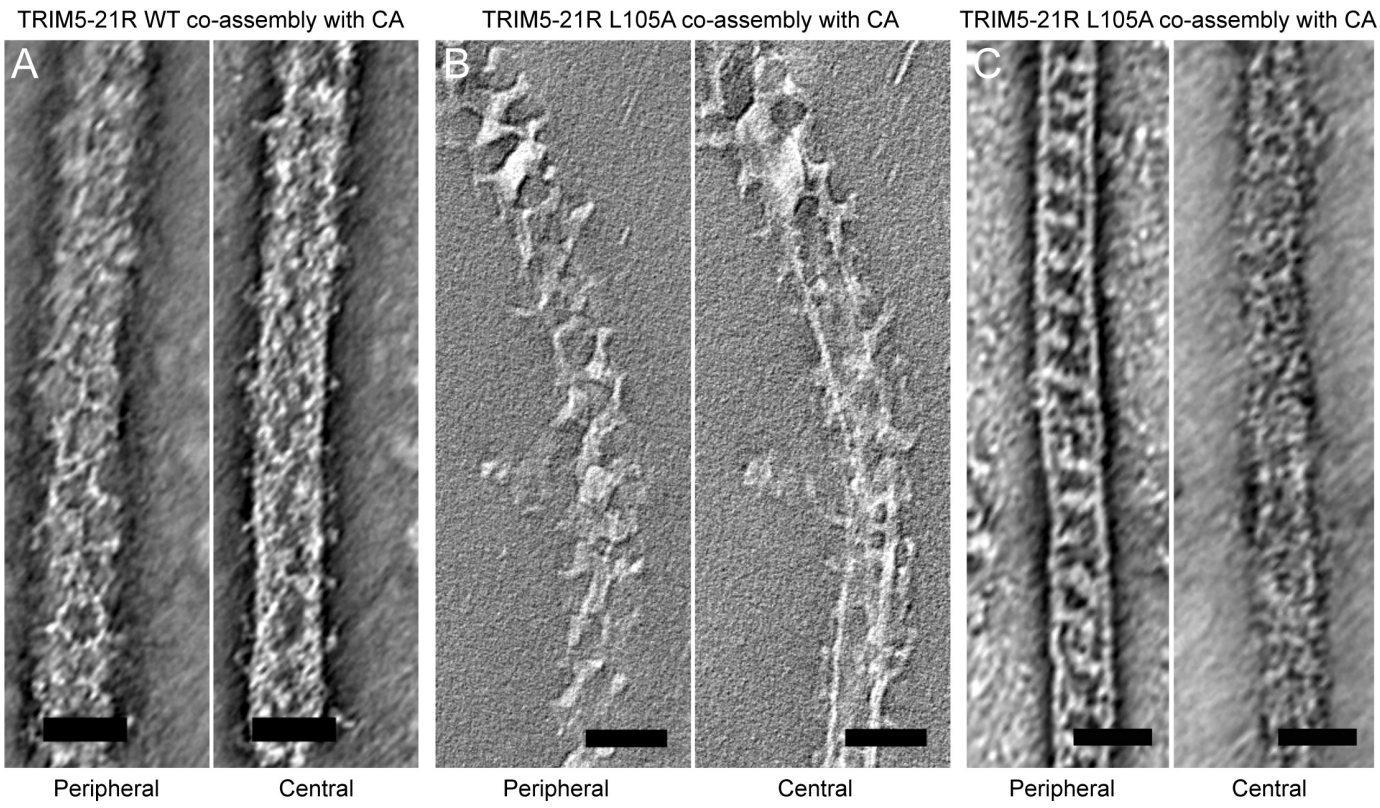


**Figure 8.** Slices of tomographic reconstructions of (**A**) WT and (**B**) L105A TRIM5-21R coated CA tubes. Left panels show peripheral slices, and right panels show central slices of the same tube. (**C**) Some of the L105A-coated tubes had ladder-like TRIM overlays that do not seem hexagonal. These could be due to overlapping lattices or an alternative arrangement of TRIM dimers. Scale bars = 50 nm.
DOI: 10.7554/eLife.16309.019

are located on one side of the lattice plane (***Figure 9B***, blue spheres), where they could bind the capsid simultaneously. At the three-fold vertexes, the N-terminal ends of the B-boxes point toward the other side of the lattice plane. This suggests that the RING domains are oriented away from the capsid (***Figure 9B***, red spheres). This molecular architecture indicates that the higher-order TRIM scaffold also compartmentalizes the biochemical activities of the RING and SPRY domains.

## The B-box/coiled-coil interface allows rigid body motions of the two domains

When TRIM5α binds to a retroviral capsid, it must accommodate the variable surface curvature of the capsid. Capsid lattice curvature is generated by rigid body hinge motions between subunits, and we have previously identified such hinges by comparing crystallographically independent structures of the hexameric and pentameric capsid building blocks (***Pornillos et al., 2009***; ***2011***). The availability of 12 independent miniTRIM structures allowed us to perform a similar analysis here. As illustrated in ***Figure 10A***, superposition of the miniTRIM structures revealed that the coiled-coil can swing relative to the B-box 2 domain. Flexion occurs about the B-box/coiled-coil interface, which is lined almost exclusively by aliphatic sidechains (***Figure 10B***). Note that in context of full-length TRIM5, this 'greasy' interface is a quaternary contact between the subunits of the native dimer. Bending of the first two turns of the coiled-coil helix in the dimer subunits produced the greatest change in orientation of the B-box relative to the coiled-coil, but the rigid body motions were also evident in comparing dimer subunits or trimer subunits alone (not shown). In context of the trimer, the three coiled-coils do not contact each other and can therefore move independently (***Figure 10C,***

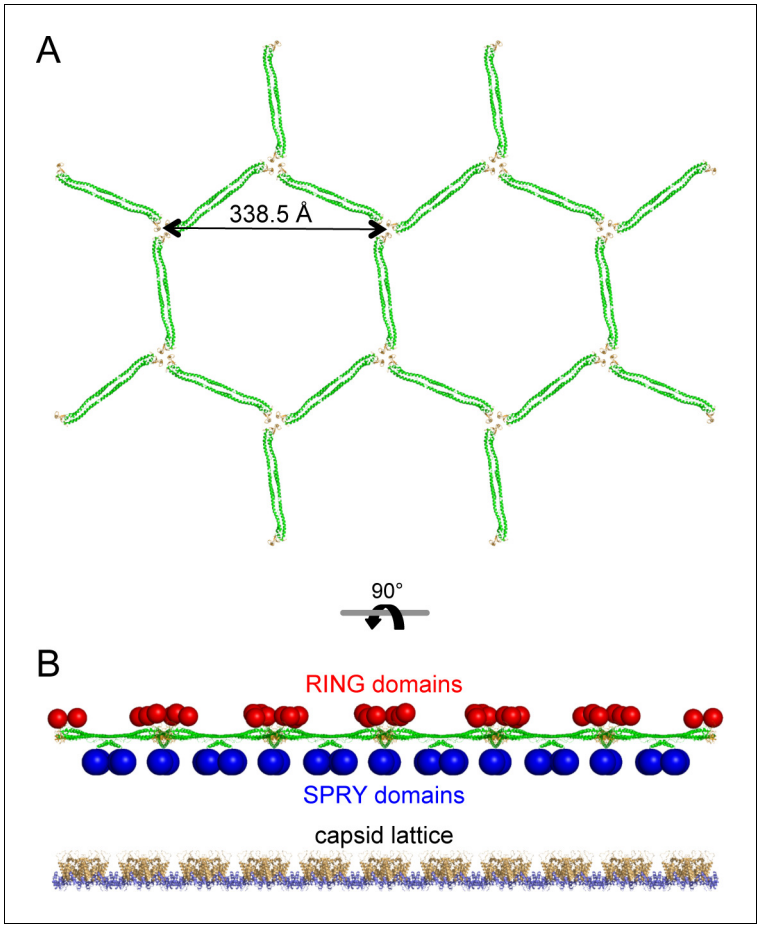


**Figure 9.** Molecular model of a flat TRIM5α hexagonal lattice. (**A**) Top view, with the B-box 2 domains colored in orange and the coiled-coil domains in green. (**B**) Side view, with the expected positions of the SPRY domains (blue) and RING domains (red) indicated by spheres. The flat capsid lattice is shown for reference.
DOI: 10.7554/eLife.16309.020

*D*). We conclude that TRIM5α uses the same general mechanism as retroviral capsids – flexion across quaternary interfaces and local conformational variations – to generate variable lattice curvature.

## B-box/B-box interactions stereochemically restrict RING domain activation

In addition to promoting avid capsid binding, B-box mediated interactions are expected to promote clustering of the upstream RING domain. Indeed, TRIM5α assembly on retroviral capsids is reported to enhance E3 ligase activity (***Pertel et al., 2011***). The RING domain dimerizes to bind E2-Ub conjugates and catalyze Ub transfer (***Yudina et al., 2015***). So far, we have been unable to solve a crystal structure of the RBcc miniTRIM, but structures of monomeric (inactive) and dimeric (active) forms of the TRIM5α RING domain are both known (***Lienlaf et al., 2011***; ***Yudina et al., 2015***), and so we used molecular modeling to determine possible configurations of the RINGs relative to the B-box trimer. An important consideration here is the structure of the L1 linker that connects the RING and B-box domains, which we define as the 23 amino acids (residues 72–94) that link the globular zinc-coordinating folds. Residues 72–82 are disordered in the monomeric RING structure, but are folded into a 4-helix bundle in the dimeric RING (***Lienlaf et al., 2011***; ***Yudina et al., 2015***). Thus, a RING monomer has a longer (and presumably more flexible) linker to the B-box than a RING dimer subunit.

We used the program RANCH (***Bernadó et al., 2007***) to calculate an ensemble of 10,000 models wherein the monomeric RING is flexibly tethered to the B-box trimer. Linker residues were modeled as impenetrable spheres, and the entire linker was assumed to be an 'intrinsically disordered'

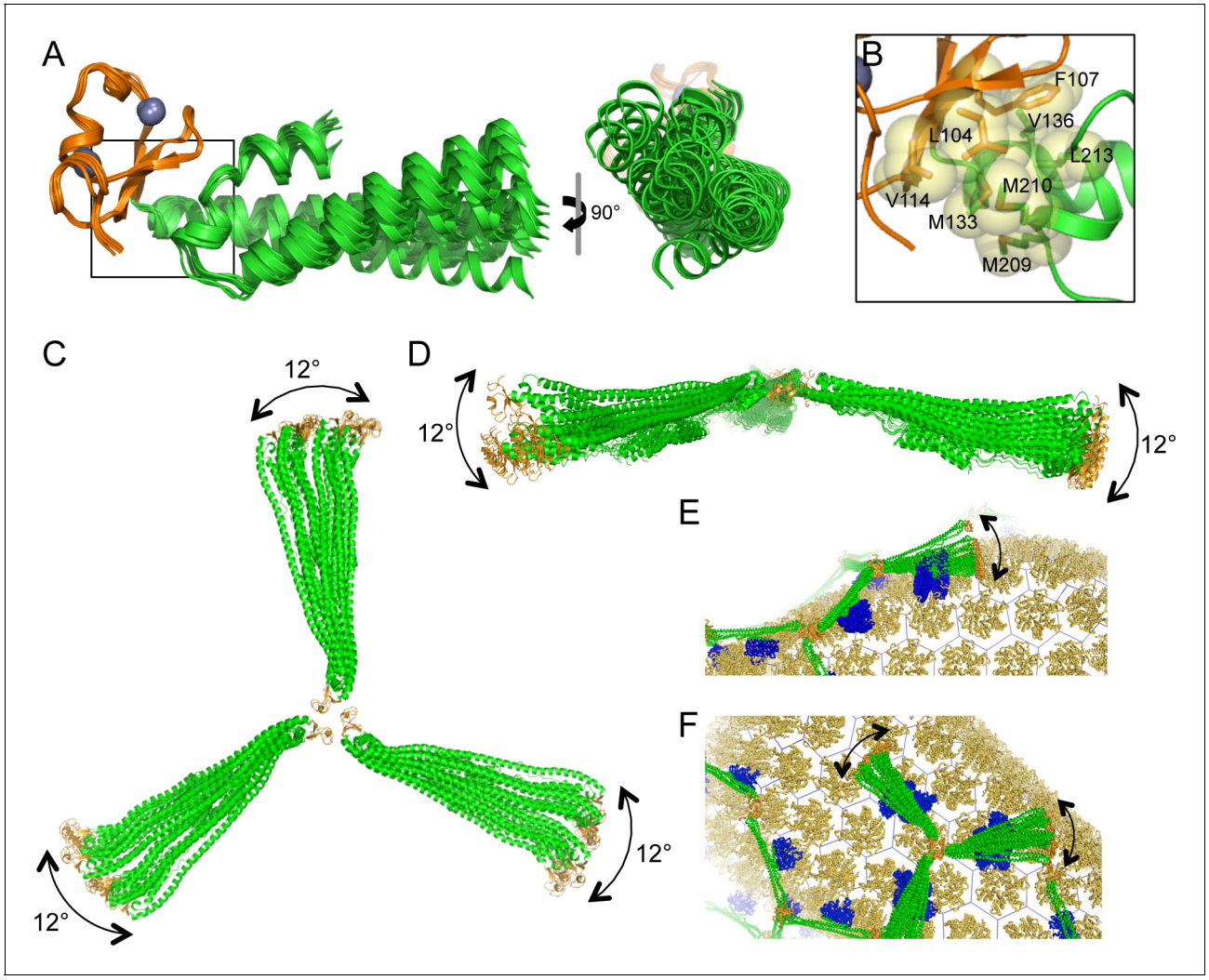


**Figure 10.** Flexible architecture of the miniTRIMs. (**A**) Orthogonal views of 12 crystallographically independent structures of Bcc miniTRIM. Superpositions of the structures on the B-box 2 domains (orange) reveals rigid body movements of the coiled-coil domains (green). (**B**) Close-up view of the B-box/coiled-coil interface boxed in A. Relevant sidechains are shown explicitly and labeled. (**C,D**) Superpositions of multiple full-length triskelion models on the B-boxes illustrate that the coiled-coil arms can swing flexibly relative to the B-box trimer vertex. (**E,F**) Speculative illustrations of how flexible triskelion arms can simultaneously allow the assembling TRIM lattice (green – coiled-coil; orange – B-box) to follow the curvature of the capsid (yellow orange) while scanning for optimal binding positions of the SPRY domains (blue).

DOI: 10.7554/eLife.16309.021

segment ('native' setting in RANCH). This treatment seemed appropriate since the linker adopts alternative secondary structures (***Lienlaf et al., 2011***; ***Yudina et al., 2015***). In the resulting ensemble, the vast majority of the RING domains are located above the plane of the trimer (***Figure 11A***, right). Thus, even flexibly tethered monomeric RINGs are predominantly located on one side of the lattice and away from the capsid. In a subset of our models, the RING/B-box linker folds down, in a configuration that brings the RING domain against the trimer vertex (***Figure 11A***, left). In principle, close packing of the RING domain and/or the RING/B-box linker against the trimer interface might explain the observation that the RING domain contributes to the efficiency of TRIM5α higher-order assembly (***Li et al., 2011***).

In the RING dimer, residues 72–82 fold into a 4-helix bundle, and destabilizing mutations in this region abrogate E3 ligase activity (***Yudina et al., 2015***). A RING dimer subunit is therefore separated from its B-box by a shorter linker of 12 residues ($_{83}$EVKLSPEEGQKV$_{94}$). Analysis of this sequence using the PEP-FOLD server (***Shen et al., 2014***) predicts that residues 87–94 have some propensity to fold into a short helix, and we therefore speculate that the dimeric RING/B-box linker

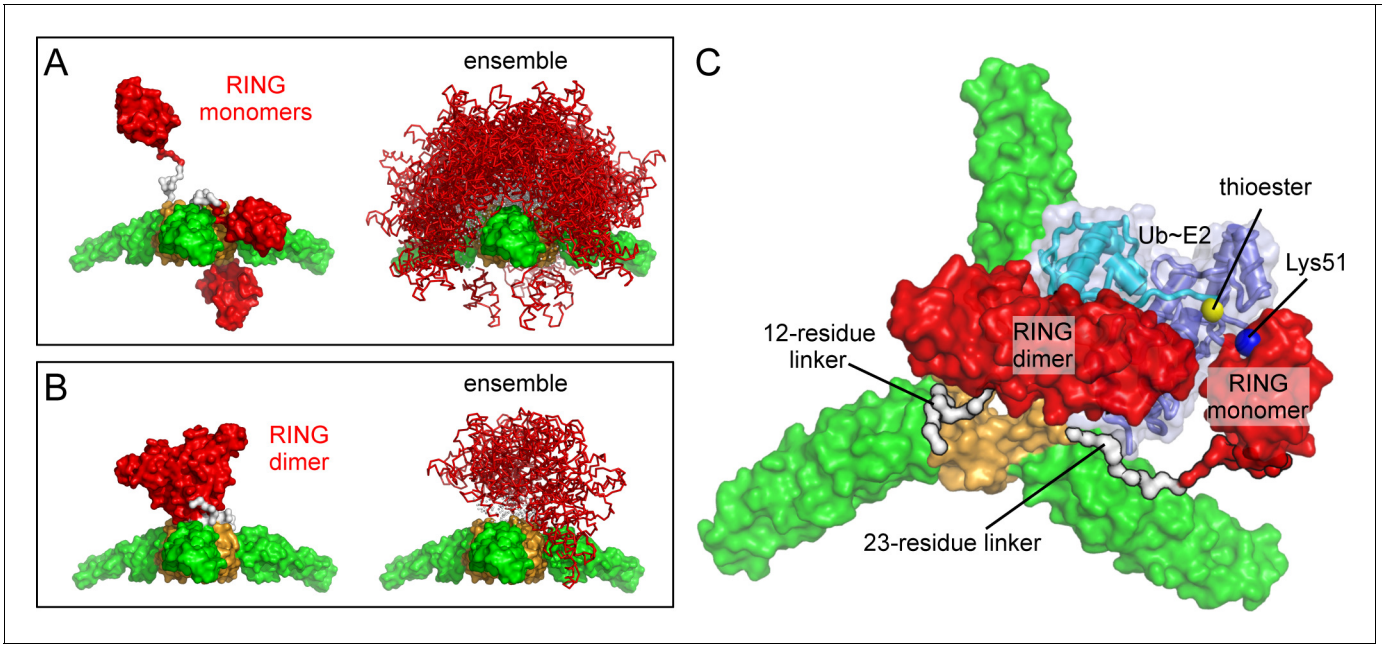


**Figure 11.** Models of RING domain configurations in context of the B-box trimer. (**A**) RING domains were modeled as monomers attached to their respective B-boxes by a flexible 23- residue linker. Left panel shows three representative configurations of the RING monomer relative to the trimer plane; above, within, and below. Right panel shows 500 of the 10,000 models calculated. (**B**) RING domains were modeled as dimers with a shorter, 12-residue linker. This resulted in only 13 configurations that were sterochemically plausible. (**C**) Computational model of a self-ubiquitination complex. Domains and proteins are color-coded as follows: RING, red; L1 linker, red (N-term) and white (C-term); B-box 2, orange; coiled-coil, green; E2, dark blue; ubiquitin, cyan. Positions of the thioester (yellow) and Lys51 amine (blue) are indicated by spheres, and are about 7 Å apart in this model.
DOI: 10.7554/eLife.16309.022

might actually be a hinge rather than a flexible tether. Since E2-Ub binding imposes additional spatial constraints, stereochemical clashes can only be avoided if the RING dimer is positioned above the B-box trimer (***Figure 11B***). We therefore conclude that in context of the TRIM hexagonal lattice, the B-box trimer spatially restricts the RING domain, such that an active E3 ligase can only form on the side of the lattice that faces the cytoplasm. We also performed the same analysis on the B-box dimer; as expected, it also restricted RING positions, but to a lesser extent than the trimer (not shown).

The functional target of TRIM5α ubiquitination has not been determined definitively, but self-ubiquitination correlates with inhibition of retroviral reverse transcription (***Campbell et al., 2015***; ***Fletcher et al., 2015***). The principal Ub attachment sites are in the RING domain (Lys45 and Lys51) (***Fletcher et al., 2015***). Although a B-box dimer is more naturally compatible with a RING dimer, a B-box trimer suggests an intuitively appealing mechanism for self-ubiquitination because it clusters three RING domains. In this model, two of the RING domains would dimerize and orient an E2-conjugated Ub for nucleophilic attack by the third RING (***Yudina et al., 2015***). To determine if such a mechanism of self-ubiquitination is stereochemically plausible, we constructed a model for a ubiquitination complex on a TRIM5α trimer vertex, by adding a third RING and an E2-Ub conjugate to one of our RING dimer/B-box trimer models. The two RING subunits that form the dimer were connected to their corresponding B-boxes by 12-residue linkers, whereas the third RING was connected by a longer and more flexible 23-residue linker. As illustrated in ***Figure 11C***, we were able to identify stereochemically acceptable conformations that simultaneously allow trimerization of the B-box, dimerization of two RINGs, binding of the RING dimer to a Ub-conjugated E2, and positioning of the appropriate lysine in the third RING for nucleophilic attack of the E2-Ub thioester bond. Thus, although our modeling approach is somewhat crude, the results indicate that B-box trimerization is compatible with RING activation and TRIM5α self-ubiquitination.

# Discussion

## Hexagonal lattice model for avid capsid binding

The 'pattern recognition' model of capsid binding postulates that higher-order assembly of TRIM5α into a hexagonal lattice positions multiple SPRY domains to match both the orientations and spacing of their binding epitopes on the capsid surface (***Ganser-Pornillos et al., 2011***; ***Li et al., 2016***). Our studies are consistent with this model, and further indicate that three-fold symmetric interactions at the vertexes of the hexagonal net are directly mediated by the B-box 2 domain. Indeed, our analysis suggests a 'rank order' of avidity promoting interactions, beginning with the 'minimal' coiled-coil dimer unit that positions (or clusters) two SPRY domains to bind the capsid simultaneously (***Goldstone et al., 2014***; ***Javanbakht et al., 2007***; ***Yap et al., 2007***). In principle, higher-order assembly of any geometry can amplify the recognition and restriction activities of the minimal dimer unit, but complete avidity and full restriction seem to occur when the TRIM5 dimers are arranged to match the lattice symmetry of the capsid. This principle appears exemplified by the L105A and W117A B-box mutants (***Table 2***). Like WT, the L105A mutant was fully restriction competent, bound to CA tubes efficiently in vitro, and formed observable hexagonal decorations on the tubes. In contrast, the W117A mutant was impaired in all three activities, even though it can clearly assemble spontaneously into higher-order but non-hexagonal arrays in vitro.

## TRIM lattice flexibility and curvature

Previous studies have analyzed how idealized (flat) capsid and TRIM lattices align in projection (***Ganser-Pornillos et al., 2011***; ***Goldstone et al., 2014***; ***Weinert et al., 2015***). This is reasonable because facets of the capsid surface are approximately flat, and because flat TRIM5α lattices assemble on two-dimensional crystals of the HIV-1 capsid protein. However, retroviral capsids present highly curved surfaces for TRIM5 binding, and the TRIM lattice must accommodate this curvature. Our structures demonstrate that the B-box/coiled-coil interface acts as a ball-and-socket joint, which imparts considerable flexibility in the way the coiled-coil arms emanate from the three-fold symmetric vertexes. Interestingly, our models define two major trajectories along which the coiled-coil can swing relative to the trimer plane (approximately parallel and approximately perpendicular). Motions parallel to the trimer plane change the angle between adjacent coiled-coils emanating from a vertex. This is consistent with the observation by ***Li et al. (2016)*** that the vertex angles in TRIM hexagonal lattices can deviate significantly from the ideal value of 120°, even in flat lattices. In our models, the coiled-coil can make an arc of about 12° along this trajectory. Angles between coiled-coil arms would therefore range from 120° ± 24°, which accounts for the full range of observed values (100–144°) (***Li et al., 2016***). Perpendicular motions, on the other hand, modulate the concavity of the triskelion and can generate lattice curvature. ***Figure 10E and F*** illustrate how the structural flexibility described above can allow the assembling TRIM lattice to scan for the most favorable SPRY domain positions and optimize local binding interactions, while simultaneously following the curvature of the bound capsid.

Flexibility in the triskelion arms also suggests a straightforward mechanism for generating multilayered TRIM assemblies, because a coiled-coil can extend a B-box 2 domain above or below its current lattice plane to nucleate a new lattice. TRIM5α lattices in vitro are frequently multilayered, whether spontaneously assembled or nucleated by capsid templates (***Ganser-Pornillos et al., 2011***; ***Li et al., 2016***; and this study). We speculate that the so-called cytoplasmic bodies that form upon overexpression of TRIM5α in cells (***Stremlau et al., 2004***; ***Campbell et al., 2007***) might also assemble in this manner.

## Flexibility in B-box/B-box interactions

Our finding that miniTRIMs can form quasi-equivalent dimers and trimers uncovers yet another mode of flexibility in TRIM5α self-assembly. B-box dimers are clearly disfavored under our 'ideal' in vitro conditions wherein full-length TRIM5α assembles into hexagonal arrays. In principle, however, B-box dimers provide a means for extending the TRIM array in regions where the local assembly environment disfavors trimers. Indeed, apparent dimer linkages can be occasionally discerned in TRIM-coated capsids in vitro (***Li et al., 2016***). Interestingly, B-box dimerization is associated with local bending of the first two turns of the coiled-coil helix, as well as altered packing of the B-box

against the coiled-coil domain. This suggests a potential mechanism of allosteric communication that can link B-box oligomerization and coiled-coil dynamics. Indeed, our observation that the L105A mutant could not assemble into flat arrays while remaining competent in forming curved arrays is another indication of a structural and functional link between B-box/B-box interactions, the coiled-coil dimer scaffold, and lattice curvature.

B-box mediated interactions also promote dimerization of the upstream RING domain and E3 ligase activity (***Ganser-Pornillos et al., 2011***; ***Pertel et al., 2011***; ***Yudina et al., 2015***). The catalytically active RING configuration is more structurally compatible with a B-box dimer, and it is therefore possible that the B-box switches its oligomeric configuration to facilitate enzymatic function. In principle, it is possible for a RING-containing subunit to act simultaneously as ligase and ubiquitination substrate within the same E2-Ub/E3 complex, as biochemically demonstrated for the RING domain of RNF4 (***Plechanovová et al., 2011***). Nevertheless, our modeling studies also support a mechanism by which the B-box trimer could contribute to TRIM5α self-ubiquitination. Specifically, a B-box trimer could bring together three RINGs, with the first two acting as the E3 ligase and the third acting as the substrate. More important, our analysis further suggests that folding of the RING/B-box linker into a 4-helix bundle restricts the RING dimer to the outer surface of the TRIM hexagonal lattice, i.e., on the opposite side of the capsid binding surface. We suggest that this spatial compartmentalization facilitates formation of exposed polyubiquitin chains that can recruit downstream cytosolic factors to promote restriction and/or interferon signaling.

# Materials and methods

## MiniTRIM construction, expression, and purification

Synthetic DNA (Genewiz, Inc., South Plainfield, NJ) encoding the RBcc miniTRIM sequence in ***Figure 1—figure supplement 1*** and upstream His-tag and yeast Smt3p (SUMO) leader sequence was subcloned into pET30a (Novagen/EMD Millipore, Germany). To create the Bcc miniTRIM plasmid, the RING domain open reading frame (residues 1–88) was excised using a PCR-based linearization and religation protocol. Point mutations were introduced using the Quikchange method (Agilent, Santa Clara, CA). All plasmid constructs were confirmed by sequencing with T7 and/or T7 terminator primers.

Transformed *E. coli* BL21(DE3) cells were grown in LB broth supplemented with appropriate antibiotics and 50 μM zinc acetate. Cultures were shaken at 250 rpm and 37˚C until the $OD_{600}$ reached 0.8–1.0. The shaker was then cooled to 18˚C during induction with 1 mM isopropyl β-D-1-thiogalactopyranoside (IPTG). Cells were harvested by centrifugation 4 hr after induction then stored at −80˚C.

Frozen *E. coli* weighing 25–30 g were resuspended in 120 mL of 2× lysis buffer (100 mM Tris, pH 8, 100 mM LiCl, 10% (v/v) glycerol, 1% (v/v) Triton X-100, 20 mM β-mercaptoethanol (βME), 2 mM phenylmethanesulfonylfluoride (PMSF)) then lysed using a microfluidizer (Microfluidics, Westwood, MA). The lysate was diluted to 1× with 120 mL cold water. Cell debris was pelleted by centrifugation at 45,000 *g* and discarded. The supernatant was then incubated with nickel agarose beads (Qiagen, Germany). The beads were washed with 10 column volumes (CV) of Wash 1 buffer (50 mM Tris, pH 8, 50 mM LiCl, 10 mM βME, 5% (v/v) glycerol), 2 CV of Wash 2 buffer (Wash 1 + 1 M LiCl), and again with 5 CV of Wash 1. Proteins were eluted by addition of 5 mL fractions of elution buffer (Wash 1 + 250 mM imidazole). The His-tag and SUMO leader sequences were cleaved off with SUMO-specific Ulp1 protease (3 μg/mL), during overnight dialysis in Wash 1 buffer. The His-SUMO protein was removed by a 15 min incubation with nickel agarose. The sample was then diluted 1.5× with water, and then applied to a HyperD anion exchange column (Pall Lifesciences, Port Washington, NY). Bound fractions were eluted with a linear gradient from 100% Wash 1 buffer to 70% Wash 1/ 30% Wash 2. Fractions were combined and concentrated to 0.5 mL then purified to homogeneity by gel filtration on a Superdex 75 column (GE Healthcare, Little Chalfont, UK) in 10 mM Tris, pH 8, 100 mM LiCl, 1 mM TCEP. Major peak fractions were pooled and concentrated to 3–15 mg/mL, flash-frozen in liquid nitrogen, then stored at −80˚C. Typical yields were around 0.3 mg per L of culture for RBcc and around 1 mg per L for Bcc.

## Crystal structure determination

Protein stock solutions for crystallization trials generally consisted of about 3 mg/mL Bcc miniTRIM in 10 mM Tris, pH 8, 100 mM LiCl, 1 mM TCEP. Crystallization was performed in hanging drop format. Initial hits were identified with commercial sparse matrix screens. Optimized conditions are summarized in ***Supplementary file 1A***. Diffraction data were collected at beamlines 22BM or 22ID at the Advanced Photon Source, and processed using HKL2000 (***Otwinowski and Minor, 1997***). We initially determined the structure of a dimeric Bcc miniTRIM (P6222 form) to 2 Å resolution by molecular replacement with a computational model derived from the rhesus TRIM5α B-box/coiled-coil structure (PDB 4TN3) (***Goldstone et al., 2014***) and residues 49–79 of *Thermus thermophilus* seryl-tRNA synthetase (PDB 1SRY) (***Fujinaga et al., 1993***). This model was partially refined and then used as a molecular replacement search model for all the other structures (***Table 1***). Structure determination and refinement were performed using the Phaser/AutoMR and phenix.refine modules of the PHENIX suite of programs (version 1.9–1692) (***Adams et al., 2010***). Secondary structure hydrogen bonding restraints and zinc coordination (bond and angle) restraints were used during refinement. Torsion angle (local) non-crystallographic symmetry (NCS) restraints were also used when appropriate. Manual model building was performed with the program Coot (***Emsley et al., 2010***). Structure validation tools, as implemented in both PHENIX and Coot were used throughout the structure refinement process.

## SEC-MALS

Mass measurements on Bcc miniTRIM were performed on a Dionex UltiMate3000 HPLC system with a UV detection module (ThermoFisher, Waltham, MA), connected to a miniDAWN TREOS static light scattering detector (Wyatt Technology, Santa Barbara, CA) and Optilab T-rEX differential refractometer (Wyatt Technology). A sample volume of 40 µL at 0.9 mM concentration was applied to a Superdex 200 HR 10/300 GL column (GE Healthcare) and developed in 30 mM Tris, pH 8.0, 100 mM NaCl at a flow rate of 0.4 mL/min. Data were recorded and processed using ASTRA software (Wyatt Technology).

## Analytical ultracentrifugation

Equilibrium sedimentation AUC experiments on Bcc miniTRIM were performed at 4°C using either XL-A or XL-1 analytical ultracentrifuges with absorbance optics (Beckman Coulter, Brea, CA). Sample cells with a six-channel centerpiece were filled with 110 µL of the protein samples at concentrations of 60, 30, and 15 µM, while 120 µL of sample buffer was loaded into the reference sectors. Absorbance scans at 280 nm were taken after equilibrium was reached (~12 h) at 14,000, 21,000, and 26,000 rpm. Protein partial specific volume and solvent density were calculated using SEDNTERP (version 20120828 BETA) available online at sedenterp.unh.edu. These values were used during curve fitting and data analysis using Heteroanalysis Software (version 1.1.58) (***Cole, 2004***).

## Restriction assays

Restriction assays were performed using HeLa cells grown in DMEM (Gibco/Thermofisher, Waltham, MA) supplemented with 10% fetal calf serum (Gibco) at 37°C in 5% $CO_2$. The cells were first transduced with a VSV-G pseudotyped lentiviral vector encoding rhesus TRIM5α with a C-terminal Flag-One-Strep (FOS) tag followed by an IRES sequence and DsRed (CSII-IDR2-TRIM5α-FOS). Three days after transduction, cells expressing TRIM5α-FOS were re-seeded in 24-well plates and transduced with increasing MOI of VSV-G pseudotyped HIV-GFP. A sample of these cells were pelleted and resuspended in SDS-PAGE sample buffer for western blot analysis of TRIM5α expression using anti-FLAG M2 antibody (Sigma, St. Louis, MO). 72 hr after HIV-GFP transduction, cells were trypsinized and analyzed for GFP expression (to determine the extent of HIV-GFP infection) and DsRed (as a marker for TRIM5α positive cells) by flow cytometry.

Lentiviral vectors for expressing TRIM5α in the above experiments were produced in the following manner. HEK293T cells were plated in 6-well plates and transfected with 1 µg pCMV-delR8.2, 0.4 µg pCMV-VSV-G, and 1.0 µg of the CSII-IDR2-TRIM5α-FOS plasmid. At 18 hr post-transfection, cells were placed in fresh media. At 48 hr post-transfection, media (containing the lentiviral particles) was removed and placed directly on HeLa cells for transduction and expression of TRIM5α-FOS and DsRed.

VSV-G pseudotyped HIV-GFP virions were produced in the same way as the TRIM5α expressing virions, but media harvested at 48 hr post-transfection was filtered through a 0.45 µ filter, layered on a 20% sucrose cushion in HS buffer (10 mM HEPES, pH 7.4, 140 mM NaCl) and centrifuged for 2 hr at 28,000 rpm in a Beckman SW32 Ti rotor. After centrifugation, the pellet containing viral particles was resuspended in HS buffer, aliquoted, and frozen for storage at −80˚C. The number of infectious units was determined by titrating an aliquot on HeLa cells, and determining the fraction of HIV-GFP infected cells by flow cytometry three days later.

## TRIM5-21R mutagenesis, expression, and purification

The open reading frame from a previously described plasmid clone of Strep-FLAG-tagged TRIM5-21R (***Ganser-Pornillos et al., 2011***) was transferred into pFastBac1 (Invitrogen, Carlsbad, CA). Mutations were made in this vector using the Quikchange method (Agilent). Baculoviruses were made using a modification of the Invitrogen Bac-to-Bac system (***Hanson et al., 2007***). Proteins were expressed by infecting SF9 cells in shake culture format for 48 h, and purified as described previously (***Ganser-Pornillos et al., 2011***).

## TRIM5-21R assembly assays

Spontaneous TRIM5-21R assembly was achieved by incubation of purified protein samples at 4˚C, as described (***Ganser-Pornillos et al., 2011***). The templated assembly assay for flat TRIM5-21R arrays was performed as described (***Ganser-Pornillos et al., 2011***). Co-assembly of TRIM5-21R and HIV-1 CA was performed as described (***Li et al., 2016***).

## Electron microscopy

Grid preparation and projection imaging of samples made by the spontaneous or template driven assembly methods were performed as described (***Ganser-Pornillos et al., 2011***). Electron tomography was performed as follows. Samples were mixed with BSA Gold Tracer (10 nm, Electron Microscopy Sciences, Hatfield, PA) and applied to glow-discharged continuous carbon grids for 1 min, washed with 0.1 M KCl, and stained with 2% (w/v) uranyl formate for 30 s. Tilt series were collected manually from –60˚ to +60˚ with a Tecnai F20 transmission electron microscope (Philips/FEI, Hillsboro, OR) operating at 120 kV. Step sizes were 5˚ at low tilts (0˚ to 30˚), 3.5˚ at medium tilts (30˚ to 40˚), and 1˚ at high tilts (30˚ to 60˚). Images were recorded on a Gatan Ultrascan 4k × 4k CCD camera at a magnification of 29,000× (3.7 Å/pixel) and defocus of –2.5 µm. Images were aligned and binned by 4 using the IMOD software package (***Kremer et al., 1996***), and reconstructions were calculated with 16 iterations of the simultaneous iterative reconstruction technique using the TOMO3D software package (***Agulleiro and Fernandez, 2011***). Individual *z*-sections were visualized using the slicer option in IMOD. To boost the contrast and make features more visible, up to 5 sequential slices were combined.

## Capsid binding assays

The centrifugation assay was based on previously published methods (***Ganser-Pornillos et al., 2011***; ***Stremlau et al., 2006***), with modification (***Fribourgh et al., 2014***). Disulfide-stabilized HIV-1 CA tubes (1 mg/mL, 20 µL) were incubated with TRIM5-21R (1 mg/mL, 5 µL) in ice for 1 hr. A 5-µL aliquot was removed, then mixed with equal volume of 2x SDS-PAGE sample buffer (load sample). The remaining sample was centrifuged at 16,000 *g* for 30 min at 4˚C. The supernatant (20 µL) was removed and mixed with equal volume of 2x SDS-PAGE sample buffer. The pellet was resuspended in 40 µL of 1x SDS-PAGE sample buffer. Samples were boiled and then analyzed by SDS-PAGE (well volumes: 10 µL of load, 20 µL each of supernatant and pellet fractions) with Coomassie staining. Stained gels were scanned and quantified using ImageJ (***Schneider et al., 2012***). Binding activity was expressed as the fraction of TRIM5-21R in the pellet. By this method, we found that about 50% of freshly purified TRIM5-21R was consistently found in the pellet (***Figure 5***). Upon storage, the co-pelleted fraction dropped to about 30% (not shown). Mutants were therefore analyzed fresh after purification, two or three a time in parallel with a WT control.

### Molecular modeling

Model ensembles were calculated with the program RANCH as described (**Bernadó et al., 2007**), using the miniTRIM trimer structure from this study. Additional input files for the RING monomer and dimer ensembles, respectively, were the NMR structure of the RING monomer (PDB 2ECV) (**Lienlaf et al., 2011**) and the crystal structure of the RING dimer subunit (PDB 4TKP) (**Yudina et al., 2015**). Residues linking the RING and B-box domains were modeled as impenetrable spheres, with a Cα angle distribution consistent with disordered proteins (**Bernadó et al., 2007**). Thus, possible interactions with the linker were disregarded. Since RANCH cannot model symmetry mismatched PDB files, the RING dimer orientations were modeled in the following manner. An ensemble of 30,000 models was calculated in the same manner as the RING monomer. The models were then computationally filtered to identify ones that contained a pair of RING domains wherein the distance of separation between two of the zinc lobes and their corresponding C-termini were consistent with the crystal structure of the RING dimer (**Yudina et al., 2015**). The RING dimer structure was then re-aligned manually, and then rotated to avoid steric clashes. We found that the RING 4-helix bundle was an important restraint that led to identification of only a handful of plausible RING dimer/B-box trimer configurations. The model for the self-ubiquitination complex was created by superimposing one of the RING dimer/miniTRIM trimer models, the crystal structure of the TRIM5α RING dimer in complex with Ubc13 (**Yudina et al., 2015**), and the structure of the RNF4 RING dimer in complex with ubiquitin-conjugated Ubc5a (**Plechanovová et al., 2012**). To model the third, substrate RING, the ensemble of 10,000 RING monomer/miniTRIM trimer models was then screened computationally to identify an orientation that placed the appropriate RING lysine (Lys45 or Lys51) within 8 Å of the E2-ubiquitin thioester bond without steric clashes between any of the structural elements.

### Accession numbers

Coordinates and structure factors are available from http://www.rcsb.org: P212121 trimer, 5IEA; C2 dimer, 5EIU; P1 dimer, 5F7T.

## Acknowledgements

We thank members of the Pornillos, Ganser-Pornillos, and Sundquist labs for experimental support and/or critical reading of the manuscript. Electron microscopy data were collected at the Molecular Electron Microscopy Core facility at University of Virginia. X-ray diffraction data were collected at beamlines 22-BM and 22-ID at the Advanced Photon Source, Argonne National Laboratory. Crystal screening was also performed with the assistance of B. Sankaran through the Collaborative Crystallography Program, Lawrence Berkeley National Laboratory at the Advanced Light Source. This study was supported by a seed grant from the Annette Lightner Foundation (OP) and NIH grants R01-GM112508 (OP) and P50-GM082545 (WIS and BKG-P). JMW was supported by a postdoctoral NIH fellowship (F32-GM115007). MDR participated in this study while on leave from Technical University of Lodz, Poland.

## Additional information

### Competing interests

WIS: Reviewing editor, *eLife*. The other authors declare that no competing interests exist.

### Funding


| Funder | Grant reference number | Author |
|---|---|---|
| National Institutes of Health | R01 GM112508 | Owen Pornillos |
| National Institutes of Health | P50 GM082545 | Barbie K Ganser-Pornillos<br>Wesley I Sundquist |
| National Institutes of Health | F32 GM115007 | Jonathan M Wagner |
| Annette Lightner Foundation | | Owen Pornillos |

The funders had no role in study design, data collection and interpretation, or the decision to submit the work for publication.

### Author contributions

JMW, BKG-P, WIS, OP, Conception and design, Acquisition of data, Analysis and interpretation of data, Drafting or revising the article; MDR, KS, Conception and design, Acquisition of data, Analysis and interpretation of data; SLA, DC, Acquisition of data, Analysis and interpretation of data, Drafting or revising the article; GD, YW, Acquisition of data, Analysis and interpretation of data; GAF, Analysis and interpretation of data, Drafting or revising the article, Contributed unpublished essential data or reagents

### Author ORCIDs

Wesley I Sundquist, http://orcid.org/0000-0001-9988-6021
Owen Pornillos, http://orcid.org/0000-0001-9056-5002

## Additional files

### Supplementary files

• Supplementary file 1. (A) Crystallization conditions for Bcc miniTRIM. (B) Average root mean square deviations over equivalent Cα atoms from superpositions of the miniTRIM monomer structures with 4TN3 (***Goldstone et al., 2014***).
DOI: 10.7554/eLife.16309.023

### Major datasets

The following datasets were generated:

| Author(s) | Year | Dataset title | Dataset URL | Database, license, and accessibility information |
|---|---|---|---|---|
| Jonathan M Wagner, Ginna Doss, Owen Pornillos | 2016 | TRIM5 B-box2 and coiled-coil chimera | http://www.rcsb.org/pdb/explore/explore.do?structureId=5IEA | Publicly available at the Protein Data Bank (accession no. 5IEA) |
| Jonathan M Wagner, Ginna Doss, Owen Pornillos | 2016 | Mini TRIM5 B-box 2 dimer C2 crystal form | http://www.rcsb.org/pdb/explore/explore.do?structureId=5EIU | Publicly available at the Protein Data Bank (accession no. 5EIU) |
| Jonathan M Wagner, Ginna Doss, Owen Pornillos | 2016 | TRIM5 B-box2 and coiled-coil chimera | http://www.rcsb.org/pdb/explore/explore.do?structureId=5F7T | Publicly available at the Protein Data Bank (accession no. 5F7T) |

## References

**Adams PD**, Afonine PV, Bunkóczi G, Chen VB, Davis IW, Echols N, Headd JJ, Hung LW, Kapral GJ, Grosse-Kunstleve RW, McCoy AJ, Moriarty NW, Oeffner R, Read RJ, Richardson DC, Richardson JS, Terwilliger TC, Zwart PH. 2010. PHENIX: a comprehensive Python-based system for macromolecular structure solution. *Acta Crystallographica. Section D, Biological Crystallography* **66**:213–221. doi: 10.1107/S0907444909052925

**Agulleiro JI**, Fernandez JJ. 2011. Fast tomographic reconstruction on multicore computers. *Bioinformatics* **27**: 582–583. doi: 10.1093/bioinformatics/btq692

**Bernadó P**, Mylonas E, Petoukhov MV, Blackledge M, Svergun DI. 2007. Structural characterization of flexible proteins using small-angle X-ray scattering. *Journal of the American Chemical Society* **129**:5656–5664. doi: 10.1021/ja069124n

**Biris N**, Tomashevski A, Bhattacharya A, Diaz-Griffero F, Ivanov DN. 2013. Rhesus monkey TRIM5α SPRY domain recognizes multiple epitopes that span several capsid monomers on the surface of the HIV-1 mature viral core. *Journal of Molecular Biology* **425**:5032–5044. doi: 10.1016/j.jmb.2013.07.025

**Biris N**, Yang Y, Taylor AB, Tomashevski A, Guo M, Hart PJ, Diaz-Griffero F, Ivanov DN. 2012. Structure of the rhesus monkey TRIM5α PRYSPRY domain, the HIV capsid recognition module. *Proceedings of the National Academy of Sciences of the United States of America* **109**:13278–13283. doi: 10.1073/pnas.1203536109

**Campbell EM**, Dodding MP, Yap MW, Wu X, Gallois-Montbrun S, Malim MH, Stoye JP, Hope TJ. 2007. TRIM5 alpha cytoplasmic bodies are highly dynamic structures. *Molecular Biology of the Cell* **18**:2102–2111. doi: 10.1091/mbc.E06-12-1075

**Campbell EM**, Weingart J, Sette P, Opp S, Sastri J, O'Connor SK, Talley S, Diaz-Griffero F, Hirsch V, Bouamr F. 2016. TRIM5α-Mediated Ubiquitin Chain Conjugation Is Required for Inhibition of HIV-1 Reverse Transcription and Capsid Destabilization. *Journal of Virology* **90**:1849–1857. doi: 10.1128/JVI.01948-15

**Cole JL**. 2004. Analysis of heterogeneous interactions. *Methods in Enzymology* **384**:212–232. doi: 10.1016/S0076-6879(04)84013-8

**Diaz-Griffero F**, Kar A, Perron M, Xiang SH, Javanbakht H, Li X, Sodroski J. 2007. Modulation of retroviral restriction and proteasome inhibitor-resistant turnover by changes in the TRIM5alpha B-box 2 domain. *Journal of Virology* **81**:10362–10378. doi: 10.1128/JVI.00703-07

**Diaz-Griffero F**, Li X, Javanbakht H, Song B, Welikala S, Stremlau M, Sodroski J. 2006a. Rapid turnover and polyubiquitylation of the retroviral restriction factor TRIM5. *Virology* **349**:300–315. doi: 10.1016/j.virol.2005.12.040

**Diaz-Griffero F**, Qin XR, Hayashi F, Kigawa T, Finzi A, Sarnak Z, Lienlaf M, Yokoyama S, Sodroski J. 2009. A B-box 2 surface patch important for TRIM5alpha self-association, capsid binding avidity, and retrovirus restriction. *Journal of Virology* **83**:10737–10751. doi: 10.1128/JVI.01307-09

**Diaz-Griffero F**, Vandegraaff N, Li Y, McGee-Estrada K, Stremlau M, Welikala S, Si Z, Engelman A, Sodroski J. 2006b. Requirements for capsid-binding and an effector function in TRIMCyp-mediated restriction of HIV-1. *Virology* **351**:404–419. doi: 10.1016/j.virol.2006.03.023

**Emsley P**, Lohkamp B, Scott WG, Cowtan K. 2010. Features and development of Coot. *Acta Crystallographica. Section D, Biological Crystallography* **66**:486–501. doi: 10.1107/S0907444910007493

**Fletcher AJ**, Christensen DE, Nelson C, Tan CP, Schaller T, Lehner PJ, Sundquist WI, Towers GJ. 2015. TRIM5α requires Ube2W to anchor Lys63-linked ubiquitin chains and restrict reverse transcription. *The EMBO Journal* **34**:2078–2095. doi: 10.15252/embj.201490361

**Fribourgh JL**, Nguyen HC, Matreyek KA, Alvarez FJ, Summers BJ, Dewdney TG, Aiken C, Zhang P, Engelman A, Xiong Y. 2014. Structural insight into HIV-1 restriction by MxB. *Cell Host & Microbe* **16**:627–638. doi: 10.1016/j.chom.2014.09.021

**Fujinaga M**, Berthet-Colominas C, Yaremchuk AD, Tukalo MA, Cusack S. 1993. Refined crystal structure of the seryl-tRNA synthetase from *Thermus thermophilus* at 2.5 A resolution. *Journal of Molecular Biology* **234**:222–233. doi: 10.1006/jmbi.1993.1576

**Ganser-Pornillos BK**, Chandrasekaran V, Pornillos O, Sodroski JG, Sundquist WI, Yeager M. 2011. Hexagonal assembly of a restricting TRIM5alpha protein. *Proceedings of the National Academy of Sciences of the United States of America* **108**:534–539. doi: 10.1073/pnas.1013426108

**Goldstone DC**, Walker PA, Calder LJ, Coombs PJ, Kirkpatrick J, Ball NJ, Hilditch L, Yap MW, Rosenthal PB, Stoye JP, Taylor IA. 2014. Structural studies of postentry restriction factors reveal antiparallel dimers that enable avid binding to the HIV-1 capsid lattice. *Proceedings of the National Academy of Sciences of the United States of America* **111**:9609–9614. doi: 10.1073/pnas.1402448111

**Hanson MA**, Brooun A, Baker KA, Jaakola VP, Roth C, Chien EY, Alexandrov A, Velasquez J, Davis L, Griffith M, Moy K, Ganser-Pornillos BK, Hua Y, Kuhn P, Ellis S, Yeager M, Stevens RC. 2007. Profiling of membrane protein variants in a baculovirus system by coupling cell-surface detection with small-scale parallel expression. *Protein Expression and Purification* **56**:85–92. doi: 10.1016/j.pep.2007.06.003

**Javanbakht H**, Diaz-Griffero F, Stremlau M, Si Z, Sodroski J. 2005. The contribution of RING and B-box 2 domains to retroviral restriction mediated by monkey TRIM5alpha. *Journal of Biological Chemistry* **280**:26933–26940. doi: 10.1074/jbc.M502145200

**Javanbakht H**, Diaz-Griffero F, Yuan W, Yeung DF, Li X, Song B, Sodroski J. 2007. The ability of multimerized cyclophilin A to restrict retrovirus infection. *Virology* **367**:19–29. doi: 10.1016/j.virol.2007.04.034

**Kar AK**, Diaz-Griffero F, Li Y, Li X, Sodroski J. 2008. Biochemical and biophysical characterization of a chimeric TRIM21-TRIM5alpha protein. *Journal of Virology* **82**:11669–11681. doi: 10.1128/JVI.01559-08

**Kovalskyy DB**, Ivanov DN. 2014. Recognition of the HIV capsid by the TRIM5α restriction factor is mediated by a subset of pre-existing conformations of the TRIM5α SPRY domain. *Biochemistry* **53**:1466–1476. doi: 10.1021/bi4014962

**Kremer JR**, Mastronarde DN, McIntosh JR. 1996. Computer visualization of three-dimensional image data using IMOD. *Journal of Structural Biology* **116**:71–76. doi: 10.1006/jsbi.1996.0013

**Langelier CR**, Sandrin V, Eckert DM, Christensen DE, Chandrasekaran V, Alam SL, Aiken C, Olsen JC, Kar AK, Sodroski JG, Sundquist WI. 2008. Biochemical characterization of a recombinant TRIM5alpha protein that restricts human immunodeficiency virus type 1 replication. *Journal of Virology* **82**:11682–11694. doi: 10.1128/JVI.01562-08

**Li X**, Sodroski J. 2008. The TRIM5alpha B-box 2 domain promotes cooperative binding to the retroviral capsid by mediating higher-order self-association. *Journal of Virology* **82**:11495–11502. doi: 10.1128/JVI.01548-08

**Li X**, Yeung DF, Fiegen AM, Sodroski J. 2011. Determinants of the higher order association of the restriction factor TRIM5alpha and other tripartite motif (TRIM) proteins. *Journal of Biological Chemistry* **286**:27959–27970. doi: 10.1074/jbc.M111.260406

**Li Y**, Wu H, Wu W, Zhuo W, Liu W, Zhang Y, Cheng M, Chen YG, Gao N, Yu H, Wang L, Li W, Yang M. 2014. Structural insights into the TRIM family of ubiquitin E3 ligases. *Cell Research* **24**:762–765. doi: 10.1038/cr.2014.46

**Li Y-L**, Chandrasekaran V, Carter SD, Woodward CL, Christensen DE, Dryden KA, Pornillos O, Yeager M, Ganser-Pornillos BK, Jensen GJ, Sundquist WI, Li Y. 2016. Primate TRIM5 proteins form hexagonal nets on HIV-1 capsids. *eLife* **5**:e16269. doi: 10.7554/eLife.16269

**Lienlaf M**, Hayashi F, Di Nunzio F, Tochio N, Kigawa T, Yokoyama S, Diaz-Griffero F. 2011. Contribution of E3-ubiquitin ligase activity to HIV-1 restriction by TRIM5alpha$_{(rh)}$: structure of the RING domain of TRIM5alpha. *Journal of Virology* **85**:8725–8737. doi: 10.1128/JVI.00497-11

**Meroni G**, Diez-Roux G. 2005. TRIM/RBCC, a novel class of 'single protein RING finger' E3 ubiquitin ligases. *BioEssays* **27**:1147–1157. doi: 10.1002/bies.20304

**Otwinowski Z**, Minor W. 1997. Processing of X-ray diffraction data collected in oscillation mode. *Methods Enzymol* **276**:307–326. doi: 10.1016/S0076-6879(97)76066-X.

**Pertel T**, Hausmann S, Morger D, Züger S, Guerra J, Lascano J, Reinhard C, Santoni FA, Uchil PD, Chatel L, Bisiaux A, Albert ML, Strambio-De-Castillia C, Mothes W, Pizzato M, Grütter MG, Luban J. 2011. TRIM5 is an innate immune sensor for the retrovirus capsid lattice. *Nature* **472**:361–365. doi: 10.1038/nature09976

**Plechanovová A**, Jaffray EG, McMahon SA, Johnson KA, Navrátilová I, Naismith JH, Hay RT. 2011. Mechanism of ubiquitylation by dimeric RING ligase RNF4. *Nature Structural & Molecular Biology* **18**:1052–1059. doi: 10.1038/nsmb.2108

**Plechanovová A**, Jaffray EG, Tatham MH, Naismith JH, Hay RT. 2012. Structure of a RING E3 ligase and ubiquitin-loaded E2 primed for catalysis. *Nature* **489**:115–120. doi: 10.1038/nature11376

**Pornillos O**, Ganser-Pornillos BK, Kelly BN, Hua Y, Whitby FG, Stout CD, Sundquist WI, Hill CP, Yeager M. 2009. X-ray structures of the hexameric building block of the HIV capsid. *Cell* **137**:1282–1292. doi: 10.1016/j.cell.2009.04.063

**Pornillos O**, Ganser-Pornillos BK, Yeager M. 2011. Atomic-level modelling of the HIV capsid. *Nature* **469**:424–427. doi: 10.1038/nature09640

**Roa A**, Hayashi F, Yang Y, Lienlaf M, Zhou J, Shi J, Watanabe S, Kigawa T, Yokoyama S, Aiken C, Diaz-Griffero F. 2012. RING domain mutations uncouple TRIM5α restriction of HIV-1 from inhibition of reverse transcription and acceleration of uncoating. *Journal of Virology* **86**:1717–1727. doi: 10.1128/JVI.05811-11

**Sanchez JG**, Okreglicka K, Chandrasekaran V, Welker JM, Sundquist WI, Pornillos O. 2014. The tripartite motif coiled-coil is an elongated antiparallel hairpin dimer. *Proceedings of the National Academy of Sciences of the United States of America* **111**:2494–2499. doi: 10.1073/pnas.1318962111

**Sawyer SL**, Wu LI, Emerman M, Malik HS. 2005. Positive selection of primate TRIM5alpha identifies a critical species-specific retroviral restriction domain. *Proceedings of the National Academy of Sciences of the United States of America* **102**:2832–2837. doi: 10.1073/pnas.0409853102

**Sayah DM**, Sokolskaja E, Berthoux L, Luban J. 2004. Cyclophilin A retrotransposition into TRIM5 explains owl monkey resistance to HIV-1. *Nature* **430**:569–573. doi: 10.1038/nature02777

**Schneider CA**, Rasband WS, Eliceiri KW. 2012. NIH Image to ImageJ: 25 years of image analysis. *Nature Methods* **9**:671–675. doi: 10.1038/nmeth.2089

**Sebastian S**, Luban J. 2005. TRIM5alpha selectively binds a restriction-sensitive retroviral capsid. *Retrovirology* **2**. doi: 10.1186/1742-4690-2-40

**Shen Y**, Maupetit J, Derreumaux P, Tufféry P. 2014. Improved PEP-FOLD Approach for Peptide and Miniprotein Structure Prediction. *Journal of Chemical Theory and Computation* **10**:4745–4758. doi: 10.1021/ct500592m

**Stremlau M**, Owens CM, Perron MJ, Kiessling M, Autissier P, Sodroski J. 2004. The cytoplasmic body component TRIM5alpha restricts HIV-1 infection in Old World monkeys. *Nature* **427**:848–853. doi: 10.1038/nature02343

**Stremlau M**, Perron M, Lee M, Li Y, Song B, Javanbakht H, Diaz-Griffero F, Anderson DJ, Sundquist WI, Sodroski J. 2006. Specific recognition and accelerated uncoating of retroviral capsids by the TRIM5alpha restriction factor. *Proceedings of the National Academy of Sciences of the United States of America* **103**:5514–5519. doi: 10.1073/pnas.0509996103

**Weinert C**, Morger D, Djekic A, Grütter MG, Mittl PR. 2015. Crystal structure of TRIM20 C-terminal coiled-coil/B30.2 fragment: implications for the recognition of higher order oligomers. *Scientific Reports* **5**. doi: 10.1038/srep10819

**Yang H**, Ji X, Zhao G, Ning J, Zhao Q, Aiken C, Gronenborn AM, Zhang P, Xiong Y. 2012. Structural insight into HIV-1 capsid recognition by rhesus TRIM5α. *Proceedings of the National Academy of Sciences of the United States of America* **109**:18372–18377. doi: 10.1073/pnas.1210903109

**Yap MW**, Mortuza GB, Taylor IA, Stoye JP. 2007. The design of artificial retroviral restriction factors. *Virology* **365**:302–314. doi: 10.1016/j.virol.2007.04.005

**Yudina Z**, Roa A, Johnson R, Biris N, de Souza Aranha Vieira DA, Tsiperson V, Reszka N, Taylor AB, Hart PJ, Demeler B, Diaz-Griffero F, Ivanov DN. 2015. RING Dimerization Links Higher-Order Assembly of TRIM5α to Synthesis of K63-Linked Polyubiquitin. *Cell Reports* **12**:788–797. doi: 10.1016/j.celrep.2015.06.072

# Appendix 3.

# Mechanism of Ska Recruitment by Ndc80 Complexes to Kinetochores

Paweł Ł. Janczyk, Katarzyna A. Skorupka, John G. Tooley, Daniel R. Matson, Cortney A. Kestner, Thomas West, Owen Pornillos, P. Todd Stukenberg

Developmental Cell 41, 438–449, May 22, 2017, https://doi.org/10.1016/j.devcel.2017.04.020

Article

Developmental Cell

# Mechanism of Ska Recruitment by Ndc80 Complexes to Kinetochores

## Highlights

- The Ndc80 complex orients the Ska complex along microtubule protofilaments
- The Ndc80 unstructured tail recruits the Ska complex to kinetochore
- Structural view of a putative metazoan kinetochore-microtubule attachment
- Clusters of Ndc80, which are seen on microtubules in vitro, may function in vivo

## Authors

Paweł Ł. Janczyk,
Katarzyna A. Skorupka,
John G. Tooley, ..., Thomas West,
Owen Pornillos, P. Todd Stukenberg

## Correspondence

pts7h@virginia.edu

## In Brief

The Ska complex matures kinetochore-microtubule attachments, but it is unclear how kinetochores recruit Ska. Janczyk et al. show that Ndc80 complex on microtubules can directly recruit the Ska complex and orient it along microtubules. Mutants of the Ndc80 tail that cannot cluster along microtubules do not recruit Ska to kinetochores.

Janczyk et al., 2017, Developmental Cell *41*, 438–449
May 22, 2017 
http://dx.doi.org/10.1016/j.devcel.2017.04.020

CellPress

CellPress

Developmental Cell
Article

# Mechanism of Ska Recruitment by Ndc80 Complexes to Kinetochores

Paweł Ł. Janczyk,[1,2] Katarzyna A. Skorupka,[2] John G. Tooley,[1] Daniel R. Matson,[1] Cortney A. Kestner,[1] Thomas West,[1] Owen Pornillos,[2] and P. Todd Stukenberg[1,3,*]

[1]Department of Biochemistry and Molecular Genetics, University of Virginia School of Medicine, 1340 Jefferson Park Avenue, Pinn Hall, Room 6014

[2]Department of Molecular Physiology and Biological Physics, University of Virginia School of Medicine Charlottesville, VA 22908, USA

[3]Lead Contact

*Correspondence: pts7h@virginia.edu

http://dx.doi.org/10.1016/j.devcel.2017.04.020

## SUMMARY

**Yeast use the ring-shaped Dam1 complex to slide down depolymerizing microtubules to move chromosomes, but current models suggest that other eukaryotes do not have a sliding ring. We visualized Ndc80 and Ska complexes on microtubules by electron microscopic tomography to identify the structure of the human kinetochore-microtubule attachment. Ndc80 recruits the Ska complex so that the V shape of the Ska dimer interacts along protofilaments. We identify a mutant of the Ndc80 tail that is deficient in Ska recruitment to kinetochores and in orienting Ska along protofilaments in vitro. This mutant Ndc80 binds microtubules with normal affinity but is deficient in clustering along protofilaments. We propose that Ska is recruited to kinetochores by clusters of Ndc80 proteins and that our structure of Ndc80 and Ska complexes on microtubules suggests a mechanism for metazoan kinetochores to couple the depolymerization of microtubules to power the movement of chromosomes.**

## INTRODUCTION

Current models suggest that kinetochores use the energy stored in the microtubule polymer to move chromosomes to the metaphase plate and to segregate chromatids in anaphase (Powers et al., 2009; Grishchuk et al., 2008; Grishchuk and McIntosh, 2006; Molodtsov et al., 2005). To do so, kinetochores must remain bound to the plus end of the microtubule polymer while it depolymerizes. As microtubules depolymerize, each protofilament first splays away from the tube to form a curved end, which subsequently loses subunits (Tran et al., 1997). This splaying can generate force (Grishchuk et al., 2005). Budding yeast have a ring shaped Dam1 complex that can be pushed back by the curving ends, providing a mechanism to harness the energy in a microtubule to move chromosomes (Grishchuk et al., 2008; Wang et al., 2007; Westermann et al., 2006; Molodtsov et al., 2005; Westermann et al., 2005). However, the Dam1 complex has only been found in fungi and most metazoans have the Ska complex, which has been proposed to have similar function but does not form rings.

All eukaryotes require the Ndc80 complex to generate attachments with the microtubule plus end (McCleland et al., 2004; McCleland et al., 2003; DeLuca et al., 2002; Janke et al., 2001; Wigge and Kilmartin, 2001). Ndc80 has a microtubule attachment site at the end of a long coiled coil (Ciferri et al., 2008; Ciferri et al., 2005). Current models for Ndc80 function in metazoans suggest a passive model in which multiple Ndc80 proteins interact with the same microtubule as it depolymerizes (Zaytsev et al., 2015; Zaytsev et al., 2014; Powers et al., 2009). As Ndc80 prefers to bind the microtubule polymer rather than free tubulin subunits, the kinetochore remains attached as long as some Ndc80 remains bound to the polymer. In these models, it is unclear how the curvature of depolymerizing microtubules could be used as a power stroke.

An N-terminal calponin homology domain (CHD) of the Ndc80 subunit (also called Hec1) directly binds the lateral sides of microtubules, and this attachment is critical for the movements of chromosomes on the mitotic spindle (Tooley et al., 2011; Ciferri et al., 2008; Wei et al., 2007). The binding of the CHD to microtubules is regulated by an unstructured and positively charged 80-amino-acid N-terminal tail of Ndc80 (Guimaraes et al., 2008; Miller et al., 2008; Cheeseman et al., 2006). Each kinetochore has at least seven Ndc80 complexes per microtubule attachment (Suzuki et al., 2015; Johnston et al., 2010; Joglekar et al., 2008; Joglekar et al., 2006; Emanuele et al., 2005). Ndc80 complexes can bind along protofilaments in clusters in vitro, but current models suggest that multiple Ndc80 complexes bind a microtubule as single entities in vivo (Zaytsev et al., 2015; Zaytsev et al., 2014; Powers et al., 2009). Clustering in vitro is mediated by the Ndc80 tail (Alushin et al., 2010), which sits between CHDs of adjacent subunits (Alushin et al., 2012). This region also directly binds microtubules and is phosphorylated on multiple sites by Aurora B, and dephosphorylation of this zone is required for proper alignment of chromosomes to the metaphase plate (Guimaraes et al., 2008; Miller et al., 2008; Cheeseman et al., 2006; DeLuca et al., 2011). Phosphorylation of the tail has a minimal effect on the clustering of Ndc80 molecules along microtubules in vitro (Zaytsev et al., 2015).

The spindle and kinetochore-associated complex (Ska) is enriched on kinetochores of aligned chromosomes, and has been

implicated in chromosome movements and silencing of the spindle assembly checkpoint (SAC) (Sivakumar et al., 2016; Sivakumar et al., 2014; Schmidt et al., 2012; Daum et al., 2009; Welburn et al., 2009; Hanisch et al., 2006). It binds microtubules but its central function in mitotic exit is to recruit PP1 to kinetochores (Sivakumar et al., 2016; Schmidt et al., 2012; Welburn et al., 2009). The core of the Ska complex is composed of three coiled-coil regions where the three Ska proteins come together to form a core W- or V-shaped structure (Jeyaprakash et al., 2012). Ska directly binds microtubules and can track the plus ends of depolymerizing microtubules (Schmidt et al., 2012; Welburn et al., 2009). Depletion of any member of the Ska complex results in prolonged, checkpoint-dependent metaphase arrest and eventually cell death (Daum et al., 2009). Despite lack of sequence or structural similarity, it has been suggested that the Ska complex may be functionally equivalent to the yeast Dam1 complex (Abad et al., 2014; Gaitanos et al., 2009; Welburn et al., 2009).

A critical unanswered question is how the Ska complex is recruited to kinetochores. The recruitment of Ska is dependent on the Knl1-Mis12-Ndc80 (KMN) network (Chan et al., 2012; Raaijmakers et al., 2009; Welburn et al., 2009; Hanisch et al., 2006) and is regulated by Aurora B kinase (Chan et al., 2012). Although Ndc80 and Ska have not been shown to interact in vitro, Ndc80 can increase the binding affinity of Ska to microtubules (Schmidt et al., 2012), suggesting that they may form a complex on microtubules. Moreover, expression of a mutant Ndc80 that lacks a flexible hinge in the coiled-coil region prevents Ska recruitment, but there is no evidence that Ska binds this hinged region (Zhang et al., 2012). A recent study suggests that EB1, which specifically binds polymerizing microtubules, recruits Ska to kinetochores, and orients Ska across a microtubule polymer, similarly to the Dam1 complex in yeast (Thomas et al., 2016).

Chromosome movements are predicated on the ability of kinetochores to remain attached to depolymerizing microtubule plus ends (Powers et al., 2009; Grishchuk et al., 2008; Grishchuk and McIntosh, 2006; Molodtsov et al., 2005). Individual Ndc80 complexes can track depolymerizing ends in vitro if they are oligomerized or bound to a bead at a density high enough for multiple Ndc80 proteins to interact with a single microtubule (Powers et al., 2009). However, individual Ndc80 complexes cannot track depolymerizing microtubule ends on their own (Schmidt et al., 2012; Powers et al., 2009). This has led to a passive model of depolymerization-coupled movement whereby oligomerized Ndc80 proteins can track ends because some individual complexes remain attached, while others must release when they are bound to a depolymerizing subunit. Although Ndc80 and Ska have not been shown to interact in solution, Ndc80 can increase the affinity of Ska and microtubules (Schmidt et al., 2012). We investigated the structure of the full human Ska complex that is recruited to taxol-stabilized microtubules by the Ndc80 by negative-stain electron microscopy (EM) tomography. Ndc80 CHDs orient Ska along the straight segment of the microtubule such that both Ska microtubule binding sites interact with the same or adjacent protofilaments separated by approximately five to six tubulin monomers. We provide evidence that this structure also exists in kinetochores in vivo and that Ndc80 must oligomerize to recruit Ska to kinetochores. Our data suggest mechanisms by which a complex of Ska and Ndc80 form a structure that has important implications for movements of chromosomes by kinetochores.

## RESULTS

### Ndc80 Orients the Ska Complex along a Microtubule Protofilament

We investigated the structure of the full human Ska complex and an engineered subcomplex of the Ndc80 complex that lacks the majority of its coiled-coil domains ($Ndc80^{Bonsai}$) (Ciferri et al., 2008) on taxol-stabilized microtubules by negative-stain EM tomography (Figure 1A). Throughout this study (unless specifically indicated) we used concentrations of Ska that were below the dissociation constant ($K_D$) of intrinsic microtubule binding ($K_D$ = 2.4–5.1 μM [Schmidt et al., 2012]) to specifically visualize the Ska complex that was recruited by Ndc80 to microtubules. V-shaped structures were detected on the microtubules that were incubated with both $Ndc80^{Bonsai}$ WT and Ska (Figures 1A and S1A; Movies S2 and S3). These V shapes are highly reminiscent of the dimer unit identified in the crystal structure of the Ska core complex, which is a dimer of all three Ska subunits (180 Å × 80 Å) (Jeyaprakash et al., 2012). Our V shapes have a length of 201 ± 24 Å and a width of 90 ± 13 Å (Figures 1B and S1B, n = 52 V shapes measured), and the crystal structure of the Ska core complex fits into these densities (Figure 1C and Movie S4). Since the core structure lacks the two Ska1 C-terminal domains (CTD, ~50 Å × 10 Å) and the Ska3 C-terminal regions that are in our structures, we suggest that the V shapes are the correct size and shape to contain the Ska core complex and two Ska1 CTDs. We could not see any similar densities on microtubules treated only with Ska at the concentration used to visualize the complex with $Ndc80^{Bonsai}$ WT (1 μM); however, we detected some V-shaped structures on microtubules coated with Ska complex in concentrations above the $K_D$ (4 μM) (Figure 1A). The number of those structures was significantly lower than on microtubules treated with both Ndc80 and sub-$K_D$ concentrations of Ska, suggesting that the orientation of Ska molecules along protofilaments is dependent on the presence of Ndc80 (Figure 1D; +4CT is described below). Therefore, we suggest that the V shapes recruited by Ndc80 that we observe in our tomographic reconstructions are composed of Ska complexes oriented along protofilaments on the wall of a microtubule. The V shapes that we visualize appear to be oriented along a single microtubule protofilament, although the resolution is not good enough to distinguish whether they start and finish on adjacent protofilaments.

We also measured the distance (D) from the centroid of the tip of V shapes to the attaching protofilament (as defined by the line running through centroids of tubulin monomers) (Figures 1E, 1F, and S1C). We observed that in the presence of Ndc80, V shapes were positioned further away from microtubule than in tomograms of high concentration of Ska and microtubules alone. This suggests that Ndc80 either increases the height of Ska on the microtubule or increases the frequency that Ska binds along a single protofilament rather than spanning two or more adjacent protofilaments.

### Ska Is in Close Proximity to the Calponin Homology Domain of Ndc80 at Kinetochores

It is unclear how Ska is recruited to the kinetochore, and our tomograms suggest that Ndc80 directly recruits Ska to microtubules. We sought in vivo data to support or reject such a model.

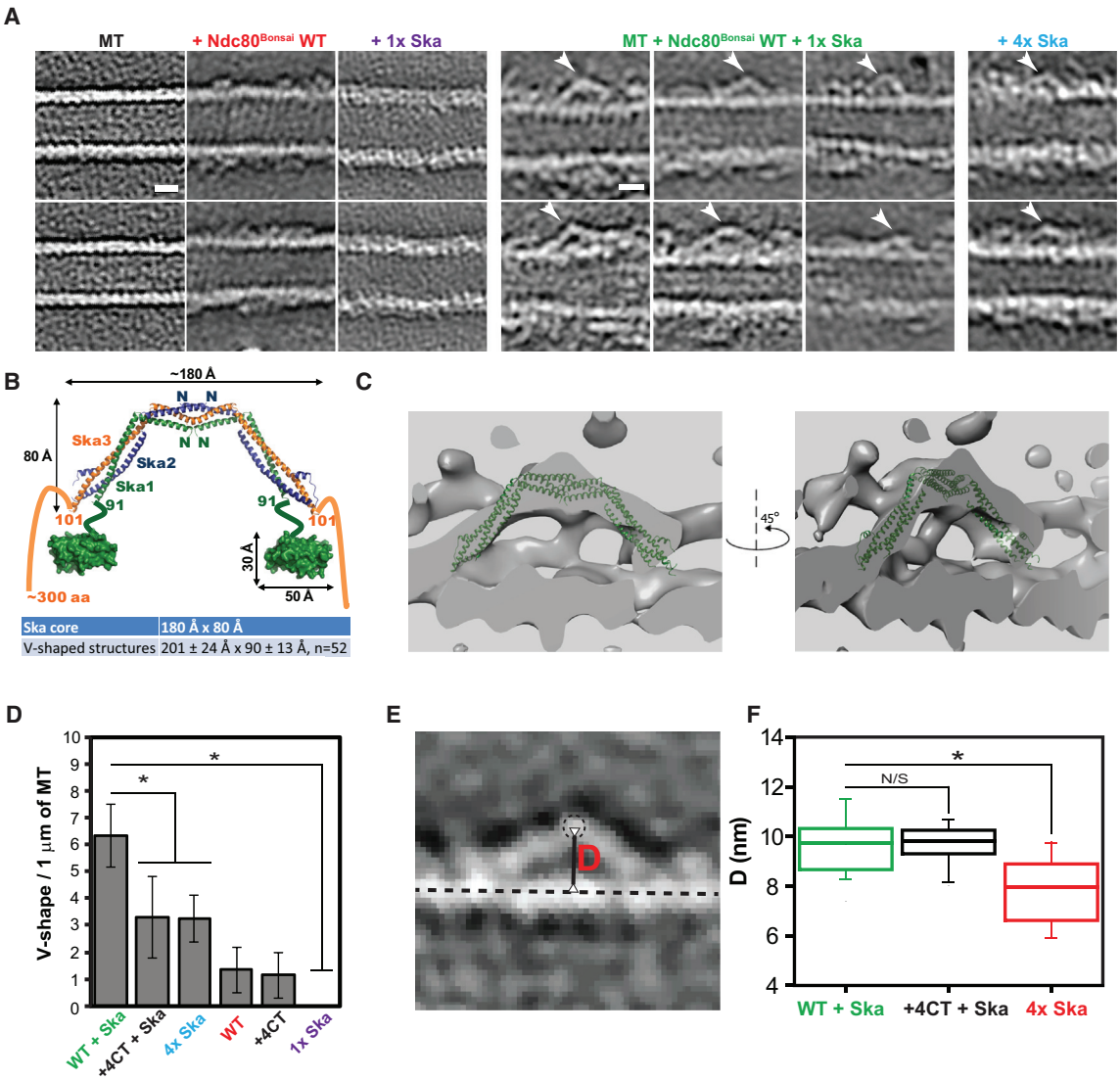


**Figure 1. Ndc80 Recruits Ska Complex to Microtubule Protofilament**

(A) Representative slices (thickness, 0.4427 nm) of tomographic reconstructions of taxol-stabilized microtubules (MT), microtubules decorated by Ndc80$^{Bonsai}$ wild-type (WT) (red, Movie S1), 1× Ska complex (purple), Ndc80$^{Bonsai}$ WT, and 1× Ska complexes (green, six images), or saturating concentration of Ska (4× Ska, cyan). White arrowheads indicate positions of the tips of the V shapes. Scale bars, 10 nm.

(B) Model of the Ska complex based on structures of the Ska complex core (PDB: 4AJ5) and Ska1 CTD (C-terminal domain = MTBD, microtubule binding domain, PDB: 4CA0). Comparison between size of the Ska core complex dimer from crystal structure and average measured size of the V shapes identified in tomographic reconstructions of microtubules incubated with both Ndc80$^{Bonsai}$ WT and Ska is shown in the table below (mean ± SD). w, width; h, height; n, number of V shapes measured.

(C) Structure of Ska core complex (PDB: 4AJ5) fitted to EM map of representative V shape. Thickness: 2.6568 nm.

(D) Quantification of the V-shaped densities on microtubules identified in tomographic reconstructions. WT, Ndc80$^{Bonsai}$ WT; +4CT, Ndc80$^{Bonsai}$ + 4CT (mean ± SD, average of seven microtubules scored; *$p < 0.0002$, Student's t test).

(E) Distance (D, red) between centroid of tip of V shape (dashed-line circle) and line connecting centroids of tubulin subunits within a single protofilament (dashed straight line) was measured and represented visually.

(F) Box-and-whisker plot of distribution of distances between tips of V shapes and microtubule protofilaments measured as shown in (D) (central line, median; whiskers represent 10%–90% range; n = 58, 18, 22, respectively). *$p < 0.000001$; N/S, not significant ($p > 0.99$) (Student's t test).

We utilized the proximity ligation assay (PLA), which produces a fluorescent signal if two antigens are closer than 25 nm to each other (Soderberg et al., 2006). We confirmed that PLA measures subkinetochore proximity by showing that antibodies recognizing a tag on the C terminus of the Ndc80 protein generates signals when coupled with antibodies to the Spc25 subunit of the Ndc80 complex, but not when coupled with a kinetochore protein in another complex (Zw10, Figure S2). PLA was used to measure the proximity between the Ndc80 CHD and the Ska3 protein. After the PLA reaction was performed, the cells were additionally

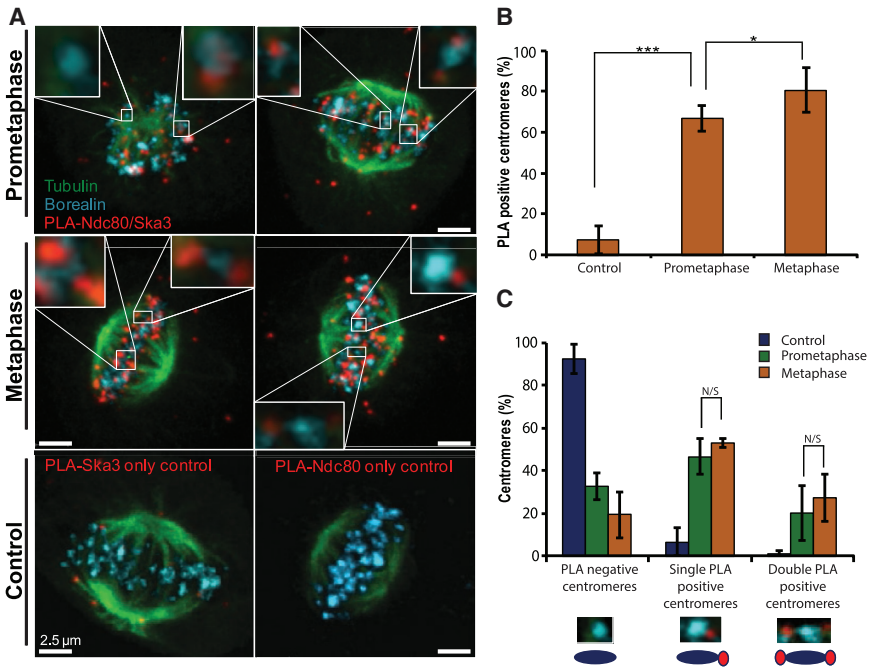


**Figure 2. Ndc80 Interacts with Ska3 in Both Prometaphase and Metaphase**

(A) Representative images of Ska3-Ndc80 proximity ligation assay (red), with additional immunostaining of Borealin (cyan) and tubulin (green). Top, prometaphase cells; middle, metaphase cells; bottom, control metaphase cells.

(B) Centromeres in prometaphase or metaphase cells, as identified by Borealin immunostaining, were scored based on the proximity to Ska3-Ndc80 PLA signal (mean ± SD; n > 100 centromeres from four cells). Cells with only Ska3 probe were used as a control. *p < 0.05, ***p < 0.0001 (Student's t test).

(C) Centromeres in prometaphase or metaphase cells, as identified by Borealin immunostaining, scored based on the number of proximal Ska3-Ndc80 PLA signals (mean ± SD; n > 100 centromeres from four cells). N/S, not significant (p > 0.05) (Student's t test).

stained with antibodies to tubulin and Borealin to identify the spindle and inner centromeres, respectively. The PLA signal was highly enriched at centromeres of mitotic cells and these signals were rarely found in control cells, where one of the two primary antibodies in the PLA reaction was omitted (Figure 2A). There were also foci of PLA signal in the cytoplasm of mitotic cells, which may represent interactions between soluble complexes. We quantified the number of Ndc80-Ska3 PLA spots adjacent to centromeres and found that Ndc80 and Ska3 appear to be in close proximity at both prometaphase and metaphase centromeres (Figure 2B). Sixty-seven percent of prometaphase centromeres were associated with at least one PLA signal and this increased to 80% of centromeres during metaphase. The number of centromeres associated with two PLA signals facing opposite poles, which would be expected when both chromatids are stably attached to microtubules, increased in metaphase relative to prometaphase, but the difference was not significant (Figure 2C). These data demonstrate that Ndc80 CHD and Ska reside in close proximity at end-on attached kinetochores.

## Point Mutations in the Ndc80 Tail Prevent Recruitment of Ska to Kinetochores In Vivo and Inhibit Formation of V Shapes In Vitro

We often saw densities reminiscent of clusters of Ndc80 on a protofilament adjacent to our V shapes in our tomograms, which suggested that Ska is recruited by a cluster of Ndc80 molecules along an end-on attached microtubule protofilament. We designed a mutant in Ndc80 that would allow us to test whether clusters of Ndc80 recruit Ska to kinetochores in vivo. Clustering of Ndc80 is mediated by an 80-amino-acid unstructured N-terminal tail of the Ndc80 protein (Alushin et al., 2010, Alushin et al., 2012). The amino acid residues within the tail have a net charge of +10, and this charge is essential for Ndc80 function (Tooley et al., 2011). Cryo-EM densities of Ndc80$^{Bonsai}$ proteins on microtubules have oriented the globular domains unambiguously on microtubules (Alushin et al., 2010). In these studies the tail can be seen as a density, but definitive assignments are not possible, consistent with the tail region being more loosely structured after microtubule binding. Instead, the tail can be seen as a density connected to the unambiguously assigned amino acid 81, which fills a groove formed by two adjacent Ndc80 CHDs (Alushin et al., 2012). These tail densities then emerge on the back of two adjacent Ndc80 CHDs to form a large region that appears to bridge two adjacent CHDs (Figure 3A). We examined the surface charge of the groove between adjacent CHDs and found adjacent negatively charged patches facing each other in the groove. We hypothesized that these negatively charged patches would repel adjacent subunit binding and that clustering is enabled by positive charges on the tail, which negate this repulsion. Therefore, we mutated the positively charged regions that bridge two adjacent subunits by generating the mutant Ndc80$^{K(42,47,53,59)A,R(52,60)A}$ (Figure 3B). We have named this mutant +4CT because the overall charge of the unstructured tail is now +4 (instead of +10) and the charge has been removed from the C-terminal region. As a control, we generated a similar mutant (Ndc80$^{K(2,26,35)A,R(3,13,20)A}$ (Ndc80$^{+4NT}$), Figure 3B), which eliminates the same amount of charge on amino acids in the N-terminal part of the Ndc80 tail. Both of these mutants could be phosphorylated by Aurora B in vitro (Figures S3A–S3C).

We depleted endogenous Ndc80 from HeLa cells and expressed a small interfering RNA (siRNA)-resistant Ndc80$^{+4CT}$-GFP or Ndc80-GFP from an integrated loci. We then measured the levels of the endogenous Ska complex at kinetochores using antibodies to the Ska3 protein. Cells complemented with the Ndc80$^{+4CT}$ protein had significantly reduced levels of the Ska protein, but not another outer kinetochore protein Dsn1, relative to those rescued with the wild-type (WT) Ndc80 protein (Figures 3C, 3D, S4A, and S4B). Cells complemented with Ndc80$^{+4NT}$-GFP had similar amounts of Ska as those complemented with the WT Ndc80 protein, demonstrating that the location of the

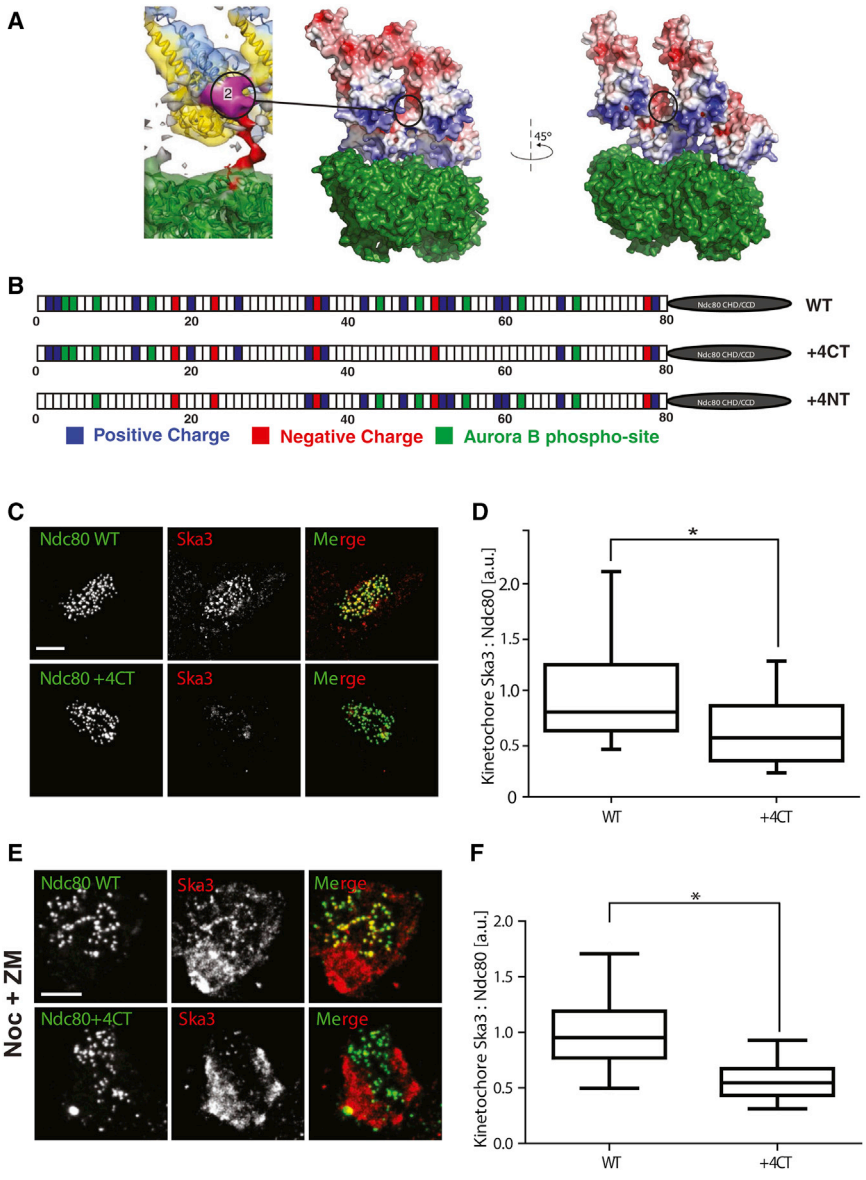


**Figure 3. Ndc80$^{+4CT}$ Mutant Is Deficient in Recruitment of Ska3 to the Kinetochore**

(A) Left: purple indicates localization of electron density patch attributed to the C-terminal region of Ndc80 tail. Note that it sits between two adjacent calponin homology domains (CHDs) (adapted from Alushin et al., 2012). Right: electrostatic surface potential of two Ndc80 CHDs bound to tubulin dimer with the tail densities removed, bound to a microtubule (PDB: 3IZ0) to illustrate the negatively charged surface between the Ndc80 CHD molecules. Black ellipse represents the localization of the purple patch visualized on the left panel. We mutated positively charged residues in the C-terminal region of the patch, assuming that they bridged the negatively charged surfaces on the Ndc80 CHD to generate cooperative binding.

(B) Cartoon depicting the wild-type (WT) Ndc80, Ndc80$^{+4CT}$, and Ndc80$^{+4NT}$ tail mutants to illustrate the change in charge that is created by the K/R to A changes in the Ndc80$^{+4CT}$ and Ndc80$^{+4NT}$ proteins. Although it is likely that we are also affecting Aurora B phosphorylation sites since they are defined by K/RxS/T amino acids, we do not observe significant differences in in vitro phosphorylation by Aurora B between mutants and WT protein (Figures S3A–S3C). CHD, calponin homology domain; CCD, coiled-coil domain. Drawing not to scale.

(C) Immunofluorescence staining of Ndc80$^{WT}$ and Ndc80$^{+4CT}$ stable cell lines after depletion of endogenous Ndc80 shows reduced levels of Ska3 on the kinetochores of Ndc80$^{+4CT}$ stable cell lines. Scale bar, 5 μm.

(D) Box-and-whisker plots representing the quantification of Ska staining intensities on kinetochores represented in (C) (n > 100 kinetochores from at least five cells; whiskers represent 5th–95th percentile). a.u., arbitrary units. *p < 0.0001 (unpaired t test with Welch's correction).

(E) Immunofluorescence staining of Ndc80$^{WT}$ and Ndc80$^{+4CT}$ stable cell lines treated with 3.3 μM nocodazole (Noc) and 2 μM ZM447439 (ZM) after depletion of endogenous Ndc80 shows reduced levels of Ska3 (red) on kinetochores. Scale bar, 5 μm.

(F) Box-and-whisker plot representing the quantification of the Ska staining intensities on kinetochores in cells treated with nocodazole and ZM447439 represented in (E) (n > 100 kinetochores from at least five cells; whiskers represent 5th–95th percentile). a.u., arbitrary units. *p < 0.0001 (unpaired t test with Welch's correction).

positive charge on the tail, and not simply the overall charge, is critical to localize Ska (Figures S4C and S4D). Aurora kinases directly phosphorylate the Ska protein to inhibit its localization to kinetochores (Chan et al., 2012), thus ensuring that the Ska protein is not recruited to kinetochores before microtubule attachment. However, cells treated with nocodazole can recruit Ska complex if the cells are also treated with Aurora inhibitors (Chan et al., 2012). The Ndc80$^{+4CT}$ mutant was also defective in recruiting Ska under these conditions (Figures 3E and 3F). Thus, the Ndc80 tail regulates the recruitment of the Ska complex to kinetochores under all known conditions that have been shown to localize Ska.

We also visualized complexes generated by Ndc80$^{Bonsai}$ +4CT, Ska, and microtubules by negative-stain EM tomography in vitro. The V-shaped Ska-containing complexes that were easily seen with Ndc80$^{Bonsai}$ WT were observed significantly less often on microtubules visualized by tomography after incubation with Ndc80$^{Bonsai}$ +4CT and Ska (Figure 1D). We think that Ndc80$^{Bonsai}$ +4CT can recruit Ska, albeit with reduced frequency to Ndc80$^{Bonsai}$ WT, since the increased distance from the top of the V shape to the microtubule was similar in Ndc80$^{Bonsai}$ +4CT and Ndc80$^{Bonsai}$ WT (Figure 1F). Together, our identification of a mutant that is deficient at forming V shapes with Ndc80 in vitro and recruitment at kinetochores provides evidence that the tail of Ndc80 has an important function in recruiting the Ska protein to kinetochores, and suggests that V shapes we see in vitro can form on microtubules at kinetochores.

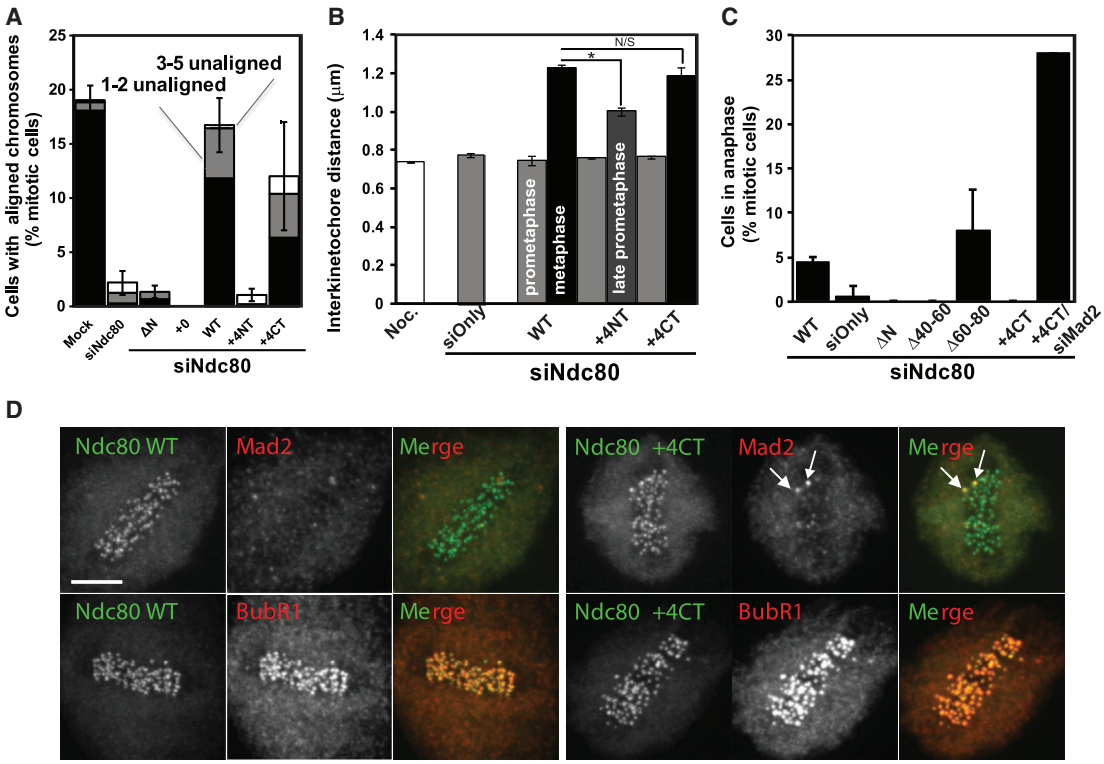


**Figure 4. Ndc80$^{+4CT}$ Tail Mutant Metaphase Arrest Does Not Satisfy Spindle Assembly Checkpoint and Is Aurora Dependent**

(A) Graph representing chromosome alignment among mitotic cells expressing Ndc80 mutants. Mitotic cells were scored for chromosome alignment into a metaphase plate, and the percentage of metaphase cells was plotted. Metaphase cells were further subdivided to indicate cells with all chromosomes aligned (black), cells with 1–2 unaligned chromosomes (gray), and cells with 3–5 unaligned chromosomes (white). Mitotic cells with six or more unaligned chromosomes are not shown on the graph. n > 100 mitotic cells counted per experiment (n = 3). WT, wild-type. Data represent mean ± SD (SD represents total of cells with 0–5 unaligned chromosomes).

(B) Graph representing inter-kinetochore distance measurements in cells expressing Ndc80 mutants. Ten sister kinetochores in at least five cells (n > 50) were identified by anti-centromere antibody (ACA) staining between Ndc80 signals, and the distance between those sister kinetochores was measured (n = 3). The distance (mean ± SD) is plotted for early prometaphase (EPM) (gray), late prometaphase (LPM) (dark gray), and metaphase (black) cells, Noc, nocodazole-treated cells (white). *p < 0.0002; N/S, not significant (p > 0.2) (Student's t test).

(C) The percentage of mitotic cells in anaphase was plotted for Ndc80$^{WT}$, Ndc80 knockdown, and indicated Ndc80 tail mutant cells (mean ± SD). For the Ndc80$^{+4CT}$ mutant, cells were also co-transfected with siRNA targeting Mad2. For Ndc80 tail mutants, 100 mitotic cells were counted per experiment (n = 3). For Mad2 co-transfection with Ndc80$^{+4CT}$, 25 cells were counted.

(D) Immunofluorescence staining of Ndc80$^{WT}$ and Ndc80$^{+4CT}$ (green) stable lines after depletion of endogenous Ndc80. Ndc80$^{+4CT}$ cells arrest with at least one Mad2-positive kinetochore (indicated by arrows, red, upper row) with no loss of BubR1 localization (red, lower row). Scale bar, 5 μm.

## The Ndc80$^{+4CT}$ Phenocopies Loss of Ska Complex, while the Ndc80$^{+4NT}$ Recruits Ska to Kinetochores that Lack "End-On" Microtubule Attachments

We characterized the mitotic phenotypes of HeLa cells depleted of the endogenous Ndc80 protein and rescued with the Ndc80$^{+4CT}$ and Ndc80$^{+4NT}$ mutants. The Ndc80$^{+4CT}$ mutant was capable of aligning chromosomes, although slightly less efficiently than cells rescued with the WT protein (12.0% ± 1.7% of total mitotic cells) (Figure 4A). This phenotype is similar to the reduction of Ska, which slightly delays chromosome congression (Daum et al., 2009; Gaitanos et al., 2009; Hanisch et al., 2006). Strikingly, the Ndc80$^{+4NT}$ mutant was far less effective at aligning chromosomes than the Ndc80$^{+4CT}$. Only 1.7% ± 0.8% of mitotic Ndc80$^{+4NT}$ cells were able to align their chromosomes (Figure 4A), making the Ndc80$^{+4NT}$ alignment phenotype more comparable with the phenotype achieved by complete depletion of the Ndc80 complex or by the loss of all net positive charges from the tail (Tooley et al., 2011). This result reinforces the concept that the Ndc80 tail is instead composed of two distinct regions and not a random stretch of positive charges (Alushin et al., 2012).

Next, we determined the ability of kinetochores with mutated Ndc80 to exert pulling forces on bound microtubules. We measured the distance between the sister kinetochores (inter-kinetochore distance) of aligned chromosomes as a readout for the strength of the kinetochore-microtubule interaction. Cells in early prometaphase have formed few productive kinetochore-microtubule interactions, and inter-kinetochore distance measurements for these cells were therefore comparable with those of Ndc80 knockdown cells or cells treated with high doses of nocodazole (Figure 4B). Few cells expressing the Ndc80$^{+4NT}$ mutant had metaphase-aligned chromosomes, so we measured late prometaphase Ndc80$^{+4NT}$ cells instead. The average inter-kinetochore distance in these cells was 1.00 ± 0.02 μm,

suggesting that kinetochores containing the Ndc80$^{+4NT}$ mutant generated reduced force. In contrast, aligned chromosomes in Ndc80$^{+4CT}$ metaphase cells had an average inter-kinetochore distance measurement of 1.18 ± 0.04 μm, which is similar to the average measurement for Ndc80$^{WT}$ metaphase chromosomes (1.23 ± 0.02 μm). We conclude that the Ndc80$^{+4CT}$ mutant can move chromosomes and generate full inter-kinetochore pulling forces, although the Ndc80$^{+4NT}$ loses all Ndc80 function and acts like mutants that completely lose microtubule binding activities (Tooley et al., 2011; Miller et al., 2008), even though it still efficiently recruits Ska complex to the kinetochores (Figures S4C and S4D). This suggests that Ska recruitment is not triggered by the generation of end-on attachments.

If the Ndc80$^{+4CT}$ mutant is deficient in recruitment of Ska to kinetochores, it should phenocopy loss of Ska. Cells depleted of the Ska complex align chromosomes to the metaphase plate but fail to silence the SAC because Ska has a second function as a protein that directly recruits PP1 to kinetochores (Sivakumar et al., 2016; Daum et al., 2009). Ndc80$^{+4CT}$ cells were capable of forming a metaphase plate and generating full tension on aligned chromosomes; however, no cells expressing this mutant entered anaphase over the course of the experiment. A similar phenotype was seen when this mutated C-terminal region of the Ndc80 tail was deleted (Ndc80$^{\Delta 40-60}$). In contrast, 4.4% ± 0.7% of Ndc80$^{WT}$ mitotic cells and 8.0% ± 4.6% of Ndc80$^{\Delta 60-80}$ mitotic cells were observed in anaphase (Figure 4C). This suggests that impairing the function of the C-terminal microtubule binding region, either by engineering point mutations or by making wholesale deletions, halts anaphase entry and phenocopies loss of Ska.

To determine whether this cell-cycle delay was caused by an active SAC signal, we performed a knockdown and rescue experiment of Ndc80 and concurrently depleted the SAC protein Mad2. Twenty-eight percent of Ndc80$^{+4CT}$ cells depleted of Mad2 were observed in anaphase, in sharp contrast to the absence of anaphase figures in Ndc80$^{+4CT}$ cells with functional SAC (Figure 4C). When we examined the kinetochore localization of Mad2 in metaphase Ndc80$^{+4CT}$ cells, we found that Mad2 was lost from most kinetochores, similarly to Ndc80$^{WT}$ controls. However, we almost always observed one kinetochore with robust Mad1 staining. This is consistent with either an inability to silence the SAC or the loss of stable microtubule attachments in a small population of cells (Figure 4D). We also found similar levels of BubR1 at the kinetochores of metaphase Ndc80$^{+4CT}$ or Ndc80$^{WT}$ complemented cells. We conclude that the failure of our Ndc80$^{+4CT}$ mutant to progress into anaphase was due to active SAC signaling. Together, these data argue that the Ndc80$^{+4CT}$ mutant phenocopies loss of the Ska protein, which is consistent with Ndc80-dependent recruitment of Ska to kinetochores.

### Ndc80$^{+4CT}$ Binds Microtubules with Wild-Type Affinity but Is Deficient in Clustering along Microtubule Protofilaments

Structural analysis suggests that the C-terminal region of the Ndc80 unstructured tail has two functions. First, it interacts with the E hooks of tubulin and second, it bridges two adjacent Ndc80 proteins on microtubules (Alushin et al., 2012). To determine whether either or both of these activities are affected in the Ndc80$^{+4CT}$ mutant, we characterized the biophysical properties of Ndc80$^{+4CT}$ using Ndc80$^{Bonsai}$ +4CT expressed in *Escherichia coli*. We first measured the interaction of Ndc80$^{Bonsai}$ +4CT with taxol-stabilized microtubules by fluorescence anisotropy. The interaction between Ndc80$^{Bonsai}$ +4CT and microtubules had a higher binding affinity than Ndc80$^{Bonsai}$ WT, with a $K_D$ of 131.8 ± 55.2 nM (Figure 5A). This distinguishes Ndc80$^{+4CT}$ mutant from other reported phosphomimetic mutants in the C-terminal region of the Ndc80 tail which demonstrate reduced affinity for microtubules (Zaytsev et al., 2015). These measurements complement our observation that Ndc80$^{+4CT}$ cells are capable of forming stable kinetochore-microtubule attachments and generating pulling forces during metaphase (Figure 4). Strikingly, the Hill coefficient was noticeably reduced between Ndc80$^{Bonsai}$ WT (h = 0.842 ± 0.229) and Ndc80$^{Bonsai}$ +4CT (h = 0.415 ± 0.148). In fact, this change in slope of the binding curve suggests that Ndc80$^{Bonsai}$ +4CT binds with negative cooperativity to microtubules. We suggest that negative cooperativity arises because the Ndc80$^{+4CT}$ proteins cannot negate the repulsive forces generated by the negative patches that line the groove between adjacent subunits (Figure 3A). Therefore, if an Ndc80$^{+4CT}$ that interacts with a tubulin subunit next to a second Ndc80$^{+4CT}$, this is less likely than Ndc80 WT to be a productive binding event.

Ndc80$^{Bonsai}$ +4NT bound microtubules with lower affinity than Ndc80$^{Bonsai}$ WT ($K_D$ = 345 ± 47 nM), but did not affect the Hill coefficient in our binding assays (Figure S5A). Thus, the charge on the N-terminal part of the tail is required for binding microtubules in vitro and in vivo.

Structural studies show that the Ndc80 complex oligomerizes along microtubule protofilaments in vitro (Alushin et al., 2012; Alushin et al., 2010; Ciferri et al., 2008). Our model to explain the negative cooperativity of Ndc80$^{Bonsai}$ +4CT binding to microtubules predicts that Ndc80$^{Bonsai}$ +4CT should have reduced clustering. We visualized the binding of Ndc80$^{Bonsai}$ by negative-stain EM tomography to directly measure the binding of adjacent Ndc80 proteins along protofilaments. The formation of clusters was significantly decreased in the Ndc80$^{Bonsai}$ +4CT mutant compared with Ndc80$^{Bonsai}$ WT (Figures 5B, 5C, and S5B). We additionally observed a significantly reduced amount of V-shaped structures on microtubules incubated with Ska and Ndc80$^{Bonsai}$ +4CT mutant, as compared with Ndc80$^{Bonsai}$ WT (Figure 1D). This suggests that the clustering of Ndc80 along microtubule protofilament is important for Ndc80-Ska complex formation.

## DISCUSSION

Here we provide important insight into three critical processes that are required for mitotic progression. First, we identify the molecular steps that result in recruitment of Ska to kinetochores. Second, we identify the structure of a novel Ndc80-Ska complex on microtubules, which may explain how the curvature of a depolymerizing microtubule is used as a power stroke to move chromosomes. Third, we provide evidence that the clustering of Ndc80 proteins on microtubules, a phenomenon established in vitro, also exists and functions in vivo. These conclusions provide new models of kinetochore function and provide important insights into the mechanisms of SAC silencing and chromosome segregation during anaphase.

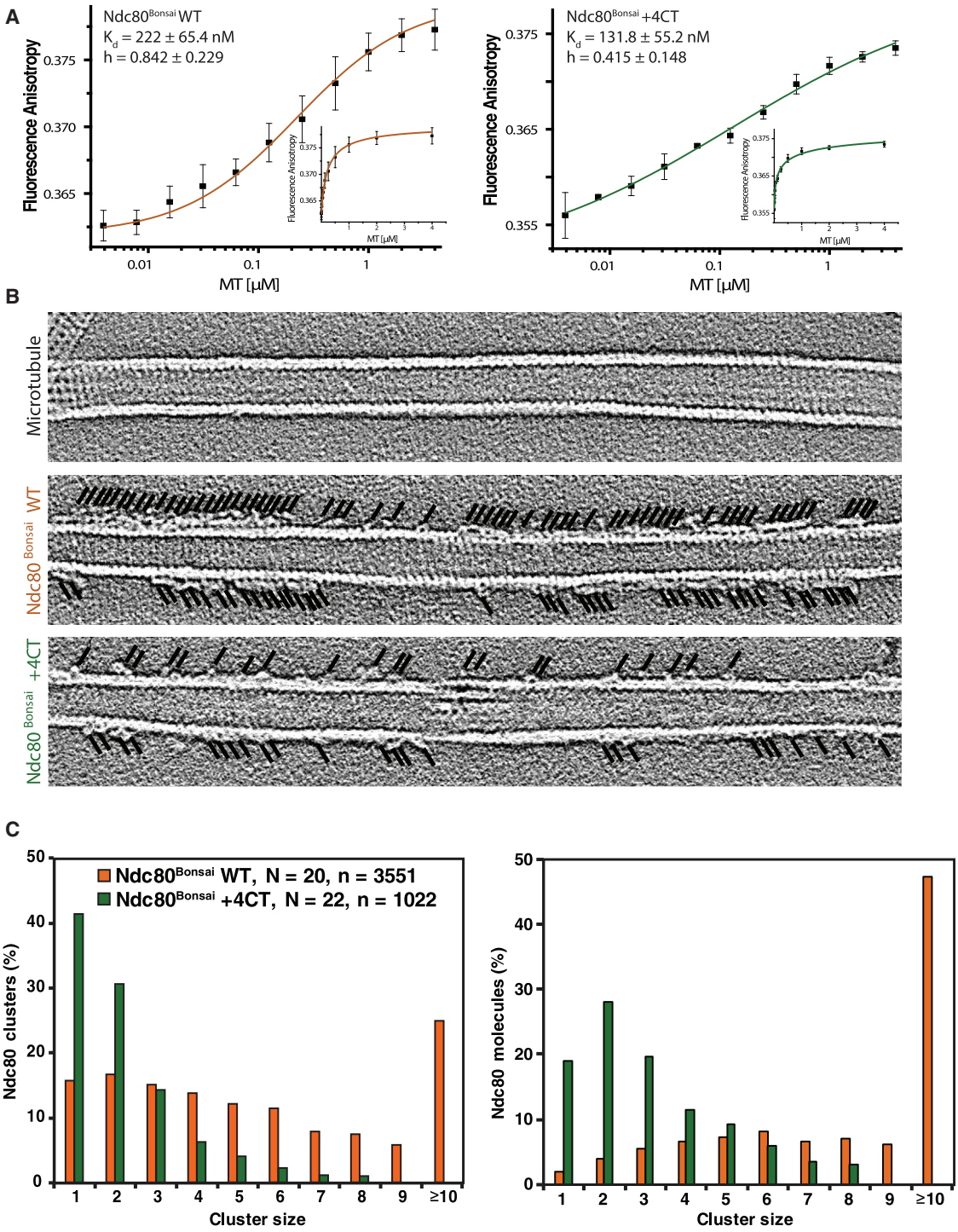


**Figure 5. Ndc80$^{+4CT}$ Tail Mutant Is Deficient in Clustering on Microtubules**

(A) Fluorescence anisotropy measurements of fluorescently labeled Ndc80$^{Bonsai}$ wild-type (WT) (left panel, orange) or Ndc80$^{Bonsai}$ +4CT (right panel, dark green) incubated with increasing concentrations of taxol-stabilized microtubules (MT), plotted on $\log_{10}$ scale (mean ± SD). Hill equation was used for fitment of the data. Small graphs represent the data on the linear scale. n = 3.

(B) Representative projections of five consecutive z sections (1.107 nm) of the tomographic reconstructions show Ndc80$^{Bonsai}$ +4CT form smaller clusters than Ndc80$^{Bonsai}$ WT. Black lines are drawn on top of the image to indicate the positions of the Ndc80 molecules. Images without black lines are shown in Figure S5B.

(C) Quantification of cluster sizes represented in (B). N, number of quantified microtubules; n, total number of Ndc80$^{Bonsai}$ molecules quantified.

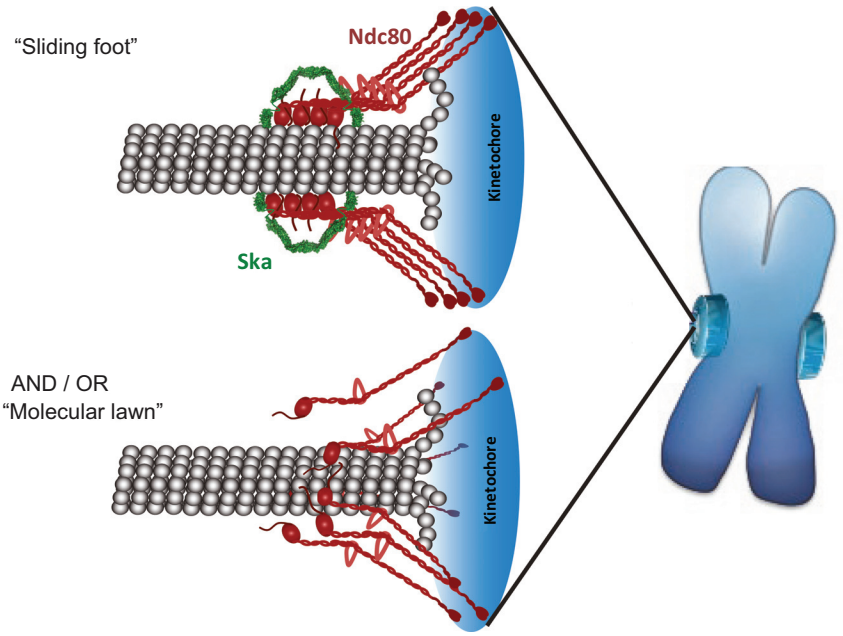


**Figure 6. Schematic Models Summarizing Potential Modes of Mature Kinetochore-Microtubule Attachment**

"Sliding foot" model: Ska complex is localized and oriented along protofilament of the depolymerizing microtubule end by clusters of Ndc80. This mechanism likely allows for utilization of energy released by curving protofilaments.

"Molecular lawn" model: current model for passive binding of multiple individual Ndc80 molecules to depolymerizing microtubule end.

The mechanisms governing recruitment of Ska to kinetochores have proved elusive. Low levels of Ska can be measured at prometaphase kinetochores and its levels are highest in metaphase, when robust kinetochore-microtubule attachments are present. However, reduced levels of Ska can also localize to kinetochores in cells treated with nocodazole, when no kinetochore-microtubule attachments are present. These seemingly incongruent observations can be explained if Ska recognizes clustered Ndc80 proteins, or if Ska recognizes the Ndc80 unstructured tail which is exposed upon microtubule binding.

There are at least five experiments that support our model of Ska recruitment to kinetochore by direct binding to the N terminus of the Ndc80 complex which contains the microtubule binding region. First, using PLA we show that Ska and the CHD of Ndc80 are in close proximity on microtubules in vivo. Second, $Ndc80^{Bonsai}$, which lacks most of the coiled-coil regions of the Ndc80 complex, orients Ska along microtubule protofilaments. Third, we have characterized mutants of the Ndc80 tail region that is deficient in Ska recruitment to microtubules in vitro and to kinetochores in vivo. Fourth and fifth, our model is consistent with published experiments showing that Ska enables the plus-end tracking of individual Ndc80 complexes on depolymerizing microtubules (Schmidt et al., 2012), and the requirement of the Ndc80 complex to recruit Ska (Chan et al., 2012; Raaijmakers et al., 2009; Welburn et al., 2009; Hanisch et al., 2006).

Our tomographic reconstructions demonstrate that Ndc80 can orient Ska along a microtubule protofilament, while it was recently shown that EB1 orients Ska across multiple protofilaments to partially encircle the microtubule (Thomas et al., 2016). We were not able to clearly visualize Ska lying across multiple protofilaments by EM tomography of either Ska alone or the protein recruited by Ndc80. We do not understand the reason for this discrepancy. EB1 is asymmetrically recruited to sister kinetochores because it binds polymerizing microtubules that are on the anti-poleward sister (Tirnauer et al., 2002). Thus, it is possible that Ska is bound along protofilaments on the poleward sister by interaction with Ndc80 to pull chromosomes, while EB1 on the anti-poleward sister binds Ska across the microtubule to allow microtubules to lengthen.

## Functions of the Ndc80 Unstructured Tail

The N-terminal tail of Ndc80 modulates Ndc80-microtubule interactions, where it acts to decrease the dissociation rate constant ($k_{off}$) of individual Ndc80 proteins (Zaytsev et al., 2015; Alushin et al., 2012; Cheeseman et al., 2006; DeLuca et al., 2006). This activity is countered by Aurora phosphorylation, which increases the $k_{off}$ to reduce binding affinity. Our studies suggest that the Ndc80 tail has an additional function in recruiting Ska. A similar conclusion was made in the accompanying paper in *Caenorhabditis elegans*, demonstrating that this function is highly conserved (Cheerambathur et al., 2017 [this issue of *Developmental Cell*]). We also demonstrate that the tail enables clustering of Ndc80 along microtubule protofilaments as suggested by a previous structural study (Alushin et al., 2012). We propose that the key event to recruit Ska is a tail-dependent clustering of Ndc80 proteins along microtubules, which forms a structure that is recognized by Ska. However, it is also possible that the C-terminal region of the Ndc80 tail controls both clustering and binding of Ska.

Cells depleted of Ska or cells expressing $Ndc80^{+4CT}$ arrest in metaphase and fail to silence the SAC. Ska recruits PP1 to kinetochores to enable progression to anaphase (Sivakumar et al., 2016). Our data place Ska and, presumably, Ska/PP1 at the plus tip of the microtubule in close proximity to the microtubule binding sites of Ndc80, where PP1 would be in a position to dephosphorylate the Ndc80 tail and other nearby substrates. We suggest that this event would enhance binding of the Ndc80 tail to microtubules and drive the maturation of kinetochore-microtubule attachments, ultimately silencing the SAC signal. We have not shown that PP1 can participate in formation of a V-shaped complex, which is an important future experiment.

## Insight into "End-On" Kinetochore-Microtubule Attachment and Depolymerization-Coupled Movement of Chromosomes

Our findings provide clues to connect the Ska structure with its function. It was unclear why the coiled coils of the Ska core

complex formed a V shape. Our data orient the core of Ska lengthwise along a microtubule protofilaments, and we suggest that the V shape allows Ska to bind clusters of Ndc80 complexes. It was unclear how the ability of Ska to bind both straight and curved microtubules contributed to its function(s) (Abad et al., 2014; Jeyaprakash et al., 2012; Schmidt et al., 2012). Our structure orients the two microtubule binding regions of the Ska1 C-terminal domain in two distinct positions, suggesting that if a depolymerizing microtubule end encounters Ska then one microtubule binding domain could interact with the curved protofilament, while the other would sit behind a cluster of Ndc80 proteins on the straight region of the polymer.

Current models, known as unbiased diffusion or the molecular lawn, suggest that the Ndc80 complex acts passively in eukaryotes. It is theorized that each kinetochore contains more than seven Ndc80s and that each Ndc80 protein binds microtubules independently to form a molecular lawn. Kinetochores maintain attachment with depolymerizing microtubules because some Ndc80 molecules are still associated with straight regions of microtubule, while others dissociate from depolymerizing subunits. Kinetochore remains attached to the microtubule as long as dissociated Ndc80 proteins are able to rebind to the straight protofilaments. Our data do not disprove this model, and it is possible that the clustering of Ndc80 complexes is transient and functions to recruit Ska/PP1 to dephosphorylate substrates, allowing the end-on attachments to mature.

In contrast, many fungi have evolved the Dam1 complex that can form a ring around microtubules at kinetochores (Wang et al., 2007; Westermann et al., 2006; Westermann et al., 2005). This ring creates a topologically constrained interaction with the polymer and enables sliding activities in a manner similar to the sliding clamps of DNA polymerases (Kong et al., 1992; Stukenberg et al., 1991). Elegant biophysical experiments have shown that the curvature of the depolymerizing microtubule produces a force that pushes the Dam1 rings toward the minus end (Grishchuk et al., 2008; Grishchuk and McIntosh, 2006; Westermann et al., 2006). Our data suggest, but do not prove, that the Ndc80-Ska complex could similarly couple the curvature of depolymerizing microtubules into a pushing force and thus act similarly to the Dam1 clamp, albeit without encircling the microtubule. The V shapes we observed suggest a speculative "sliding foot" model that can drive future experiments (Figure 6). We propose that clusters of Ndc80 allow the complex to remain tightly bound to the microtubule protofilament, while the complex is pushed backwards. While there is a single interaction between the "toe" of the Ndc80 CHD and the tubulin surface (Tooley et al., 2011; Alushin et al., 2010), there are also at least two important interactions between the Ndc80 complex and tubulin that are built from unstructured tails and are required for the Ndc80 complex to interact with microtubules (Alushin et al., 2012; Tooley et al., 2011; Miller et al., 2008). Clustering of four Ndc80 subunits would build an attachment with 12 distinct microtubule attachment points, eight of which would be made from unstructured regions of proteins, allowing Ndc80 to maintain an interaction with tubulin as it slides between adjacent tubulin subunits.

We propose that the "molecular lawn" represents an intermediate to forming the "sliding foot" and that either can move chromosomes. Cells depleted of the Ska complex still congress chromosomes to the metaphase plate (Sivakumar et al., 2014; Daum et al., 2009). We can phenocopy this result using a mutant of the Ndc80 tail that is deficient in Ska recruitment. Therefore, the available data suggest that chromosomes move without a sliding foot, and we suggest that this is accomplished by a molecular lawn model of microtubule binding or by the motor CENP-E (centrosome-associated protein E). However, as Ska is at all kinetochores that make mature attachments and remains bound during anaphase, we propose that the sliding foot is the mature coupler of depolymerization energy into chromosome movement.

## STAR★METHODS

Detailed methods are provided in the online version of this paper and include the following:

- KEY RESOURCE TABLE
- CONTACT FOR REAGENT AND RESOURCE SHARING
- EXPERIMENTAL MODEL AND SUBJECT DETAILS
  - Cell Culture
- METHOD DETAILS
  - Electron Microscopy and Tomography
  - Immunofluorescence
  - Protein Purification
  - Knockdown and Rescue of Ndc80
  - Creation of Stable Cell Lines
  - Proximity Ligation Assay
  - Fluorescence Anisotropy
  - Kinase Assay
- QUANTIFICATION AND STATISTICAL ANALYSIS

### SUPPLEMENTAL INFORMATION

Supplemental Information includes five figures and four movies and can be found with this article online at http://dx.doi.org/10.1016/j.devcel.2017.04.020.

### AUTHOR CONTRIBUTIONS

P.Ł.J. performed experiments in Figures 1, 3, 5, S1, and S3–S5. P.Ł.J., K.A.S., and O.P. designed and/or performed electron tomography. C.A.K. performed PLA, which was quantified by P.Ł.J. P.Ł.J., J.T., T.W., and D.R.M. performed experiments depicted in Figures 3, 4, and S4. P.Ł.J. and P.T.S. designed the study and wrote the manuscript.

### ACKNOWLEDGMENTS

The authors wish to thank Eva Nogales and Greg Alushin for help with tomography and the original observation of the V shapes on microtubules. We thank Iain Cheeseman and Andrea Musacchio for plasmids and Dan Burke, Gary Gorbsky, Bob Nakamoto, and Zygmunt Derewenda for helpful discussions about the work. D.R.M. was supported by NIGMS grant T32 GM008136. The work was supported by NIGMS grants GM081576 and GM112508.

Received: September 28, 2016
Revised: March 20, 2017
Accepted: April 23, 2017
Published: May 22, 2017

### REFERENCES

Abad, M.A., Medina, B., Santamaria, A., Zou, J., Plasberg-Hill, C., Madhumalar, A., Jayachandran, U., Redli, P.M., Rappsilber, J., Nigg, E.A.,

et al. (2014). Structural basis for microtubule recognition by the human kinetochore Ska complex. Nat. Commun. *5*, 2964.

Abramoff, M.D., Magelhaes, P.J., and Ram, S.J. (2004). Image processing with ImageJ. Biophotonics Int. *11*, 36–42.

Alushin, G.M., Ramey, V.H., Pasqualato, S., Ball, D.A., Grigorieff, N., Musacchio, A., and Nogales, E. (2010). The Ndc80 kinetochore complex forms oligomeric arrays along microtubules. Nature *467*, 805–810.

Alushin, G.M., Musinipally, V., Matson, D., Tooley, J., Stukenberg, P.T., and Nogales, E. (2012). Multimodal microtubule binding by the Ndc80 kinetochore complex. Nat. Struct. Mol. Biol. *19*, 1161–1167.

Banerjee, B., Kestner, C.A., and Stukenberg, P.T. (2014). EB1 enables spindle microtubules to regulate centromeric recruitment of Aurora B. J. Cell Biol. *204*, 947–963.

Chan, Y.W., Jeyaprakash, A.A., Nigg, E.A., and Santamaria, A. (2012). Aurora B controls kinetochore-microtubule attachments by inhibiting Ska complex-KMN network interaction. J. Cell Biol. *196*, 563–571.

Cheerambathur, D.K., Prevo, B., Corbett, K.D., Oegema, K., and Desai, A. (2017). Dephosphorylation of the Ndc80 tail stabilizes kinetochore-microtubule attachments via the Ska complex. Dev. Cell *41*, this issue, 423–437.

Cheeseman, I.M., Chappie, J.S., Wilson-Kubalek, E.M., and Desai, A. (2006). The conserved KMN network constitutes the core microtubule-binding site of the kinetochore. Cell *127*, 983–997.

Ciferri, C., De Luca, J., Monzani, S., Ferrari, K.J., Ristic, D., Wyman, C., Stark, H., Kilmartin, J., Salmon, E.D., and Musacchio, A. (2005). Architecture of the human ndc80-hec1 complex, a critical constituent of the outer kinetochore. J. Biol. Chem. *280*, 29088–29095.

Ciferri, C., Pasqualato, S., Screpanti, E., Varetti, G., Santaguida, S., Dos Reis, G., Maiolica, A., Polka, J., De Luca, J.G., De Wulf, P., et al. (2008). Implications for kinetochore-microtubule attachment from the structure of an engineered Ndc80 complex. Cell *133*, 427–439.

Daum, J.R., Wren, J.D., Daniel, J.J., Sivakumar, S., McAvoy, J.N., Potapova, T.A., and Gorbsky, G.J. (2009). Ska3 is required for spindle checkpoint silencing and the maintenance of chromosome cohesion in mitosis. Curr. Biol. *19*, 1467–1472.

DeLuca, J.G., Moree, B., Hickey, J.M., Kilmartin, J.V., and Salmon, E.D. (2002). hNuf2 inhibition blocks stable kinetochore-microtubule attachment and induces mitotic cell death in HeLa cells. J. Cell Biol. *159*, 549–555.

DeLuca, J.G., Gall, W.E., Ciferri, C., Cimini, D., Musacchio, A., and Salmon, E.D. (2006). Kinetochore microtubule dynamics and attachment stability are regulated by Hec1. Cell *127*, 969–982.

DeLuca, K.F., Lens, S.M., and DeLuca, J.G. (2011). Temporal changes in Hec1 phosphorylation control kinetochore-microtubule attachment stability during mitosis. J. Cell Sci. *124*, 622–634.

Emanuele, M.J., McCleland, M.L., Satinover, D.L., and Stukenberg, P.T. (2005). Measuring the stoichiometry and physical interactions between components elucidates the architecture of the vertebrate kinetochore. Mol. Biol. Cell *16*, 4882–4892.

Gaitanos, T.N., Santamaria, A., Jeyaprakash, A.A., Wang, B., Conti, E., and Nigg, E.A. (2009). Stable kinetochore-microtubule interactions depend on the Ska complex and its new component Ska3/C13Orf3. EMBO J. *28*, 1442–1452.

Grishchuk, E.L., and McIntosh, J.R. (2006). Microtubule depolymerization can drive poleward chromosome motion in fission yeast. EMBO J. *25*, 4888–4896.

Grishchuk, E.L., Molodtsov, M.I., Ataullakhanov, F.I., and McIntosh, J.R. (2005). Force production by disassembling microtubules. Nature *438*, 384–388.

Grishchuk, E.L., Efremov, A.K., Volkov, V.A., Spiridonov, I.S., Gudimchuk, N., Westermann, S., Drubin, D., Barnes, G., McIntosh, J.R., and Ataullakhanov, F.I. (2008). The Dam1 ring binds microtubules strongly enough to be a processive as well as energy-efficient coupler for chromosome motion. Proc. Natl. Acad. Sci. USA *105*, 15423–15428.

Guimaraes, G.J., Dong, Y., McEwen, B.F., and Deluca, J.G. (2008). Kinetochore-microtubule attachment relies on the disordered N-terminal tail domain of Hec1. Curr. Biol. *18*, 1778–1784.

Hanisch, A., Sillje, H.H., and Nigg, E.A. (2006). Timely anaphase onset requires a novel spindle and kinetochore complex comprising Ska1 and Ska2. EMBO J. *25*, 5504–5515.

Janke, C., Ortiz, J., Lechner, J., Shevchenko, A., Shevchenko, A., Magiera, M.M., Schramm, C., and Schiebel, E. (2001). The budding yeast proteins Spc24p and Spc25p interact with Ndc80p and Nuf2p at the kinetochore and are important for kinetochore clustering and checkpoint control. EMBO J. *20*, 777–791.

Jeyaprakash, A.A., Santamaria, A., Jayachandran, U., Chan, Y.W., Benda, C., Nigg, E.A., and Conti, E. (2012). Structural and functional organization of the ska complex, a key component of the kinetochore-microtubule interface. Mol. Cell *46*, 274–286.

Joglekar, A.P., Bouck, D.C., Molk, J.N., Bloom, K.S., and Salmon, E.D. (2006). Molecular architecture of a kinetochore-microtubule attachment site. Nat. Cell Biol. *8*, 581–585.

Joglekar, A.P., Salmon, E.D., and Bloom, K.S. (2008). Counting kinetochore protein numbers in budding yeast using genetically encoded fluorescent proteins. Methods Cell Biol. *85*, 127–151.

Johnston, K., Joglekar, A., Hori, T., Suzuki, A., Fukagawa, T., and Salmon, E.D. (2010). Vertebrate kinetochore protein architecture: protein copy number. J. Cell Biol. *189*, 937–943.

Kong, X.P., Onrust, R., O'Donnell, M., and Kuriyan, J. (1992). Three-dimensional structure of the beta subunit of *E. coli* DNA polymerase III holoenzyme: a sliding DNA clamp. Cell *69*, 425–437.

Kremer, J.R., Mastronarde, D.N., and McIntosh, J.R. (1996). Computer visualization of three-dimensional image data using IMOD. J. Struct. Biol. *116*, 71–76.

Mastronarde, D.N. (2005). Automated electron microscope tomography using robust prediction of specimen movements. J. Struct. Biol. *152*, 36–51.

McCleland, M.L., Gardner, R.D., Kallio, M.J., Daum, J.R., Gorbsky, G.J., Burke, D.J., and Stukenberg, P.T. (2003). The highly conserved Ndc80 complex is required for kinetochore assembly, chromosome congression, and spindle checkpoint activity. Genes Dev. *17*, 101–114.

McCleland, M.L., Kallio, M.J., Barrett-Wilt, G.A., Kestner, C.A., Shabanowitz, J., Hunt, D.F., Gorbsky, G.J., and Stukenberg, P.T. (2004). The vertebrate Ndc80 complex contains Spc24 and Spc25 homologs, which are required to establish and maintain kinetochore-microtubule attachment. Curr. Biol. *14*, 131–137.

Miller, S.A., Johnson, M.L., and Stukenberg, P.T. (2008). Kinetochore attachments require an interaction between unstructured tails on microtubules and Ndc80(Hec1). Curr. Biol. *18*, 1785–1791.

Molodtsov, M.I., Grishchuk, E.L., Efremov, A.K., McIntosh, J.R., and Ataullakhanov, F.I. (2005). Force production by depolymerizing microtubules: a theoretical study. Proc. Natl. Acad. Sci. USA *102*, 4353–4358.

Pettersen, E.F., Goddard, T.D., Huang, C.C., Couch, G.S., Greenblatt, D.M., Meng, E.C., and Ferrin, T.E. (2004). UCSF chimera—a visualization system for exploratory research and analysis. J. Comput. Chem. *25*, 1605–1612.

Powers, A.F., Franck, A.D., Gestaut, D.R., Cooper, J., Gracyzk, B., Wei, R.R., Wordeman, L., Davis, T.N., and Asbury, C.L. (2009). The Ndc80 kinetochore complex forms load-bearing attachments to dynamic microtubule tips via biased diffusion. Cell *136*, 865–875.

Raaijmakers, J.A., Tanenbaum, M.E., Maia, A.F., and Medema, R.H. (2009). RAMA1 is a novel kinetochore protein involved in kinetochore-microtubule attachment. J. Cell Sci. *122*, 2436–2445.

Schmidt, J.C., Arthanari, H., Boeszoermenyi, A., Dashkevich, N.M., Wilson-Kubalek, E.M., Monnier, N., Markus, M., Oberer, M., Milligan, R.A., Bathe, M., et al. (2012). The kinetochore-bound Ska1 complex tracks depolymerizing microtubules and binds to curved protofilaments. Dev. Cell *23*, 968–980.

Sivakumar, S., Daum, J.R., Tipton, A.R., Rankin, S., and Gorbsky, G.J. (2014). The Spindle and kinetochore-associated (Ska) complex enhances binding of

the Anaphase-Promoting Complex/Cyclosome (APC/C) to chromosomes and promotes mitotic exit. Mol. Biol. Cell *25*, 594–605.

Sivakumar, S., Janczyk, P.L., Qu, Q., Brautigam, C.A., Stukenberg, P.T., Yu, H., and Gorbsky, G.J. (2016). The human SKA complex drives the metaphase-anaphase cell cycle transition by recruiting protein phosphatase 1 to kinetochores. Elife *5*, e12902.

Soderberg, O., Gullberg, M., Jarvius, M., Ridderstrale, K., Leuchowius, K.J., Jarvius, J., Wester, K., Hydbring, P., Bahram, F., Larsson, L.G., et al. (2006). Direct observation of individual endogenous protein complexes in situ by proximity ligation. Nat. Methods *3*, 995–1000.

Stukenberg, P.T., Studwell, P.S., and O'Donnell, M. (1991). Mechanism of the sliding beta-clamp of DNA polymerase III holoenzyme. J. Biol. Chem. *266*, 21681–21686.

Suzuki, A., Badger, B.L., and Salmon, E.D. (2015). A quantitative description of Ndc80 complex linkage to human kinetochores. Nat. Commun. *6*, 8161.

Thomas, G.E., Bandopadhyay, K., Sutradhar, S., Renjith, M.R., Singh, P., Gireesh, K.K., Simon, S., Badarudeen, B., Gupta, H., Banerjee, M., et al. (2016). EB1 regulates attachment of Ska1 with microtubules by forming extended structures on the microtubule lattice. Nat. Commun. *7*, 11665.

Tirnauer, J.S., Canman, J.C., Salmon, E.D., and Mitchison, T.J. (2002). EB1 targets to kinetochores with attached, polymerizing microtubules. Mol. Biol. Cell *13*, 4308–4316.

Tooley, J.G., Miller, S.A., and Stukenberg, P.T. (2011). The Ndc80 complex employs a tripartite attachment point to couple microtubule depolymerization to chromosome movement. Mol. Biol. Cell. http://dx.doi.org/10.1091/mbc.E10-07-0626.

Tran, P.T., Joshi, P., and Salmon, E.D. (1997). How tubulin subunits are lost from the shortening ends of microtubules. J. Struct. Biol. *118*, 107–118.

Wang, H.W., Ramey, V.H., Westermann, S., Leschziner, A.E., Welburn, J.P., Nakajima, Y., Drubin, D.G., Barnes, G., and Nogales, E. (2007). Architecture of the Dam1 kinetochore ring complex and implications for microtubule-driven assembly and force-coupling mechanisms. Nat. Struct. Mol. Biol. *14*, 721–726.

Wei, R.R., Al-Bassam, J., and Harrison, S.C. (2007). The Ndc80/HEC1 complex is a contact point for kinetochore-microtubule attachment. Nat. Struct. Mol. Biol. *14*, 54–59.

Welburn, J.P., Grishchuk, E.L., Backer, C.B., Wilson-Kubalek, E.M., Yates, J.R., 3rd, and Cheeseman, I.M. (2009). The human kinetochore Ska1 complex facilitates microtubule depolymerization-coupled motility. Dev. Cell *16*, 374–385.

Westermann, S., Avila-Sakar, A., Wang, H.W., Niederstrasser, H., Wong, J., Drubin, D.G., Nogales, E., and Barnes, G. (2005). Formation of a dynamic kinetochore- microtubule interface through assembly of the Dam1 ring complex. Mol. Cell *17*, 277–290.

Westermann, S., Wang, H.W., Avila-Sakar, A., Drubin, D.G., Nogales, E., and Barnes, G. (2006). The Dam1 kinetochore ring complex moves processively on depolymerizing microtubule ends. Nature *440*, 565–569.

Wigge, P.A., and Kilmartin, J.V. (2001). The Ndc80p complex from *Saccharomyces cerevisiae* contains conserved centromere components and has a function in chromosome segregation. J. Cell Biol. *152*, 349–360.

Zaytsev, A.V., Sundin, L.J., DeLuca, K.F., Grishchuk, E.L., and DeLuca, J.G. (2014). Accurate phosphoregulation of kinetochore-microtubule affinity requires unconstrained molecular interactions. J. Cell Biol. *206*, 45–59.

Zaytsev, A.V., Mick, J.E., Maslennikov, E., Nikashin, B., DeLuca, J.G., and Grishchuk, E.L. (2015). Multisite phosphorylation of the NDC80 complex gradually tunes its microtubule-binding affinity. Mol. Biol. Cell *26*, 1829–1844.

Zhang, G., Kelstrup, C.D., Hu, X.W., Kaas Hansen, M.J., Singleton, M.R., Olsen, J.V., and Nilsson, J. (2012). The Ndc80 internal loop is required for recruitment of the Ska complex to establish end-on microtubule attachment to kinetochores. J. Cell Sci. *125*, 3243–3253.

## STAR★METHODS

### KEY RESOURCE TABLE

| REAGENT or RESOURCE | SOURCE | IDENTIFIER |
|---|---|---|
| Antibodies | | |
| Alexa Fluor 568 Donkey Anti-Rabbit IgG Antibody | Life Technologies | Cat# A10042, RRID: AB_2534017 |
| Alexa Fluor 647 AffiniPure Donkey Anti-Human IgG (H+L) | Jackson Immuno Research Labs | Cat# 709-605-149, RRID: AB_2340578 |
| Cy5 conjugated rabbit polyclonal anti-Borealin | This paper | N/A |
| FITC conjugated mouse monoclonal anti-tubulin | Sigma-Aldrich | Cat# F2168, RRID: AB_476967 |
| Goat anti-Mouse IgG (H+L) Cross-Adsorbed Secondary Antibody, Alexa Fluor 488 | Thermo Fisher Scientific | Cat# A11001, RRID: AB_2534069 |
| Goat anti-Mouse IgG (H+L) Highly Cross-Adsorbed Secondary Antibody, Alexa Fluor 568 | Thermo Fisher Scientific | Cat# A11031, RRID: AB_144696 |
| Human anti-ACA | Antibodies Incorprated | Cat# 15-234-0001 |
| Mouse monoclonal anti-GFP | Abcam | Cat# ab1218, RRID: AB_298911 |
| Mouse monoclonal anti-Ndc80 9G3 | GeneTex | Cat# GTX70268, RRID: AB_371632 |
| Mouse monoclonal anti-tubulin (DM1$\alpha$) | Lab Vision | Cat# MS-581, RRID: AB_144075 |
| Rabbit polyclonal anti-BubR1 | This paper | N/A |
| Rabbit polyclonal anti-Dsn1 | This paper | N/A |
| Rabbit polyclonal anti-Mad2 | Gary Gorbsky | N/A |
| Rabbit polyclonal anti-Ska3 | Gary Gorbsky | N/A |
| Rabbit polyclonal anti-Zw10 | This paper | N/A |
| Bacterial and Virus Strains | | |
| *Escherichia coli* BL21 (DE3) | New England BioLabs | Cat# C2527I |
| Chemicals, Peptides, and Recombinant Proteins | | |
| 16% Paraformaldehyde (formaldehyde) aqueous solution | Electron Microscopy Sciences | Cat# 15710 |
| ATP, [$\gamma$-$^{32}$P] | Perkin Elmer | Cat# NEG002H 250UC |
| Bovine Serum Albumin Fraction V, heat shock | Roche | Cat# 3116956001 |
| Dublecco's Modified Eagle Medium | Gibco | Cat# 11965-092 |
| Dublecco's PBS | Gibco | Cat# 14190-144 |
| Duolink In Situ Detection Reagents Orange | Sigma-Aldrich | Cat# DUO92007 |
| Duolink In Situ PLA Probe Anti-Mouse MINUS Affinity purified Donkey anti-Mouse IgG (H+L) | Sigma-Aldrich | Cat# DUO92004 |
| Duolink In Situ PLA Probe Anti-Rabbit PLUS Affinity purified Donkey anti-Rabbit IgG (H+L) | Sigma-Aldrich | Cat# DUO92002 |
| Fetal Bovine Serum, qualified, heat inactivated, US origin | Gibco | Cat# 16140071 |
| Hygromycin B | Gibco | Cat# 10687010 |
| Isopropyl 1-thio-$\beta$-D-galactopyranoside | Denville Scientific | Cat# CI8280-13 |
| KCl | Fisher Scientific | Cat# P217-500 |
| $KH_2PO_4$ | Fisher Scientific | Cat# P382-500 |
| Lipofectamine 2000 | Life Technologies | Cat# 11668027 |
| Lipofectamine RNAiMAX | Life Technologies | Cat# 13778075 |
| $MgCl_2$ | Fisher Scientific | Cat# M33-500 |
| $Na_2HPO_4$ | Santa Cruz Biotechnology | Cat# sc-203277 |
| Nocodazole | Sigma-Aldrich | Cat# M1404-10MG |
| Oregon Green 488 Maleimide | ThermoFisher Scientific | Cat# O6034 |
| Paclitaxel | Sigma | Cat# T7402-5MG |

(*Continued on next page*)

*Continued*

| REAGENT or RESOURCE | SOURCE | IDENTIFIER |
|---|---|---|
| Recombinant Aurora B-Incenp$^{790-856}$ | Banerjee et al., 2014 | N/A |
| Recombinant Human Ndc80$^{Bonsai}$ WT, +4CT, +4NT | This paper | N/A |
| Recombinant Human Ska complex | This paper | N/A |
| Thymidine | Sigma-Aldrich | Cat# T1895-5G |
| Uranyl Formate | Electron Microscopy Sciences | Cat# 22450 |
| ZM 447439 | R&D Systems | Cat# 2458 |
| Experimental Models: Cell Lines | | |
| HeLa (ATCC CCL-2) | ATCC | Cat# ATCC CCL-2, RRID: CVCL_0030 |
| T-Rex HeLa | ThermoFisher Scientific | Cat# R71407 |
| Oligonucleotides | | |
| siRNA targeting sequence, Ndc80: GAGUAGAA CUAGAAUGUGA | Dharmacon | N/A |
| Recombinant DNA | | |
| pCB4 GST-Ska3 | Schmidt et al., 2012 | N/A |
| pCDNA5/FRT | ThermoFisher Scientific | Cat# V6010-20 |
| pCDNA5/FRT Ndc80 +4CT (siRNA resistant) | This paper | N/A |
| pCDNA5/FRT Ndc80 +4NT (siRNA resistant) | This paper | N/A |
| pCDNA5/FRT Ndc80 WT (siRNA resistant) | This paper | N/A |
| pEGFP-N1 | Addgene | Cat# 6085-1 |
| pEGFP-N1 Ndc80 +0 | Tooley et al., 2011 (Hec1$^{NEU}$) | N/A |
| pEGFP-N1 Ndc80 +4CT | This paper | N/A |
| pEGFP-N1 Ndc80 +4NT | This paper | N/A |
| pEGFP-N1 Ndc80 Δ40-60 | This paper | N/A |
| pEGFP-N1 Ndc80 Δ40-80 | This paper | N/A |
| pEGFP-N1 Ndc80 ΔN | This paper | N/A |
| pEGFP-N1 Ndc80 WT | Tooley et al., 2011 | N/A |
| pGEX6P-2rbs Ndc80$^{Bonsai}$ +4CT (codon optimized) | This paper | N/A |
| pGEX6P-2rbs Ndc80$^{Bonsai}$ +4NT (codon optimized) | This paper | N/A |
| pGEX6P-2rbs Ndc80$^{Bonsai}$ WT | Ciferri et al., 2008 | N/A |
| pGEX6P-2rbs Ndc80$^{Bonsai}$ WT (codon optimized) | This paper | N/A |
| pIC316 Ska2/Ska1 | Schmidt et al., 2012 | N/A |
| pOG44 | ThermoFisher Scientific | Cat# V600520 |
| Software and Algorithms | | |
| GraphPad Prism | GraphPad | https://www.graphpad.com/scientific-software/prism/ |
| ImageJ | Abramoff et al., 2004 | https://imagej.nih.gov/ij/download.html |
| IMOD software package | Kremer et al., 1996 | http://bio3d.colorado.edu/imod/ |
| OriginPro 7.5 | OriginLab | http://www.originlab.com/Origin |
| SerialEM | Mastronarde, 2005 | http://bio3d.colorado.edu/SerialEM/ |
| softWoRX | GE Healthcare | http://www.api.com/softworx-suite.asp |
| UCSF Chimera 1.11.2 | Pettersen et al., 2004 | https://www.cgl.ucsf.edu/chimera/ |
| Volocity 6.3 | Perkin-Elmer | http://cellularimaging.perkinelmer.com/downloads/detail.php?id=14 |

## CONTACT FOR REAGENT AND RESOURCE SHARING

Further information and requests for resources and reagents should be directed to and will be fulfilled by the Lead Contact, P. Todd Stukenberg (pts7h@virginia.edu)

## EXPERIMENTAL MODEL AND SUBJECT DETAILS

### Cell Culture

HeLa cells (ATCC) or HeLa T-Rex (ThermoFisher Scientific) were maintained in Dulbecco's Modified Eagle's Medium (Invitrogen) supplemented with 10% fetal bovine serum (Invitrogen) in a humidified incubator at 37°C with 5% $CO_2$.

## METHOD DETAILS

### Electron Microscopy and Tomography

Preparation of negatively stained samples was done essentially as previously described (Alushin et al., 2012). For experiment depicted in Figures 1A and 1B EM grids were incubated with 2 μM taxol-stabilized microtubules in BRB80 supplemented with 10 μM taxol for 30 seconds, then with 2 μM $Ndc80^{Bonsai}$ WT or $Ndc80^{Bonsai}$ +4CT and 1 μM of the Ska complex for 2 min, followed by staining with 2% uranyl formate. 1 μM and 4 μM of the Ska complex was used for 1x Ska and 4x Ska samples, respectively. Tilt series from -60 to 60 degrees were collected semi-automatically by SerialEM software package (Mastronarde, D.N. 2005) with Tecnai F20 operating at 120 kV, at nominal magnification of 50,000x and 1.2 or 2.5 μm underfocus. IMOD software packages (Kremer et al., 1996) were used for tomographic reconstructions: following alignment, tilt series were binned by two and filtered before first inversion of the 'contrast transfer function'. Tomographic reconstructions were calculated using back projection algorithm. For experiment depicted in Figures 5B and S5B EM grids were incubated with 2 μM taxol-stabilized microtubules for 30 seconds in BRB80 supplemented with 10 μM taxol, then with 3.3 μM $Ndc80^{Bonsai}$ WT or $Ndc80^{Bonsai}$ +4CT for 2 min, followed by brief wash in BRB80 and staining with 2% uranyl formate. Tilt series from -60 to 60 degrees were then collected manually and processed using IMOD software packages, with no subsequent binning and filtering of the acquired micrographs. Analysis was performed only on microtubules that were not significantly flattened or deformed during grid preparation.

### Immunofluorescence

For most of the immunofluorescence experiments, coverslips were co-fixed and extracted in PHEM buffer containing 2% paraformaldehyde and 0.5% Triton X-100 for 20 min at room temperature. Antibodies used were anti-Ndc80 9G3 (1:500 [vol/vol]; GTX70268, GeneTex), anti-GFP (1:500 [vol/vol]; ab1218, Abcam), anti-ACA (1:500 [vol/vol]; 15-234-0001, Antibodies Incorporated), anti-tubulin (1:500 [vol/vol]; DM1α, NeoMarkers), anti-BubR1 (1:500 [vol/vol]), anti-Mad2 (1:100 [vol/vol]; a kind gift from Gary Gorbsky), anti-Ska3 (1.5 μg/mL; a kind gift from Gary Gorbsky), anti-Dsn1 (1:1000 [vol/vol]) and FITC conjugated anti-tubulin (1:500 [vol/vol]; DM1α, Sigma). DAPI staining (1:20000 of a 5 mg/ml stock; Invitrogen) was used to visualize DNA. The images from Figures 3C and 4D were collected using a 100x lens on a Deltavision microscope (Applied Precision) and deconvoluted z-projections are shown. Images from Figures 2, 3, S2, and S4 were captured using Zeiss Axiovert 200 inverted microscope with a Perkin Elmer confocal attachment, a krypton/argon laser and AOTF control for detecting fluorescence at 488, 568, and 647 nm, using 63x lens. Images were captured with a Hamamatsu digital CCD camera. Image acquisition and processing was done using Volocity 6.3 imaging software (Perkin Elmer). Quantification of the fluorescence intensities was done by semi-automated detection of kinetochore volumes using ACA mask in Volocity 6.3 imaging software. Each kinetochore signal was divided by its volume, then normalized to equivalent Ndc80 signal following background subtraction. Inter-kinetochore distance measurements were quantified using softWoRX imaging software.

### Protein Purification

Expressions in BL21 (DE3) cells of both GST-Ska3 and untagged Ska2/Ska1 (kind gifts from Iain M. Cheeseman) were induced by addition of 0.1 M imidazole, and continued for 4hrs at 20°C. Cells were subsequently pelleted and lysed in PBS, pH 7.4, supplemented with 250 mM NaCl and 1 mM DTT (Wash Buffer), and cell debris was removed by centrifugation. GST-Ska3 was immobilized on Glutathione Agarose Resin (Gold Biotechnology), briefly washed with Wash Buffer, and incubated with cell lysate containing untagged Ska2/Ska1 for 1 hr at 4°C. After subsequent wash with Wash Buffer the Ska complex was eluted with Wash Buffer supplemented with 15 mM L-Glutathione Reduced and gel filtered on Superdex 200 column 10/300 GL size-exclusion column (GE Healthcare Life Sciences), previously equilibrated to 50 mM Tris, pH 7.4, 150 mM NaCl, 1 mM DTT.

For fluorescence anisotropy and kinase assay $Ndc80^{Bonsai}$ constructs were expressed, lysed and pre-cleared similarly to GST-Ska3. Cell lysate was then incubated with Glutathione Agarose Resin (Gold Biotechnology) followed by extensive wash with PBS supplemented with 250 mM NaCl and 1 mM DTT (Wash Buffer). Untagged proteins were eluted by overnight incubation with HRV 3C protease and gel filtered on Superdex 200 column 10/300 GL size-exclusion column (GE Healthcare Life Sciences), previously equilibrated to 50 mM Tris, pH 7.4, 150 mM NaCl, 1 mM DTT.

For electron tomography experiments $Ndc80^{Bonsai}$ constructs were purified similarly as described above, with following modifications. After incubation of the cell lysate with the Glutathione Agarose Resin (Gold Biotechnology) proteins were washed with Wash Buffer, eluted with Wash Buffer supplemented with 15 mM reduced L-glutathione, and flash frozen in liquid nitrogen for storage in -80°C. Prior to grid preparation, samples were thawed and subjected to gel filtration on Superdex 200 10/300 GL size-exclusion column in (20 mM Tris pH 7.2, 100 mM KCl, 1 mM DTT). Protein were then re-bound to glutathione resin and washed into BRB80 + 1 mM DTT. Untagged $Ndc80^{Bonsai}$ was eluted by overnight cleavage of GST-tag by HRV 3C Protease. Samples were then precleared at 240,000 x g for 20 min at 4°C, warmed to room temperature and centrifuged in table-top centrifuge at 17,000 x g for 10 min prior to EM grid preparation.

### Knockdown and Rescue of Ndc80

For synchronization, cells were seeded in media containing 2mM thymidine for 24 hr, released into fresh media for 12 hr, arrested again in 2mM thymidine for 12 hr, released for 8-12 hr, and fixed for immunofluorescence with 2% PFA in PHEM buffer + 0.5% Triton X-100 or ice-cold methanol. For knock-down experiments in stable T-Rex HeLa cell lines lines (Figures 3, 4D, and S4), transfection of Ndc80 siRNA (see Key Resource Table for sequence, 75 nM final concentration) was done at first thymidine release and second thymidine block using RNAiMAX (Life Technologies), according to manufacturer's description. For experiment depicted in Figure 3E 3.3 μM Nocodazol (Sigma-Aldrich) and 2 μM ZM 447439 (R&D Systems) were added two hours before fixation. For knockdown and replacement experiments (Figures 4A–4C), HeLa cells were co-transfected at the first thymidine release with siRNA oligos (75 nM for Ndc80, 20 nM for Mad2) and 100 ng rescue plasmid using Lipofectamine 2000 (Life Technologies). Cells were transfected a second time with siRNA oligos at the second thymidine block using RNAiMAX (Life Technologies). For mock and siRNA only controls, an empty pEGFP vector was used as the rescue plasmid. For transient transfection Ndc80 tail experiments, 75 nM GAPD siRNA oligos (Thermo Scientific) were included as mock controls.

### Creation of Stable Cell Lines

To create a stable cell line expressing the $Ndc80^{WT}$, $Ndc80^{+4CT}$ and $Ndc80^{+4NT}$ tail mutant, appropriate sequences were cloned into the pCDNA5/FRT plasmid (Invitrogen) using flanking Not1 restriction sites. The plasmid was co-transfected into T-Rex HeLa cells (Invitrogen) with the pOG44 plasmid (Invitrogen) and the cells were cultured in DMEM + 10% FBS (Gibco) supplemented with hygromycin B (Invitrogen) for 14 days. At the end of the selection period, remaining cells were pooled and used for subsequent experiments.

### Proximity Ligation Assay

After fixation of HeLa cells PLA was performed using Duolink In-Situ PLA probe anti-Mouse MINUS and anti-Rabbit PLUS and Duolink II Detection Reagents Orange, according to manufacturer's instructions (Sigma-Aldrich), using the provided blocking solution and antibody diluent. Samples were incubated with primary antibodies overnight at 4°C. Following primary antibodies were used for the assay: anti-Ska3 (gift from Gary Gorbsky, rabbit polyclonal), anti-Ndc80 9G3 (GTX70268, GeneTex), FITC conjugated mouse monoclonal anti-tubulin (Sigma-Aldrich), and Cy5 conjugated anti-Borealin (Stukenberg Lab, rabbit polyclonal). Quantification of PLA-positive centromeres was done in Volocity 6.3 software (PerkinElmer) in 3D Opacity mode, by semi-automatic detection of the centromeric volumes and manual scoring of surrounding PLA signals.

### Fluorescence Anisotropy

$Ndc80^{Bonsai}$ WT, $Ndc80^{Bonsai}$ +4CT and $Ndc80^{Bonsai}$ +4NT were labeled with Oregon Green 488 maleimide (ThermoFisher Scientific) according to manufacturer instructions and the un-reacted dye was removed by size exclusion chromatography. Efficiency of labeling was estimated to be between 1.5 to 2 dye molecules per $Ndc80^{Bonsai}$ molecule. Increasing concentrations of taxol stabilized MT were incubated at room temperature overnight with 50 nM fluorescently labeled $Ndc80^{Bonsai}$, then 35 μL of mixture was loaded in triplicates into 384-well plate (Greiner Bio-One) and fluorescence anisotropy measurements were done in PHERAstar FS plate reader (BMG Labtech). The anisotropy data were fitted using Hill equation by OriginPro 7.5 software (Built-in non-linear fitting function Hill1, $y = Start + (End - Start) * x^n / (k^n + x^n)$).

### Kinase Assay

Aurora B-$Incenp^{790-856}$ (Banerjee et al., 2014) was diluted to 0.03 mg/ml in Kinase Buffer (20 mM Tris, pH 7.5, 25 mM KCl, 1 mM $MgCl_2$, 1 mM DTT) supplemented with 1 mM ATP/10 μM γ-[$^{32}$P] ATP. Following mixture was added in 1:10 v/v ratio to 1 μM $Ndc80^{Bonsai}$ WT, $Ndc80^{Bonsai}$ +4CT or $Ndc80^{Bonsai}$ +4NT, previously dialyzed to Kinase Buffer. 20μL samples were taken from the reaction mixture at appropriate time points and added to 5 μL 5xSample Buffer to quench the reaction. Samples were further subjected to SDS-PAGE, followed by Coomassie staining. Gels were dehydrated on Whatman paper and exposed to Phosphor Screen overnight. Phosphor Screens were scanned on Storm 860, Molecular Dynamics, and resulting images were quantified using ImageJ software. Amount of incorporated $PO_4$ was calculated based on initial concentrations of ATP and γ-[$^{32}$P] ATP and standard curves obtained by serial dilutions of the reaction mixture.

## QUANTIFICATION AND STATISTICAL ANALYSIS

Statistical parameters and tests used for analysis are reported in Figures and Figure Legends. Statistical analysis was performed by GraphPad Prism (GraphPad). $p < 0.05$ was considered to be statistically significant.

**Developmental Cell, Volume *41***

## Supplemental Information

# Mechanism of Ska Recruitment by Ndc80 Complexes to Kinetochores

**Paweł Ł. Janczyk, Katarzyna A. Skorupka, John G. Tooley, Daniel R. Matson, Cortney A. Kestner, Thomas West, Owen Pornillos, and P. Todd Stukenberg**

## SUPPLEMENTAL FIGURES

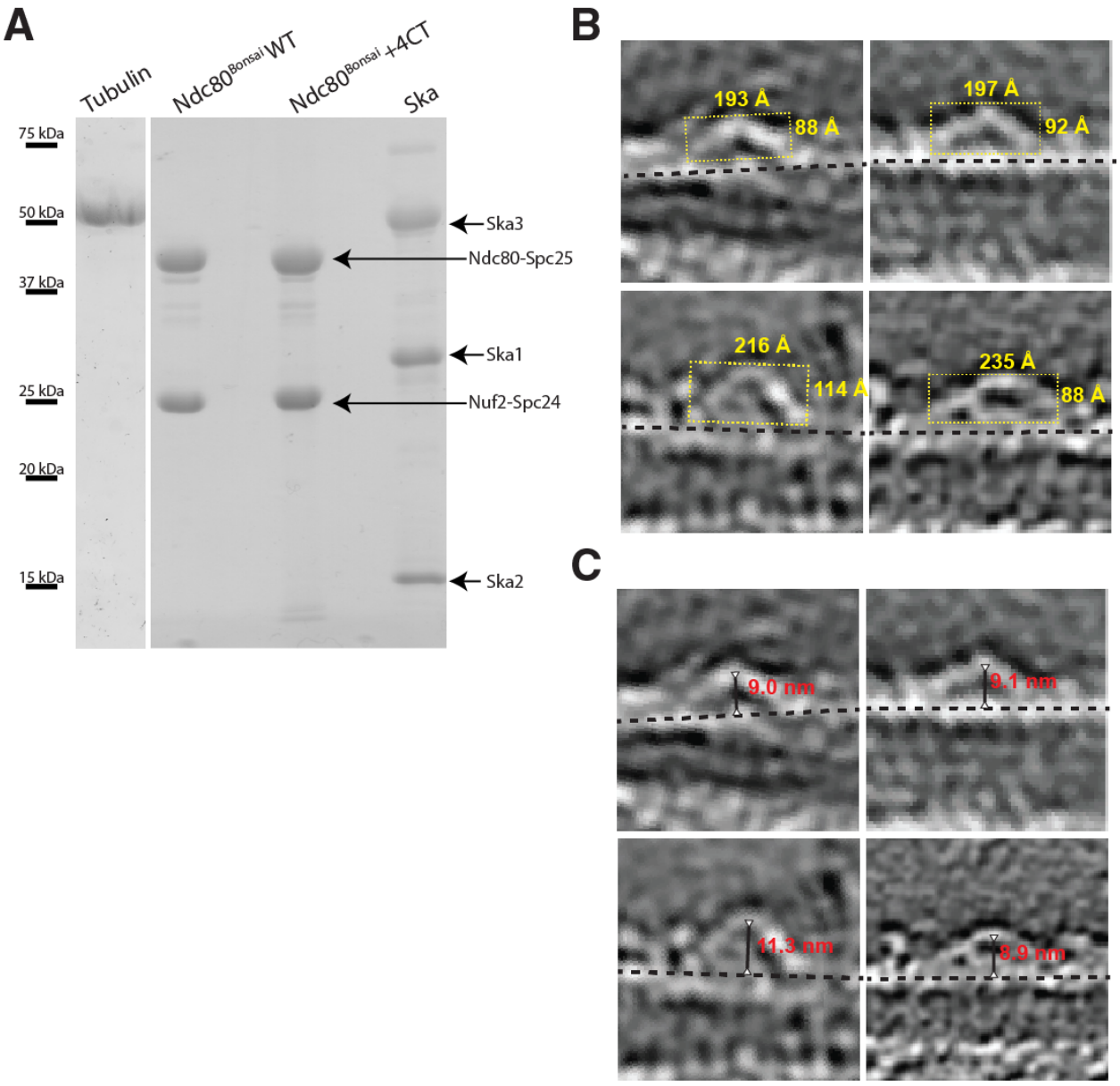


**Figure S1. Measurements of V shape dimensions and distance from the tip of the V shape to the microtubule, related to Figure 1.**

**(A)** Coomassie stained gel showing purified bovine brain tubulin, recombinant Ndc80$^{Bonsai}$ WT, Ndc80$^{Bonsai}$ +4CT and Ska complexes.

**(B)** Method employed to analyze dimensions of the V shapes using a bounding box (yellow). Width and height of representative V-shapes from Figure 1A are shown.

**(C)** Representative measurements of the distance from the tip of the V shape to the microtubule lattice are shown (black solid line).

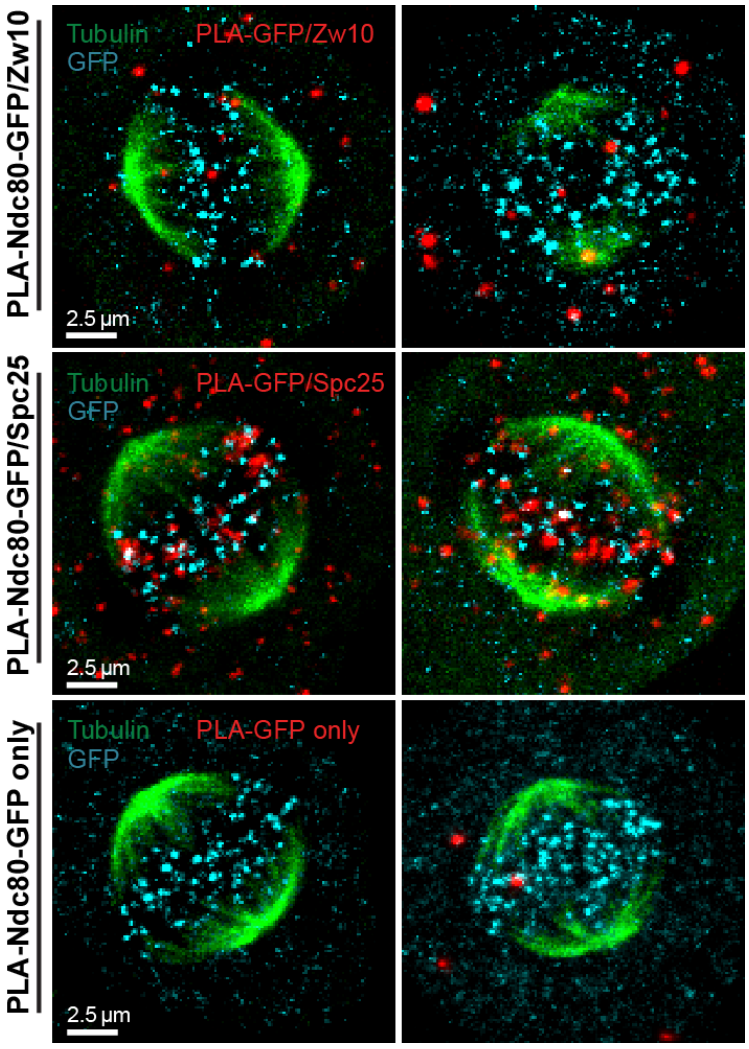


**Figure S2. Additional controls for the proximity ligation assay, related to Figure 2.**

The C-terminal GFP fusion the Ndc80 protein is close enough to Spc25, but not to Zw10, to generate a PLA signal. Representative images of Proximity Ligation Assay (red) in cells expressing Ndc80-GFP (C-term), with additional immunostaining of GFP (cyan) and tubulin (green). Top – PLA Zw10/GFP middle – PLA Spc25/GFP, bottom – control PLA-GFP only. Green and Cyan channel were scaled independently between the images.

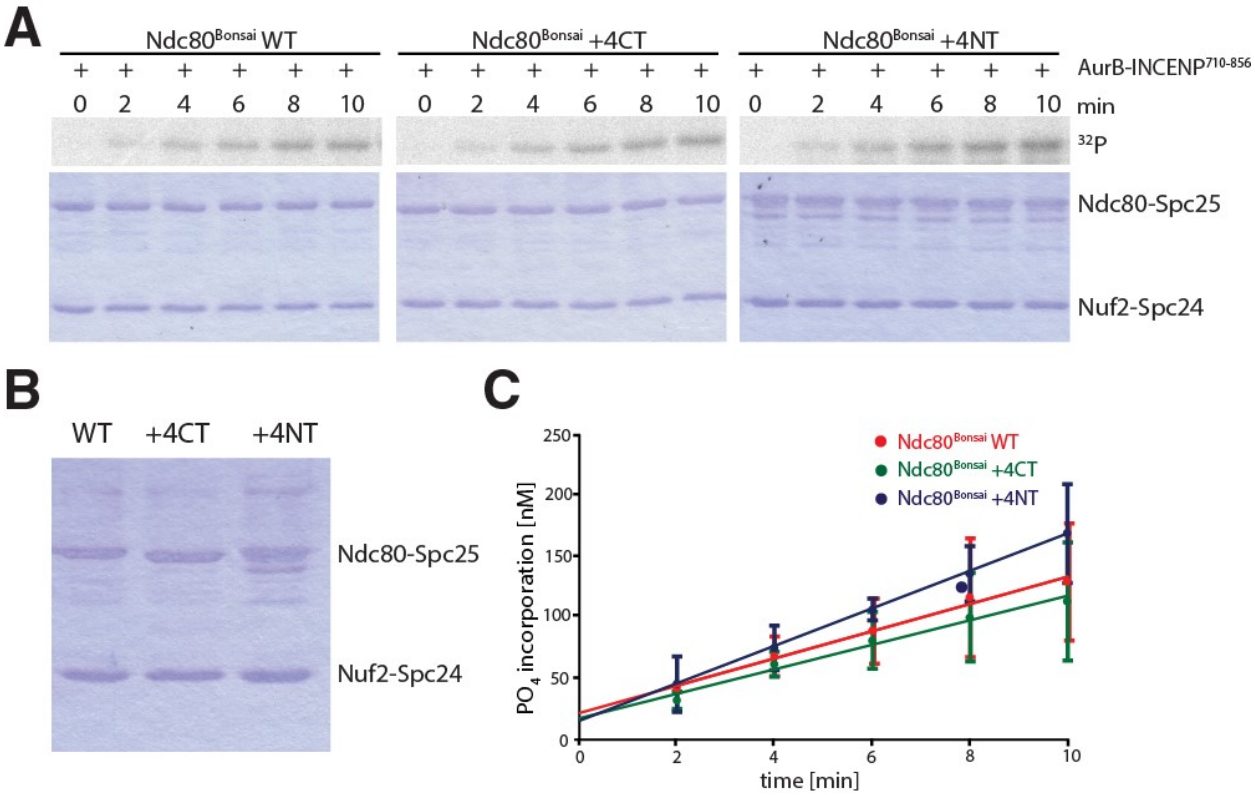


**Figure S3. Ndc80 tail mutants are phosphorylated in vitro by Aurora B at similar rates as the wild-type protein, related to Figure 3.**

**(A)** Phosphorylation of Ndc80$^{Bonsai}$ tail mutants by Aurora B-INCENP$^{710-856}$. **Top:** Representative images showing incorporation of $^{32}$P to Ndc80 in presence of Aurora B. **Bottom:** Coomassie stained gels representing Ndc80$^{Bonsai}$ samples taken from different time-points during phosphorylation reaction.

**(B)** Representative Coomassie stained gel showing similar amounts of Ndc80$^{Bonsai}$ tail mutants were used for the kinase assay.

**(C)** Graph representing quantification of time dependent incorporation of [$PO_4$] to Ndc80Bonsai tail mutants by Aurora B (mean ± SD, N = 2).

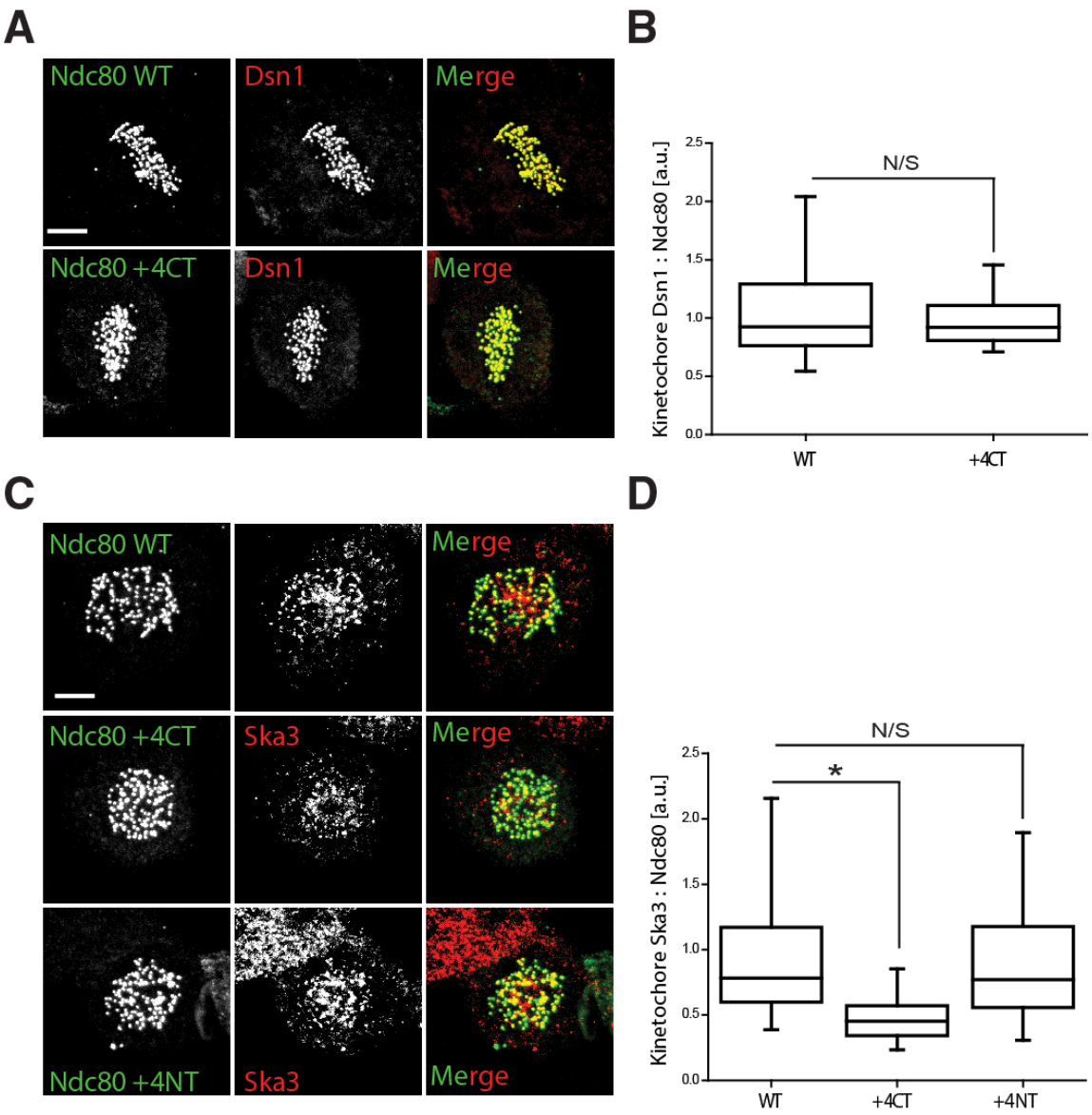


**Figure S4. The recruitment of Ska, but not Dsn1, to kinetochores requires charge in 40-60aa region of Ndc80 tail, related to Figure 3.**

**(A)** Immunofluorescence staining of Ndc80$^{WT}$, Ndc80$^{+4CT}$ and Ndc80$^{+4NT}$ stable cell lines after depletion of endogenous Ndc80 shows reduced levels of Ska3 on prometaphase kinetochores of Ndc80$^{+4CT}$ stable cell lines, but not on the prometaphase kinetochores of Ndc80$^{+4NT}$ stable cell lines. Scale bar = 5 µm.

**(B)** Box and whisker plots representing the quantification of Dsn1 staining intensities on kinetochores represented in **(A)** (N > 100 kinetochores from at least 4 cells, Whiskers – 5-95% percentile). a.u. = arbitrary units. N/S - p = 0.84 (Unpaired t-test with Welch's correction).

**(C)** Immunofluorescence staining of Ndc80$^{WT}$ and Ndc80$^{+4CT}$ stable cell lines after depletion of endogenous Ndc80 does not show significantly changed kinetochore levels of Dsn1 cells expressing Ndc80$^{+4CT}$. Scale bar = 5 µm.

**(D)** Box and whisker plots representing the quantification of Ska staining intensities on kinetochores represented in **(C)** (N > 100 kinetochores from at least 4 cells, Whiskers – 5-95% percentile). a.u. = arbitrary units. * - p < 0.0001, N/S – p = 0.1114 (Unpaired t-test with Welch's correction).

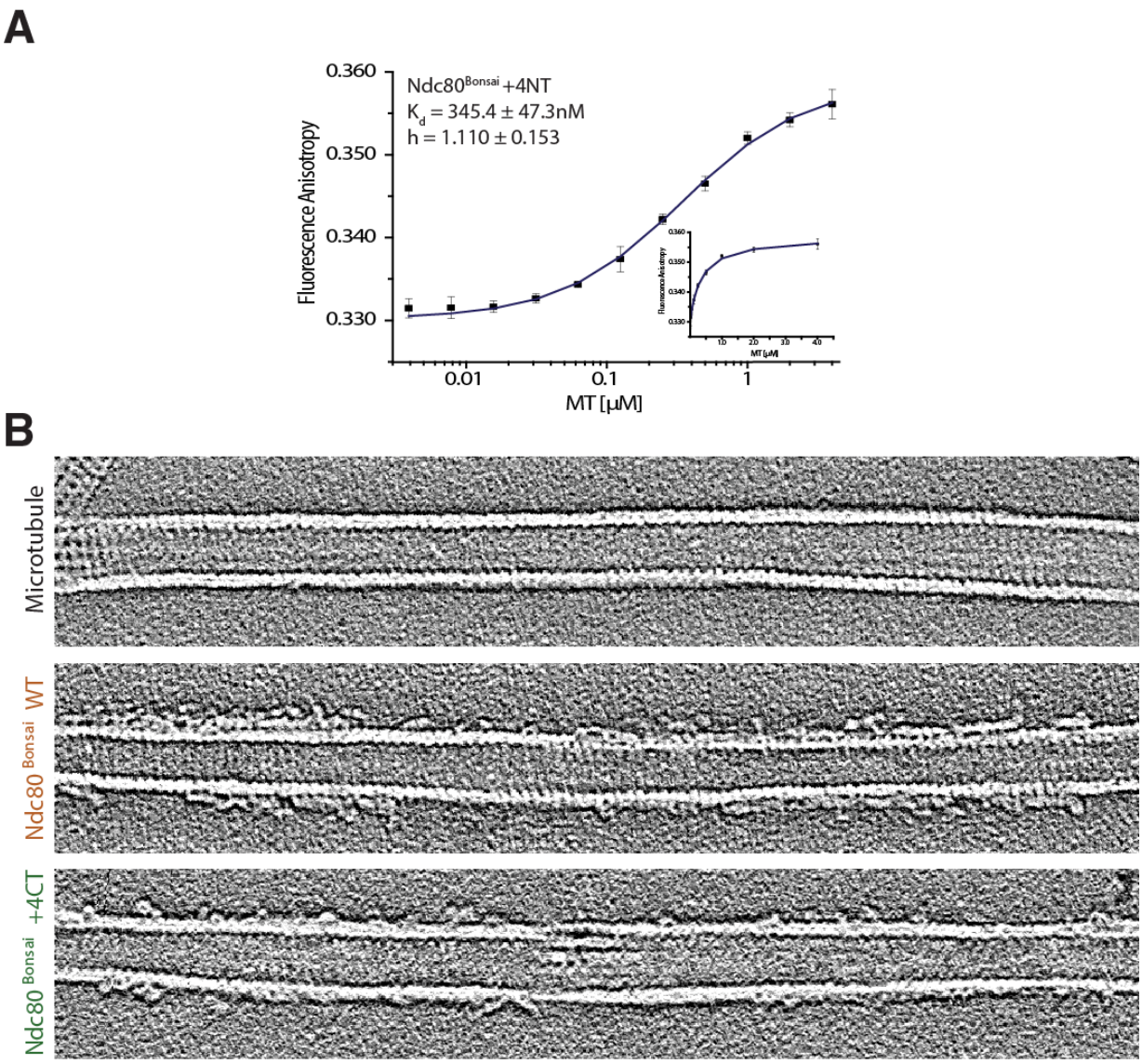


**Figure S5. Ndc80$^{+4CT}$ tail mutant is deficient in clustering on microtubules, related to Figure 5.**

**(A)** Fluorescence anisotropy measurements of fluorescently labeled Ndc80$^{Bonsai}$ +4NT (blue) incubated with increasing concentrations of taxol-stabilized microtubules, plotted on $\log_{10}$ scale (mean ± SD). Hill equation was used for fitment of the data. Small graphs represent the data in the linear scale.

**(B)** Representative projections (same as in **Figure 5**) of 5 consecutive Z-sections (1.107 nm) of the tomographic reconstructions show Ndc80$^{Bonsai}$ +4CT form smaller clusters than Ndc80$^{Bonsai}$ WT. Black lines to indicate positions of Ndc80 molecules are omitted for clarity.

## SUPPLEMENTAL MOVIES

**Movie S1. Serial slices of tomographic projections of microtubules coated with Ndc80$^{Bonsai}$ WT, related to Figure 1.**

Movie displays series of slices (slice thickness: 0.4427 nm) of the tomographic reconstructions shown in Figure 1A. Scale bar = 10 nm.

**Movies S2. Serial slices of tomographic reconstruction of microtubules coated with Ndc80$^{Bonsai}$ WT and Ska complex showing representative V shape, related to Figure 1.**

Movie displays series of slices (slice thickness: 0.4427 nm) of the tomographic reconstructions shown in Figure 1A. Representative V-shape is indicated by white arrow. Scale bar = 10 nm.

**Movies S3. Serial slices of tomographic reconstruction of microtubules coated with Ndc80$^{Bonsai}$ WT and Ska complex showing second representative V shape, related to Figure 1.**

Movie displays series of slices (slice thickness: 0.4427 nm) of the tomographic reconstructions shown in Figure 1A. Representative V-shape is indicated by white arrow. Scale bar = 10 nm.

**Movie S4. Movie showing structure of Ska core complex (PDB: 4AJ5) fitted to representative V shape, related to Figure 1**

Structure of Ska core complex was fitted to EM map of tomographic reconstruction. Thickness of visible map: 2.6568 nm (12 consecutive z-slices). Visualization was done in Chimera 1.11.2.

# Appendix 4.

# TRIM5α SPRY/coiled-coil interactions optimize avid retroviral capsid recognition

Marcin D. Roganowicz, Sevnur Komurlu, Santanu Mukherjee, Jacek Plewka, Steven L. Alam, Katarzyna A. Skorupka, Yueping Wan, Damian Dawidowski, David S. Cafiso, Barbie K. Ganser-Pornillos, Edward M. Campbell, Owen Pornillos

PLoS Pathog 13 (10): e1006686. https://doi.org/10.1371/journal. ppat.1006686

PLOS | PATHOGENS

RESEARCH ARTICLE

# TRIM5α SPRY/coiled-coil interactions optimize avid retroviral capsid recognition

**Marcin D. Roganowicz[1], Sevnur Komurlu[2], Santanu Mukherjee[2], Jacek Plewka[1], Steven L. Alam[3], Katarzyna A. Skorupka[1], Yueping Wan[1], Damian Dawidowski[4], David S. Cafiso[4], Barbie K. Ganser-Pornillos[1], Edward M. Campbell[2], Owen Pornillos[1]***

**1** Department of Molecular Physiology and Biological Physics, University of Virginia School of Medicine, Charlottesville, Virginia, United States of America, **2** Department of Microbiology and Immunology, Stritch School of Medicine, Loyola University Chicago, Maywood, Illinois, United States of America, **3** Department of Biochemistry, University of Utah, Salt Lake City, Utah, United States of America, **4** Department of Chemistry, University of Virginia, Charlottesville, Virginia, United States of America

* opornillos@virginia.edu





**Citation:** Roganowicz MD, Komurlu S, Mukherjee S, Plewka J, Alam SL, Skorupka KA, et al. (2017) TRIM5α SPRY/coiled-coil interactions optimize avid retroviral capsid recognition. PLoS Pathog 13 (10): e1006686. https://doi.org/10.1371/journal.ppat.1006686

**Editor:** Félix A. Rey, Institut Pasteur, FRANCE

**Received:** May 3, 2017

**Accepted:** October 10, 2017

**Published:** October 17, 2017



**Data Availability Statement:** All relevant data are within the paper and its Supporting Information files.

**Funding:** This work was funded by National Institutes of Health grants R01-GM112508 (OP), R01-GM123538 (EMC), and P50-GM082545 (BKGP, EMC, SLA). The funders had no role in study design, data collection and analysis, decision to publish, or preparation of the manuscript.

**Competing interests:** The authors have declared that no competing interests exist.

## Abstract

Restriction factors are important components of intrinsic cellular defense mechanisms against viral pathogens. TRIM5α is a restriction factor that intercepts the incoming capsid cores of retroviruses such as HIV and provides an effective species-specific barrier to retroviral infection. The TRIM5α SPRY domain directly binds the capsid with only very weak, millimolar-level affinity, and productive capsid recognition therefore requires both TRIM5α dimerization and assembly of the dimers into a multivalent hexagonal lattice to promote avid binding. Here, we explore the important unresolved question of whether the SPRY domains are flexibly linked to the TRIM lattice or more precisely positioned to maximize avidity. Biochemical and biophysical experiments indicate that the linker segment connecting the SPRY domain to the coiled-coil domain adopts an α-helical fold, and that this helical portion mediates interactions between the two domains. Targeted mutations were generated to disrupt the putative packing interface without affecting dimerization or higher-order assembly, and we identified mutant proteins that were nevertheless deficient in capsid binding *in vitro* and restriction activity in cells. Our studies therefore support a model wherein substantial avidity gains during assembly-mediated capsid recognition by TRIM5α come in part from tailored spacing of tethered recognition domains.

## Author summary

TRIM5α is a cytosolic protein that provides effective protection for mammalian cells against retroviral infection. This anti-viral defense mechanism is an unprecedented example of how the cell can recognize entire capsids, which are large, megadalton-sized particles. TRIM5α achieves this by assembling into a hexagonal scaffold that coats the capsid. An important unresolved question is how the capsid-binding SPRY domain of TRIM5α is positioned to optimize its contact points on the capsid surface. Here, we use a variety of techniques to determine that the SPRY domains in the TRIM lattice are organized in pairs

and likely to be stably tethered against the hexagonal scaffold. Such an arrangement maximizes the avidity of capsid binding, and allows TRIM5α to act as a "molecular ruler" that matches the spacings and orientations of the capsid subunits.

## Introduction

TRIM5α is a restriction factor that recognizes and binds the incoming cores of retroviruses such as HIV [1–3], and represents a first-line intracellular antiviral defense mechanism. Upon core binding, TRIM5α induces accelerated capsid dissociation or uncoating, inhibits reverse transcription, and activates innate immune signaling pathways [1, 3, 4]. Like other members of the TRIM family [5], TRIM5α contains a tripartite or RBCC motif at its N-terminus (RING, B-box 2, and coiled-coil domains)–the RING domain mediates E3 ubiquitin ligase effector functions required to inhibit reverse transcription and signal interferon [4, 6, 7], whereas the coiled-coil and B-box 2 domains respectively mediate TRIM5α dimerization and higher-order assembly [8–16]. The TRIM5α RBCC motif is connected by a long linker (L2 or linker 2) to a C-terminal SPRY domain that directly contacts retroviral capsids [1–3, 17].

Retroviral capsids are higher-order macromolecular assemblages composed of about 1,500 viral CA protein subunits, which assemble on a hexagonal lattice of several hundred hexamers and 12 pentamers [18, 19]. Accordingly, TRIM5α also undergoes higher-order assembly in order to bind retroviral capsids [10, 20]. Although an individual SPRY domain does not have appreciable affinity for the capsid (estimated to be in the mM range [21]), dimerization of the coiled-coil domain [8, 9, 12] and trimerization of the B-box 2 domain [15, 16, 20, 22] creates a hexagonal TRIM lattice that displays an array of SPRY domains for multivalent, avid capsid binding [10, 23]. This "pattern recognition" model and the architecture of the TRIM lattice are supported by structural and biochemical studies of *in vitro* TRIM5α/capsid complexes and crystal structures of individual domains and fragments of TRIM5α and other TRIM proteins [3, 8–16, 20, 22, 23]. However, the molecular details of SPRY domain positioning–whether it is flexibly displayed or tethered–remain experimentally undefined. This unresolved issue is a core concept of the avidity-driven recognition mechanism.

The L2 linker that connects the SPRY domain to the coiled-coil is likely to facilitate positioning of the SPRY domain. Mutagenesis studies have shown that an intact L2 sequence is required for efficient retroviral restriction [24, 25], and L2 polymorphisms have been reported to correlate with susceptibility to HIV-1 infection [26]. Furthermore, evolutionary sequence analysis has shown that some L2 residues are under positive selection, even though the linker itself does not contact the capsid [17]. In crystal structures of TRIM protein dimerization domains, the L2 linkers display substantial degrees of disorder but have been seen to fold into a short C-terminal helix that packs against the center of the coiled-coil dimer [11–14]. This packing interaction can be therefore quite flexible, and this flexibility has been proposed to underlie degenerate binding of the SPRY domain to capsid surface epitopes as well as a mechanism to destabilize the capsid lattice [11–13, 27, 28]. Alternatively, it has been proposed that the C-terminal L2 helix is integrated with the downstream SPRY domain fold, and that this L2/SPRY helix packs more stably against the coiled-coil helices and thereby positions two SPRY domains at a defined spacing and orientation relative to each other [11, 12]. This issue has not yet been resolved, in part because structures of TRIM5α constructs containing the coiled-coil, L2, and SPRY domains have been notoriously difficult to obtain. Here, we describe biochemical, biophysical, and cell biological experiments to test the models for SPRY domain positioning. Our results are consistent with a tethered mechanism: the residues at the L2/

SPRY boundary are indeed helical, and packing of this helix to the main coiled-coil helix not only facilitates capsid recognition, but also modulates stability of the TRIM5α dimer, efficiency of higher-order assembly, and overall antiviral activity.

## Results

### Packing of the L2/SPRY helix against the coiled-coil helix

In the published crystal structure of the TRIM5 B-box 2/coiled-coil/L2 fragment, both of the subunits in the antiparallel dimer had substantial disorder in their L2 regions, but in one subunit the L2 C-terminus was folded into a short α-helix [12]. Crystal structures of other TRIM proteins displayed similar variations in L2 configurations, and some of the variations appeared to have been caused by crystal packing interactions [11, 13]. We therefore first sought confirmation that L2 packed against the coiled-coil helix in solution, using site-directed spin labeling and paramagnetic double electron-electron resonance (DEER) spectroscopy (Fig 1 and S1 Fig). In this experiment, the distance of separation between a pair of labels can be determined provided that phase modulation can be reliably measured (<8 nm) [29]. Measurements were performed on a purified recombinant CC-L2 fragment of rhesus TRIM5α (residues 133–300) that includes the full sequence of the putative L2/SPRY helix ($_{281}$PDLKGMLDMFRELTDARRYW$_{300}$) [11].

In a control experiment, we first confirmed that labels appended to the main coiled-coil helix (W196R1) had a single distance distribution peaking at the expected distance–about 3 nm–between the two labels (Fig 1A). In contrast, labels appended to the terminal L2 helix (D288R1, E292R1, W300R1) returned progressively broader distance distributions with multiple peaks as the labels approached the C-terminus (Fig 1B–1D). These are indicative of either a dynamic helical configuration or dynamic packing of the L2/SPRY helix against the coiled-coil. These results are consistent with the crystal structures [11–13], as well as a recent biochemical analysis of the CC-L2 fragment of rhesus TRIM5α [28].

Given the likelihood that L2 disorder in CC-L2 was caused by the absence of the SPRY domain, it was important to perform a comparative DEER analysis with a protein construct containing an intact SPRY. Unfortunately, we were unable to perform these experiments because the recombinant CC-L2-SPRY protein did not tolerate removal of its 7 native cysteine residues to allow for site-directed thiol-based labeling. We therefore determined the effect of the SPRY domain on L2 flexibility by comparing CC-L2 and CC-L2-SPRY stabilities using a thermal melting experiment called differential scanning fluorimetry. In this assay, protein unfolding is monitored with a dye that fluoresces upon binding hydrophobic residues that become exposed with increasing temperature [11]. As shown in Fig 2A, the CC-L2 construct (blue curve) displayed the expected melting profile for a coiled-coil protein, with a single transition reflecting the coupled folding and dimerization; the apparent melting point ($T_m$) was about 41˚C. The SPRY domain alone also displayed a single transition, consistent with its monomeric configuration in isolation, with a $T_m$ of about 50˚C (green curve). The CC-L2-SPRY protein (maroon curve) had an intermediate $T_m$ about halfway between CC-L2 and SPRY. Most notably, the CC-L2 profile had significantly elevated signals at the start of the experiment, which is distinct from the flat profiles of CC-L2-SPRY and SPRY (boxed area in Fig 2A). The elevated signals indicated that CC-L2 had exposed hydrophobic residues even at low temperature. The simplest interpretation of this observation is that the L2 linker was undergoing dynamic packing (association and dissociation) with the coiled-coil in this construct. Conversely, the flat signals for CC-L2-SPRY suggested that in the presence of the SPRY domain, L2 is more stably packed against the coiled-coil.

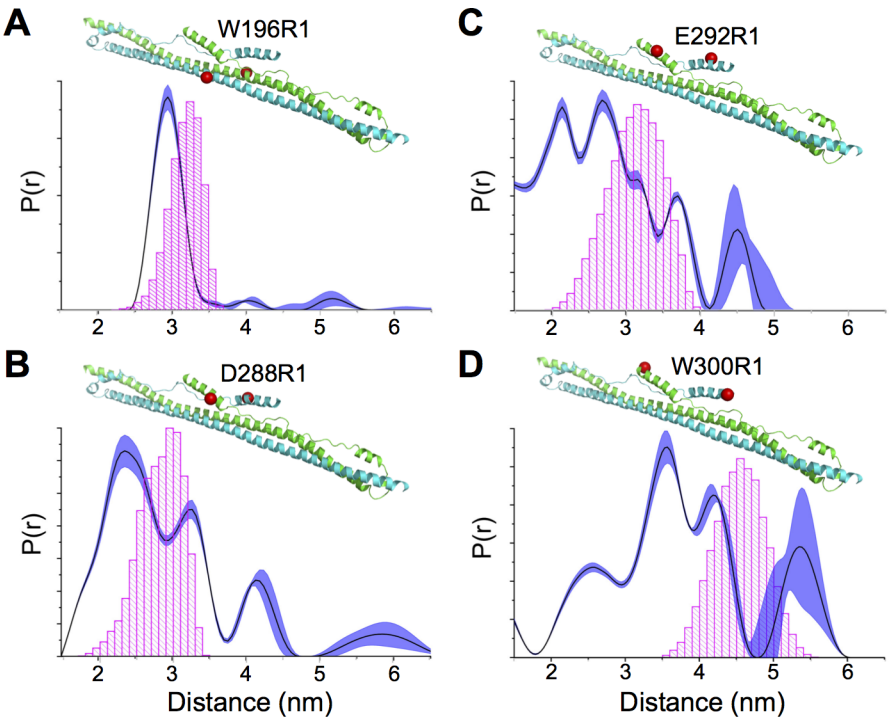


**Fig 1. Conformationally heterogeneous packing of the terminal L2 helix against the coiled-coil scaffold in context of the CC-L2 fragment of rhesus TRIM5α.** (A-D) Distance distribution curves show a single well-defined peak when R1 is attached to coiled-coil helix (W196R1). Multiple peaks are obtained when labels are appended to the indicated L2 helix residues (D288R1, B; E292R1, C; W300R1, D). Note that since the protein is a dimer, a single cysteine substitution can be used to attach two labels for distance measurements. The shaded regions represent fits to the DEER data that are within 15% root mean square deviation of the best fit (dark trace). Corresponding time-traces and subtracted dipolar evolutions are shown in S1 Fig. Expected distances calculated from the static structural model are indicated by the histograms in magenta. These are based upon all the available rotamers given the steric constraints in the model.

https://doi.org/10.1371/journal.ppat.1006686.g001

## N-terminal extensions of the SPRY domain have helical propensity

We next performed a complementary analysis of the putative L2/SPRY helix in context of the isolated SPRY domain. Published structures of the TRIM5α SPRY domain have revealed that residues 292–300 (the C-terminal half of the L2/SPRY boundary) are indeed helical and appear to pack stably against the main body of the domain [30, 31]. However, in one of the structures, residues that form part of the predicted helix (287–291) adopt a non-helical, random coil configuration [31]. To test whether these and additional N-terminal residues would actually adopt a helical configuration in solution, we used NMR spectroscopy to analyze a SPRY construct starting at residue 281 and compared this to a truncated construct starting at residue 292. Control spectra indicated that the two SPRY proteins had the same fold (S2 Fig). Importantly, we found three complementary indications that the additional residues in the longer construct were likely to be helical. First, significant chemical shift perturbations were observed for residues located in a loop (encircled in Fig 3A) that would physically encounter the extended helix. Second, analysis of chemical shift deviations from random coil values for backbone carbon and proton atoms indicated the presence of contiguous α-helical secondary structure in the segment spanning residues 283–300 (Fig 3B). Third, we observed three 4-residue segments ($_{285}$GMLD$_{288}$, $_{290}$FREL$_{293}$, and $_{293}$LTDA$_{296}$) with fortuitously well-resolved sequential proton-amide cross-peaks in an $^{15}$N-filtered NOESY spectrum (Fig 3C). The absolute peak intensities

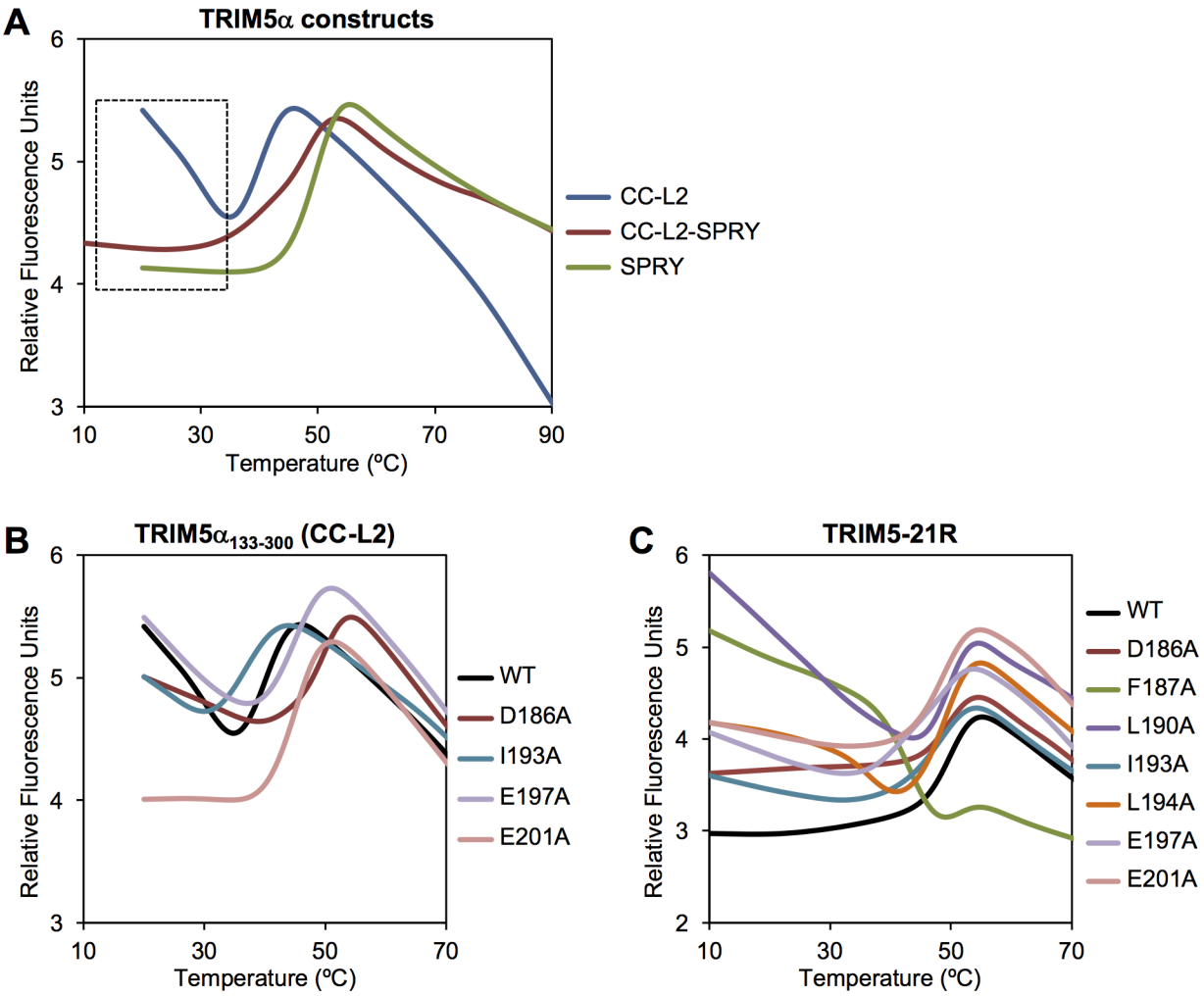


**Fig 2. Differential scanning fluorimetry thermal stability profiles of purified TRIM5α proteins.** (A) Comparison of CC-L2, CC-L2-SPRY, and SPRY constructs. (B) Effect of model-based mutations in context CC-L2. (C) Effect of model-based mutations in context of the restriction-competent TRIM5-21R protein.

https://doi.org/10.1371/journal.ppat.1006686.g002

obey the expected sequential pattern for α-helical segments, with strong/medium $i \rightarrow i+1$ cross-peaks, very weak $i \rightarrow i+2$, and weak $i \rightarrow i+3$. Collectively, these data indicated that the helical termini observed separately in the crystal structures of the CC-L2 and SPRY fragments of TRIM5α probably constitute a single, contiguous helix in the full-length protein.

## Modeling of the putative coiled-coil/L2/SPRY packing interface

Given the above results and in the absence of an experimentally determined structure as yet, we computed a molecular model of the CC-L2-SPRY dimer (Fig 4A) and designed a mutagenesis study to test it. The model was built by first symmetrizing the B-box 2/coiled-coil/L2/lysozyme structure [12] to obtain ordered L2 regions for both subunits in the dimer, and then modeling a contiguous helix spanning residues 283–300 in the L2/SPRY boundary by superimposing matching residues in the isolated SPRY domain structure [30]. In this model, the orientations of the SPRY domains were dictated primarily by interactions between the two L2/SPRY helices and the middle of the two coiled-coil helices, as previously suggested [11, 12].

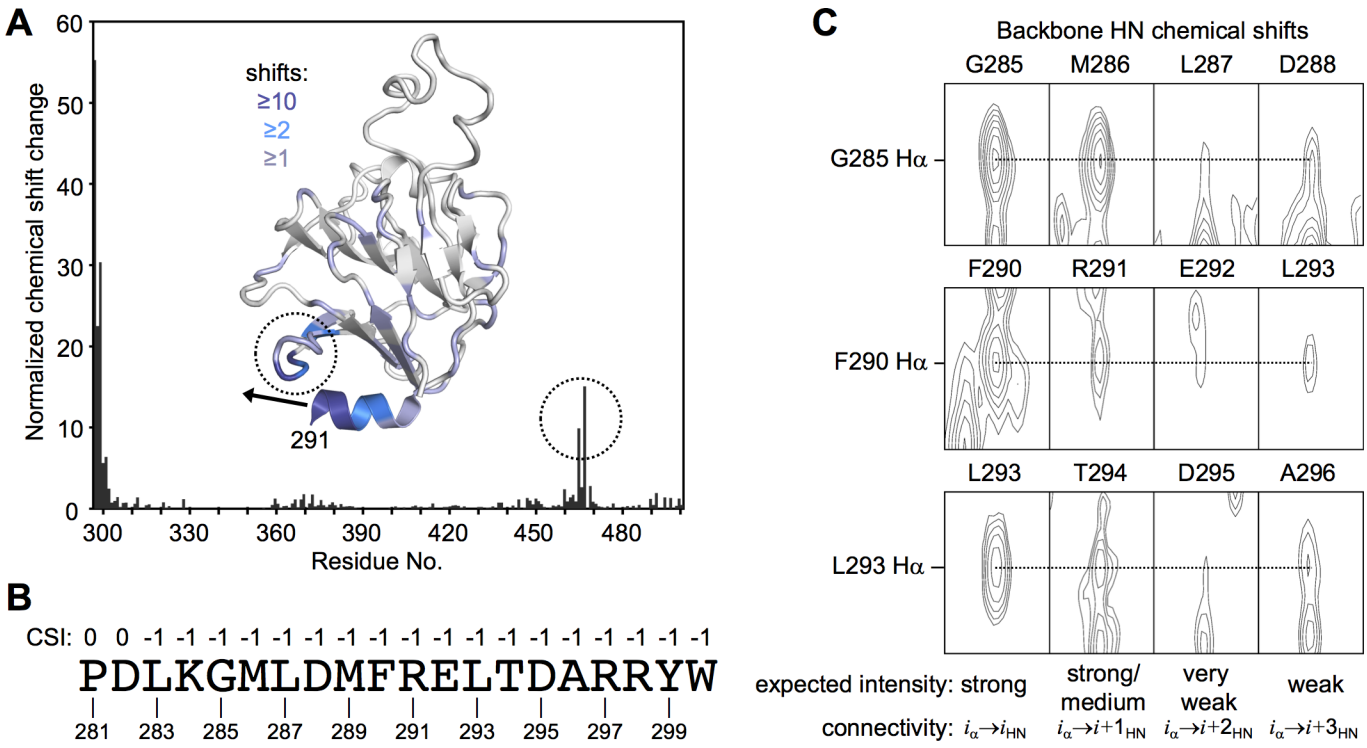


**Fig 3. NMR analysis of N-terminal extensions of the isolated TRIM5α SPRY domain.** (A) Normalized backbone amide chemical shift differences in comparing rhesus TRIM5α constructs spanning residues 292–497 and 281–497. Chemical shift changes were also mapped onto the SPRY domain structure (PDB 2LM3 [30]). Dashed circles highlight the loop that undergoes the greatest changes, apart from the N-terminal residues. Black arrow indicates the trajectory of the putative extended helix. (B) Normalized chemical shift indices calculated from assigned Cα, Cβ, C (carbonyl), and Hα resonances by using the program PREDITOR [64], shown for each of the indicated residues in the putative L2/SPRY helix. Values indicate predicted secondary structure: 1 = β-strand, 0 = random coil, -1 = α-helix. (C) Sections of an $^{15}$N-edited 3-dimensional NOESY spectrum with well-resolved sequential Hα-HN cross-peaks. Resonance overlap precluded identification of cross-peaks for the entire helical sequence.

https://doi.org/10.1371/journal.ppat.1006686.g003

Given significant model uncertainties in the positions of the L2/SPRY residues in the interface, we focused on the reliably defined coiled-coil residues for mutagenesis. Fourteen coiled-coil residues (7 per subunit) were buried within the putative packing interface, and we selected these for alanine substitution (Fig 4B and 4C). For biochemical experiments, mutations were made in the CC-L2 fragment described above and in TRIM5-21R, a chimeric construct described in previous studies as a useful recombinant surrogate for TRIM5α [8–10, 15, 23, 32]. Mutations were also made in context of full-length rhesus TRIM5α in a mammalian expression vector for analysis of assembly and restriction phenotypes in cells. The collective functional data are summarized in Table 1.

## Effects of mutations on protein dimerization and stability

Studies of the related protein, TRIM25, have shown that single alanine substitutions in the center of the elongated coiled-coil helix can severely destabilize the dimer, even though the dimerization interface is quite extensive [11]. We therefore used the thermal melting assay above to determine which of the model-based TRIM5α mutants were deficient in dimerization. In context of the CC-L2 construct, we found that the F187A, L190A, and L194A mutants were very prone to aggregation and could not be purified easily, indicating that the mutations severely destabilized the dimer. These results are consistent with their positions within the interface, as these three hydrophobic residues bridge contacts between the coiled-coil helices as well as

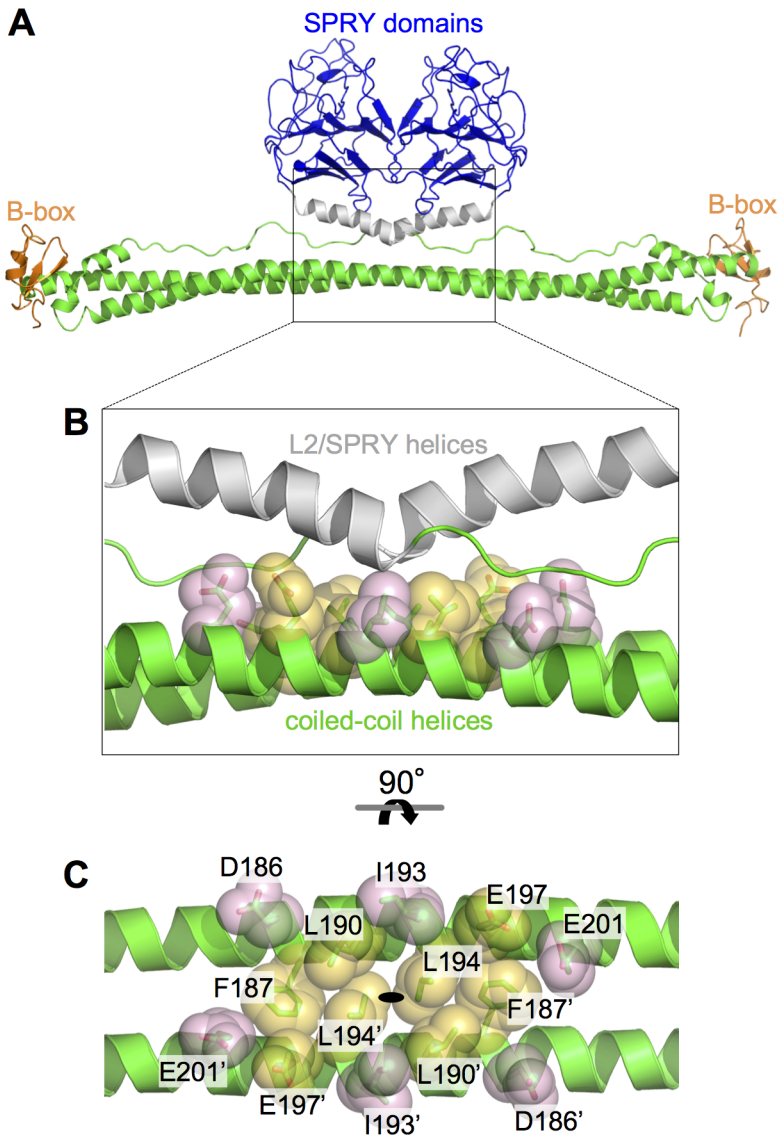


**Fig 4. Modeling of SPRY/coiled-coil packing in TRIM5α.** (A) Ribbon model of the TRIM5α dimer, which was obtained by combining the crystal structures of the B-box/coiled-coil dimer [12] and isolated SPRY domain [30, 31]. Domains and structural elements are colored as follows: RING, not included in model; B-box 2, orange; coiled-coil, green; L2 linker helix, gray; SPRY, blue. (B) Expanded view of the central region of the antiparallel dimer, in the same orientation as A. Residues selected for mutagenesis in this study are represented by sticks and transluscent spheres. Orange, class I residues; pink, class II residues. (C) Orthogonal view rotated as indicated, with individual residues labeled. The L2 helices are omitted in this panel for clarity. The two subunits are distinguished by an apostrophe. The coiled-coil dimer's two-fold symmetry axis is indicated by the black oval.

https://doi.org/10.1371/journal.ppat.1006686.g004

between the coiled-coil and L2/SPRY helices (Fig 4B and 4C). Similar results were observed for equivalent mutations in the CC-L2 dimer of TRIM25 [11]. In contrast, the remaining mutations produced purifiable CC-L2 proteins. Of these, I193A measurably reduced the stability of the dimer ($T_m$ = 37˚C), whereas the others (D186A, E197A, E201A) had no effect or even slightly increased the apparent $T_m$ compared to the wildtype control (Fig 2B).

To more rigorously determine oligomerization states, we also analyzed the CC-L2 mutants by using SEC-MALS (size exclusion chromatography coupled with multi-angle light

**Table 1. Functional phenotypes of TRIM5α mutants.**

| Mutation | Class | Tube Binding | *In Vitro* Assembly | Cytoplasmic Bodies | Restriction Activity |
|---|---|---|---|---|---|
| None (WT) | | ++ | ++ | ++ | ++ |
| D186A | II | + | n.d.* | + | + |
| F187A | I | – | n.d. | – | – |
| L190A | I | + | n.d. | +/– | – |
| I193A | II | – | ++ | ++ | + |
| L194A | I | + | n.d. | – | – |
| E197A | I | + | n.d. | +/– | + |
| E201A | II | – | ++ | ++ | + |

* n.d. = not determined

https://doi.org/10.1371/journal.ppat.1006686.t001

scattering). Consistent with the thermal shift data, SEC-MALS showed that D186A (Fig 5B), I193A (Fig 5C), and E201A (Fig 5E) were dimeric just like wildtype control (Fig 5A). The E197A mutant was likewise dimeric, but the major peak also had a significant trailing shoulder indicating dissociation into monomer (Fig 5D). Thus, this CC-L2 mutant was also deficient in dimerization, although not to the same extent as the F187A, L190A, and L194A mutants.

We next tested the mutations in context of TRIM5-21R, a restriction-competent chimeric construct wherein the RING domain of rhesus TRIM5α has been replaced by that of human TRIM21 [32, 33]. It was previously shown that this protein expresses both as a monomer and dimer–the two oligomers can be cleanly separated by sequential anion exchange and size exclusion chromatography steps (S3A and S3B Fig) [8–10]. In this case, all the mutants were purifiable, but the monomer fractions of F187A, L190A, L194A, and E197A during initial purification steps comprised 50% or more of the total protein, consistent with significant defects in dimerization (S3C Fig). In contrast, the D186A, I193A, and E201A mutants were more similar to wildtype, with the dimers being the major fraction (S3D Fig). For thermal melting analysis, we purified the dimer fraction for each mutant. Compared to the CC-L2-SPRY construct, the melting curve of wildtype TRIM5-21R had a sharper transition and higher $T_m$ of 50˚C (Fig 2C, black curve). The increased stability is likely due to "capping" of the coiled-coil ends by the B-box 2 domains, as observed in crystal structures [12, 15, 16]. Consistent with severe destabilization of the F187A, L190A, and L194A CC-L2 constructs, the equivalent TRIM5-21R proteins were still clearly unstable, with high signals at early time points similar to the wildtype CC-L2 construct (Fig 2C). In particular, F187A, which eliminated a significant proportion of the hydrophobic core, produced a non-canonical melting profile (Fig 2C, green curve). The remaining mutants did not significantly perturb the $T_m$ of the TRIM5-21R dimer, but also had elevated signals at low temperature, which we interpret to mean that the mutations also weakened packing of L2/SPRY against the coiled-coil, as predicted by the computational model.

On the basis of the thermal melting and chromatography data, we classified mutations within the putative CC/L2/SPRY interface into two groups: class I mutants (F187A, L190A, L194A, and E197A; orange in Fig 4B and 4C) had significant or measurable effects on dimerization, whereas class II mutants (D186A, I193A, and E201A; pink in Fig 4B and 4C) had little or no effect on dimerization but still likely important for CC/L2/SPRY packing. We therefore considered this second group to be more informative in the experiments below.

## Effects of mutations on capsid binding activity *in vitro*

If the positions of the SPRY domains in the TRIM5α dimer were tailored to match the spacing of epitopes on retroviral capsids, then destabilization of coiled-coil/L2/SPRY packing would

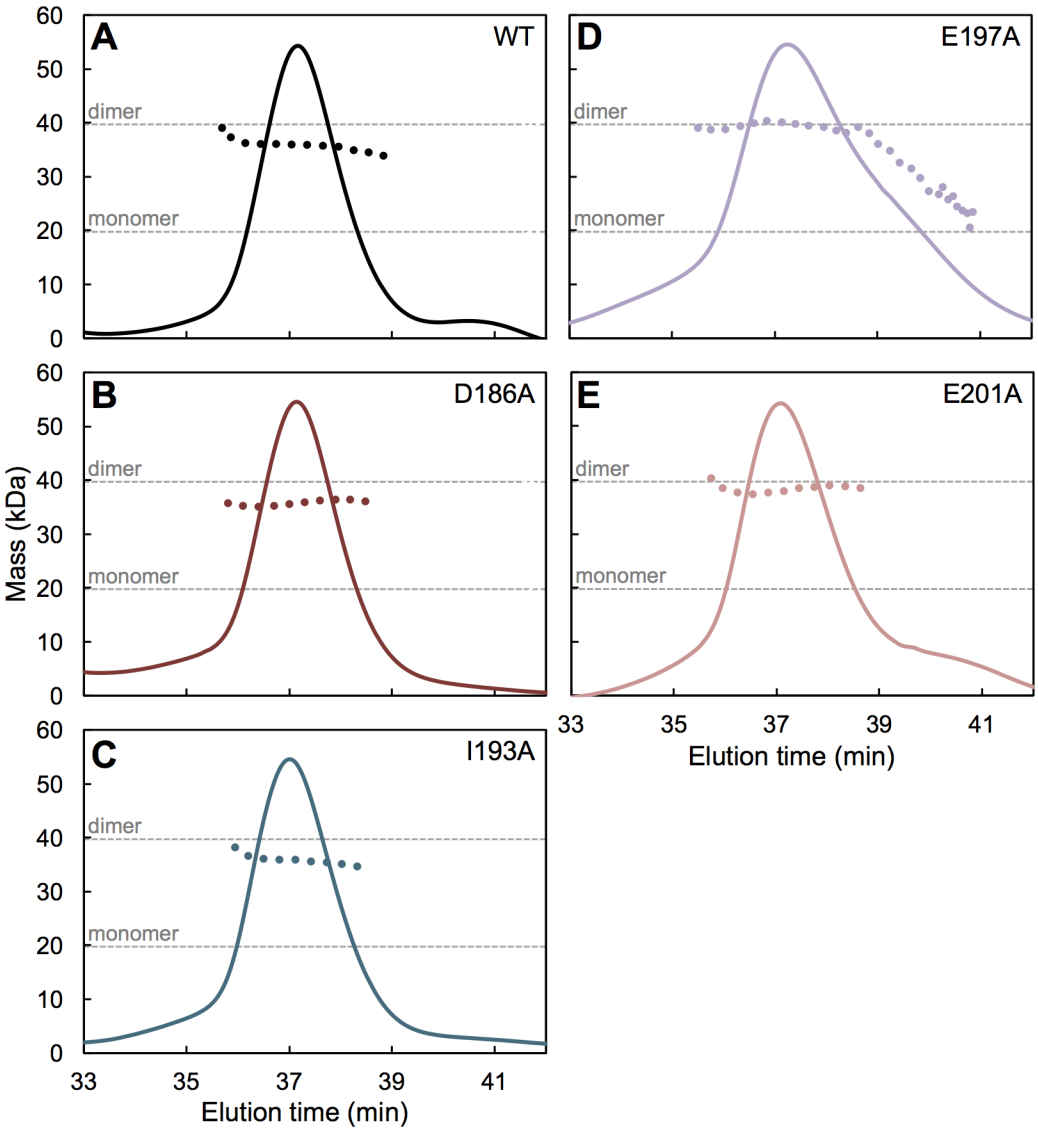


**Fig 5. Dimerization of CC-L2 mutants.** Purified mutant proteins were analyzed by using SEC-MALS (size exclusion chromatography coupled with multi-angle light scattering). The solid curves represent the normalized UV absorbance trace (arbitrary units) of eluting components. The dotted curves show the population averaged molecular mass calculated from the measured protein concentration and light scattering data. Dashed gray lines indicate the expected masses of the monomer and dimer species. (A) Wildtype control. (B) D186A. (C) I193A. (D) E197A. The major peak had a substantial trailing edge indicating dissociation into monomers. (E) E201A.

https://doi.org/10.1371/journal.ppat.1006686.g005

also disrupt capsid recognition. We therefore tested the mutant TRIM5-21R proteins for their ability to bind disulfide-stabilized HIV-1 CA tubes by using an established centrifugation assay [3, 10, 15, 34]. Using our specific protocol, about 50% of wildtype TRIM5-21R was consistently found to co-pellet with the CA tubes [15]. Given the propensity of TRIM5-21R to spontaneously assemble and the reduced stabilities of the mutants, experiments were performed right after purification. Each mutant was analyzed at least twice with independent protein preparations, and always in parallel with a wildtype control. Representative results are shown in Fig 6.

Consistent with expectation that the dimer is the minimal capsid-binding unit of TRIM5α, the F187A class I mutant pelleted only at background levels. The L190A and L194A mutations

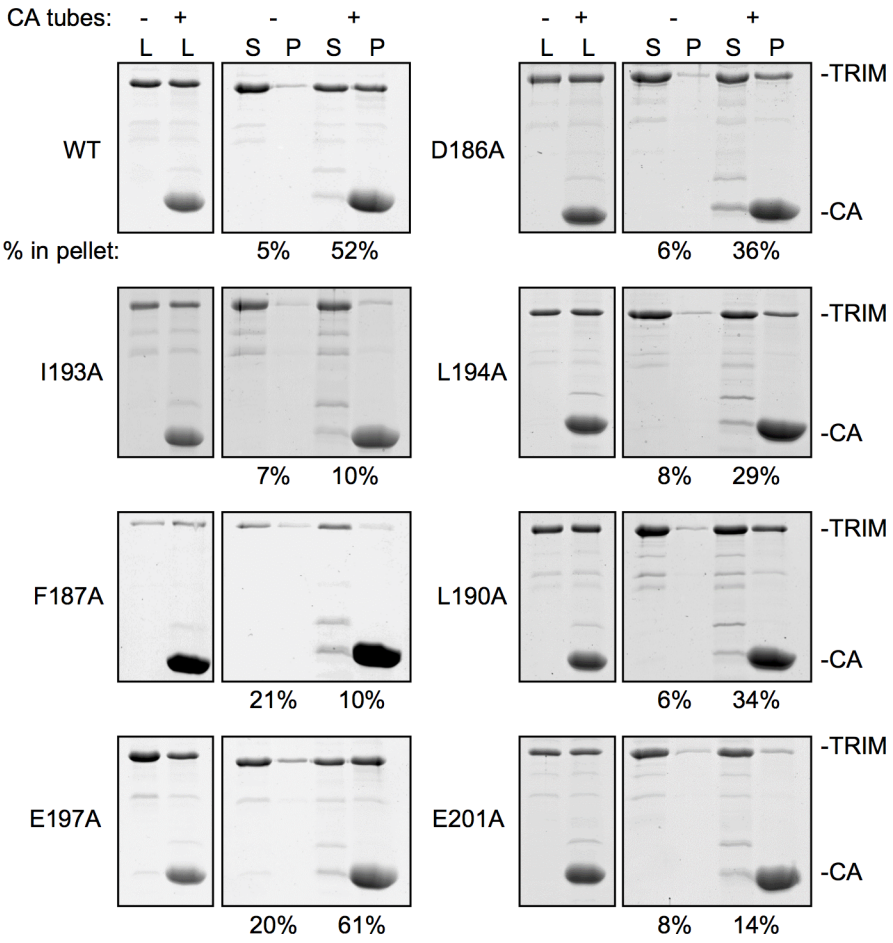


**Fig 6. Capsid binding activities of TRIM5-21R proteins.** Representative results of pull-down assays. Purified TRIM5-21R (5 μM) was incubated with disulfide-stabilized HIV-1 CA tubes, fractionated by centrifugation, and visualized by SDS-PAGE with Coommassie staining. L, load; S, soluble fraction; P, pellet fraction. Band intensities were quantified by densitometry. Experiments were repeated at least 2 times for each mutant using independent protein preparations, with similar results.

https://doi.org/10.1371/journal.ppat.1006686.g006

had less severe defects (with 34% and 29% pellet, respectively), consistent with the less severe biophysical defects observed in the thermal stability assays. E197A pelleted efficiently with the tubes (61%), although we consider this mutant to be also an intermediate binder because in four independent experiments it reproducibly showed high levels of background pelleting (20–30%), likely due to aggregation. For reference, these levels of residual binding are similar to those observed for the R121E and W117E mutations, which disrupt higher-order interactions mediated by the B-box 2 domain and essentially abolish restriction activity [10, 15]. Among the class II mutants, D186A had significant residual binding (36%), whereas I193A and E201A only pelleted at background levels. Thus, there is good correlation between the expected structural effects of the mutations, the biophysical properties of the mutant proteins, and their capsid binding activities.

## Effects of mutations on higher-order assembly

Mutations in the L2 linker have been previously shown to disrupt TRIM5α self-association and higher-order assembly [24, 25, 27, 35]. To test the alternative possibility that the capsid

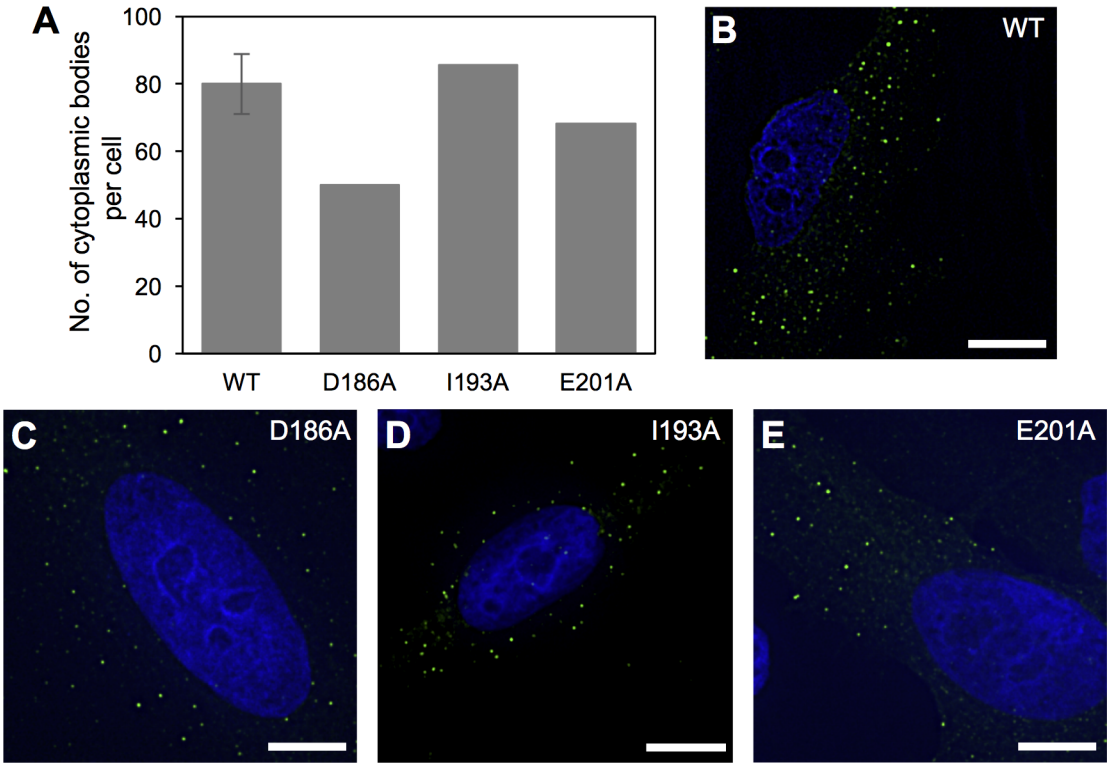


**Fig 7. Cytoplasmic body assembly activities of YFP-TRIM5α proteins.** (A) The number of cytoplasmic bodies was counted in each cell and normalized to the intracellular YFP concentration as described [24]. (B) Representative image of HeLa cells stably expressing the wildtype control. (C) D186A. (D) I193A. (E) E201A. Cytoplasmic bodies appear as green puncta. DAPI was used to stain nuclei blue. Scale bars = 10 μ.

https://doi.org/10.1371/journal.ppat.1006686.g007

binding defects we observed simply reflected this property, we overexpressed YFP-tagged rhesus TRIM5α in HeLa cells and tested the mutants for their ability to form fluorescent puncta called cytoplasmic bodies. Although not yet definitively proven, these cytoplasmic bodies are reasonably believed to reflect the intrinsic ability of purified TRIM5α proteins to assemble *in vitro* [1, 10, 15]. In these experiments, the wildtype control produced around 80–100 individual puncta per cell (Fig 7A and 7B). As expected, the class I mutants that were appreciably deficient in dimerization were also significantly impaired in cytoplasmic body formation (S4 Fig). F187A and L194A, which were the most severe mutations in our *in vitro* assays, produced virtually no cytoplasmic bodies (S4A and S4C Fig), again confirming that the dimer is the fundamental building block of higher-order assemblies of TRIM5α.

Results also showed that the three class II mutants retained the ability to assemble into cytoplasmic bodies (Fig 7). Importantly, I193A and E201A, which showed only background levels of capsid binding *in vitro*, assembled puncta about as efficiently as wildtype (Fig 7D and 7E). To correlate these results with *in vitro* assembly phenotypes, we assembled purified TRIM5-21R harboring these two mutations, and confirmed that both mutant proteins efficiently assembled into a large hexagonal lattice with the expected unit cell dimensions (Fig 8) [10, 15, 23]. These results also provide further evidence that the mutants were stably dimeric, because monomeric TRIM5-21R is severely impaired in assembly *in vitro* [10]. We therefore conclude that the significant binding defects caused by the I193A and E201A mutations were not due to disruption of dimerization or higher-order assembly, but more likely due to impaired positioning of the SPRY domain relative to the coiled-coil domain.

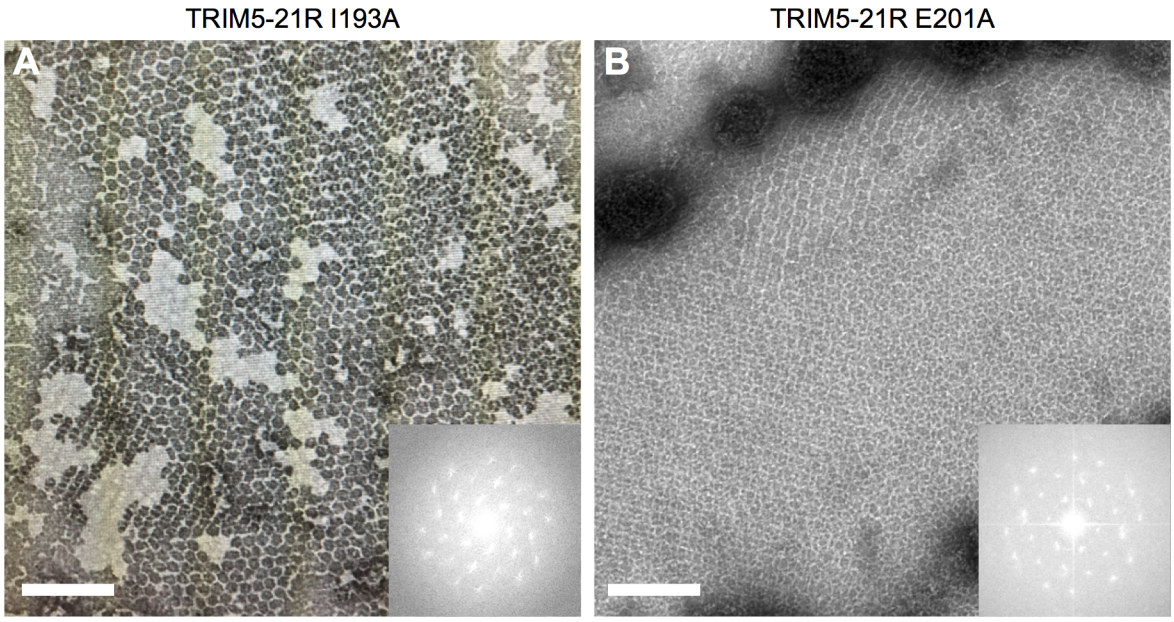


**Fig 8. *In vitro* assembly activities of class II TRIM5-21R mutants.** Purified TRIM5-21R proteins were incubated in assembly buffer overnight and the resulting precipitates were examined by negative stain electron microscopy. (A) I193A. (B) E201A. Insets: Fourier transforms of the associated images. Scale bars = 200 nm.

https://doi.org/10.1371/journal.ppat.1006686.g008

## Effects of mutations on restriction activity

We then determined the ability of our mutants to inhibit HIV-1 replication in cultured HeLa cells. Consistent with expectation from the above analysis, the class I mutants were significantly impaired in restriction, and the extent of impairment correlated with the degree to which each mutant was deficient in dimerization *in vitro* (Fig 9A). Of the class II mutations, D186A only had a minor defect in restriction (Fig 9B, maroon), which correlated with its *in vitro* properties and intermediate defect in the capsid-binding assay (Fig 6). This residue is located at the outer edges of the modeled SPRY/coiled-coil interface, and therefore probably does not significantly contribute to the packing interaction (Fig 4C). In contrast, the I193A and E201A mutants were more significantly impaired in restriction (Fig 9B, blue and pink), which again correlated with more severe loss of binding activity *in vitro* and more significant interactions with the L2/SPRY helix in the modeled TRIM5α dimer (Fig 4B and 4C). Note, however, that both the I193A and E201A mutants still retained measurable levels of antiviral activity. We speculate that the relatively high protein expression levels in our stably transfected cell lines, combined with the intact ability of the mutant proteins to form higher-order assemblies, may have buffered the effects of the mutations (see also Discussion below).

Finally, we tested the mutations in context of owl monkey TRIMCyp, which we predicted would be relatively insensitive to positioning effects due to its higher intrinsic affinity for the HIV-1 capsid protein [36–40]. Indeed, both the TRIMCyp I192A and E200A mutants (equivalent to TRIM5α I193A and E201A) were just as restriction-competent as the wildtype control (Fig 10). Importantly, these results also help exclude pleiotropic effects of the mutations.

# Discussion

Multivalency is commonly found in nature to achieve tight binding, even though each component univalent interaction is by itself very weak, by bonding or linking together multiple copies

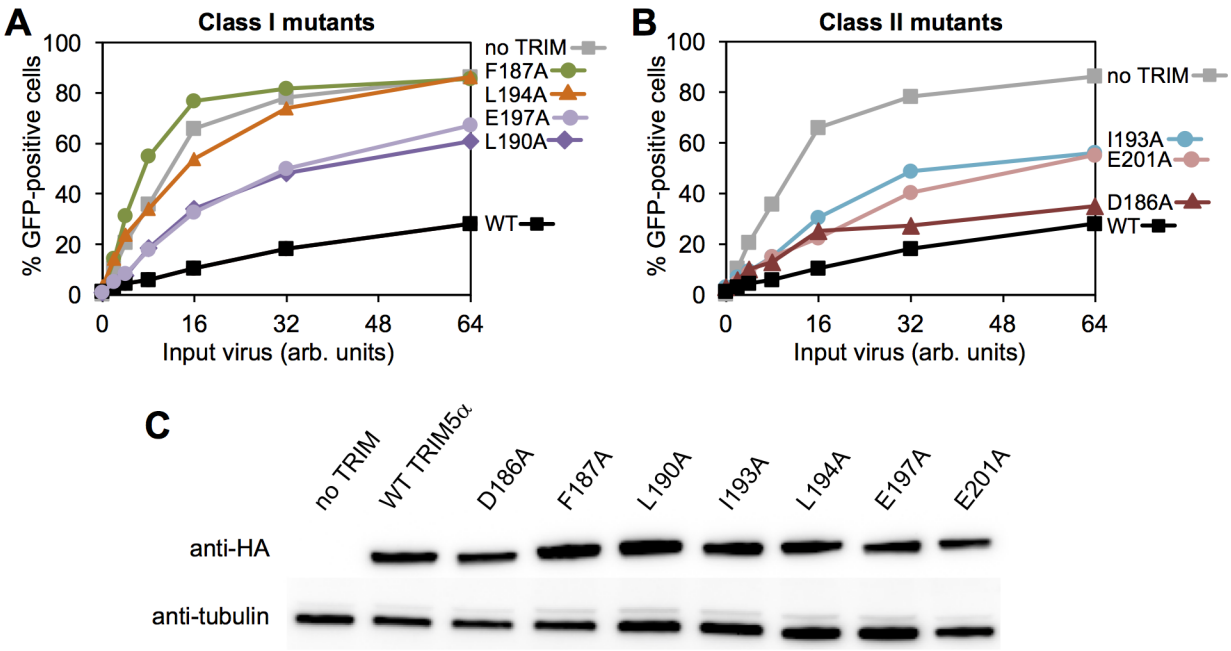


**Fig 9. Restriction activities rhesus TRIM5α proteins.** HeLa cells that stably expressed the indicated HA-tagged TRIM5α proteins were infected with GFP-labeled HIV and the extent of viral replication was quantified. (A) Class I mutants. (B) Class II mutants. (C) Expression levels were quantified by immunoblotting. Experiments were repeated 6 times independently with similar results.

https://doi.org/10.1371/journal.ppat.1006686.g009

of the interacting subunits. In these systems, simple clustering of binding domains can already result in significant binding, but truly substantial avidity gains are observed when the spacing of tethered recognition domains is matched to the spacing of their corresponding epitopes [41]. Here, we provide experimental evidence that in the TRIM5α dimer, the two SPRY domains are tethered by an α-helical segment that integrates into the SPRY domain fold and packs against the center of the coiled-coil scaffold. The simplest interpretation of our structural and biophysical data (and those of others) is that this molecular tether is a single contiguous helix that spans residues 283–300 [11, 12], although precise molecular details will have to await direct structure determination. We propose that CC/L2/SPRY packing limits the flexibility

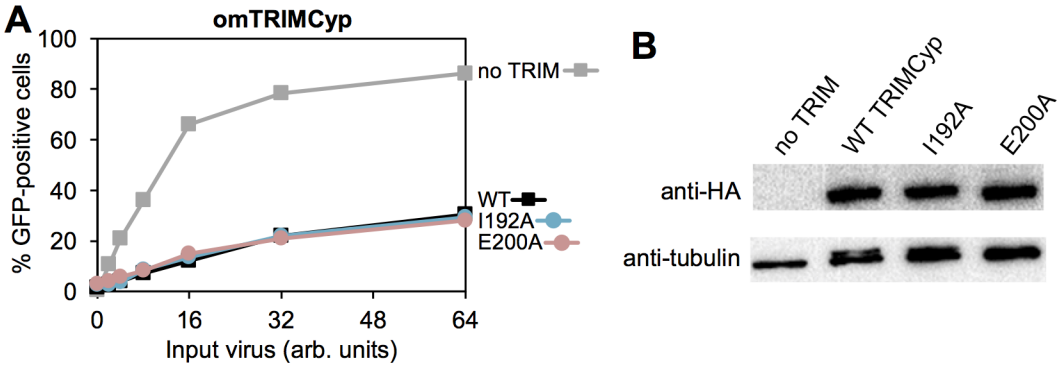


**Fig 10. Restriction activities of TRIMCyp proteins.** (A) HeLa cells that stably expressed the indicated HA-tagged owl monkey TRIM5α proteins were infected with GFP-labeled HIV and the extent of viral replication was quantified. (B) Expression levels were quantified by immunoblotting. Experiments were repeated 2 times independently with similar results.

https://doi.org/10.1371/journal.ppat.1006686.g010

and range of orientations that the two SPRY domains can adopt relative to each other, and that this tethering mechanism significantly contributes to the avidity gains observed upon multivalent binding of TRIM5α to retroviral capsids by allowing more precise (or tailored) matching with the spacing of binding epitopes on the capsid surface. In support of this model, we identified mutations (I193A and E201A) within the putative CC/L2/SPRY packing interface that did not significantly affect dimerization or higher-order assembly but still abrogated capsid binding *in vitro* and disrupted restriction activity in cells. The simplest explanation of our data is that the impaired restriction activities of these two mutants arise from impaired CC/L2/SPRY packing. Our studies therefore support the proposed "minimum design feature" of capsid-dependent restriction factors [12, 42, 43], in which the minimal capsid-binding unit is a dimer. Higher-order assembly of the TRIM hexagonal lattice further amplifies affinity, both by spreading the interactions across the entire capsid surface and by matching the rotations of the subunits in the capsid lattice. The basal positioning mechanism occurs in context of the dimer, however, which explains the observation that TRIM5α proteins impaired in higher-order assembly (e.g., B-box mutants or deletions) can still retain the ability to bind CA tubes or other capsid mimics *in vitro*, provided that the reagents are supplied at high enough concentrations in the binding reactions [3, 10, 15, 44]. We also note that this model is compatible with the ability of a single TRIM5α protein to restrict multiple different retroviruses, because even though CA proteins have widely divergent sequences, retroviral capsids have the same underlying hexagonal arrangement with a conserved lattice spacing. Interestingly, the relative spacings of interaction modules have been found to play an important role in defining binding specificity in some avidity-driven systems [45–47]. Capsid binding specificity is dictated by the SPRY domain, and we speculate that coiled-coil/SPRY packing may contribute to specificity because productive recognition will still not occur if otherwise compatible binding epitopes on the surface of a capsid are not within the reach of allowable SPRY spacings and orientations. Testing this model will require a more precise understanding of the local SPRY/CA contacts than currently known.

It is notable that the I193A and E201A mutations did not abolish restriction activity of TRIM5α, despite apparently causing complete loss of binding in our centrifugation assay. Because the I193A and E201A mutant proteins were not impaired in higher-order assembly, our interpretation of these results is that the mutants still retained some capsid-binding activity in cells that was amplified by multivalent clustering and hexagonal lattice formation (and perhaps also further mitigated by high expression levels). Thus, SPRY/coiled-coil interactions do not appear to be fundamentally essential to recognition, but rather help to optimize avidity and maximize binding efficiency. This is consistent with studies showing that artificial restriction factors can be created by appending exogenous capsid-binding domains to the TRIM5α tripartite motif [48–50]. In these artificial systems, it is unlikely that the exogenous domains are tethered in the same manner as the native SPRY domain, yet the avidity afforded by multivalency is sufficient to generate measurable anti-viral activity.

An interesting counter-example is TRIMCyp, which contains the TRIM5α tripartite motif but harbors a cyclophilin domain for capsid binding instead of SPRY [2]. The L2 linker in TRIMCyp retains the C-terminal helical segment, but the helix is followed by an additional 11 random coil residues such that the two cyclophilin domains are likely to be flexibly connected to the coiled-coil [12]. We suggest that this high degree of flexibility is compensated for by both higher-order assembly and the significantly higher intrinsic affinity of the cyclophilin fold for the HIV-1 CA protein (with a dissociation constant of about 10 μM [36–40]). Consistent with this idea, we found that the I192A and E200A mutations had no effect on TRIMCyp's restriction activity. The degree of affinity amplification required by TRIMCyp to allow for functional capsid recognition therefore appears to be more relaxed compared to TRIM5α.

## Materials and methods

### Protein expression and purification

Recombinant TRIM5-21R and TRIM5α$_{133–300}$ (CC-L2) proteins were expressed and purified as described [9–11]. Briefly, TRIM5α$_{133–300}$ proteins were expressed as a His-SUMO-tagged construct in *E. coli* BL21(DE3) cells using the autoinduction method [51]. The tagged construct was initially purified on Ni-NTA resin (Qiagen), the His-SUMO leader sequence was cleaved with Ulp1 protease, and the released protein was purified to homogeneity by using anion exchange and size exclusion chromatography. TRIM5-21R proteins were expressed in Sf9 cells with a Strep-FLAG leader sequence. The tagged construct was initially purified on StrepTactin resin (GE Healthcare), the leader sequence was removed by incubation with Prescission protease (GE Healthcare), and the protein purified to homogeneity using anion exchange and size exclusion. The latter two steps were particularly important in separating contaminating monomers from the dimer fraction that we used for these studies (S3A and S3B Fig). TRIM5α$_{133–497}$ (CC-L2-SPRY) was made from the TRIM5-21R construct by deleting the RING and B-box 2 domains, expressed in Sf9 cells, and purified in the same manner as the full-length protein. All single point mutations were introduced into the appropriate constructs using the Quikchange method (Agilent) and mutants were expressed and purified in the same way as their respective wildtype constructs. Given the established propensity of TRIM5 proteins to spontaneously aggregate or assemble *in vitro*, biochemical assays were performed as soon as possible after purification. SPRY constructs lacking the V1 loop were expressed as His-GB1 fusion proteins (derived from a plasmid kindly provided by D. Ivanov) and purified as described [30].

### Electron paramagnetic resonance (EPR) experiments

Purified TRIM5α$_{133–300}$ harboring the W196C, D288C, E292C, and W300C mutations were briefly incubated with excess dithiothreitol to reduce the exogenous cysteines, then exchanged into labeling buffer (20 mM Tris, pH 8, 100 mM NaCl) using a desalting column. The proteins were then incubated with excess MTSL (*S*-(1-oxyl-2,2,5,5-tetramethyl-2,5-dihydro-1H-pyrrol-3-yl)methylmethanesulfonothioate) overnight at 4˚C. After removing unreacted label with a desalting column, the labeled proteins were concentrated to 20 μM. Deuterated glycerol (Cambridge Isotope Laboratories) at approximately 10% final concentration was added to the samples before freezing. DEER EPR measurements were performed and analyzed as described previously [52]. In brief, samples were placed inside quartz capillaries and frozen using a dry ice/isopropanol bath. Standard four-pulse DEER measurements [53] were performed with a Q-band Bruker Elexsys E580 spectrometer and EN5107D2 dielectric resonator (Bruker Biospin). Dipolar evolution data were processed and distance distributions determined using Tikhonov regularization, as implemented in the DeerAnalysis2015 software package [54]. The validation route in DeerAnalysis was used to estimate uncertainty in the distance distributions due to subtraction of the background form factor. Distance estimates from the molecular model of CC-L2 were made using the PyMol plug-in MTSSLWizard [55].

### Differential scanning fluorimetry

Thermofluor melting assays were performed as previously described [11], with final protein concentrations of 1 mg/mL for TRIM5-21R constructs and 2 mg/mL for CC-L2, CC-L2-SPRY, and SPRY constructs. Each sample was set-up in 3 or 4 replicates, and melting curves for each protein were determined at least twice, with independent protein preparations.

## NMR spectroscopy

SPRYΔV1 constructs for NMR experiments were uniformly labeled with $^{15}N$ and/or $^{13}C$ by growing transformed bacteria in minimal media supplemented with $^{15}NH_4Cl$ and/or $^{13}C$-glucose. Assignments for $SPRY_{292-497}$ were kindly provided by D. Ivanov [30]. Resonance assignments (including all N-terminal residues) were independently determined for $SPRY_{281-497}$ by using the following experiments: $^{15}N/^{1}H$ HSQC [56], CBCA(CO)NH [57], HNCA [58], HNCACB [59], HNCO [58], HNCOCA [60]. NOE cross-peaks were obtained from an $^{15}N$-edited NOESY-HSQC [56, 61]. Spectra were recorded on a Varian Inova 600 MHz spectrometer, processed with NMRPipe [62], and analyzed using the tools in SPARKY [63]. Chemical shift indices were calculated using the program PREDITOR [64]. Normalized chemical shift changes were calculated as described [65].

## Computational modeling

The TRIM5α coiled-coil/L2/SPRY model was built as described in the main text, using PyMol software (Schrödinger Scientific).

## SEC-MALS

These experiments were performed as described [15]. Purified CC-L2 mutants (50 μL) were injected into the column at 0.5–1 mg/mL concentrations.

## Capsid binding assays

*In vitro* pull-down assays with disulfide-stabilized HIV-1 CA tubes and purified TRIM5-21R proteins were performed as described [15].

## *In vitro* assembly of TRIM5-21R

Assembly and negative stain electron microscopy imaging of the I193A and E201A TRIM5-21R mutants were performed as described [10].

## Cell culture reagents and methods

The hemagglutinin (HA)-tagged and/or yellow fluorescent protein (YFP)-labeled rhesus TRIM5α and owl monkey TRIMCyp constructs were generated as previously described [27]. Overlapping PCR was used to generate single point mutations in the coiled-coil regions. HeLa and human embryonic kidney 293T (HEK293T) cells (from an already existing collection in-house) were cultured in complete Dulbecco's modified Eagle's medium (DMEM) containing 10% fetal bovine serum, penicillin (100 U/mL), and streptomycin (100 μg/mL). Vectors expressing YFP- or HA-tagged rhesus TRIM5α were made by transfecting 293T cells with the respective wildtype and mutant TRIM5 plasmids along with VSV-G and pCig-B. HeLa cells stably expressing the YFP-tagged proteins were generated by G418 (400 μg/mL) selection at 48 h post-transduction. The stable cell lines were then analyzed by immunofluorescence and western blotting.

## Cytoplasmic body assembly assays

HeLa cells (from an already existing collection in-house) stably expressing YFP-tagged TRIM5α proteins were plated onto fibronectin-treated coverslips, allowed to adhere, and fixed with 3.7% formaldehyde and stained with DAPI. Images were collected with a DeltaVision microscope (Applied Precision) equipped with a digital camera (CoolSNAP HQ; Photometrics), using a 1.4 numerical aperture objective lens, and were deconvolved with SoftWoRx deconvolution

software (Applied Precision). *Z*-stack images of each cell line were acquired by using identical acquisition parameters. Deconvolved images were analyzed for fluorescent cytoplasmic bodies by using the Surface Finder function of the Imaris software package (Bitplane).

### Restriction assays

Vesicular stomatitis virus G protein (VSV-G)-pseudotyped R7ΔEnv HIV-GFP was produced by transfecting HEK293T cells as previously described [66]. Virus infectivity was assessed by infecting equivalent numbers of cells in a 24-well plate, and green fluorescent protein (GFP) expression was determined at 48h post-infection by using a FACSCanto II flow cytometer (Becton, Dickinson).

## Supporting information

**S1 Fig. Raw DEER data.** Left panels: Uncorrected DEER traces, V(t)/V(0), for each of the four mutants. The mutant W196R1 that is labeled within the coiled-coil helices produce a noticeable DEER echo, indicating a well-defined distance. Red lines indicate the background form factor. Right panels: Corrected dipolar evolution curves, F(t)/F(0), after subtraction of the background form factor. The red traces represent the best fits to the DEER data, and yield the distributions shown in Fig 1.
(TIFF)

**S2 Fig. Overlayed $^{15}$N-$^{1}$H HSQC spectra showing backbone amide footprints of indicated SPRY domain constructs.** Top panel: Residues that undergo the largest chemical shift changes (apart from N-terminal residues) in comparing the two constructs are encircled and labeled. Bottom panel: Enlarged view of central region containing helical resonances, with complete residue assignments for the longer construct ($SPRY_{281-497}$).
(TIFF)

**S3 Fig. Oligomerization status of TRIM5-21R proteins during purification.** (A) Anion exchange chromatography reveals the relative fractions of monomer and dimer species at the start of purification. Wildtype TRIM5-21R elutes as a doublet peak, with the minor monomer fraction eluting early and the major dimer fraction eluting late. Blue curve = UV absorbance trace. Brown curve = conductivity trace arising from application of a linear salt gradient. (B) Size exclusion chromatography of pooled anion exchange fractions allows further separation of contaminating monomers from the desired dimer species. (C) Representative anion exchange profiles of class I mutants indicate significantly elevated monomer fractions. (D) Representative anion exchange profiles of class II mutants.
(TIFF)

**S4 Fig. Cytoplasmic bodies formed by wildtype control rhesus YFP-TRIM5α and class I mutants.** (A-D) Representative images of HeLa cells stably expressing the indicated constructs. Cytoplasmic bodies appear as green puncta. DAPI was used to stain nuclei blue. Scale bars = 10 μ. (E) The number of cytoplasmic bodies was counted in each cell and normalized to the intracellular YFP concentration.
(TIFF)

## Acknowledgments

We thank members of our laboratories for technical advice and support, and for critical reading of the manuscript.

## Author Contributions

**Conceptualization:** Marcin D. Roganowicz, David S. Cafiso, Barbie K. Ganser-Pornillos, Edward M. Campbell, Owen Pornillos.

**Formal analysis:** Jacek Plewka, Steven L. Alam, David S. Cafiso.

**Investigation:** Marcin D. Roganowicz, Sevnur Komurlu, Santanu Mukherjee, Jacek Plewka, Steven L. Alam, Katarzyna A. Skorupka, Yueping Wan, Damian Dawidowski, David S. Cafiso, Barbie K. Ganser-Pornillos, Owen Pornillos.

**Methodology:** Marcin D. Roganowicz, Sevnur Komurlu, Santanu Mukherjee, Jacek Plewka, Steven L. Alam, Katarzyna A. Skorupka, Yueping Wan, Damian Dawidowski, David S. Cafiso, Barbie K. Ganser-Pornillos, Owen Pornillos.

**Resources:** Steven L. Alam, Edward M. Campbell.

**Supervision:** David S. Cafiso, Barbie K. Ganser-Pornillos, Edward M. Campbell, Owen Pornillos.

**Validation:** Marcin D. Roganowicz, Sevnur Komurlu, Katarzyna A. Skorupka, Barbie K. Ganser-Pornillos, Owen Pornillos.

**Writing – original draft:** Owen Pornillos.

**Writing – review & editing:** Marcin D. Roganowicz, David S. Cafiso, Barbie K. Ganser-Pornillos, Edward M. Campbell, Owen Pornillos.

## References


1. Stremlau M, Owens CM, Perron MJ, Kiessling M, Autissier P, Sodroski J. The cytoplasmic body component TRIM5α restricts HIV-1 infection in Old World monkeys. Nature. 2004; 427: 848–853. https://doi.org/10.1038/nature02343 PMID: 14985764.
2. Sayah DM, Sokolskaja E, Berthoux L, Luban J. Cyclophilin A retrotransposition into TRIM5 explains owl monkey resistance to HIV-1. Nature. 2004; 430: 569–573. https://doi.org/10.1038/nature02777 PMID: 15243629.
3. Stremlau M, Perron M, Lee M, Li Y, Song B, Javanbakht H, et al. Specific recognition and accelerated uncoating of retroviral capsids by the TRIM5α restriction factor. Proc Natl Acad Sci U S A. 2006; 103: 5514–5519. https://doi.org/10.1073/pnas.0509996103 PMID: 16540544.
4. Pertel T, Hausmann S, Morger D, Zuger S, Guerra J, Lascano J, et al. TRIM5 is an innate immune sensor for the retrovirus capsid lattice. Nature. 2011; 472: 361–365. https://doi.org/10.1038/nature09976 PMID: 21512573.
5. Meroni G, Diez-Roux G. TRIM/RBCC, a novel class of 'single protein RING finger' E3 ubiquitin ligases. Bioessays. 2005; 27: 1147–1157. https://doi.org/10.1002/bies.20304 PMID: 16237670.
6. Fletcher AJ, Christensen DE, Nelson C, Tan CP, Schaller T, Lehner PJ, et al. TRIM5α requires Ube2W to anchor Lys63-linked ubiquitin chains and restrict reverse transcription. EMBO J. 2015; 34: 2078–2095. https://doi.org/10.15252/embj.201490361 PMID: 26101372.
7. Campbell EM, Weingart J, Sette P, Opp S, Sastri J, O'Connor SK, et al. TRIM5α-mediated ubiquitin chain conjugation is required for inhibition of HIV-1 reverse transcription and capsid destabilization. J Virol. 2015; 90: 1849–1857. https://doi.org/10.1128/JVI.01948-15 PMID: 26676782.
8. Kar AK, Diaz-Griffero F, Li Y, Li X, Sodroski J. Biochemical and biophysical characterization of a chimeric TRIM21-TRIM5α protein. J Virol. 2008; 82: 11669–11681. https://doi.org/10.1128/JVI.01559-08 PMID: 18799572.
9. Langelier CR, Sandrin V, Eckert DM, Christensen DE, Chandrasekaran V, Alam SL, et al. Biochemical characterization of a recombinant TRIM5α protein that restricts human immunodeficiency virus type 1 replication. J Virol. 2008; 82: 11682–11694. https://doi.org/10.1128/JVI.01562-08 PMID: 18799573.
10. Ganser-Pornillos BK, Chandrasekaran V, Pornillos O, Sodroski JG, Sundquist WI, Yeager M. Hexagonal assembly of a restricting TRIM5α protein. Proc Natl Acad Sci U S A. 2011; 108: 534–539. https://doi.org/10.1073/pnas.1013426108 PMID: 21187419.

11. Sanchez JG, Okreglicka K, Chandrasekaran V, Welker JM, Sundquist WI, Pornillos O. The tripartite motif coiled-coil is an elongated antiparallel hairpin dimer. Proc Natl Acad Sci U S A. 2014; 111: 2494–2499. https://doi.org/10.1073/pnas.1318962111 PMID: 24550273.

12. Goldstone DC, Walker PA, Calder LJ, Coombs PJ, Kirkpatrick J, Ball NJ, et al. Structural studies of postentry restriction factors reveal antiparallel dimers that enable avid binding to the HIV-1 capsid lattice. Proc Natl Acad Sci U S A. 2014; 111: 9609–9614. https://doi.org/10.1073/pnas.1402448111 PMID: 24979782.

13. Li Y, Wu H, Wu W, Zhuo W, Liu W, Zhang Y, et al. Structural insights into the TRIM family of ubiquitin E3 ligases. Cell Res. 2014; 24: 762–765. https://doi.org/10.1038/cr.2014.46 PMID: 24722452.

14. Weinert C, Morger D, Djekic A, Grütter MG, Mittl PR. Crystal structure of TRIM20 C-terminal coiled-coil/B30.2 fragment: implications for the recognition of higher order oligomers. Sci Rep. 2015; 5: 10819. https://doi.org/10.1038/srep10819 PMID: 26043233.

15. Wagner JM, Roganowicz MD, Skorupka K, Alam SL, Christensen D, Doss G, et al. Mechanism of B-box 2 domain-mediated higher-order assembly of the retroviral restriction factor TRIM5α. Elife. 2016; 5: e16309. https://doi.org/10.7554/eLife.16309 PMID: 27253059.

16. Keown JR, Yang JX, Douglas J, Goldstone DC. Characterisation of assembly and ubiquitylation by the RBCC motif of Trim5α. Sci Rep. 2016; 6: 26837. https://doi.org/10.1038/srep26837 PMID: 27230667.

17. Sawyer SL, Wu LI, Emerman M, Malik HS. Positive selection of primate TRIM5α identifies a critical species-specific retroviral restriction domain. Proc Natl Acad Sci U S A. 2005; 102: 2832–2837. https://doi.org/10.1073/pnas.0409853102 PMID: 15689398.

18. Ganser BK, Li S, Klishko VY, Finch JT, Sundquist WI. Assembly and analysis of conical models for the HIV-1 core. Science. 1999; 283: 80–83. PMID: 9872746.

19. Mattei S, Glass B, Hagen WJ, Kräusslich HG, Briggs JA. The structure and flexibility of conical HIV-1 capsids determined within intact virions. Science. 2016; 354: 1434–1437. https://doi.org/10.1126/science.aah4972 PMID: 27980210.

20. Li X, Sodroski J. The TRIM5α B-box 2 domain promotes cooperative binding to the retroviral capsid by mediating higher-order self-association. J Virol. 2008; 82: 11495–11502. https://doi.org/10.1128/JVI.01548-08 PMID: 18799578.

21. Biris N, Tomashevski A, Bhattacharya A, Diaz-Griffero F, Ivanov DN. Rhesus monkey TRIM5α SPRY domain recognizes multiple epitopes that span several capsid monomers on the surface of the HIV-1 mature viral core. J Mol Biol. 2013; 425: 5032–5044. https://doi.org/10.1016/j.jmb.2013.07.025 PMID: 23886867.

22. Diaz-Griffero F, Qin XR, Hayashi F, Kigawa T, Finzi A, Sarnak Z, et al. A B-box 2 surface patch important for TRIM5α self-association, capsid binding avidity, and retrovirus restriction. J Virol. 2009; 83: 10737–10751. https://doi.org/10.1128/JVI.01307-09 PMID: 19656869.

23. Li YL, Chandrasekaran V, Carter SD, Woodward CL, Christensen DE, Dryden KA, et al. Primate TRIM5 proteins form hexagonal nets on HIV-1 capsids. Elife. 2016; 5: e16269. https://doi.org/10.7554/eLife.16269 PMID: 27253068.

24. Sastri J, O'Connor C, Danielson CM, McRaven M, Perez P, Diaz-Griffero F, et al. Identification of residues within the L2 region of rhesus TRIM5α that are required for retroviral restriction and cytoplasmic body localization. Virology. 2010; 405: 259–266. https://doi.org/10.1016/j.virol.2010.06.015 PMID: 20633914.

25. Li X, Yeung DF, Fiegen AM, Sodroski J. Determinants of the higher order association of the restriction factor TRIM5α and other tripartite motif (TRIM) proteins. J Biol Chem. 2011; 286: 27959–27970. https://doi.org/10.1074/jbc.M111.260406 PMID: 21680743.

26. Nakayama EE, Nakajima T, Kaur G, Mimaya JI, Terunuma H, Mehra N, et al. A naturally occurring single amino acid substitution in human TRIM5α linker region affects its anti-HIV type 1 activity and susceptibility to HIV type 1 infection. AIDS Res Hum Retroviruses. 2013; 29: 919–924. https://doi.org/10.1089/AID.2012.0369 PMID: 23379364.

27. Sastri J, Johnsen L, Smolin N, Imam S, Mukherjee S, Lukic Z, et al. Restriction of HIV-1 by rhesus TRIM5α is governed by alpha helices in the Linker2 region. J Virol. 2014; 88: 8911–8923. https://doi.org/10.1128/JVI.01134-14 PMID: 24872590.

28. Lamichhane R, Mukherjee S, Smolin N, Pauszek RF, 3rd, Bradley M, Sastri J, et al. Dynamic conformational changes in the rhesus TRIM5α dimer dictate the potency of HIV-1 restriction. Virology. 2017; 500: 161–168. https://doi.org/10.1016/j.virol.2016.10.003 PMID: 27821283.

29. Jeschke G. DEER distance measurements on proteins. Annu Rev Phys Chem. 2012; 63: 419–446. https://doi.org/10.1146/annurev-physchem-032511-143716 PMID: 22404592.

30. Biris N, Yang Y, Taylor AB, Tomashevski A, Guo M, Hart PJ, et al. Structure of the rhesus monkey TRIM5α PRYSPRY domain, the HIV capsid recognition module. Proc Natl Acad Sci U S A. 2012; 109: 13278–13283. https://doi.org/10.1073/pnas.1203536109 PMID: 22847415.

31. Yang H, Ji X, Zhao G, Ning J, Zhao Q, Aiken C, et al. Structural insight into HIV-1 capsid recognition by rhesus TRIM5α. Proc Natl Acad Sci U S A. 2012; 109: 18372–18377. https://doi.org/10.1073/pnas.1210903109 PMID: 23091002.

32. Diaz-Griffero F, Li X, Javanbakht H, Song B, Welikala S, Stremlau M, et al. Rapid turnover and polyubiquitylation of the retroviral restriction factor TRIM5. Virology. 2006; 349: 300–315. https://doi.org/10.1016/j.virol.2005.12.040 PMID: 16472833.

33. Li X, Li Y, Stremlau M, Yuan W, Song B, Perron M, et al. Functional replacement of the RING, B-box 2, and coiled-coil domains of tripartite motif 5α (TRIM5α) by heterologous TRIM domains. J Virol. 2006; 80: 6198–6206. https://doi.org/10.1128/JVI.00283-06 PMID: 16775307.

34. Fribourgh JL, Nguyen HC, Matreyek KA, Alvarez FJ, Summers BJ, Dewdney TG, et al. Structural insight into HIV-1 restriction by MxB. Cell Host Microbe. 2014; 16: 627–638. https://doi.org/10.1016/j.chom.2014.09.021 PMID: 25312384.

35. Javanbakht H, Yuan W, Yeung DF, Song B, Diaz-Griffero F, Li Y, et al. Characterization of TRIM5α trimerization and its contribution to human immunodeficiency virus capsid binding. Virology. 2006; 353: 234–246. https://doi.org/10.1016/j.virol.2006.05.017 PMID: 16808955.

36. Caines ME, Bichel K, Price AJ, McEwan WA, Towers GJ, Willett BJ, et al. Diverse HIV viruses are targeted by a conformationally dynamic antiviral. Nat Struct Mol Biol. 2012; 19: 411–416. https://doi.org/10.1038/nsmb.2253 PMID: 22407016.

37. Gamble TR, Vajdos FF, Yoo S, Worthylake DK, Houseweart M, Sundquist WI, et al. Crystal structure of human cyclophilin A bound to the amino-terminal domain of HIV-1 capsid. Cell. 1996; 87: 1285–1294. PMID: 8980234.

38. Price AJ, Marzetta F, Lammers M, Ylinen LM, Schaller T, Wilson SJ, et al. Active site remodeling switches HIV specificity of antiretroviral TRIMCyp. Nat Struct Mol Biol. 2009; 16: 1036–1042. https://doi.org/10.1038/nsmb.1667 PMID: 19767750.

39. Vajdos FF, Yoo S, Houseweart M, Sundquist WI, Hill CP. Crystal structure of cyclophilin A complexed with a binding site peptide from the HIV-1 capsid protein. Protein Sci. 1997; 6: 2297–2307. https://doi.org/10.1002/pro.5560061103 PMID: 9385632.

40. Yoo S, Myszka DG, Yeh C, McMurray M, Hill CP, Sundquist WI. Molecular recognition in the HIV-1 capsid/cyclophilin A complex. J Mol Biol. 1997; 269: 780–795. PMID: 9223641.

41. Kitov PI, Bundle DR. On the nature of the multivalency effect: a thermodynamic model. J Am Chem Soc. 2003; 125: 16271–16284. https://doi.org/10.1021/ja038223n PMID: 14692768.

42. Yap MW, Mortuza GB, Taylor IA, Stoye JP. The design of artificial retroviral restriction factors. Virology. 2007; 365: 302–314. https://doi.org/10.1016/j.virol.2007.04.005 PMID: 17493656.

43. Javanbakht H, Diaz-Griffero F, Yuan W, Yeung DF, Li X, Song B, et al. The ability of multimerized cyclophilin A to restrict retrovirus infection. Virology. 2007; 367: 19–29. https://doi.org/10.1016/j.virol.2007.04.034 PMID: 17574642.

44. Zhao G, Ke D, Vu T, Ahn J, Shah VB, Yang R, et al. Rhesus TRIM5α disrupts the HIV-1 capsid at the inter-hexamer interfaces. PLoS Pathog. 2011; 7: e1002009. https://doi.org/10.1371/journal.ppat.1002009 PMID: 21455494.

45. Lo YC, Lin SC, Rospigliosi CC, Conze DB, Wu CJ, Ashwell JD, et al. Structural basis for recognition of diubiquitins by NEMO. Mol Cell. 2009; 33: 602–615. https://doi.org/10.1016/j.molcel.2009.01.012 PMID: 19185524.

46. Sims JJ, Cohen RE. Linkage-specific avidity defines the lysine 63-linked polyubiquitin-binding preference of Rap80. Mol Cell. 2009; 33: 775–783. https://doi.org/10.1016/j.molcel.2009.02.011 PMID: 19328070.

47. Peisley A, Wu B, Xu H, Chen ZJ, Hur S. Structural basis for ubiquitin-mediated antiviral signal activation by RIG-I. Nature. 2014; 509: 110–114. https://doi.org/10.1038/nature13140 PMID: 24590070.

48. Schaller T, Ocwieja KE, Rasaiyaah J, Price AJ, Brady TL, Roth SL, et al. HIV-1 capsid-cyclophilin interactions determine nuclear import pathway, integration targeting and replication efficiency. PLoS Pathog. 2011; 7: e1002439. https://doi.org/10.1371/journal.ppat.1002439 PMID: 22174692.

49. Lee K, Mulky A, Yuen W, Martin TD, Meyerson NR, Choi L, et al. HIV-1 capsid-targeting domain of cleavage and polyadenylation specificity factor 6. J Virol. 2012; 86: 3851–3860. https://doi.org/10.1128/JVI.06607-11 PMID: 22301135.

50. Matreyek KA, Yucel SS, Li X, Engelman A. Nucleoporin NUP153 phenylalanine-glycine motifs engage a common binding pocket within the HIV-1 capsid protein to mediate lentiviral infectivity. PLoS Pathog. 2013; 9: e1003693. https://doi.org/10.1371/journal.ppat.1003693 PMID: 24130490.

51. Studier FW. Protein production by auto-induction in high density shaking cultures. Protein Expr Purif. 2005; 41: 207–234. PMID: 15915565.

52. Dawidowski D, Cafiso DS. Allosteric control of syntaxin 1a by Munc18-1: characterization of the open and closed conformations of syntaxin. Biophys J. 2013; 104: 1585–1594. https://doi.org/10.1016/j.bpj.2013.02.004 PMID: 23561535.

53. Pannier M, Veit S, Godt A, Jeschke G, Spiess HW. Dead-time free measurement of dipole-dipole interactions between electron spins. J Magn Reson. 2000; 142: 331–340. https://doi.org/10.1006/jmre.1999.1944 PMID: 10648151.

54. Jeschke G, Chechik V, Ionita P, Godt A, Zimmermann H, Banham J, et al. DeerAnalysis2006—a comprehensive software package for analyzing pulsed ELDOR data. Appl Magn Reson. 2006; 30: 473–498.

55. Hagelueken G, Ward R, Naismith JH, Schiemann O. MtsslWizard: In silico spin-labeling and generation of distance distributions in PyMOL. Appl Magn Reson. 2012; 42: 377–391. https://doi.org/10.1007/s00723-012-0314-0 PMID: 22448103.

56. Mori S, Abeygunawardana C, Johnson MO, van Zijl PC. Improved sensitivity of HSQC spectra of exchanging protons at short interscan delays using a new fast HSQC (FHSQC) detection scheme that avoids water saturation. J Magn Reson B. 1995; 108: 94–98. PMID: 7627436.

57. Grzesiek S, Döbeli H, Gentz R, Garotta G, Labhardt AM, Bax A. $^{1}H$, $^{13}C$, and $^{15}N$ NMR backbone assignments and secondary structure of human interferon-gamma. Biochemistry. 1992; 31: 8180–8190. PMID: 1525157.

58. Kay LE, Ikura M, Tschudin R, Bax A. Three-dimensional triple-resonance NMR spectroscopy of isotopically enriched proteins. J Magn Reson. 1990; 89: 496–514.

59. Wittekind M. HNCACB, a high-sensitivity 3D NMR experiment to correlate amide-proton and nitrogen resonances with the alpha and beta carbon resonances in proteins. J Magn Reson B. 1993; 101: 201–205.

60. Brutscher B, Cordier F, Simorre JP, Caffrey M, Marion D. High-resolution 3D HNCOCA experiment applied to a 28 kDa paramagnetic protein. J Biomol NMR. 1995; 5: 202–206. https://doi.org/10.1007/BF00208811 PMID: 22911467.

61. Zhang O, Kay LE, Olivier JP, Forman-Kay JD. Backbone $^{1}H$ and $^{15}N$ resonance assignments of the N-terminal SH3 domain of *drk* in folded and unfolded states using enhanced-sensitivity pulsed field gradient NMR techniques. J Biomol NMR. 1994; 4: 845–858. PMID: 7812156.

62. Delaglio F, Grzesiek S, Vuister GW, Zhu G, Pfeifer J, Bax A. NMRPipe: a multidimensional spectral processing system based on UNIX pipes. J Biomol NMR. 1995; 6: 277–293. PMID: 8520220.

63. Lee W, Tonelli M, Markley JL. NMRFAM-SPARKY: enhanced software for biomolecular NMR spectroscopy. Bioinformatics. 2015; 31: 1325–1327. https://doi.org/10.1093/bioinformatics/btu830 PMID: 25505092.

64. Berjanskii MV, Neal S, Wishart DS. PREDITOR: a web server for predicting protein torsion angle restraints. Nucleic Acids Res. 2006; 34: W63–69. https://doi.org/10.1093/nar/gkl341 PMID: 16845087.

65. Pornillos O, Alam SL, Rich RL, Myszka DG, Davis DR, Sundquist WI. Structure and functional interactions of the Tsg101 UEV domain. EMBO J. 2002; 21: 2397–2406. https://doi.org/10.1093/emboj/21.10.2397 PMID: 12006492.

66. Campbell EM, Perez O, Anderson JL, Hope TJ. Visualization of a proteasome-independent intermediate during restriction of HIV-1 by rhesus TRIM5α. J Cell Biol. 2008; 180: 549–561. https://doi.org/10.1083/jcb.200706154 PMID: 18250195.

# Appendix 5.

# Nup153 Unlocks the Nuclear Pore Complex for HIV-1 Nuclear Translocation in Nondividing Cells

Cindy Buffone, Alicia Martinez-Lopez, Thomas Fricke, Silvana Opp, Marco Severgnini, Ingrid Cifola, Luca Petiti, Stella Frabetti, Katarzyna Skorupka, Kaneil K. Zadrozny, Barbie K. Ganser-Pornillos, Owen Pornillos, Francesca Di Nunzio, Felipe Diaz-Griffero

J Virol 92:e00648-18. https://doi.org/10 .1128/JVI.00648-18.

AMERICAN SOCIETY FOR MICROBIOLOGY | Journal of Virology®

VIRUS-CELL INTERACTIONS

# Nup153 Unlocks the Nuclear Pore Complex for HIV-1 Nuclear Translocation in Nondividing Cells

**Cindy Buffone,[a] Alicia Martinez-Lopez,[a] Thomas Fricke,[a] Silvana Opp,[a] Marco Severgnini,[b] Ingrid Cifola,[b] Luca Petiti,[b] Stella Frabetti,[c] Katarzyna Skorupka,[d] Kaneil K. Zadrozny,[d] Barbie K. Ganser-Pornillos,[d] Owen Pornillos,[d] Francesca Di Nunzio,[c] Felipe Diaz-Griffero[a]**

[a]Department of Microbiology and Immunology, Albert Einstein College of Medicine, Bronx, New York, USA

[b]Institute for Biomedical Technologies, CNR, Segrate, Milan, Italy

[c]Molecular Virology and Vaccinology Unit, CNRS UMR 3569, Department of Virology, Institut Pasteur, Paris, France

[d]Department of Molecular Physiology and Biological Physics, University of Virginia, Charlottesville, Virginia, USA

**ABSTRACT** Human immunodeficiency virus type 1 (HIV-1) displays the unique ability to infect nondividing cells. The capsid of HIV-1 is the viral determinant for viral nuclear import. To understand the cellular factors involved in the ability of HIV-1 to infect nondividing cells, we sought to find capsid mutations that allow the virus to infect dividing but not nondividing cells. Because the interaction of capsid with the nucleoporin protein 153 (Nup153) is important for nuclear import of HIV-1, we solved new crystal structures of hexameric HIV-1 capsid in complex with a Nup153-derived peptide containing a phenylalanine-glycine repeat (FG repeat), which we used to guide structure-based mutagenesis of the capsid-binding interface. HIV-1 viruses with mutations in these capsid residues were tested for their ability to infect dividing and nondividing cells. HIV-1 viruses with capsid N57 substitutions infected dividing but not nondividing cells. Interestingly, HIV-1 viruses with N57 mutations underwent reverse transcription but not nuclear translocation. The mutant capsids also lost the ability to interact with Nup153 and CPSF6. The use of small molecules PF74 and BI-2 prevented the interaction of FG-containing nucleoporins (Nups), such as Nup153, with the HIV-1 core. Analysis ofintegration sites in HIV-1 viruses with N57 mutations revealed diminished integration into transcriptionally active genes in a manner resembling that of HIV-1 in CPSF6 knockout cells or that of HIV-1-N74D. The integration pattern of the N57 mutant HIV-1 can be explained by loss of capsid interaction with CPSF6, whereas capsid interaction with Nup153 is required for HIV-1 to infect nondividing cells. Additionally, the observed viral integration profiles suggested that integration site selection is a multiparameter process that depends upon nuclear factors and the state of the cellular chromatin.

**IMPORTANCE** One of the key advantages that distinguish lentiviruses, such as HIV-1, from all other retroviruses is its ability to infect nondividing cells. Interaction of the HIV-1 capsid with Nup153 and CPSF6 is important for nuclear entry and integration; however, the contribution of each of these proteins to nuclear import and integration is not clear. Using genetics, we demonstrated that these proteins contribute to different processes: Nup153 is essential for the HIV-1 nuclear import in nondividing cells, and CPSF6 is important for HIV-1 integration. In addition, nuclear factors such as CPSF6 and the state of the chromatin are known to be important for integration site selection; nevertheless, the preferential determinant influencing integration site selection is not known. This work demonstrates that integration site selection is a multiparameter process that depends upon nuclear factors and the state of the cellular chromatin.

**Received** 16 April 2018 **Accepted** 20 June 2018

**Accepted manuscript posted online** 11 July 2018

**Citation** Buffone C, Martinez-Lopez A, Fricke T, Opp S, Severgnini M, Cifola I, Petiti L, Frabetti S, Skorupka K, Zadrozny KK, Ganser-Pornillos BK, Pornillos O, Di Nunzio F, Diaz-Griffero F. 2018. Nup153 unlocks the nuclear pore complex for HIV-1 nuclear translocation in nondividing cells. J Virol 92:e00648-18.https://doi.org/10.1128/JVI.00648-18

**Editor** FrankKirchhoff, Ulm University Medical Center



Addresscorrespondence to Francesca Di Nunzio, dinunzio@pasteur.fr, or Felipe Diaz-Griffero, felipe.diaz-griffero@einstein.yu.edu.

**KEYWORDS** HIV-1, Nup153, CPSF6, nondividing cells, capsid binding, nuclear import, integration, HIV integration, HIV nuclear import, NPC

The critical influence of the physiological state of cells on retroviral replication was initially demonstrated by experiments showing that cell division arrest with X-rays or UV light prevents Rous sarcoma virus replication (1). Subsequent research established the relationship between cell cycle stage and retroviral infection, revealing that retroviruses do not all have the same requirements for productive infection. For example, productive infection by gammaretroviruses, such as murine leukemia virus (MLV), requires host cells to pass through mitosis (2, 3). In contrast, lentiviruses such as human immunodeficiency virus type 1 (HIV-1) show no difference in productive infection of dividing versus nondividing cells (4). This suggests that lentiviruses have developed specific molecular mechanisms for the infection of nondividing cells. The ability of HIV-1 to infect nondividing cells has been attributed to its capacity to transport the preintegration complex (PIC) to the nucleus through nuclear pores (5, 6). Translocation of the HIV-1 PIC into the nucleus is not a simple process, as its size is similar to that of a ribosome, which is at least 56 nm in diameter (5, 7). Because ofits large size, it is unlikely that the PIC enters the nucleus by passive diffusion (8). Instead, HIV-1 PIC translocation into the nucleus is likely to be an active process. Several components of the PIC, such as matrix, Vpr, integrase, and the central DNA flap, have been proposed to be involved in PIC nuclear translocation (9–11). Although barely detectable amounts of capsid can be found on the HIV-1 PIC (5, 12–14), recent evidence has shown that the capsid nonetheless plays a role in HIV-1 infection of nondividing cells (15–17). In agreement with this evidence, several studies suggest that the HIV-1 core associates with the nuclear pore (18, 19). While the mechanism used by HIV-1 PIC to enter the nucleus is not completely understood, it is accepted that nuclear import of the complex is an active and energy-dependent process (6).

In addition to the viral determinants involved in HIV-1 PIC nuclear import, several host factors have been implicated in the process: (i) importin 7 (20–22), (ii) importin a3 (23), (iii) importin $\alpha$/importin $\beta$ heterodimer (20, 24, 25), (iv) transportin-SR2/TNPO3 (26–33), (v) RanBP2/Nup358 (19, 34), and (vi) Nup98 and Nup153 (19, 32, 35–38).

Recent studies have also proposed an important role for Nup153 in HIV-1 replication (19, 32, 35, 38–40). Nup153 localizes to the nuclear side of the nuclear pore and was initially described as being necessary for HIV-1 replication by three independent genome-wide short interfering RNA (siRNA) screens (28, 32, 33). Although the C-terminal domain of Nup153 has been shown, via use of bacterially purified proteins, to bind the HIV-1 integrase protein (36), the genetic determinant for the Nup153 requirement during HIV-1 infection has been mapped to the capsid protein (38). Interestingly, HIV-1 with capsid mutations showed different infectivities as a function of Nup153 depletion (37, 38, 41). In agreement with these findings, we and others have found that Nup153 interacts directly with the capsid via phenylalanine-glycine (FG) repeats (35, 40), which directly bind to a pocket generated by the so-called N-terminal/C-terminal (NTD-CTD) interface between adjacent subunits in the capsid hexamer (42, 43). Because Nup153 depletion affects HIV-1 nuclear import, these findings suggested that Nup153 interaction with the viral core must be important for infection.

Even though CPSF6 and Nup153 have been shown to compete for the same binding site on the HIV-1 capsid hexamer (42–44), the two proteins appear to mediate distinct processes, with CPSF6 directing HIV-1 integration to transcriptionally active chromatin, whereas Nup153 is important for nuclear translocation (28, 45). It is possible that interaction of Nup153 and CPSF6 with the capsid occurs at different stages of viral replication, governing discrete events at each stage. For example, Nup153 could govern nuclear import, while CPSF6 could govern viral integration. Understanding the precise role of Nup153 and CPSF6 in HIV-1 infection of nondividing cells remains an ongoing challenge in retroviral research.

Although it is generally agreed that Nup153 has a role in HIV-1 nuclear translocation,

the pathways and specific proteins on which the virus relies to infect nondividing cells have not been elucidated. In order to address the role of Nup153 in the ability of HIV-1 to infect nondividing cells, we performed structure-based mutagenesis to identify HIV-1 capsid mutations that modulate Nup153-capsid interaction. For this purpose, we solved the crystal structure of a complex between a Nup153-derived peptide containing a capsid-binding FG repeat and the hexameric HIV-1 capsid in order to identify capsid residues that are interacting with Nup153. This allowed us to identify mutant capsid HIV-1 viruses that are unable to infect nondividing cells but can infect dividing cells. The most interesting change was on capsid residue N57, which directly interacts with the FG repeat of Nup153. Infection of nondividing cells by HIV-1 viruses with these capsid mutations was found to be defective for nuclear translocation but unaffected for reverse transcription. HIV-1 capsid with these mutations lost the ability to interact with Nup153, suggesting that this interaction is essential for the HIV-1 infection of nondividing cells. Given the observed role of CPSF6 in determining HIV-1 integration sites and the fact that Nup153 and CPSF6 bind to the capsid at the same site, we also examined integration sites for N57 mutant HIV-1 in dividing cells and found these sites to closely resemble those of wild-type HIV-1 in the absence of CPSF6. The integration pattern of HIV-1 viruses with changes on N57 is explained by the loss ofinteraction with CPSF6, whereas interaction of the capsid with Nup153 is required for HIV-1 infection of nondividing cells. Taken together, our findings show how different capsid mutations can delineate functional interactions between different host factors that modulate HIV-1 infectivity and help unravel the complex processes that govern nuclear translocation and integration.

## RESULTS

**Interaction of Nup153 with HIV-1 capsid.** We and others have previously demonstrated the ability of Nup153 to interact with HIV-1 capsid (35, 40, 42). Accordingly, to identify specific residues in the hexameric HIV-1 capsid that interact with Nup153, we attempted to cocrystallize a number of FG-containing peptides derived from Nup153 with the disulfide-stabilized HIV-1 capsid hexamer. Remarkably, only one of the tested peptides was found to bind capsid in the crystals, which we interpret to mean that binding of the FG region is modulated by surrounding residues and that certain FG sequences are preferred over others. Our structures all contained a peptide derived from $Nup153_{1407–1429}$ ($^{1407}$TNNSPSGVFTFGANSSTPAASAQ$^{1429}$), previously described to be a high-affinity motiffor the HIV-1 capsid ( 40). We obtained two different crystal forms distinct from those reported by Price and colleagues (43). Interestingly, even though each hexamer has six potential binding sites, none of our structures showed saturation despite the excess of peptide in the crystallization mixture. Three crystallographically independent hexamers were observed, two of which had three bound peptides while the third contained only two. Our interpretation of these results is that the hexamer architecture is incompatible with saturation binding of FG repeats, perhaps because full occupancy has a destabilizing effect.

As reported previously (43), the $Nup153_{1407–1429}$ peptide binds at the NTD-CTD interface, and we found that it interacts with capsid residues P34, I37, P38, N53, L56, N57, V59, V142, and Q176 (Fig. 1A and Tables 1 and 2). Notably, capsid residue N57 is buried within the binding site and makes hydrogen bonds with the FG peptide backbone. The mode ofinteraction is similar to that observed with HIV-1 inhibitors PF74 and BI-2 (42, 43) (Fig. 1C and D). We also attempted to cocrystallize the hexamer and the $Nup153_{1407–1429}$ peptide with an N57S mutation; however, repeated screening of multiple crystals failed to reveal any binding. These experiments highlight the importance of the N57 residue for many different interactions involving the capsid. This residue is therefore likely to be an important determinant for translocation of the PIC through nuclear pores.

**HIV-1 viruses bearing capsid mutations that affect their ability to infect nondividing cells.** The interaction of capsid with Nups is an important early step in HIV-1 replication. All residues found to interact with Nup153 in our structural studies are

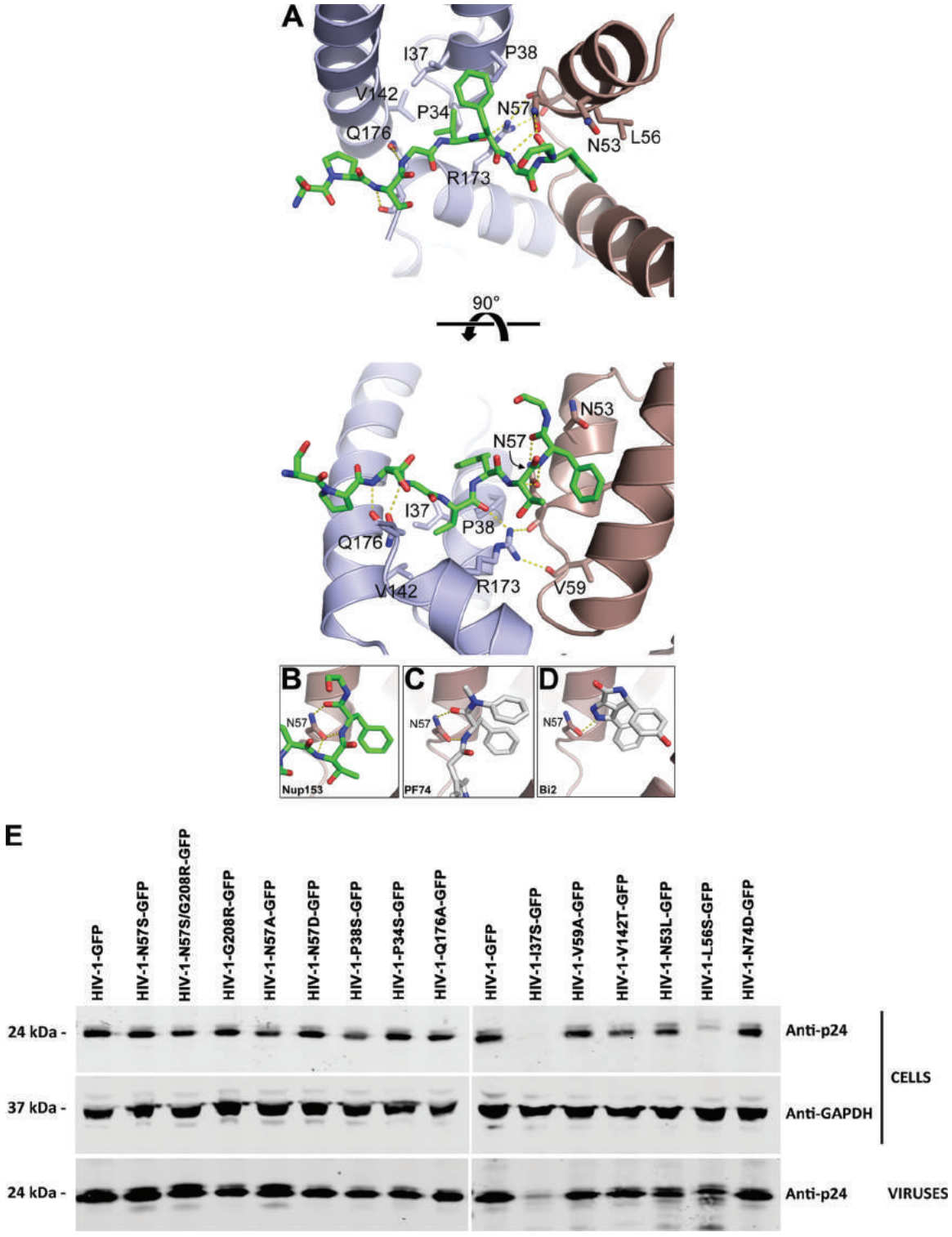


**FIG 1** Structure of Nup153 FG in complex with hexameric HIV-1 capsid. (A) Structure of NUP153 FG peptide (green) in its binding pocket within the hexameric HIV-1 capsid. The capsid side chains that contact the peptide are shown as sticks and labeled. N57 is binding Nup153 (B), PF74 (C) (42), and BI2 (D) (43). Hydrogen bonds are shown as dashed yellow lines. (E) Production and maturation of HIV-1 capsid mutants viruses. The indicated HIV-1 viruses were produced in human 293T cells. Producer cells and purified viruses were analyzed for HIV-1 capsid expression by Western blotting using anti-p24 antibodies. Producer cells validated for glyceraldehyde-3-phosphate dehydrogenase (GAPDH) expression were used as loading controls. Experiments were performed three times, and a representative example is shown.

**TABLE 1** Infection of nondividing cells by HIV-1 variants[d]

| | THP1-SAMHD1-KO[a] | | HT1080[b] | | Cf2Th[b] | | HeLa[b] | | HeLa-Nup153-KO[c] | |
|---|---|---|---|---|---|---|---|---|---|---|
| HIV-1 variant | Dividing | Nondividing | Dividing | Nondividing | Dividing | Nondividing | Dividing | Nondividing | Dividing | Nondividing |
| WT | + | + | + | + | + | + | + | + | − | ND |
| N57S | + | − | + | − | + | + | ND | ND | + | ND |
| N57A | + | − | + | − | + | + | ND | ND | ND | ND |
| N57D | + | − | + | − | + | + | ND | ND | ND | ND |
| G208R | + | + | + | + | + | + | ND | ND | ND | ND |
| N57S/G208R | + | − | + | − | + | + | + | − | + | ND |
| P38S | + | + | + | + | + | + | ND | ND | ND | ND |
| Q176A | + | + | + | + | + | + | ND | ND | ND | ND |
| P34S | − | − | − | − | − | − | ND | ND | ND | ND |
| I37S | − | − | − | − | − | − | ND | ND | ND | ND |
| N53L | − | − | − | − | − | − | ND | ND | ND | ND |
| L56S | − | − | − | − | − | − | ND | ND | ND | ND |
| V59A | − | − | − | − | − | − | ND | ND | ND | ND |
| V142T | − | − | − | − | − | − | ND | ND | ND | ND |
| N74D | + | + | + | + | + | + | + | + | − | ND |

[a]PMA-treated (nondividing) or untreated (dividing) THP-1–SAMHD1-KO cells were challenged with increasing amounts of HIV-1-GFP viruses containing the indicated capsid change.
[b]Aphidicolin-treated or untreated HT1080, Cf2Th, or HeLa cells were challenged with increasing amounts of HIV-1-GFP viruses containing the indicated capsid change.
[c]HeLa cells transiently knocked down for expression of Nup153 were challenged with the indicated HIV-1 variants.
[d]Infection was measured 48 hpi by determining the percentage of GFP-positive cells by flow cytometry. A plus or minus indicates infection or the absence of infection, respectively. Experiments were repeated at least three times, and typical results are shown. ND, not determined.

highly conserved in primate lentiviruses, such as HIV-1, HIV-2, and simian immunodeficiency virus (SIV) (53). Guided by the crystal structures, we synthesized HIV-1 viruses with the following single-point mutations on each of the residues that directly contact the FG peptide: P34S, I37S, P38S, N53L, L56S, N57S, N57A, N57D, V59A, V142T, and Q176A. As shown in Table 1, we found several HIV-1 viruses containing capsid mutants that infected dividing cells: N57S, N57A, N57D, P38S, and Q176A. In contrast, HIV-1 viruses containing capsid mutants P34S, I37S, N53L, L56S, V59A, and V142T were either not released or were infectivity defective.

We further characterized these capsid mutants by analyzing expression in cells, viral production, viral maturation, and infectivity (Table 1 and Fig. 1E). All HIV-1 capsid variants studied here expressed similar levels of p55 in producer cells. Levels of p24 protein were detected in producer cells for all variants, with the exception of I37S and N53L (Fig. 1E). Analysis of semipurified viral particles revealed that HIV-1 capsid variants showed no defects on maturation, as detected by the levels of p24 in viruses, with the exception of I37S (Fig. 1E). Infectivity assay revealed that HIV-1 capsid variants N57S, N57A, N57D, P38S, and Q176A were infectious; however, HIV-1 capsid variants P34S, I37S, N53L, L56S, V59A, and V142T were not infectious (Table 1).

We next wanted to test whether any of these capsid mutants could abrogate the ability of HIV-1 to infect nondividing cells. For this purpose, we tested the ability of p24-normalized HIV-1 viruses with capsid mutations to infect nondividing cells. As a model to study nondividing cells, we treated THP-1 monocytes lacking the restriction factor SAMHD1 (THP-1–SAMHD1-KO) with phorbol 12-myristate 13-acetate (PMA), which induces differentiation of THP-1 cells to a nondividing macrophage-like state (54). The SAMHD1-KO eliminated a restriction factor that would otherwise inhibit viral replication by a mechanism different from the process being studied in this experiment. As shown in Fig. 2A, HIV-1-GFP viruses with capsid mutation N57S, N57A, or N57D poorly infected THP-1–SAMHD1-KO nondividing cells (PMA treated). In contrast, HIV-1 viruses with these capsid changes were able to infect dividing cells (Mock). HIV-1 viruses with mutations on capsid residue N57 resulted in decreased capsid stability, as shown by the "fate of the capsid" assay (Fig. 2B) (55). In an effort to restore this defect in capsid stability, we produced HIV-1 containing the double mutations N57S and G208R, which is known to increase the cytosolic stability of the viral core. Interestingly, HIV-1-N57S/G208R recovered core stability in the cytoplasm ofinfected cells ( Fig. 2B), which allowed us to partially repair the stability defect of HIV-1-N57S. As expected,

**TABLE 2** Crystallographic statistics

| Parameter | Value(s) for[a]: R3 | P1 |
|---|---|---|
| Diffraction data | | |
| Beamline | APS 23-ID-D | APS 23-ID-D |
| Wavelength | 1.000 | 1.000 |
| Processing program | HKL2000 | HKL2000 |
| Space group | R3 | P1 |
| Cell dimensions | | |
| *a* (Å) | 151.924 | 57.333 |
| *b* (Å) | 151.924 | 91.487 |
| *c* (Å) | 69.646 | 150.047 |
| Angle (°) | $\alpha = \beta = 90$, $\gamma = 120$ | $\alpha = 89.54$, $\beta = 90.94$, $\gamma = 96.08$ |
| Resolution range (Å) | 50–2.50 (2.54–2.50) | 50–1.90 (1.97–1.90) |
| $R_{sym}/R_{meas}/R_{pim}$ | 0.09 (0.46)/0.11 (0.64)/0.07 (0.45) | 0.07 (0.75)/0.09 (1.00)/0.07 (0.75) |
| Mean $I/\sigma<I>$ | 10.6 (1.2) | 9.6 (1.0) |
| Completeness (%) | 75.3 (23.7) | 96.5 (92.0) |
| Avg redundancy | 2.4 (1.5) | 1.7 (1.6) |
| Wilson B factor (Å$^2$) | 31.58 | 19.16 |
| Refinement | | |
| Refinement program | Phenix | Phenix |
| Resolution range | 47.83–2.50 (2.60–2.50) | 45.50–1.90 (1.92–1.90) |
| No. of unique reflections | 12,545 (190) | 205,470 (1,577) |
| Reflections in free set | 1,266 (23) | 10,123 (66) |
| $R_{work}$ | 0.20 (0.30) | 0.18 (0.31) |
| $R_{free}$ | 0.25 (0.36) | 0.23 (0.29) |
| NCS copies | 2 | |
| No. of nonhydrogen atoms | | |
| Protein | 3,415 | 22,652 |
| Solvent | 0 | 2,179 |
| Avg B factor (Å$^2$) | | |
| Protein | 47.24 | 27.78 |
| Solvent | NA | 29.54 |
| Validation and deposition | | |
| Coordinate deviations | | |
| Bond lengths (Å$^2$) | 0.002 | 0.007 |
| Bond angles (°) | 0.475 | 0.784 |
| Ramachandran plot (%) | | |
| Favored | 96.5 | 98.9 |
| Outliers | 0 | 0 |
| MolProbity clashscore | 1.03 | 1.3 |
| PDB entry | 5TSV | 5TSX |

[a]Values in parentheses are for the highest-resolution shell.

HIV-1-N57S/G208R viruses behave like N57S in PMA-treated THP-1–SAMHD1 KO cells (nondividing) (Fig. 2A and Table 1). We also tested the ability of p24-normalized HIV-1 with capsid mutations to infect human HT1080 and canine Cf2Th cells in the presence of the cell cycle inhibitor aphidicolin, which blocks the cell cycle at early S phase. As shown in Fig. 2C and D, HIV-1 with capsid mutations N57S, N57S/G208R, N57D, and N57A poorly infected aphidicolin-treated cells. Similar effects were observed for infection of aphidicolin-treated human HeLa cells by HIV-1-N57S and HIV-1-N57S/G208R expressing luciferase as a reporter ofinfection ( Fig. 2E). As a control, we tested the ability of HIV-1-N74D viruses to infect nondividing cells and found that it efficiently infected nondividing cells compared to wild-type virus. The results of these experiments suggested that in contrast to N74, capsid residue N57 confers upon HIV-1 the ability to infect nondividing cells (Fig. 2E). Furthermore, the results raised the possibility that interaction of the HIV-1 capsid with Nup153 is essential for the ability of HIV-1 to infect nondividing cells.

To further expand the number of cell lines used to examine our viruses, we tested the myeloid cell line U937, which does not express SAMHD1. As shown in Fig. 2F, HIV-1-N57S/G208R-GFP viruses poorly infected PMA-treated U937 (nondividing) cells compared to untreated (dividing) cells.

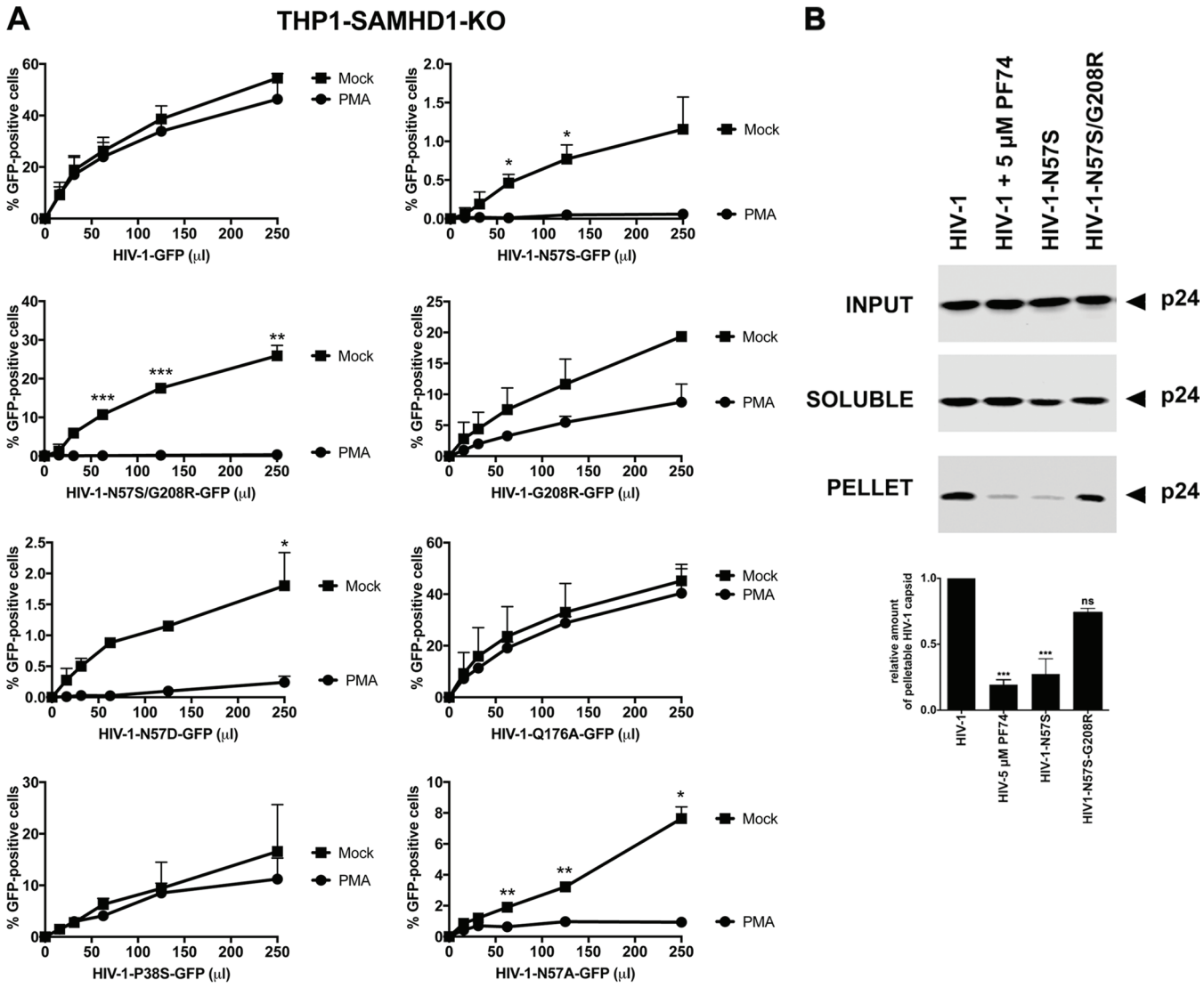


**FIG 2** HIV-1 viruses bearing changes on the capsid residue N57 are not able to infect nondividing cells. (A) PMA-treated (PMA) or untreated (Mock) THP-1–SAMHD1 knockout (KO) cells were challenged with increasing amounts of the indicated HIV-1-GFP viruses. Infection was determined by measuring the percentage of GFP-positive cells at 48 hpi. PMA-treated THP-1–SAMHD1 KO cells are used as a model of noncycling cells. (B) HIV-1-N57S/G208R recovers core stability during infection. Canine Cf2Th cells were challenged with the indicate viruses, and core stability was assayed by performing the fate-of-the-capsid assay. Eight hpi, cells were lysed and a postnuclear fraction (INPUT) was separated into SOLUBLE and PELLET fractions by using a 50% sucrose gradient, as described in Materials and Methods. INPUT, SOLUBLE, and PELLET fractions were analyzed for capsid using anti-p24 antibodies. PELLET represents the fraction of capsid that is forming cores. Experiments were performed at least three times, and a representative example is shown. (C to E) Human HT1080 (C), dog Cf2Th (D), or human HeLa (E) cells pretreated for 12 h with 0.5 $\mu$g/ml aphidicolin were challenged with increasing amounts of the indicated HIV-1 viruses. The use of 0.5 $\mu$g/ml of aphidicolin for 12 h stops the cell cycle at S phase, as determined by analyzing DNA content per cell using propidium iodide. Infection was determined by measuring the percentage of GFP-positive cells or the luciferase activity at 48 hpi, and standard deviations for triplicates are shown. Results were analyzed using two-tailed Student's *t* test. Differences were considered statistically significant at a *P* value of $<0.05$ (*), $<0.01$ (**), or $<0.001$ (***) or were nonsignificant. (F) PMA-treated (PMA) or untreated (Mock) U937 cells were challenged with increasing amounts of HIV-1-N57S/G208R-GFP viruses. Infection was determined by measuring the percentage of GFP-positive cells at 48 hpi. Experiments were performed at least three times, and a representative example is shown.

**HIV-1 viruses with mutations on capsid residue N57 undergo reverse transcription but not nuclear translocation in nondividing cells.** In the preceding section, we showed that mutations in the capsid residue N57 inhibit infection of nondividing cells by HIV-1. We next tested whether HIV-1-N57S/G208R undergoes reverse transcription in nondividing cells. For this purpose, we challenged PMA-treated THP-1–SAMHD1 KO cells (nondividing cells) and measured the ability of HIV-1-N57S/G208R expressing GFP (HIV-1-N57S/G208R-GFP) as a reporter ofinfection to undergo reverse transcription at 7 h postinfection (hpi). As shown in Fig. 3A, HIV-1 with the capsid mutations N57S/G208R did not infect nondividing cells (upper) but underwent reverse transcription

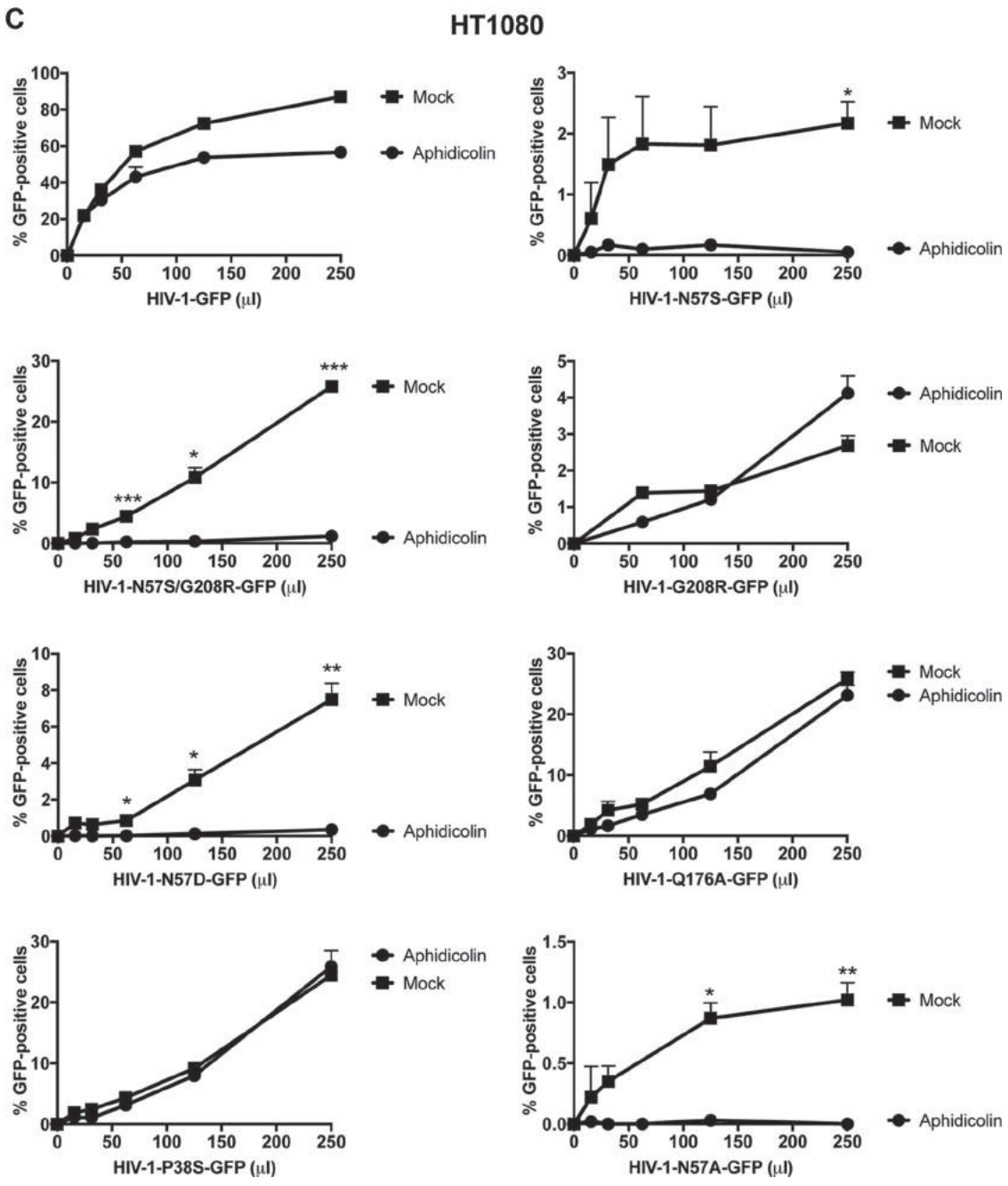


**FIG 2** (Continued)

(lower). As a control, we used nevirapine (Nev), which inhibits HIV-1 reverse transcription. These experiments suggested that HIV-1 with mutations on capsid residue N57 is defective only after reverse transcription in nondividing cells.

To further investigate the defect imposed by N57 mutations on HIV-1 replication, we monitored reverse transcription and formation of two long terminal repeat (2-LTR) circles in aphidicolin-treated cells at 7 and 24 hpi, respectively. Aphidicolin-treated human HeLa cells (nondividing) were challenged with luciferase-expressing HIV-1-N57S-Luc, and infection (at 48 hpi), reverse transcription (at 7 hpi), formation of 2-LTR circles (at 24 hpi), and integration by Alu-PCR (at 24 hpi) were measured. In agreement with our previous results, HIV-1-N57S-Luc viruses did not infect aphidicolin-treated cells but underwent normal reverse transcription (Fig. 3B, upper). Interestingly, HIV-1-N57S-

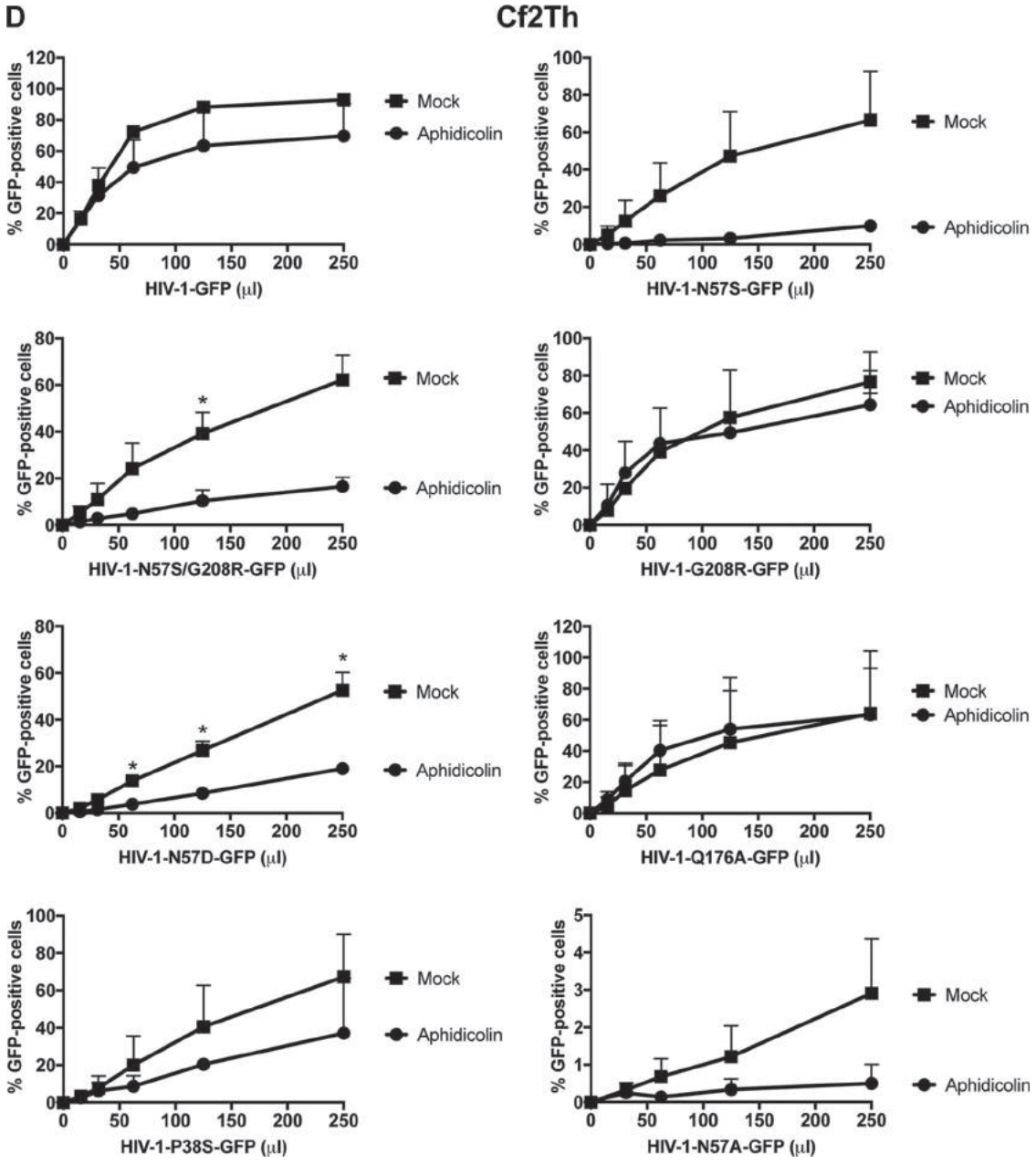


**FIG 2** (Continued)

Luc viruses were defective for the formation of 2-LTR circles and integration, suggesting a defect in nuclear translocation (Fig. 3B, lower). As controls, we monitored infection, reverse transcription, formation of 2-LTR circles, and integration by HIV-1-N74D-Luc viruses, which are not affected in their ability to infect aphidicolin-treated cells (nondividing) (Fig. 3B, lower). Taken together, these experiments demonstrated that HIV-1 viruses containing mutations on capsid residue N57 caused a defect after reverse transcription but before nuclear translocation in nondividing cells. Interestingly, a less than 2-fold increase in reverse transcription was observed for HIV-1 viruses bearing N57 changes. Although this increase on reverse transcription was highly reproducible, this phenotype remains to be fully investigated.

**HIV-1 capsids bearing mutations on residue N57 lose the ability to interact with Nup153.** Based on our structure-function studies, we hypothesized that HIV-1 capsid with N57 mutations loses the ability to interact with Nup153, an essential

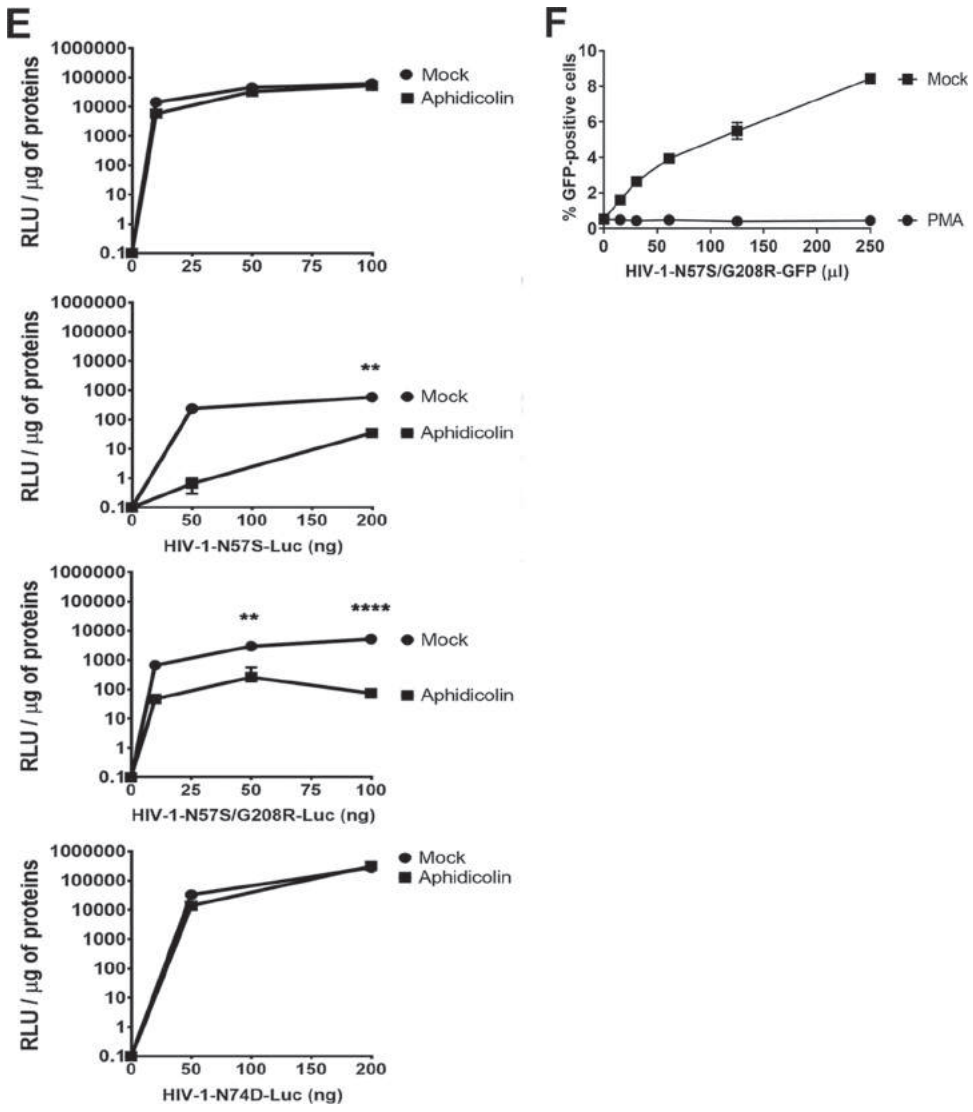


**FIG 2** (Continued)

protein for infection (28). To test this hypothesis, we evaluated the ability of Nup153-GFP to bind to HIV-1 capsid-nucleocapsid (CA-NC) complexes assembled *in vitro*, which recapitulates the surface of the HIV-1 core (35, 46). As shown in Fig. 4A, Nup153-GFP lost its ability to bind *in vitro*-assembled HIV-1 CA-NC complexes with the N57S mutation. Similarly, Nup153 was unable to interact with complexes bearing the N57S/G208R mutations. In contrast, Nup153-GFP could bind effectively to the wild-type complexes. To rule out the possibility that the GFP moiety of Nup153-GFP is responsible for the binding of Nup153-GFP to capsid, we measured the ability of Nup153-HA, which contains a small hemagglutinin (HA) tag of 8 amino acids, to bind wild-type and mutant *in vitro*-assembled HIV-1 CA-NC complexes. Similarly, Nup153-HA bound wild-type but not N57S capsids (Fig. 4A). This suggests that the ability of HIV-1 to infect nondividing cells requires the interaction of capsid with Nup153. Interestingly, Nup98-GFP was also defective in its ability to bind complexes with the N57S mutation; however, it should be noted that depletion of Nup98 expression in human cells poorly affects HIV-1 infection compared to Nup153 depletion (35). Nup98, like Nup153, contains FG repeats that are likely to allow capsid interaction, consistent with our own crystallographic analysis indicating that capsid residue N57 interacts with one of the FG repeats of Nup153. We showed in a control experiment that RanBP2/Nup358 interacts with both wild-type and

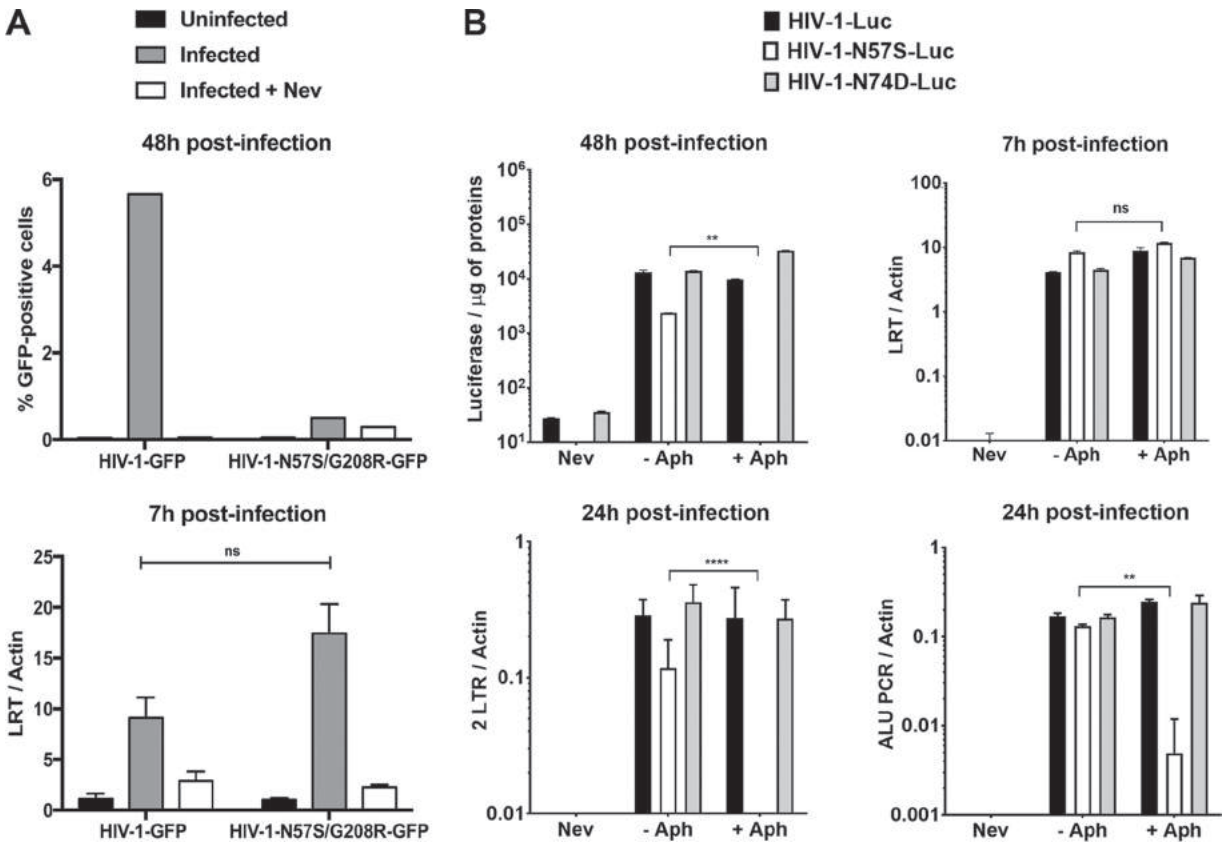


**FIG 3** Infection of nondividing cells by HIV-1-N57S is stopped after reverse transcription but prior to nuclear translocation. (A) PMA-treated THP-1–SAMHD1 knockout (KO) cells were challenged with the indicated DNase-pretreated HIV-1-GFP viruses. (Upper) Infection was determined by measuring the percentage of GFP-positive cells by flow cytometry at 48 hpi. (Lower) In parallel, cells from similar infections were lysed at 7 hpi and total DNA extracted. The DNA samples collected at 7 hpi postinfection were used to determine the levels oflate reverse transcripts by real-time PCR. As a control, we used 10 $\mu$M the reverse transcription inhibitor nevirapine (Nev). Late reverse transcript levels were normalized to actin. (B) Similarly, HeLa cells pretreated with 0.5 $\mu$g/ml aphidicolin for 12 h were subsequently infected by the indicated DNase-pretreated HIV-1–Luc viruses. (Upper) Infection was determined by measuring luciferase activity at 48 hpi. In parallel, cells from similar infections were lysed at 7 and 24 hpi, and total DNA was extracted. The DNA samples collected at 7 hpi were used to determine the levels oflate reverse transcripts by real-time PCR. (Lower) HIV-1 2-LTR circles, a marker for nuclear import, were quantified by real-time PCR of DNA samples collected at 24 hpi. In addition, integration was measured by Alu-PCR in DNA samples collected at 24 hpi. The levels oflate reverse transcripts, 2-LTR circle, and products of Alu-PCR were normalized to actin. Nevirapine was used as a control. Experiments were repeated at least three times, and a representative example is shown. Results were analyzed using two-tailed Student's *t* test. Differences were considered statistically significant at a *P* value of $<0.05$ (*), $<0.01$ (**), $<0.001$ (***), or $<0.0001$ (****) or were nonsignificant (ns).

mutant HIV-1 CA-NC complexes (Fig. 4A), which was to be expected, since RanBP2/Nup358 is known to bind to capsid using both FG repeats and a cyclophilin-like domain (19). These experiments suggested that the interaction of capsid with Nup153 is essential for the ability of HIV-1 to infect nondividing cells. By the same token, our results suggested that RanBP2/Nup358 is not important for the ability of HIV-1 with changes on N57 to infect nondividing cells.

To further support these results, we expressed and purified a glutathione *S*-transferase (GST) fusion protein containing the entire FG repeat region of human Nup153 (residues 896 to 1475) (Fig. 4Bi). As shown in Fig. 4Bii, the GST-NUP-FG fusion protein pulled down wild-type HIV-1 capsid hexamers but not those of the N57S mutant. Importantly, GST-NUP-FG also did not bind monomeric HIV-1 capsid, confirming that the FG repeats bind the NTD-CTD interface that can exist only in fully assembled capsid. These experiments are the first to show direct interaction of the entire FG repeat region of Nup153 with the HIV-1 capsid hexamer using purified proteins.

Similar to our findings on the N57S mutant, hexameric HIV-1 capsids with an R173A mutation did not bind to GST-NUP-FG (Fig. 4Biii). In contrast, the R173K capsid retained the ability to interact with GST-NUP-FG. It is ofinterest that, even though the capsid

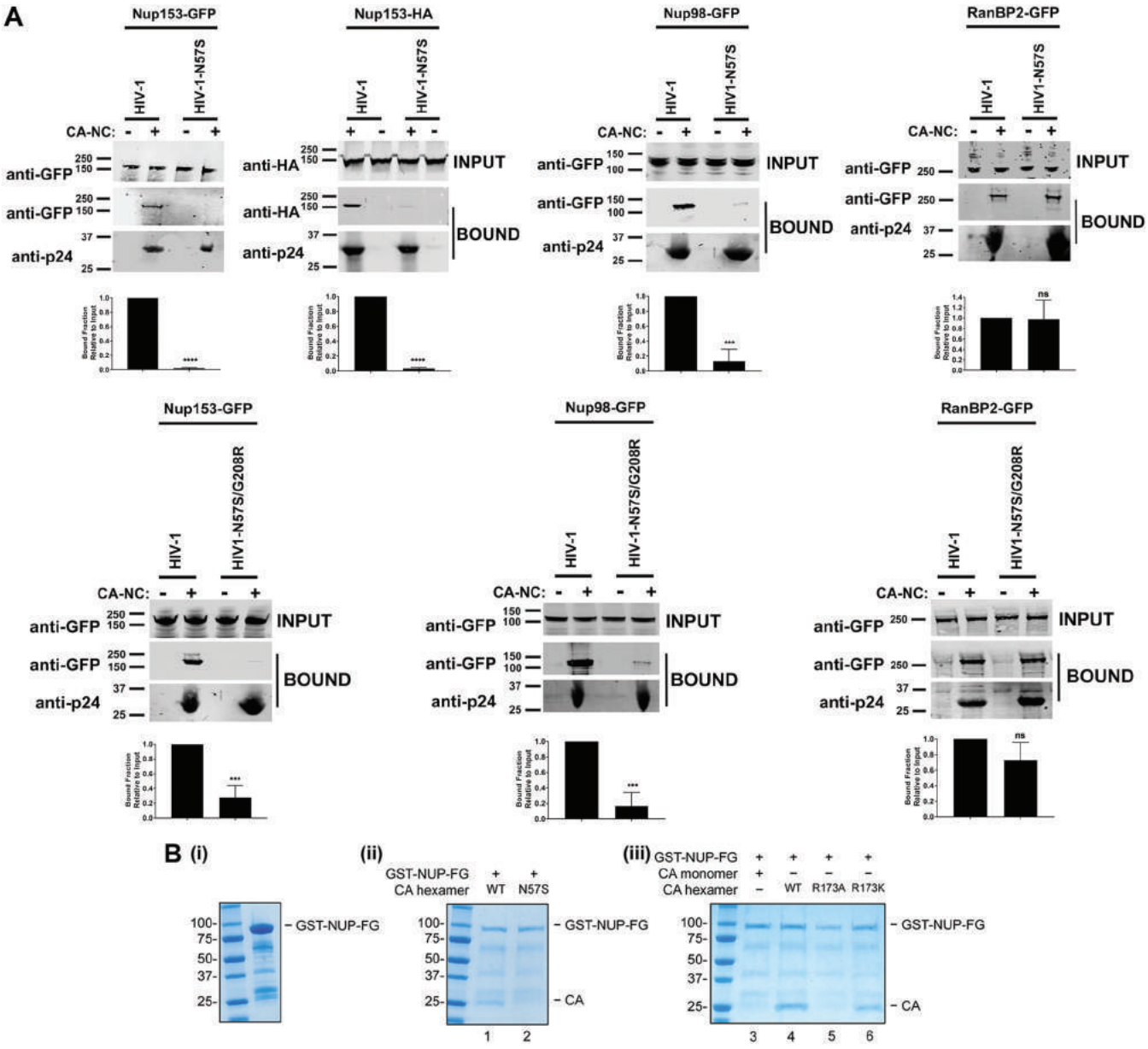


**FIG 4** HIV-1 capsids bearing the N57S change do not bind Nup-153. (A) The ability of Nup153-GFP, Nup153-HA, Nup98-GFP, and RanBP2/Nup358-GFP to bind the indicated *in vitro*-assembled HIV-1 CA-NC complexes was measured as described in Materials and Methods. INPUT and BOUND fractions were analyzed by Western blotting using anti-GFP, anti-HA, or anti-p24 antibodies. Experiments were repeated at least three times, and a representative experiment is shown. (B) GST protein fused to the Nup153 residues 896 to 1475 containing the FG repeat (GST-NUP-FG) binds to HIV-1 hexameric capsid. (i) Purified GST-NUP-FG proteins were incubated with hexameric capsids bearing the indicated changes. (ii and iii) Subsequently, complexes were pulldown using glutathione beads and analyzed by SDS-PAGE. (C) The ability of Nup153 that does not contain FG repeats [Nup153Δ(896-1475)-GFP] to bind the indicated *in vitro*-assembled HIV-1 CA-NC complexes was measured as described in Materials and Methods. Similarly, INPUT and BOUND fractions were analyzed by Western blotting using anti-GFP or anti-p24 antibodies. Experiments were repeated at least three times, and a representative experiment is shown. (D) HIV-1-N57S virus infection of Nup-153-depleted cells. Nup153-depleted HeLa cells (Nup153 KD) were challenged with the indicated HIV-1-Luc viruses. (Upper) Infection was determined by measuring luciferase activity 48 h postinfection. (Lower) Depletion of Nup153 was achieved transiently using shRNA, and expression knockdown was confirmed by Western blotting using anti-Nup153 antibodies, as described in Materials and Methods. Results were analyzed using two-tailed Student's *t* test. Differences were considered statistically significant at a *P* value of $<0.05$ (*), $<0.01$ (**), $<0.001$ (***), or $<0.0001$ (****) or were nonsignificant (ns). Experiments were repeated at least three times, and a representative example is shown.

mutant R173A did not bind GST-NUP-FG, HIV-1 viruses with the capsid mutation R173A are not infectious (56).

We next measured the capsid-binding ability of Nup153 that does not contain FG repeats [Nup153Δ(896-1475)-GFP]. As shown in Fig. 4C, Nup153Δ(896-1475)-GFP did not bind *in vitro*-assembled HIV-1 CA-NC complexes, unlike Nup153-GFP, suggesting that FG repeats are necessary for the ability of Nup153 to bind to the HIV-1 core.

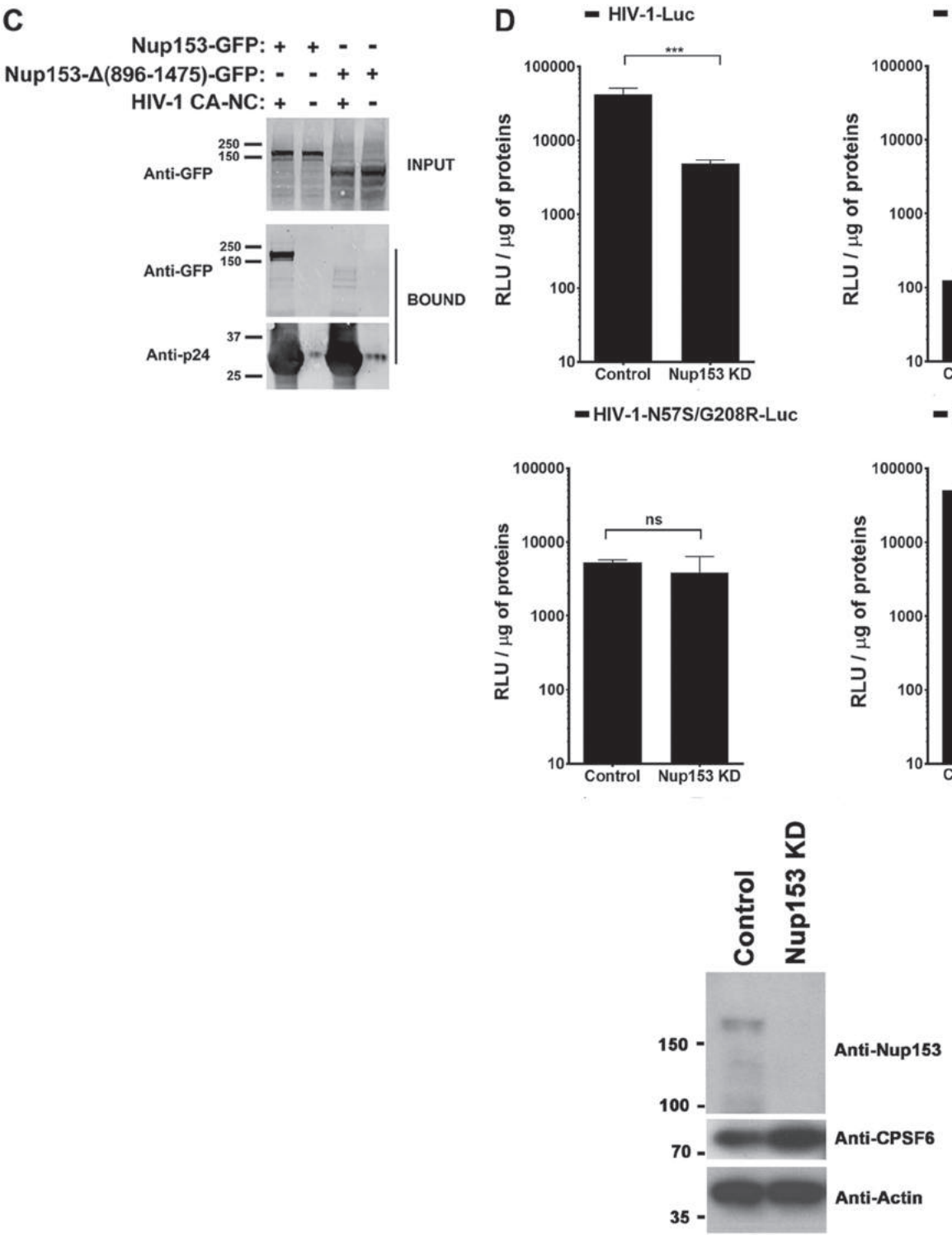


**FIG 4** (Continued)

We next tested whether Nup153 is required for the cellular infectivity of HIV-1 with the N57S mutation. For this purpose, Nup153-depleted HeLa cells were challenged with HIV-1-N57S-Luc and HIV-1-N57S/G208R-Luc. As shown in Fig. 4D, both viruses were insensitive to Nup153 depletion in dividing cells. These results suggested that HIV-1 with the N57S mutation utilizes a different mode ofinfection independent of Nup153. As previously shown (35), infection of Nup-153-depleted cells by wild-type and HIV-1-

N74D viruses was severely diminished. These experiments raise the possibility that the N57S mutant has gained the ability to infect dividing cells by a mechanism in which Nup153 is not required.

**FG repeats mediate the interaction of Nup proteins with HIV-1 capsid.** Our crystallization experiments suggested that the HIV-1 capsid has some preference for certain FG-containing peptides. We therefore tested other Nups for the ability to bind to *in vitro*-assembled HIV-1 CA-NC complexes. We found that Nups that contain FG repeats (RanBP2/Nup358, Nup214, Nup153, Nup98, and Nup62) bound to the CA-NC complexes (Fig. 5A and B), whereas non-FG Nups (Tpr and Nup107) did not (Fig. 5A and B). As a control, we tested the ability of rhesus monkey TRIM5$\alpha$ (TRIM5$\alpha_{rh}$) protein to bind to HIV-1 CA-NC complexes; TRIM5$\alpha_{rh}$ is known to bind capsid (57) (Fig. 5B). Binding of the FG-containing Nups was abrogated by the N57S mutation (Fig. 5C), confirming that the same pocket in the capsid protein lattice mediated the interaction.

We also tested the ability of CPSF6 to bind to HIV-1 CA-NC complexes with the N57S mutation. As shown in Fig. 5C, CPSF6 similarly lost the ability to bind the N57S mutant capsid, as we have previously shown (58). These results demonstrate that N57S behaves similarly to N74D in terms of binding to CPSF6 (37, 59). As a control, we confirmed that CPSF6 does not bind HIV-1 capsids with the N74D substitution (Fig. 5C) (37). Unlike the N57S mutant, the N74D capsid mutant did not lose the ability to bind Nup153 (35).

We also tested whether the binding of Nup153-HA to the HIV-1 capsid is affected by the use ofincreasing concentrations of the FG peptide used in our crystallographic studies (Nup153$_{1407–1429}$) (data not shown). These results showed that increasing concentrations of the peptide containing an FG repeat were not sufficient to outcompete the binding offull-length Nup153 to capsid. One possibility is that the avidity effect present in the binding offull-length Nup153 to capsid, which arises from the presence of multiple capsid-binding segments in Nup153, enhances Nup153 affinity for capsid. This avidity effect is not present in the peptide that only contains one binding site for capsid.

We next tested whether HIV-1 viruses with mutations on capsid residue N57 require Nup153 expression for infectivity. To this end, we transiently knocked down expression of Nup153 in HeLa cells and challenged the cells with HIV-1 viruses containing mutations in capsid residue N57. As shown in Fig. 5D, HIV-1-N57S-Luc and HIV-1-N57S/G208R-Luc viruses were able to infect Nup153-depleted cells, suggesting that these viruses are using a different pathway to infect cells. In contrast, wild-type and HIV-1-N74D-Luc viruses were not able to infect Nup153-depleted cells (28, 35, 40). To understand the effect of depleting other Nups on HIV-1 viruses with mutations on capsid residue N57, we depleted the expression of RanBP2/Nup358, Nup214, and Tpr. In the case of RanBP2/Nup358-depleted cells, we found that, unlike wild-type HIV-1, viruses with mutations on capsid residue N57 were not affected in infectivity (Fig. 5D), as previously shown (37, 41). In contrast, depletion of Nup214, Nup62, and Tpr did affect the infectivity of both wild-type and mutant viruses. In agreement with this result, we and others have previously shown that Nup214, Nup62, and Tpr act after the HIV-1 nuclear translocation step (19, 39, 60, 61). In particular, Nup214 has an indirect role on HIV-1 infection, because it is involved in global mRNA export (19). Nup62 interacts with HIV-1 integrase and is involved in the integration step (60), and Tpr organizes the chromatin underneath the NPC; however, strong depletion of Tpr can interfere with the cell cycle step, explaining the defect in infectivity of all tested viruses (39). These experiments suggested that HIV-1 viruses with a capsid change on N57 are using a mode ofinfection independent of Nup153 and RanBP2/Nup358. A caveat for these experiments is the possibility that depletion of one Nup is affecting the expression of other Nups, which has not been extensively tested here.

**HIV-1 viruses with mutations at capsid residue N57 are not subject to the influence of PF-74 and BI-2.** Previous observations suggested that capsid residue N57 interacts with PF74 and BI-2 (42, 43), raising the possibility that HIV-1 viruses mutated at capsid residue N57 are resistant to the small-molecule inhibitors PF74 and BI-2. To

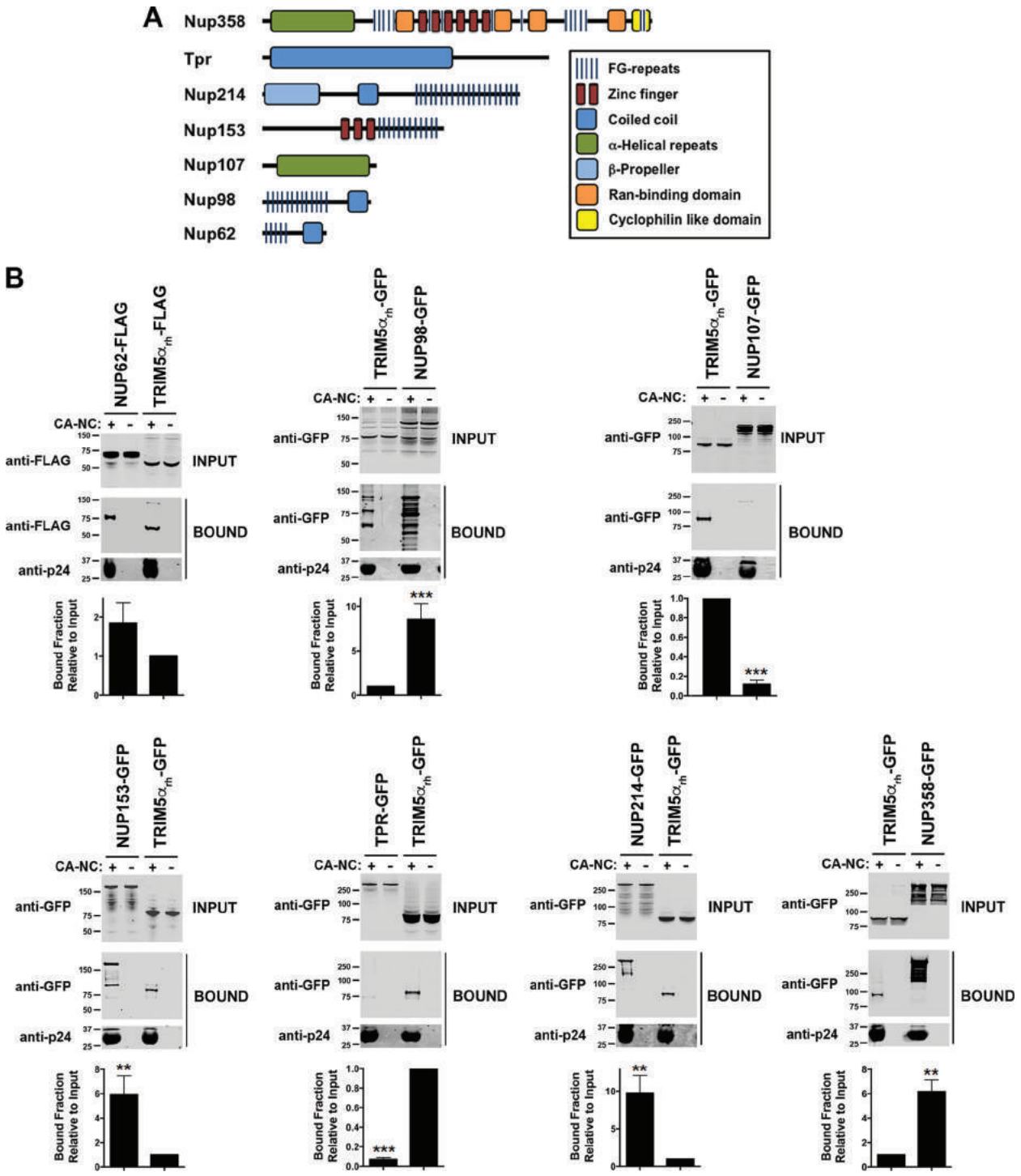


**FIG 5** HIV-1-N57S viruses do not interact with Nups containing FG repeats. (A) Several Nups that do or do not contain FG repeats are shown. (B) Binding of Nups to HIV-1 capsid. The ability of the indicated Nups to bind *in vitro*-assembled HIV-1 CA-NC complexes was measured as described in Materials and Methods. INPUT and BOUND fractions were analyzed by Western blotting using anti-GFP or anti-p24 antibodies. As a positive control, we measured the ability of rhesus TRIM5$\alpha$ (TRIM5$\alpha_{rh}$) to bind *in vitro*-assembled HIV-1 CA-NC complexes. (C) Binding of Nups to HIV-1 capsids bearing the mutation N57S or N74D. Similarly, the ability of the indicated Nups to bind *in vitro*-assembled HIV-1 CA-NC bearing the mutation N57S or N74D was measured. INPUT and BOUND fractions were analyzed by Western blotting using anti-GFP or anti-p24 antibodies. As a control, we measured the ability of CPSF6 to bind *in vitro*-assembled HIV-1 CA-NC complexes bearing the mutation N57S or N74D. Results were analyzed using two-tailed Student's *t* test. Differences were considered statistically significant at a *P* value of $<0.05$ (*), $<0.01$ (**), $<0.001$ (***), or $<0.0001$ (****) or were nonsignificant (ns). (D) HIV-1-N57S virus infection of cells depleted for the expression of different Nups. HeLa cells depleted for the expression of the different Nups were challenged with the indicated HIV-1-Luc viruses. (Upper) Infection was determined by measuring luciferase activity 48 h postinfection. Statistical analysis by one-way analysis of variance was applied (****, $P < 0.0001$). (Lower) Depletion of the indicated Nup was achieved transiently using shRNA, and expression knockdown was confirmed by Western blotting using the indicated antibodies, as described in Materials and Methods. Experiments were repeated at least three times, and a representative experiment is shown.

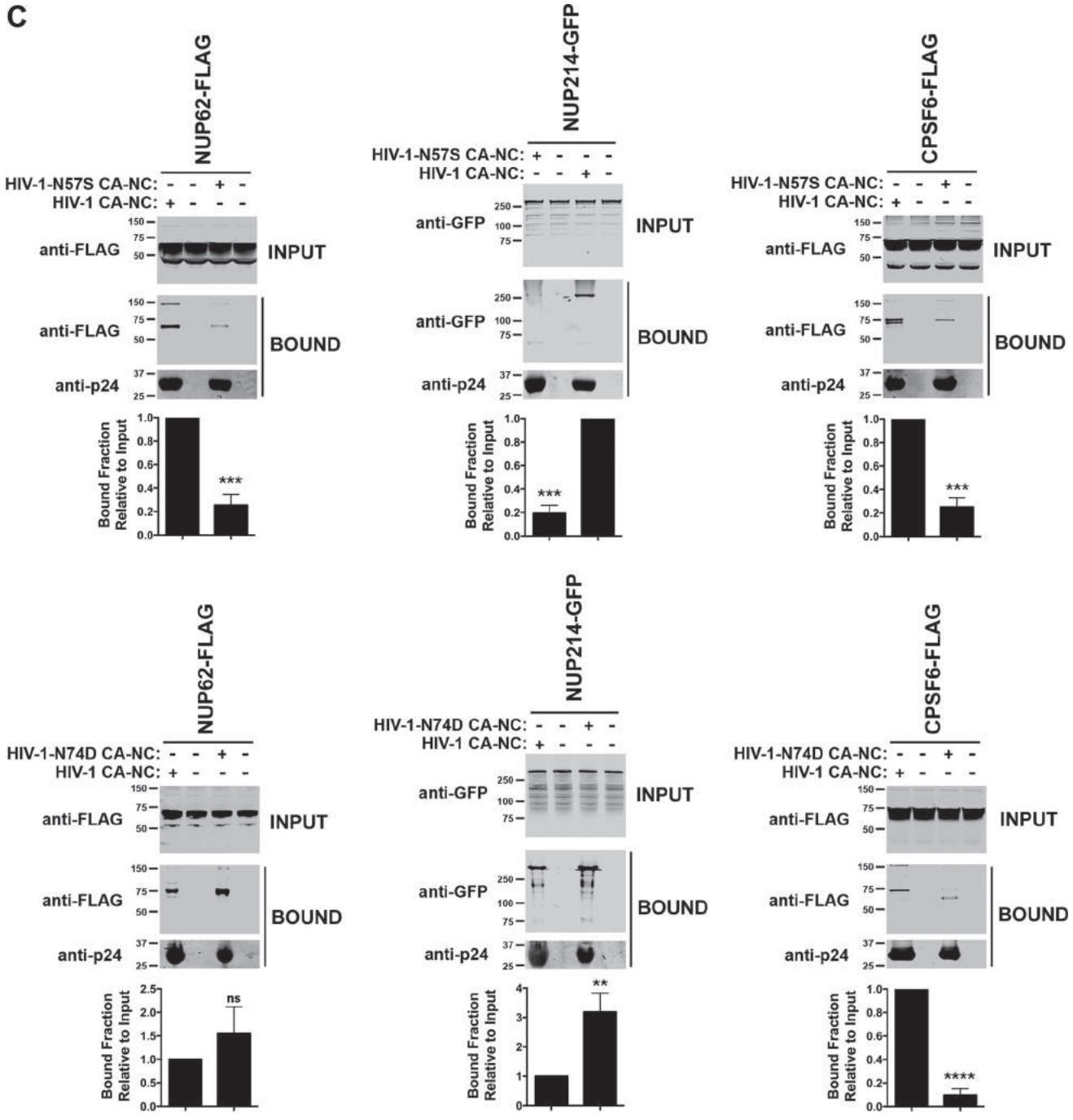


**FIG 5** (Continued)

test this hypothesis, we challenged human HT1080 (Fig. 6A), dog Cf2Th (Fig. 6B), human HeLa (Fig. 6C), and human Jurkat cells (Fig. 6D) with HIV-1 viruses mutated at capsid residue N57 in the presence ofincreasing concentrations of PF74 and BI-2. As shown in Fig. 6, HIV-1-N57S, HIV-1-N57S/G208R, and HIV-1-N57A were unaffected by PF74 and BI-2. We also tested infectivity of HIV-1-N74D in the presence ofincreasing concentrations of PF74. Infection of HIV-1-N74D viruses was inhibited by PF74, similar to the wild type (data not shown). These experiments suggested that PF74 and BI-2 are preventing the ability of HIV-1 capsid to interact with proteins containing FG repeats, such as Nups and CPSF6. To directly test this hypothesis, we measured the ability of FG repeat-containing proteins Nup62, Nup98, Nup153, Nup214, and CPSF6 to interact with HIV-1

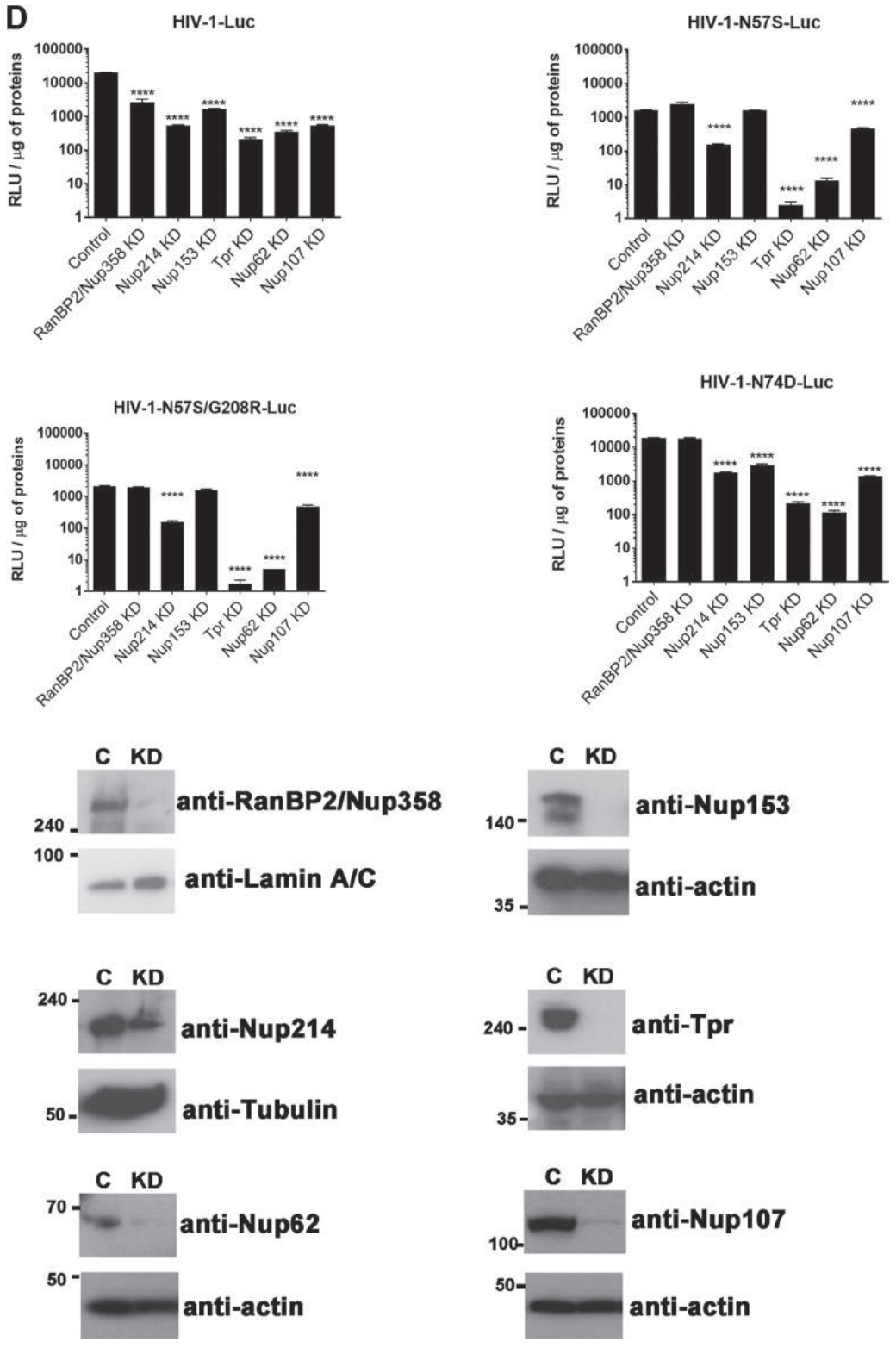


**FIG 5** (Continued)

CA-NC complexes in the presence of PF74 and BI-2. As shown in Fig. 6E, PF74 and BI-2 prevented the ability of these proteins to bind to *in vitro*-assembled HIV-1 CA-NC complexes. To verify that the small molecules PF74 and BI-2 are specifically preventing the binding of Nups that contain FG repeats to capsid, we tested the ability of PF74 and

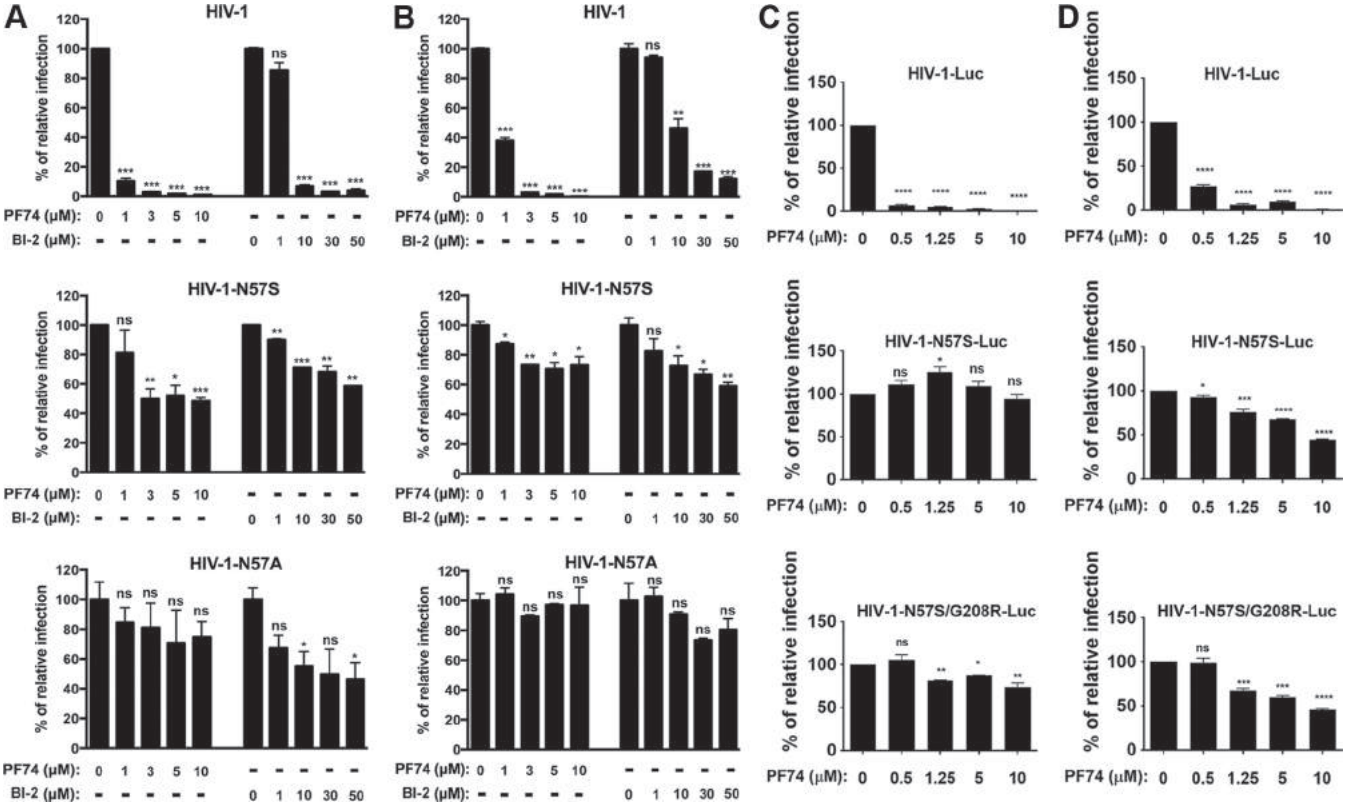


**FIG 6** Small-molecule inhibitors PF74 and BI-2 prevent the binding of Nups containing FG repeats to the HIV-1 capsid. (A) HIV-1 viruses bearing changes on residue N57 are resistant to the inhibitory effects of PF74 and BI-2. Human HT1080 cells were challenged with the indicated HIV-1-GFP viruses in the presence ofincreasing concentrations of PF74 or BI-2. Infection was determined by measuring the percentage of GFP-positive cells 48 h postinfection. The percentage ofinfection relative to that of untreated samples is shown. Similar experiments were performed using human HeLa (B), dog Cf2Th (C), and human Jurkat (D) as target cells. (E) Binding of Nups to HIV-1 capsid is inhibited by PF74 and BI-2. The ability of the indicated Nups to bind *in vitro*-assembled HIV-1 CA-NC complexes in the presence of PF74 or BI-2 was measured as described in Materials and Methods. As a specificity control, we tested the ability of TRIMCyp to bind *in vitro*-assembled HIV-1 CA-NC complexes in the presence of PF74, BI-2, or cyclosporine (CsA). INPUT and BOUND fractions were analyzed by Western blotting using anti-GFP, anti-FLAG, or anti-p24 antibodies. As a positive control, we measured the ability of CPSF6 to bind *in vitro*-assembled HIV-1 CA-NC complexes in the presence of PF74 or BI-2. Results were analyzed using two-tailed Student's *t* test. Differences were considered statistically significant at a *P* value of $<0.05$ (*), $<0.01$ (**), $<0.001$ (***), or $<0.0001$ (****) or were nonsignificant (ns).

BI-2 to affect the ability of TRIMCyp to bind capsid. As shown in Fig. 6E, the ability of TRIMCyp to bind capsid was affected by cyclosporine (CsA) (62) but not by PF74 or BI-2. These experiments suggested that PF74 and BI-2 affected the ability of capsid residue N57 to interact with various cellular factors, which might more fully explain how these drugs inhibit HIV-1.

**HIV-1 viruses with capsid mutation N57S showed different integration site preferences.** Wild-type HIV-1 integration is favored in chromosomal regions containing high gene density and high transcriptional activity (63). Previously, we showed that depletion of Nup153 or Tpr reduces HIV-1 integration frequency in high-gene-density regions, establishing a link between HIV-1 translocation and integration (35, 39). To investigate the contribution of capsid-Nup153 interactions to HIV-1 integration, we investigated the proviral integration pattern of HIV-1 viruses bearing the change N57S on Jurkat T cells by next-generation sequencing (NGS). As a control, we studied integration of HIV-1 viruses bearing the change N74D. Infection of Jurkat cells by HIV-1-N57S supported levels of reverse transcription similar to those of wild-type HIV-1 (Fig. 7A). We also observed a decrease ofluciferase expression exclusively for the virus carrying the mutation N57S, consistent with the number of proviruses integrated as assessed by Alu-PCR (Fig. 7A). Our results revealed that the integration pattern of HIV-1 N57S mutant is very similar to that of HIV-1 N74D (Fig. 7B and Tables 3 and 4). HIV-1-N57S viruses showed a decreased ability to integrate in intragenic regions compared to that of wild-type HIV-1 (Fig. 7B and Table 4). We detected fewer HIV-1-N74D-Luc (57.2%) and HIV-1-N57S-Luc (59.8%) integrations in intra-

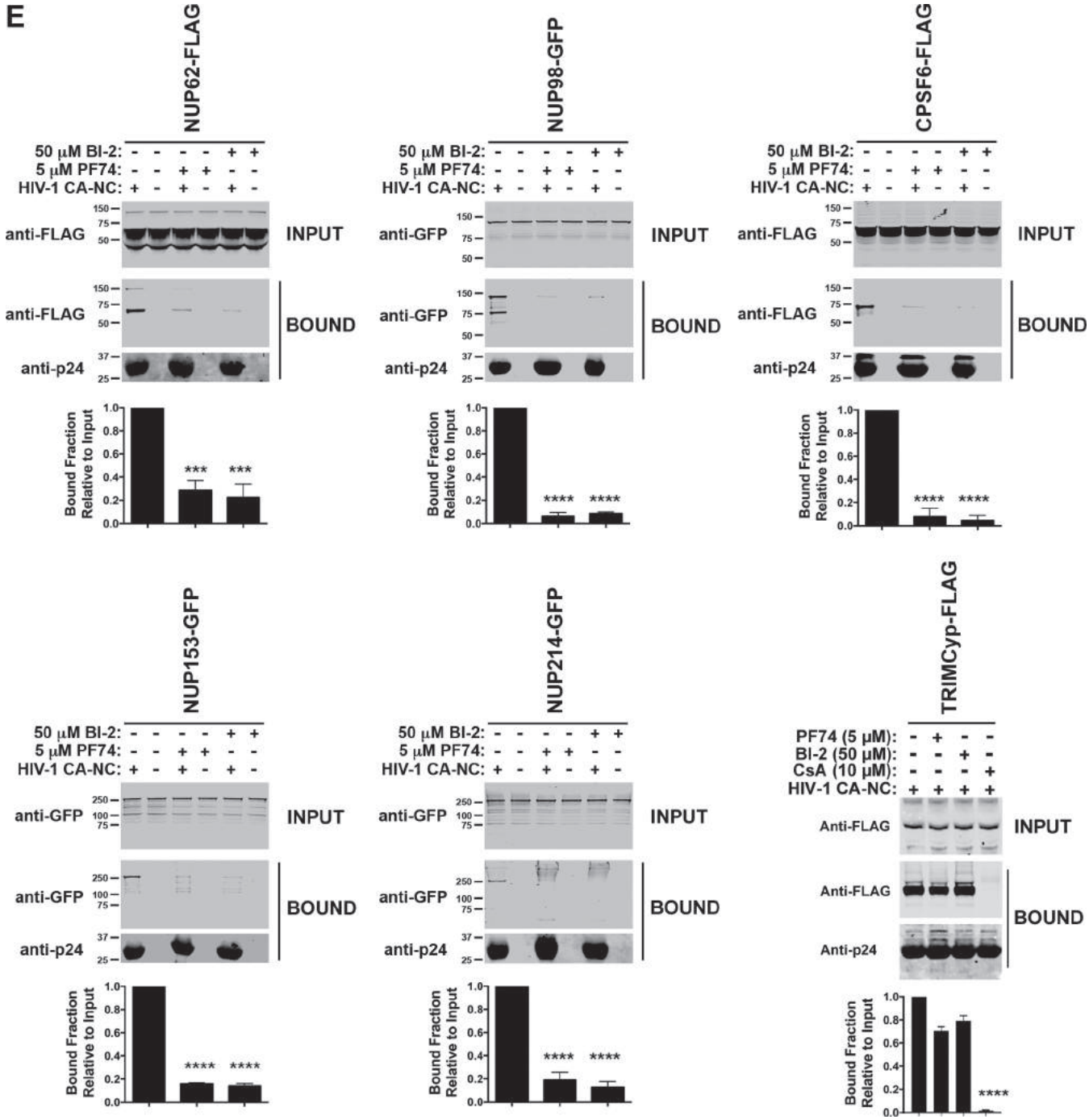


**FIG 6** (Continued)

genic regions, mapping inside exons or introns of known genes, than wild-type integrations (69.2%) (Fig. 7B and Table 4). Instead, we detected an increase ofintegration sites in intergenic regions, upstream or downstream of known genes, for N57S (38%) and N74D (40.9%) mutants compared to those for the wild type (27.5%) (Fig. 7B and Table 4). Consistent with gene-targeting preferences into gene-dense regions, integrations at distances of ≥100 kb from transcription start sites (TSSs) were highly disfavored for wild-type virus, while N57S and N74D mutant viruses were more similar or exceed the matched random control (MRC) (Fig. 7C and Table 4). All of the differences observed among samples were statistically significant (*P* value of <0.001 by Wilcoxon rank-sum statistical and

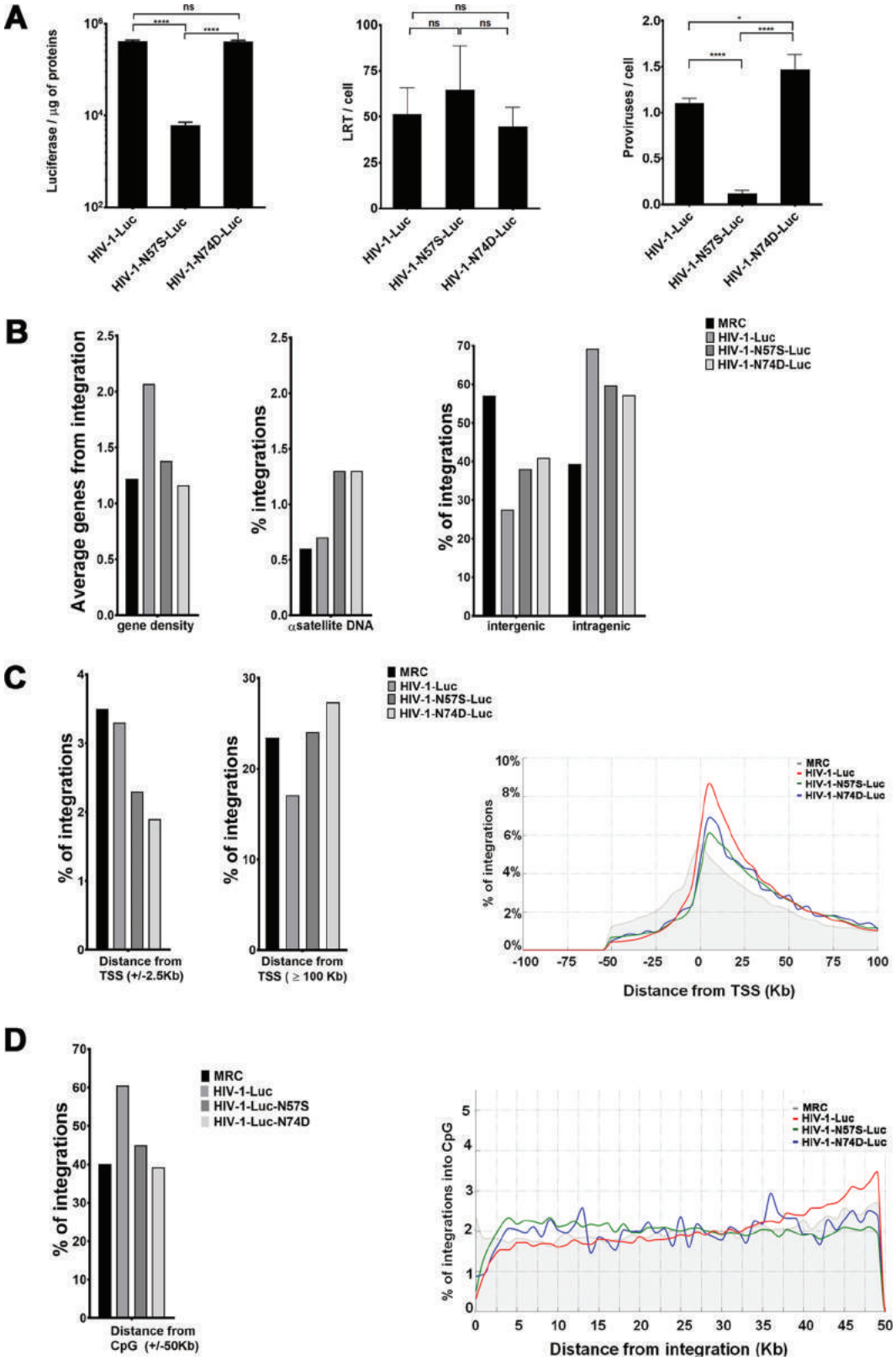


**FIG 7** HIV-1 infection and integration site distribution. Shown is integration site distribution for wild-type and N57S and N74D HIV capsid mutant viruses: intergenic, intragenic, gene density, and alpha satellite. (A) Jurkat cells were challenged with the indicated HIV-1-Luc viruses. (Left) Infectivity was determined by measuring luciferase reporter activity at 48 hpi. (Middle) Late reverse transcription (LRT) was measured by quantitative PCR at 7 hpi as described in Materials and Methods. (Right) The number of proviruses integrated to the genome per cell (proviruses/cell) was determined using Alu-PCR. Asterisks indicate

(Continued on next page)

**TABLE 3** Integration of HIV-1 viruses[a]

| Parameter | WT | | N57S | | N74D | |
|---|---|---|---|---|---|---|
| | No. | % lost | No. | % lost | No. | % lost |
| Initial filtered reads[b] | 1,288,748 | | 1,655,553 | | 1,517,568 | |
| Reads matching on human genome[c] | 1,014,432 | 21.3 | 1,237,632 | 25.2 | 1,222,659 | 19.4 |
| Quality filtered reads[d] | 771,358 | 24.0 | 912,662 | 26.3 | 931,713 | 23.8 |
| HIV Nef matches[e] | 323,998 | 58.0 | 71,815 | 92.1 | 395,932 | 57.5 |
| Reads with unique mapping[f] | 310,619 | 4.1 | 69,787 | 2.8 | 383,341 | 3.2 |
| Genomic integrations[g] | 105,329 | 66.1 | 6,137 | 91.2 | 116,138 | 69.7 |

[a]Number or percent lost indicates the number ofintegrations conserved or lost after the mapping steps.
[b]Raw reads from HIV-1 integration sites library.
[c]Filtered reads of HIV-1 integration sites were mapped against the UCSC hg19 release of the human genome.
[d]Filtered reads of HIV-1 integration sites were mapped against the UCSC hg19 release of the human genome and processed for their quality.
[e]Filtered reads of HIV-1 integration sites were mapped against the UCSC hg19 release of the human genome, processed for their quality, and matched with HIV Nef sequence.
[f]Reads obtained after unique mapping.
[g]The number of reads and percentage of HIV-1 integration sites is indicated for every HIV-1 variant.

proportions test). Indeed, the majority ofintegrations of wild-type HIV-1 occurred ~2.5 to 50 kb downstream from TSSs (Fig. 7C and Table 4). Integration of capsid mutant viruses occurred less frequently at and near TSSs than for wild-type virus. In contrast, integrations of wild-type and mutant viruses were similarly disfavored ~50 kb downstream from TSSs (Fig. 7C and Table 4). HIV-1-N57S and -N74D mutant viruses favor integration within transcription units; however, their integration site distributions statistically diverged from that of wild-type virus. Interestingly, we observed that these two mutants, N57S and N74D, integrated in chromatin regions with lower gene density as well as in CpG islands, which are chromatin features associated with promoters (Fig. 7D and Table 4). The differences observed among the three viruses in the percent distribution ofintegrations in host chromatin regions and chromatin features all were statistically significant. The distribution of all integration sites as a function of gene density for the three viruses was studied. Interestingly, the capsid mutations studied here reduced the ability of HIV-1 to target gene-dense regions in the host chromatin (data not shown).

The average gene density within a ±50-kb window surrounding integration sites was 2.07 transcription units for wild-type virus, 1.38 transcription units for N57S, and 1.16 transcription units for N74D (Table 4). The two capsid mutants showed an integration curve profile shifted to the left with respect to wild-type virus, consistent with a lower preference for integration into regions containing higher gene density. Wild-type HIV-1 preferentially targeted the midsections of genes roughly encompassing 15 to 60% of the genes' lengths. N74D and N57S capsid mutant viruses showed a less marked preference for integration into the midsection of genes compared to that of the wild type while showing an increase in the targeting of 3=gene regions (data not shown). The curve of the N74D capsid mutant more closely resembles that of the MRC than that of the N57S mutant (Fig. 7D). Interestingly, N74D and N57S mutant viruses showed reduced integration near CpG islands compared to wild-type HIV-1 (Fig. 7D and Table 4). We also observed a decreased integration of the mutant viruses into DNase I-hypersensitive sites (DHSs), which are characteristic features of active chromatin (Table 4). Finally, we also analyzed proviral integration into chromatin regions that are

**FIG 7** Legend (Continued)
statistical significance in comparisons of one virus to another virus (determined by paired two-tailed Student's *t* tests; ns, nonsignificant; *, $P < 0.05$; ****, $P < 0.0001$). (B, left) Histograms representing the average gene density. (Middle) Percentage ofintegrations having an $\alpha$-satellite region within an interval of 50 kb. (Right) Percentage ofintegrations classified as inter- or intragenic; intragenic integrations are those localized within 50 kb of a gene. (C, left) Percentage ofintegrations having a TSS within a 2.5-kb window. (Middle) Histogram recapitulating the percentage ofintegration sites at a distance of ≥100 kb from the TSS. (Right) Plots of the percentage ofintegrations grouped by distance from TSS in a 100-kb window; the matched random control (MRC) is represented in gray. (D, left) Percentage ofintegrations falling within a 50-kb window from any CpG island. (Right) Plot representing the percentage ofintegrations grouped by their distance from any CpG in a 0- to 50-kb range.

**TABLE 4** Effect of capsid mutations on HIV-1 integration sites in Jurkat cells

| Genomic feature | Value[a] (%) for: | | | |
|---|---|---|---|---|
| | MRC[b] | WT | N57S | N74D |
| Intergenic (±50 kb) | 57.1 | 27.5 | 38.0 | 40.9 |
| Intragenic (±50 kb) | 39.4 | 69.2 | 59.8 | 57.2 |
| TSS (±2.5 kb) | 3.5 | 3.3 | 2.3 | 1.9 |
| CpG islands (±50 kb) | 40.2 | 60.5 | 45.0 | 39.2 |
| DNase I HS (±50 kb) | 83.7 | 96.2 | 91.5 | 90.7 |
| $\alpha$-Satellite (±50 kb) | 0.6 | 0.7 | 1.3 | 1.3 |
| $\beta$-Satellite (±50 kb) | 0.2 | 0.2 | 0.2 | 0.2 |
| Avg no. of genes in ±50 kb | 1.22 | 2.07 | 1.38 | 1.16 |

[a]Values are shown relative to the number of unique integration sites per genomic feature, except those for gene-dense regions. Integration of wild-type and mutant HIV-1 viruses in different regions of chromatin from Jurkat T cells is shown as a percentage of total integration: intragenic, intergenic, transcriptional start sites (TSS), CpG, alpha and beta satellites, and DNase I-hypersensitive regions. The predicted integration for an MRC is shown. Pearson's chi-squared test was used ($P < 2.2e{-}16$).

[b]MRC, matched random control containing coordinates for 14 million computer-generated integration sites in the vicinity of BfaI and BglII restriction sites in hg19.

usually excluded, such as alpha- and beta-satellites, which are enriched in heterochromatin. Both mutants integrated to a greater extent than the wild-type virus into alpha-satellite regions (Fig. 7B and Table 4). In contrast, integration of these mutant viruses was disfavored in beta-satellite regions (Table 4).

In parallel, we have also performed a nucleosome density analysis around viral integration sites, and we found an increase of the preference for nucleosome-dense regions for all three viruses with respect to MRC (Fig. 8A).

To identify the relationship between viral integration sites and histone modifications, we also analyzed the coverage profile for different histone modifications in a window of ±50 kb around the integration sites for each virus (WT, N57S, N74D, and MRC) (Fig. 8B). We observed that HIV-1 WT provirus accumulation was positively correlated with histone methylation patterns characteristic of active transcription units, such as H3K4me1, H4K20me1, and H3K36me3, as has been previously reported (64). In addition, we found a few histone modifications that show clear differences between wild-type and mutant viruses.

H3K4me3, which is a mark of regulatory regions usually excluded around HIV-1 integration sites, showed a pick enrichment around integration sites for both mutant viruses (N57S and N74D) (39, 64), while we observed a reduction for this histone modification density near the integration sites of the WT virus (± 2.5 kb from integration site). This result suggests a relocation of HIV-1 integrations due the viral capsid mutation.

Interestingly, all three viruses showed a peak of H3K36me3 enrichment around integration sites (Fig. 8B). This phenomenon could be due to the fact that all of these viruses interact with LEDGF/p75, which binds this particular histone modification, helping the virus to integrate in selected sites of the host chromatin (39, 65). The persistent tendency of the tested viruses to integrate into open chromatin probably is due not only to the role of LEDGF/p75 (Table 4) but also to the intrinsic preference of HIV-1 IN for open chromatin structures, as previously reported (66, 67).

## DISCUSSION

Nups hold a critical role in HIV-1 nuclear import and integration. Although Nup153 and RanBP2/Nup358 are known to be required for HIV-1 nuclear translocation, the experiments that previously established this requirement were only performed in cycling cells (19, 34, 35, 37, 40). Therefore, the factors required for nuclear translocation in nondividing cells remain unknown. In addition, the study of HIV-1 nuclear translocation typically has been performed in cells that are depleted for Nup153 and RanBP2/Nup358 expression (28, 32, 33), which could disrupt the architectural integrity of nuclear pores or affect expression of other Nups. Moreover, interference with the structural components of nuclear pores could lead to erroneous interpretation of HIV-1 phenotypes. Use of HIV-1 with capsid mutations has the advantage that it does not

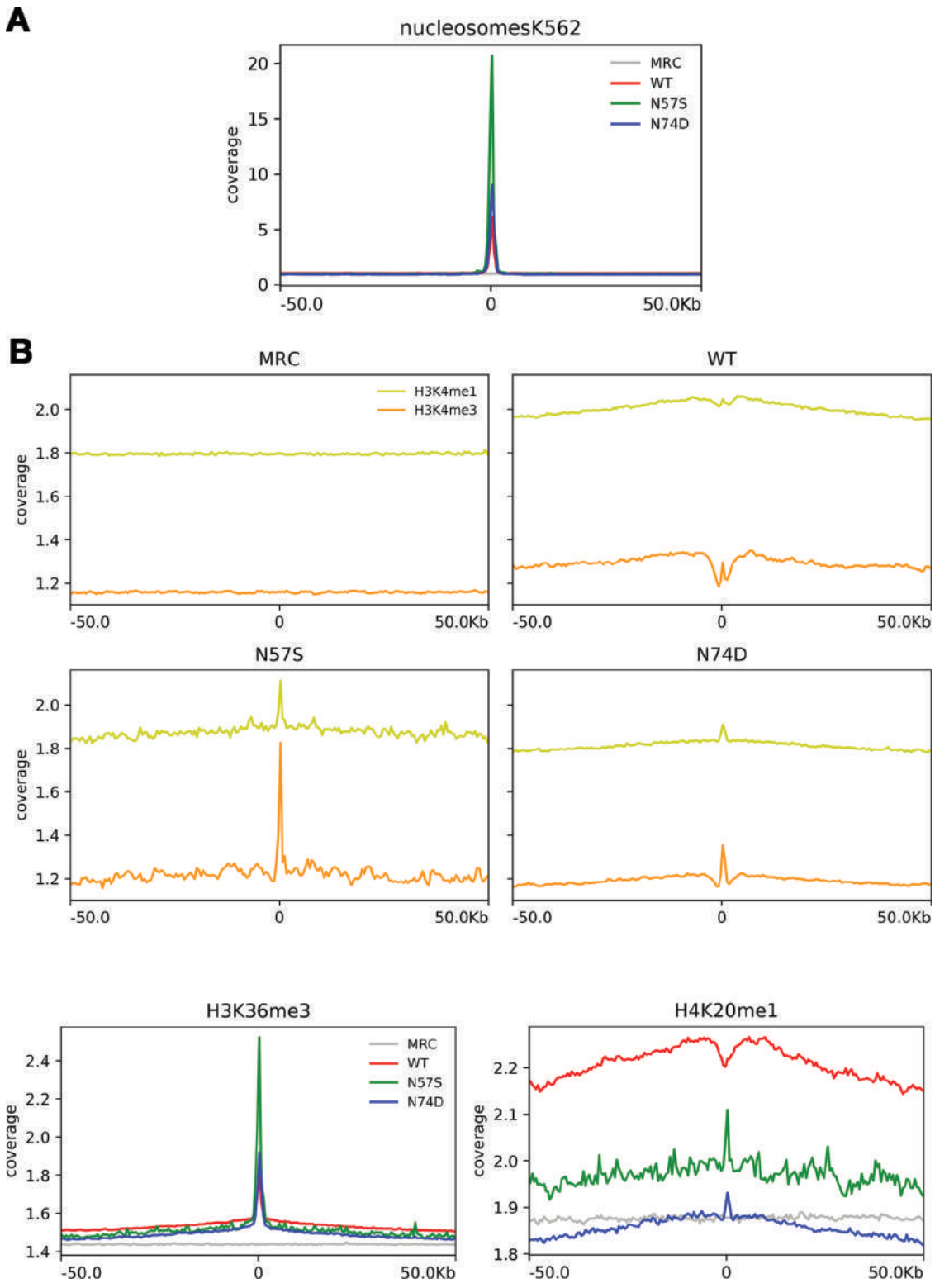


**FIG 8** Analysis of nucleosome density around viral integration sites and the relationship between integration frequency and epigenetic mark density. (A) The plot shows the mean normalized coverage in 100-kb windows around the viral integration sites of each virus (WT, N57S, and N74D), as well as of matched random controls (MRC) for nucleosome density feature (data available for K562 cells in the UCSC database). (B) The plots show the mean normalized coverage for different histone modifications (derived from ChIP-seq data) in 100-kb windows around the viral integration sites of each virus (WT, N57S, and N74D) as well as of matched random controls (MRC). The plots show curve coverage signal for H3K4me1, H3K4me3, H3K36me3, and H4K20me1. Coverage was normalized to the number of tags.

disrupt the integrity of nuclear pores. Accordingly, we chose HIV-1 capsid mutants to understand the cellular factors involved in lentiviral nuclear translocation in nondividing cells. For this purpose, we solved the structure of the peptide containing the FG repeat of Nup153 ($Nup153_{1407–1429}$) in complex with the hexameric HIV-1 capsid. Our crystal structure was consistent with previous findings on the interaction of capsid with an FG repeat (43) and highlighted several capsid residues that interact with the FG repeat. We then mutated these residues and screened for mutant viruses that could infect dividing but not nondividing cells. Our results revealed that HIV-1 with capsid mutations N57S, N57A, or N57D can infect dividing cells but are abrogated in their ability to infect nondividing cells. Using the fate-of-the-capsid assay, we demonstrated that mutations on N57 residue decreased the stability of the HIV-1 core during infection. Because core stability during infection might be the reason that N57-mutated HIV-1 viruses cannot infect nondividing cells, we improved core stability by simultaneously introducing the capsid mutations N57S/G208R. We then showed that even though HIV-1-N57S/G208R cores were more stable than HIV-1-N57S cores, these mutants were still unable to infect nondividing cells. Therefore, the inability of HIV-1-N57S to infect nondividing cells cannot be attributed to defects in core stability.

We next examined the viral replication stage at which the infection by HIV-1-N57S and HIV-1-N57S/G208R viruses was inhibited. Interestingly, these viruses underwent reverse transcription but did not generate 2-LTR circles, suggesting a defect in nuclear translocation. This is in agreement with the hypothesis that these mutant viruses are unable to enter the nucleus. One possibility is that the core is no longer interacting with an important Nup needed for HIV-1 infection of nondividing cells. This concept is consistent with our finding that the N57 residue directly interacts with the FG repeats of Nup153. By the same token, this observation raises the possibility that the N57 region of the HIV-1 capsid is important for the ability of the core to generally interact with Nups containing FG repeats.

Depletion of Nup153 or RanBP2/Nup358 expression in human cells prevents HIV-1 nuclear translocation, suggesting a role for these proteins in nuclear entry. We therefore tested the ability of HIV-1 capsid containing N57 mutations to bind to the Nups Nup153 and RanBP2/Nup358, which contain FG repeats and are essential for HIV-1 nuclear translocation in cycling cells. Capsids with N57 mutations lost the ability to bind Nup153 but not RanBP2/Nup358, suggesting that Nup153 is directly involved in HIV-1 nuclear translocation in nondividing cells. Although N57 mutant capsids did not bind any of the tested Nups containing FG repeats, the only functional interactions related to nuclear translocation are capsid-Nup153 and capsid-RanBP2/Nup358, indicating that interaction of capsid with Nup153 plays an important role in HIV-1 nuclear translocation in nondividing cells. One possibility is that the HIV-1 core or preintegration complex interacts with Nup153 in the cytosol, and that it is this interaction that is essential for guiding the complex into the nuclear pore. This is in agreement with evidence suggesting that Nup153 shuttles between the nucleus and cytoplasm (68).

Structural studies revealed that N57 is also used by the HIV-1 capsid to interact with the drugs PF74 and BI-2, suggesting that these inhibitors disrupt the ability of capsid to interact with Nups containing FG repeats. In agreement with this hypothesis, we found that PF74 and BI-2 prevent capsid binding to Nups with FG repeats. One possibility is that PF74 and BI-2 can block HIV-1 infection by preventing the interaction of capsid with FG-containing Nups such as Nup153. This notion is in agreement with independent reports suggesting that PF74 and BI-2 block HIV-1 infection at a step prior to nuclear translocation (69, 70).

Lentiviruses such as HIV-1 have the ability to infect both dividing and nondividing cells. HIV-1 infection of nondividing cells requires the HIV-1 preintegration complexes to cross the nuclear pore. In contrast, infection of dividing cells provides easier access to the cellular genome, where transport across the nucleopore is not required. Gammaretroviruses such as MLV are unable to infect nondividing cells and require mitosis for efficient infection (3). Similarly, mitosis provides gammaretroviruses easier access to the cellular genome. These observations raise the possibility that lentiviruses and gammaretroviruses encounter cellu-

lar chromatin in various transcriptional states, resulting in different integration patterns, as previously observed for HIV-1 and MLV (63). Although the chromatin topology is likely to play a role in retroviral integration, several recently described cellular factors have been reported to modulate site selection of retroviral integration: (i) LEDGF/p75 and HRP-2 are important for site selection of HIV-1 integration (71–80), (ii) CPSF6 directs HIV-1 integration into transcriptionally active chromatin (45, 81), and (iii) the BET family of proteins targets murine leukemia virus integration into transcription start sites (82). Taken together, this evidence suggests that integration site selection is a multiparameter mechanism that involves nuclear factors and the state of the chromatin. Unlike HIV-1, which favors integration into transcriptionally active chromatin, MLV favors integration into transcription start sites (63, 81). We have shown that HIV-1 viruses with the N57S capsid mutation integrate differently than wild-type HIV-1. We found that expression ofintegrated proviruses derived from N57S viruses is decreased by ~6-fold compared to that of the WT. This observation is in agreement with our results, suggesting that integration of N57S occurs in regions of the chromatin other than those of the wild type. Our results showed that N57S viruses integrate in regions with low gene density. The integration of N57S viruses in different regions of the chromatin explains the decrease in proviral expression.

We observed that the integration pattern of HIV-1-N57S is very similar to that of HIV-1-N74D, which is similar to the HIV-1 integration pattern of HIV-1 in CPSF6 knockout cells (45, 83). This is in agreement with our data showing that N57 mutant capsids do not interact with CPSF6. Thus, the integration pattern observed for N57S is likely due to loss ofits ability to interact with CPSF6. Unlike HIV-1-N57S viruses, HIV-1-N74D does not show a defect in ability to infect nondividing cells, which is likely to be due to the fact that the N74D-mutant capsid interacts with Nup153 (35). This combined evidence allowed the following conclusions regarding early steps of HIV-1 infection: (i) the interaction of capsid with CPSF6 is required for achieving normal patterns of HIV-1 integration, since the loss of capsid interaction with CPSF6 by N74D or N57S results in an integration pattern similar to the one produced by HIV-1 viruses in CPSF6 knockout cells (45), and (ii) the interaction of capsid with Nup153 is important solely for the ability of HIV-1 to infect nondividing cells.

## MATERIALS AND METHODS

Wild-type and mutant HIV-1 CA-NC expression and purification. HIV-1 CA-NC protein was expressed, purified, and assembled as previously described (46). The pET11a expression vector (Novagen) expressing the CA-NC protein of HIV-1 was used to transform BL-21(DE3) *Escherichia coli*. CA-NC expression was induced with 1 mM isopropyl-$\beta$-D-thiogalactopyranoside (IPTG) when the culture reached an optical density of 0.6 at 600 nm. After 4 h of induction, the cells were harvested and resuspended in 20 mM Tris-HCl (pH 7.5), 1 $\mu$M $ZnCl_2$, 10 mM 2-mercaptoethanol, and protease inhibitors (Roche). Lysis was performed by sonication, and debris was pelleted (35,000 $\times$ *g*, 30 min). Nucleic acids were stripped from the solution by adding 0.11 equivalents of 2 M $(NH_4)_2SO_4$ and the same volume of 10% polyethylenimine. Nucleic acids were removed by stirring and centrifugation (29,500 $\times$ *g*, 15 min). The protein was recovered by addition of 0.35 equivalents of saturated $(NH_4)_2SO_4$. The protein was centrifuged at (9,820 $\times$ *g*, 15 min) and resuspended in 100 mM NaCl, 20 mM Tris-HCl (pH 7.5), 1 $\mu$M $ZnCl_2$, and 10 mM 2-mercaptoethanol. Lastly, the CA-NC protein was dialyzed against 50 mM NaCl, 20 mM Tris-HCl (pH 7.5), 1 $\mu$M $ZnCl_2$, and 10 mM 2-mercaptoethanol and stored at −80°C.

***In vitro* assembly of HIV-1 CA-NC complexes.** HIV-1 CA-NC particles were assembled *in vitro* by diluting the CA-NC protein to a concentration of 0.3 mM in 50 mM Tris-HCl (pH 8.0), 0.5 M NaCl, and 2 mg/ml DNA oligo$(TG)_{50}$. The mixture was incubated at 4°C overnight and centrifuged at 8,600 $\times$ *g* for 5 min. The pellet was resuspended in assembly buffer (50 mM Tris-HCl [pH 8.0], 0.5 M NaCl) at a final protein concentration of 0.15 mM (46, 47) and stored at 4°C until needed.

**Binding to HIV-1 capsid complexes.** 293T cells were transfected with plasmids expressing the different Nups fused to GFP or the indicated proteins. Forty-eight hours after transfection, cell lysates were prepared by resuspending washed cells in capsid-binding buffer (10 mM Tris, pH 7.4, 1.5 mM $MgCl_2$, 10 mM KCl, 0.5 mM dithiothreitol [DTT]). The cell suspension was frozen, thawed, and incubated on ice for 10 min. The lysate next was centrifuged in a refrigerated Eppendorf microcentrifuge (~14,000 $\times$ *g*, 5 min). The supernatant was supplemented with 1/10 volume of 10$\times$ phosphate-buffered saline (PBS) and then used in the binding assay. To test binding, 5 $\mu$l of CA-NC particles preassembled *in vitro* was incubated with 200 $\mu$l of cell lysate at room temperature for 1 h. A portion of this mixture, here referred to as INPUT, was stored. The mixture was spun through a 70% sucrose cushion (70% sucrose, 1$\times$ PBS, and 0.5 mM DTT) at 100,000 $\times$ *g* in an SW55 rotor (Beckman) for 1 h at 4°C. After centrifugation, the supernatant was carefully removed and the pellet resuspended in 1$\times$ SDS-PAGE loading buffer and here

is referred to as BOUND. The level of protein was determined by Western blotting using the appropriate antibody. The level of HIV-1 CA-NC protein in the pellet was assessed by Western blotting with an anti-p24 capsid antibody.

**Luciferase assays.** Luciferase (Promega) activity was measured at 48 hpi, according to the manufacturer's instructions, using a microplate fluorimeter (Victor, PerkinElmer). Protein quantification by Bio-Rad protein assay was carried out on the same lysates to normalize the luciferase data for protein content.

**Lentiviral vector carrying shRNA and HIV-1 infection.** Complementary oligonucleotides coding for a short hairpin RNA (shRNA) cassette against Nup153, Tpr, Nup358/RanBP2, and Nup214 have been previously cloned in the HIV-1-derived vector (LV-shRNA) TRIP-GFP, which is ΔU3. Vector cloning and LV production were performed as recently described (35). Titers of LV-shRNAs carrying GFP were determined in HeLa cells using flow cytometry to assess GFP expression at 3 days postinfection. Capsid N74D, N57S, and N57S/G208R mutations were introduced into pNL4.3 Luc ENV$^-$ by site-directed mutagenesis. HeLa and Jurkat cells were transduced with LV-shRNA against Nups at different multiplicities ofinfection of up to 100 to generate knockdown cells. Single-cycle HIV-1 viruses were produced by transient transfection of 293T cells using calcium phosphate coprecipitation with NL4.3 Luc ENV$^-$, with or without the capsid mutation N74D, N57S, or N57S/G208R (luciferase gene in place of *nef*) and cotransfection with the vesicular stomatitis virus glycoprotein (VSV-G) envelope expression plasmid pHCMV-G (VSV-G). The viruses harvested from 293T cells 48 h posttransfection were treated with 25 U/ml of DNase I (Roche) and with 100 mM $MgCl_2$ at 37°C for 30 min. Virus normalizations were performed by p24 enzyme-linked immunosorbent assay (ELISA) according to the manufacturer's instructions (PerkinElmer).

**Quantitative PCR.** Infectivity, DNA synthesis, and integration during acute HIV-1 infection were quantified by real-time PCR. We analyzed for (i) infectivity by luciferase expression (the luciferase gene is a reporter gene inserted in place of *nef* in the HIV genome), (ii) late reverse transcription (LRT) products representing all near-full-length HIV-1 DNA in the cell, and (iii) integration of proviruses into human genome. Viruses were treated for 30 min at 37°C with 1,000 U of DNase I (Roche), with 10 $\mu$M nevirapine used in infected cells as a control. Total cellular DNA was isolated using the QIAamp DNA micro kit (Qiagen) at 7 and 24 hpi. Viral DNA synthesis products at 7 hpi were measured by real-time PCR using Sybr green and luciferase-specific primers (5=GAATCCATCTTGCT CCAACAC and 5=TTCGTCCACAAACACAACTC) located exclusively in the HIV-1-Luc but not in the LV shRNA used to generate Nup knockdown (KD) or control cells. Two long terminal repeat (2-LTR)-containing circles were detected using primers MH535/536 and probe MH603 (48) and for the standard curve the pUC2LTR plasmid, which contains the HIV-1 2-LTR junction. Integration was assessed by Alu-PCR as previously described (35).

**Crystallography.** Soluble hexamers were mixed with excess peptides (2- to 5-fold) and then crystallized with tacsimate and polyethylene glycol as precipitants. Binding was determined by molecular replacement phasing with the original hexameric capsid structure followed by examination of electron density maps for the presence of bound peptide. Several FG-containing peptides derived from NUP153 were tested, but only the previously characterized high-affinity peptide ($_{1407}$TNNSPSGVFTFGANSSTPAA SAQ$_{1429}$) was observed within the crystals. We refined structures containing fluorescein-tagged peptide and also analyzed crystals containing unlabeled peptide. Synchrotron diffraction data were collected at beamline 23-ID-D at the Advanced Light Source and processed with HKL2000. Surprisingly, two crystal forms (R3 and P1) were obtained with the fluorescently labeled peptide, which grew in separate drops but under similar conditions. Crystal packing and peptide occupancies in both crystals were distinct from previously described structures. Molecular replacement phasing, model building, refinement, and model validation were performed using the tools in Phenix. Structure statistics are summarized in Table 2.

**GST-NUP-FG purification and pulldowns.** DNA encoding residues 896 to 1475 of human NUP153 was subcloned into the NdeI and BamHI sites of a modified pGEX2T vector, a kind gift of W. I. Sundquist. The fusion protein was expressed in *Escherichia coli* DH5$\alpha$ cells by isopropyl-$\beta$-D-thiogalactopyranoside (IPTG) induction. Cells were lysed in buffer (25 mM Tris, pH 7.5, 200 mM NaCl, 10 mM $\beta$-mercaptoethanol, 1 mM EDTA) by lysozyme treatment and sonication. GST-NUP-FG was then bound to glutathione-Sepharose resin and eluted in buffer containing 20 mM reduced glutathione. For pulldown experiments, purified GST-NUP-FG (1.8 mg/ml) was preincubated with 25 $\mu$l of beads for 30 min at 4°C. The beads were washed with binding buffer (50 mM Tris, pH 8, 150 mM NaCl, 1 mM EDTA) and then resuspended in binding buffer containing 1% (wt/vol) bovine serum albumin (BSA). Capsid hexamers were then added and incubated for 1 h at 4°C. After extensive washing with binding buffer, bound fractions were eluted and analyzed by SDS-PAGE.

**Integration site sequencing and bioinformatics analysis.** Integration site sequencing was performed using $2 \times 10^8$ Jurkat cells infected with 10 $\mu$g of the p24 antigen of NL4.3-Luc ENV-carrying wild-type or mutant viruses. Two days later, genomic DNA was extracted by using a QIAamp DNA micro kit (Qiagen) and digested with the 4-cutter enzymes BfaI and BglII to prevent amplification ofinternal 3=LTR fragments, as previously described (35). 5=LTR-genome junctions were amplified by ligation-mediated PCR using primers specific for the linker and the HIV 5=LTR and including overhang adapter sequences compatible with the Illumina sequencing platform. A final indexing PCR (eight cycles) was performed to tag each sample with specific Nextera XT dual barcodes (Illumina, San Diego, CA, USA) before sample pooling and sequencing on a single-read 150-cycle run on the MiSeq platform (Illumina).

Raw reads were filtered and trimmed by a properly developed bioinformatics pipeline to remove HIV LTR proviral and linker sequences from the sequencing data. The mapping procedure was based on that described in Cattoglio et al. (49). Only nonredundant trimmed reads longer than 20 bases were retained. Filtered reads were mapped against human reference genome (UCSC hg19) using gmap software (50). Putative integration sites were filtered for match quality, requiring an identity score of $\geq$0.9 (identity score

calculated as matching nucleotides − [mismatching nucleotides + query gap + tile gap]/query size) and discarding reads with multiple identically scoring matches on the reference genome. We obtained 105,329 unique integration sites for wild-type HIV-1, 116,138 sites for the capsid mutant N74D, and 6,137 sites for the mutant N57S (Table 3). Chromosomal distributions were then compared, and a comparable number of integrations (i.e., 101,879) was selected from an MRC data set containing more than 14 million random integration sites. MRC was generated as in Cattoglio et al. (49). Each integration site was annotated for genes mapping in a ±50-kb interval and for genomic features, such as CpG islands, DNase I-hypersensitive sites, and $\alpha$- and $\beta$-satellite regions, using UCSC Genome Browser tracks. For pairwise statistical comparisons, a two-sample test for equality of proportions with continuity correction was applied, whereas to compare the average number of genes in a ±50-kb interval the Wilcoxon rank-sum test was used. All statistical analyses were performed in MATLAB (Natick, MA, USA). The full filtering, mapping, annotation, and MRC generation pipeline is freely available upon request to the authors.

**Analysis of provirus accumulation near histone modification sites.** Chromatin immunoprecipitation sequencing (ChIP-seq) histone modification data were downloaded from http://dir.nhlbi.nih.gov/papers/lmi/epigenomes/hgtcell.html as bed files of mapped data, and genome coordinates were converted from hg18 to hg19/GRCh37 genome build by the liftOver utility (51). Low-complexity regions were filtered out using the DAC Blacklist table from the UCSC Mappability track. Bed files were converted to bedGraph using BEDTools (v 2.26.0), and the data value columns were normalized on library size (i.e., total number of mapped reads). The mean signal distributions relative to the viral integration sites of the different viruses as well as of MRC were computed and plotted using deepTools2 (v 3.0.1).

**Analysis of nucleosome density around viral integration sites.** MNase-seq nucleosome positioning data publicly available for K562 cells from the ENCODE Project were downloaded from the UCSC database as a bigwig file (http://hgdownload.soe.ucsc.edu/goldenPath/hg19/encodeDCC/wgEncodeSydhNsome/wgEncodeSydhNsomeK562Sig.bigWig) (52). Data were normalized, processed, and plotted as mentioned above for ChIP-seq data.

**Accession number(s).** Coordinates and structure factors were deposited in the PDB database under accession codes 5TSV and 5TSX, respectively. Raw sequence data ofintegration experiments were uploaded to the NCBI Short Reads Archive under accession number SRP096351. The full data set, including information about the samples, can be retrieved under BioProject accession number PRJNA358663.

## ACKNOWLEDGMENTS

We are thankful to the NIH/AIDS Repository Program for providing valuable reagents, such as antibodies and drugs. We thank Jonathan Wagner for assistance with crystallography and for performing early crystallization screens. We also gratefully acknowledge technical support by Demetrio Turati and Philippe Souque.

The work was funded by NIH grants R01-GM123540 and R01-AI087390 to F.D.-G., R01-AI129678 to O.P. and B.K.G.-P., and R01-AI120956 to F.D.-G. and O.P. The work was also supported by grants from the Agence Nationale des Recherches Scientifiques (ANRS ECTZ4469), Sidaction/FRM and the Pasteur Institute, and the Italian Ministry of Health (GR-2011-02352026).

## REFERENCES

1. Rubin H, Temin HM. 1959. A radiological study of cell-virus interaction in the Rous sarcoma. Virology 7:75–91. https://doi.org/10.1016/0042-6822(59)90178-3.
2. Lewis PF, Emerman M. 1994. Passage through mitosis is required for oncoretroviruses but not for the human immunodeficiency virus. J Virol 68:510–516.
3. Roe T, Reynolds TC, Yu G, Brown PO. 1993. Integration of murine leukemia virus DNA depends on mitosis. EMBO J 12:2099–2108.
4. Lewis P, Hensel M, Emerman M. 1992. Human immunodeficiency virus infection of cells arrested in the cell cycle. EMBO J 11:3053–3058.
5. Miller MD, Farnet CM, Bushman FD. 1997. Human immunodeficiency virus type 1 preintegration complexes: studies of organization and composition. J Virol 71:5382–5390.
6. Suzuki Y, Craigie R. 2007. The road to chromatin–nuclear entry of retroviruses. Nat Rev Microbiol 5:187–196. https://doi.org/10.1038/nrmicro1579.
7. Bowerman B, Brown PO, Bishop JM, Varmus HE. 1989. A nucleoprotein complex mediates the integration of retroviral DNA. Genes Dev 3:469–478. https://doi.org/10.1101/gad.3.4.469.
8. Mattaj IW, Englmeier L. 1998. Nucleocytoplasmic transport: the soluble phase. Annu Rev Biochem 67:265–306. https://doi.org/10.1146/annurev.biochem.67.1.265.
9. Zennou V, Petit C, Guetard D, Nerhbass U, Montagnier L, Charneau P. 2000. HIV-1 genome nuclear import is mediated by a central DNA flap. Cell 101:173–185. https://doi.org/10.1016/S0092-8674(00)80828-4.
10. De Rijck J, Vandekerckhove L, Christ F, Debyser Z. 2007. Lentiviral nuclear import: a complex interplay between virus and host. Bioessays 29:441–451. https://doi.org/10.1002/bies.20561.
11. Fassati A. 2006. HIV infection of non-dividing cells: a divisive problem. Retrovirology 3:74. https://doi.org/10.1186/1742-4690-3-74.
12. Fassati A, Goff SP. 2001. Characterization ofintracellular reverse transcription complexes of human immunodeficiency virus type 1. J Virol 75:3626–3635. https://doi.org/10.1128/JVI.75.8.3626-3635.2001.
13. Iordanskiy S, Berro R, Altieri M, Kashanchi F, Bukrinsky M. 2006. Intracytoplasmic maturation of the human immunodeficiency virus type 1 reverse transcription complexes determines their capacity to integrate into chromatin. Retrovirology 3:4. https://doi.org/10.1186/1742-4690-3-4.
14. Bukrinsky MI, Sharova N, McDonald TL, Pushkarskaya T, Tarpley WG, Stevenson M. 1993. Association ofintegrase, matrix, and reverse transcriptase antigens of human immunodeficiency virus type 1 with viral nucleic acids following acute infection. Proc Natl Acad Sci U S A 90:6125–6129. https://doi.org/10.1073/pnas.90.13.6125.
15. Yamashita M, Emerman M. 2006. Retroviral infection of non-dividing cells: old and new perspectives. Virology 344:88–93. https://doi.org/10.1016/j.virol.2005.09.012.
16. Yamashita M, Emerman M. 2004. Capsid is a dominant determinant of retrovirus infectivity in nondividing cells. J Virol 78:5670–5678. https://doi.org/10.1128/JVI.78.11.5670-5678.2004.
17. Yamashita M, Perez O, Hope TJ, Emerman M. 2007. Evidence for direct

involvement of the capsid protein in HIV infection of nondividing cells. PLoS Pathog 3:1502–1510. https://doi.org/10.1371/journal.ppat.0030156.
18. Arhel NJ, Souquere-Besse S, Munier S, Souque P, Guadagnini S, Rutherford S, Prevost MC, Allen TD, Charneau P. 2007. HIV-1 DNA flap formation promotes uncoating of the pre-integration complex at the nuclear pore. EMBO J 26:3025–3037. https://doi.org/10.1038/sj.emboj.7601740.
19. Di Nunzio F, Danckaert A, Fricke T, Perez P, Fernandez J, Perret E, Roux P, Shorte S, Charneau P, Diaz-Griffero F, Arhel NJ. 2012. Human nucleoporins promote HIV-1 docking at the nuclear pore, nuclear import and integration. PLoS One 7:e46037. https://doi.org/10.1371/journal.pone.0046037.
20. Fassati A, Gorlich D, Harrison I, Zaytseva L, Mingot JM. 2003. Nuclear import of HIV-1 intracellular reverse transcription complexes is mediated by importin 7. EMBO J 22:3675–3685. https://doi.org/10.1093/emboj/cdg357.
21. Zaitseva L, Cherepanov P, Leyens L, Wilson SJ, Rasaiyaah J, Fassati A. 2009. HIV-1 exploits importin 7 to maximize nuclear import ofits DNA genome. Retrovirology 6:11. https://doi.org/10.1186/1742-4690-6-11.
22. Ao Z, Huang G, Yao H, Xu Z, Labine M, Cochrane AW, Yao X. 2007. Interaction of human immunodeficiency virus type 1 integrase with cellular nuclear import receptor importin 7 and its impact on viral replication. J Biol Chem 282:13456–13467. https://doi.org/10.1074/jbc.M610546200.
23. Ao Z, Danappa Jayappa K, Wang B, Zheng Y, Kung S, Rassart E, Depping R, Kohler M, Cohen EA, Yao X. 2010. Importin alpha3 interacts with HIV-1 integrase and contributes to HIV-1 nuclear import and replication. J Virol 84:8650–8663. https://doi.org/10.1128/JVI.00508-10.
24. Gallay P, Hope T, Chin D, Trono D. 1997. HIV-1 infection of nondividing cells through the recognition ofintegrase by the importin/karyopherin pathway. Proc Natl Acad Sci U S A 94:9825–9830. https://doi.org/10.1073/pnas.94.18.9825.
25. Hearps AC, Jans DA. 2006. HIV-1 integrase is capable of targeting DNA to the nucleus via an importin alpha/beta-dependent mechanism. Biochem J 398:475–484. https://doi.org/10.1042/BJ20060466.
26. Valle-Casuso JC, Di Nunzio F, Yang Y, Reszka N, Lienlaf M, Arhel N, Perez P, Brass AL, Diaz-Griffero F. 2012. TNPO3 is required for HIV-1 replication after nuclear import but prior to integration and binds the HIV-1 core. J Virol 86:5931–5936.
27. Christ F, Thys W, De Rijck J, Gijsbers R, Albanese A, Arosio D, Emiliani S, Rain JC, Benarous R, Cereseto A, Debyser Z. 2008. Transportin-SR2 imports HIV into the nucleus. Curr Biol 18:1192–1202. https://doi.org/10.1016/j.cub.2008.07.079.
28. Brass AL, Dykxhoorn DM, Benita Y, Yan N, Engelman A, Xavier RJ, Lieberman J, Elledge SJ. 2008. Identification of host proteins required for HIV infection through a functional genomic screen. Science 319:921–926. https://doi.org/10.1126/science.1152725.
29. Krishnan L, Matreyek KA, Oztop I, Lee K, Tipper CH, Li X, Dar MJ, Kewalramani VN, Engelman A. 2010. The requirement for cellular transportin 3 (TNPO3 or TRN-SR2) during infection maps to human immunodeficiency virus type 1 capsid and not integrase. J Virol 84:397–406. https://doi.org/10.1128/JVI.01899-09.
30. Thys W, De Houwer S, Demeulemeester J, Taltynov O, Vancraenenbroeck R, Gerard M, De Rijck J, Gijsbers R, Christ F, Debyser Z. 2011. Interplay between HIV entry and transportin-SR2 dependency. Retrovirology 8:7. https://doi.org/10.1186/1742-4690-8-7.
31. Levin A, Hayouka Z, Friedler A, Loyter A. 2010. Transportin 3 and importin alpha are required for effective nuclear import of HIV-1 integrase in virus-infected cells. Nucleus 1:422–431. https://doi.org/10.4161/nucl.1.5.12903.
32. Konig R, Zhou Y, Elleder D, Diamond TL, Bonamy GM, Irelan JT, Chiang CY, Tu BP, De Jesus PD, Lilley CE, Seidel S, Opaluch AM, Caldwell JS, Weitzman MD, Kuhen KL, Bandyopadhyay S, Ideker T, Orth AP, Miraglia LJ, Bushman FD, Young JA, Chanda SK. 2008. Global analysis of host-pathogen interactions that regulate early-stage HIV-1 replication. Cell 135:49–60. https://doi.org/10.1016/j.cell.2008.07.032.
33. Zhou H, Xu M, Huang Q, Gates AT, Zhang XD, Castle JC, Stec E, Ferrer M, Strulovici B, Hazuda DJ, Espeseth AS. 2008. Genome-scale RNAi screen for host factors required for HIV replication. Cell Host Microbe 4:495–504. https://doi.org/10.1016/j.chom.2008.10.004.
34. Ocwieja KE, Brady TL, Ronen K, Huegel A, Roth SL, Schaller T, James LC, Towers GJ, Young JA, Chanda SK, Konig R, Malani N, Berry CC, Bushman FD. 2011. HIV integration targeting: a pathway involving Transportin-3 and the nuclear pore protein RanBP2. PLoS Pathog 7:e1001313. https://doi.org/10.1371/journal.ppat.1001313.
35. Di Nunzio F, Fricke T, Miccio A, Valle-Casuso JC, Perez P, Souque P, Rizzi E, Severgnini M, Mavilio F, Charneau P, Diaz-Griffero F. 2013. Nup153 and Nup98 bind the HIV-1 core and contribute to the early steps of HIV-1 replication. Virology 440:8–18. https://doi.org/10.1016/j.virol.2013.02.008.
36. Woodward CL, Prakobwanakit S, Mosessian S, Chow SA. 2009. Integrase interacts with nucleoporin NUP153 to mediate the nuclear import of human immunodeficiency virus type 1. J Virol 83:6522–6533. https://doi.org/10.1128/JVI.02061-08.
37. Lee K, Ambrose Z, Martin TD, Oztop I, Mulky A, Julias JG, Vandegraaff N, Baumann JG, Wang R, Yuen W, Takemura T, Shelton K, Taniuchi I, Li Y, Sodroski J, Littman DR, Coffin JM, Hughes SH, Unutmaz D, Engelman A, KewalRamani VN. 2010. Flexible use of nuclear import pathways by HIV-1. Cell Host Microbe 7:221–233. https://doi.org/10.1016/j.chom.2010.02.007.
38. Matreyek KA, Engelman A. 2011. The requirement for nucleoporin NUP153 during human immunodeficiency virus type 1 infection is determined by the viral capsid. J Virol 85:7818–7827. https://doi.org/10.1128/JVI.00325-11.
39. Lelek M, Casartelli N, Pellin D, Rizzi E, Souque P, Severgnini M, Di Serio C, Fricke T, Diaz-Griffero F, Zimmer C, Charneau P, Di Nunzio F. 2015. Chromatin organization at the nuclear pore favours HIV replication. Nat Commun 6:6483. https://doi.org/10.1038/ncomms7483.
40. Matreyek KA, Yucel SS, Li X, Engelman A. 2013. Nucleoporin NUP153 phenylalanine-glycine motifs engage a common binding pocket within the HIV-1 capsid protein to mediate lentiviral infectivity. PLoS Pathog 9:e1003693. https://doi.org/10.1371/journal.ppat.1003693.
41. Schaller T, Ocwieja KE, Rasaiyaah J, Price AJ, Brady TL, Roth SL, Hue S, Fletcher AJ, Lee K, KewalRamani VN, Noursadeghi M, Jenner RG, James LC, Bushman FD, Towers GJ. 2011. HIV-1 capsid-cyclophilin interactions determine nuclear import pathway, integration targeting and replication efficiency. PLoS Pathog 7:e1002439. https://doi.org/10.1371/journal.ppat.1002439.
42. Bhattacharya A, Alam SL, Fricke T, Zadrozny K, Sedzicki J, Taylor AB, Demeler B, Pornillos O, Ganser-Pornillos BK, Diaz-Griffero F, Ivanov DN, Yeager M. 2014. Structural basis of HIV-1 capsid recognition by PF74 and CPSF6. Proc Natl Acad Sci U S A 111:18625–18630. https://doi.org/10.1073/pnas.1419945112.
43. Price AJ, Jacques DA, McEwan WA, Fletcher AJ, Essig S, Chin JW, Halambage UD, Aiken C, James LC. 2014. Host cofactors and pharmacologic ligands share an essential interface in HIV-1 capsid that is lost upon disassembly. PLoS Pathog 10:e1004459. https://doi.org/10.1371/journal.ppat.1004459.
44. Price AJ, Fletcher AJ, Schaller T, Elliott T, Lee K, KewalRamani VN, Chin JW, Towers GJ, James LC. 2012. CPSF6 defines a conserved capsid interface that modulates HIV-1 replication. PLoS Pathog 8:e1002896. https://doi.org/10.1371/journal.ppat.1002896.
45. Sowd GA, Serrao E, Wang H, Wang W, Fadel HJ, Poeschla EM, Engelman AN. 2016. A critical role for alternative polyadenylation factor CPSF6 in targeting HIV-1 integration to transcriptionally active chromatin. Proc Natl Acad Sci U S A 113:E1054–E1063. https://doi.org/10.1073/pnas.1524213113.
46. Ganser BK, Li S, Klishko VY, Finch JT, Sundquist WI. 1999. Assembly and analysis of conical models for the HIV-1 core. Science 283:80–83. https://doi.org/10.1126/science.283.5398.80.
47. Ganser-Pornillos BK, von Schwedler UK, Stray KM, Aiken C, Sundquist WI. 2004. Assembly properties of the human immunodeficiency virus type 1 CA protein. J Virol 78:2545–2552. https://doi.org/10.1128/JVI.78.5.2545-2552.2004.
48. Butler SL, Hansen MS, Bushman FD. 2001. A quantitative assay for HIV DNA integration in vivo. Nat Med 7:631–634. https://doi.org/10.1038/87979.
49. Cattoglio C, Pellin D, Rizzi E, Maruggi G, Corti G, Miselli F, Sartori D, Guffanti A, Di Serio C, Ambrosi A, De Bellis G, Mavilio F. 2010. High-definition mapping of retroviral integration sites identifies active regulatory elements in human multipotent hematopoietic progenitors. Blood 116:5507–5517. https://doi.org/10.1182/blood-2010-05-283523.
50. Wu TD, Watanabe CK. 2005. GMAP: a genomic mapping and alignment program for mRNA and EST sequences. Bioinformatics 21:1859–1875. https://doi.org/10.1093/bioinformatics/bti310.
51. Barski A, Cuddapah S, Cui K, Roh TY, Schones DE, Wang Z, Wei G, Chepelev I, Zhao K. 2007. High-resolution profiling of histone methylations in the human genome. Cell 129:823–837. https://doi.org/10.1016/j.cell.2007.05.009.

52. ENCODE Project Consortium. 2012. An integrated encyclopedia of DNA elements in the human genome. Nature 489:57–74. https://doi.org/10.1038/nature11247.
53. von Schwedler UK, Stemmler TL, Klishko VY, Li S, Albertine KH, Davis DR, Sundquist WI. 1998. Proteolytic refolding of the HIV-1 capsid protein amino-terminus facilitates viral core assembly. EMBO J 17:1555–1568. https://doi.org/10.1093/emboj/17.6.1555.
54. Park EK, Jung HS, Yang HI, Yoo MC, Kim C, Kim KS. 2007. Optimized THP-1 differentiation is required for the detection of responses to weak stimuli. Inflamm Res 56:45–50. https://doi.org/10.1007/s00011-007-6115-5.
55. Yang Y, Luban J, Diaz-Griffero F. 2014. The fate of HIV-1 capsid: a biochemical assay for HIV-1 uncoating. Methods Mol Biol 1087:29–36. https://doi.org/10.1007/978-1-62703-670-2_3.
56. Kortagere S, Madani N, Mankowski MK, Schon A, Zentner I, Swaminathan G, Princiotto A, Anthony K, Oza A, Sierra LJ, Passic SR, Wang X, Jones DM, Stavale E, Krebs FC, Martin-Garcia J, Freire E, Ptak RG, Sodroski J, Cocklin S, Smith AB, III. 2012. Inhibiting early-stage events in HIV-1 replication by small-molecule targeting of the HIV-1 capsid. J Virol 86:8472–8481. https://doi.org/10.1128/JVI.05006-11.
57. Diaz-Griffero F, Qin XR, Hayashi F, Kigawa T, Finzi A, Sarnak Z, Lienlaf M, Yokoyama S, Sodroski J. 2009. A B-box 2 surface patch important for TRIM5alpha self-association, capsid binding avidity, and retrovirus restriction. J Virol 83:10737–10751. https://doi.org/10.1128/JVI.01307-09.
58. Fricke T, White TE, Schulte B, de Souza Aranha Vieira DA, Dharan A, Campbell EM, Brandariz-Nunez A, Diaz-Griffero F. 2014. MxB binds to the HIV-1 core and prevents the uncoating process of HIV-1. Retrovirology 11:68. https://doi.org/10.1186/s12977-014-0068-x.
59. Fricke T, Valle-Casuso JC, White TE, Brandariz-Nunez A, Bosche WJ, Reszka N, Gorelick R, Diaz-Griffero F. 2013. The ability of TNPO3-depleted cells to inhibit HIV-1 infection requires CPSF6. Retrovirology 10:46. https://doi.org/10.1186/1742-4690-10-46.
60. Ao Z, Jayappa KD, Wang B, Zheng Y, Wang X, Peng J, Yao X. 2012. Contribution of host nucleoporin 62 in HIV-1 integrase chromatin association and viral DNA integration. J Biol Chem 287:10544–10555. https://doi.org/10.1074/jbc.M111.317057.
61. Marini B, Kertesz-Farkas A, Ali H, Lucic B, Lisek K, Manganaro L, Pongor S, Luzzati R, Recchia A, Mavilio F, Giacca M, Lusic M. 2015. Nuclear architecture dictates HIV-1 integration site selection. Nature 521:227–231. https://doi.org/10.1038/nature14226.
62. Diaz-Griffero F, Vandegraaff N, Li Y, McGee-Estrada K, Stremlau M, Welikala S, Si Z, Engelman A, Sodroski J. 2006. Requirements for capsid-binding and an effector function in TRIMCyp-mediated restriction of HIV-1. Virology 351:404–419. https://doi.org/10.1016/j.virol.2006.03.023.
63. Mitchell RS, Beitzel BF, Schroder AR, Shinn P, Chen H, Berry CC, Ecker JR, Bushman FD. 2004. Retroviral DNA integration: ASLV, HIV, and MLV show distinct target site preferences. PLoS Biol 2:E234. https://doi.org/10.1371/journal.pbio.0020234.
64. Wang GP, Levine BL, Binder GK, Berry CC, Malani N, McGarrity G, Tebas P, June CH, Bushman FD. 2009. Analysis oflentiviral vector integration in HIV+ study subjects receiving autologous infusions of gene modified CD4+ T cells. Mol Ther 17:844–850. https://doi.org/10.1038/mt.2009.16.
65. Ciuffi A, Llano M, Poeschla E, Hoffmann C, Leipzig J, Shinn P, Ecker JR, Bushman F. 2005. A role for LEDGF/p75 in targeting HIV DNA integration. Nat Med 11:1287–1289. https://doi.org/10.1038/nm1329.
66. Benleulmi MS, Matysiak J, Henriquez DR, Vaillant C, Lesbats P, Calmels C, Naughtin M, Leon O, Skalka AM, Ruff M, Lavigne M, Andreola ML, Parissi V. 2015. Intasome architecture and chromatin density modulate retroviral integration into nucleosome. Retrovirology 12:13. https://doi.org/10.1186/s12977-015-0145-9.
67. Lesbats P, Botbol Y, Chevereau G, Vaillant C, Calmels C, Arneodo A, Andreola ML, Lavigne M, Parissi V. 2011. Functional coupling between HIV-1 integrase and the SWI/SNF chromatin remodeling complex for efficient in vitro integration into stable nucleosomes. PLoS Pathog 7:e1001280. https://doi.org/10.1371/journal.ppat.1001280.
68. Nakielny S, Shaikh S, Burke B, Dreyfuss G. 1999. Nup153 is an M9-containing mobile nucleoporin with a novel Ran-binding domain. EMBO J 18:1982–1995. https://doi.org/10.1093/emboj/18.7.1982.
69. Fricke T, Buffone C, Opp S, Valle-Casuso J, Diaz-Griffero F. 2014. BI-2 destabilizes HIV-1 cores during infection and prevents binding of CPSF6 to the HIV-1 capsid. Retrovirology 11:120. https://doi.org/10.1186/s12977-014-0120-x.
70. Lamorte L, Titolo S, Lemke CT, Goudreau N, Mercier JF, Wardrop E, Shah VB, von Schwedler UK, Langelier C, Banik SS, Aiken C, Sundquist WI, Mason SW. 2013. Discovery of novel small-molecule HIV-1 replication inhibitors that stabilize capsid complexes. Antimicrob Agents Chemother 57:4622–4631. https://doi.org/10.1128/AAC.00985-13.
71. Singh PK, Plumb MR, Ferris AL, Iben JR, Wu X, Fadel HJ, Luke BT, Esnault C, Poeschla EM, Hughes SH, Kvaratskhelia M, Levin HL. 2015. LEDGF/p75 interacts with mRNA splicing factors and targets HIV-1 integration to highly spliced genes. Genes Dev 29:2287–2297. https://doi.org/10.1101/gad.267609.115.
72. Le Rouzic E, Bonnard D, Chasset S, Bruneau JM, Chevreuil F, Le Strat F, Nguyen J, Beauvoir R, Amadori C, Brias J, Vomscheid S, Eiler S, Levy N, Delelis O, Deprez E, Saib A, Zamborlini A, Emiliani S, Ruff M, Ledoussal B, Moreau F, Benarous R. 2013. Dual inhibition of HIV-1 replication by integrase-LEDGF allosteric inhibitors is predominant at the post-integration stage. Retrovirology 10:144. https://doi.org/10.1186/1742-4690-10-144.
73. Wang H, Jurado KA, Wu X, Shun MC, Li X, Ferris AL, Smith SJ, Patel PA, Fuchs JR, Cherepanov P, Kvaratskhelia M, Hughes SH, Engelman A. 2012. HRP2 determines the efficiency and specificity of HIV-1 integration in LEDGF/p75 knockout cells but does not contribute to the antiviral activity of a potent LEDGF/p75-binding site integrase inhibitor. Nucleic Acids Res 40:11518–11530. https://doi.org/10.1093/nar/gks913.
74. Schrijvers R, Vets S, De Rijck J, Malani N, Bushman FD, Debyser Z, Gijsbers R. 2012. HRP-2 determines HIV-1 integration site selection in LEDGF/p75 depleted cells. Retrovirology 9:84. https://doi.org/10.1186/1742-4690-9-84.
75. Levin A, Rosenbluh J, Hayouka Z, Friedler A, Loyter A. 2010. Integration of HIV-1 DNA is regulated by interplay between viral rev and cellular LEDGF/p75 proteins. Mol Med 16:34–44. https://doi.org/10.2119/molmed.2009.00133.
76. Levin A, Hayouka Z, Friedler A, Loyter A. 2010. Peptides derived from the HIV-1 integrase promote HIV-1 infection and multi-integration of viral cDNA in LEDGF/p75-knockdown cells. Virol J 7:177.
77. Michel F, Crucifix C, Granger F, Eiler S, Mouscadet JF, Korolev S, Agapkina J, Ziganshin R, Gottikh M, Nazabal A, Emiliani S, Benarous R, Moras D, Schultz P, Ruff M. 2009. Structural basis for HIV-1 DNA integration in the human genome, role of the LEDGF/P75 cofactor. EMBO J 28:980–991. https://doi.org/10.1038/emboj.2009.41.
78. Botbol Y, Raghavendra NK, Rahman S, Engelman A, Lavigne M. 2008. Chromatinized templates reveal the requirement for the LEDGF/p75 PWWP domain during HIV-1 integration in vitro. Nucleic Acids Res 36:1237–1246. https://doi.org/10.1093/nar/gkm1127.
79. Shun MC, Raghavendra NK, Vandegraaff N, Daigle JE, Hughes S, Kellam P, Cherepanov P, Engelman A. 2007. LEDGF/p75 functions downstream from preintegration complex formation to effect gene-specific HIV-1 integration. Genes Dev 21:1767–1778. https://doi.org/10.1101/gad.1565107.
80. Raghavendra NK, Engelman A. 2007. LEDGF/p75 interferes with the formation of synaptic nucleoprotein complexes that catalyze full-site HIV-1 DNA integration in vitro: implications for the mechanism of viral cDNA integration. Virology 360:1–5. https://doi.org/10.1016/j.virol.2006.12.022.
81. Sharma A, Larue RC, Plumb MR, Malani N, Male F, Slaughter A, Kessl JJ, Shkriabai N, Coward E, Aiyer SS, Green PL, Wu L, Roth MJ, Bushman FD, Kvaratskhelia M. 2013. BET proteins promote efficient murine leukemia virus integration at transcription start sites. Proc Natl Acad Sci U S A 110:12036–12041. https://doi.org/10.1073/pnas.1307157110.
82. De Rijck J, de Kogel C, Demeulemeester J, Vets S, El Ashkar S, Malani N, Bushman FD, Landuyt B, Husson SJ, Busschots K, Gijsbers R, Debyser Z. 2013. The BET family of proteins targets moloney murine leukemia virus integration near transcription start sites. Cell Rep 5:886–894. https://doi.org/10.1016/j.celrep.2013.09.040.
83. Koh Y, Wu X, Ferris AL, Matreyek KA, Smith SJ, Lee K, Kewalramani VN, Hughes SH, Engelman A. 2013. Differential effects of human immunodeficiency virus type 1 capsid and cellular factors nucleoporin 153 and LEDGF/p75 on the efficiency and specificity of viral DNA integration. J Virol 87:648–658. https://doi.org/10.1128/JVI.01148-12.